# MAGNETIC PROPERTIES OF Co AND Mn SUBSTITUTED Fe–Zr–B ALLOYS PREPARED BY MELT SPINNING AND MECHANICAL ALLOYING PROCESSES

*A thesis submitted*

by

**Debabrata Mishra**

to

Indian Institute of Technology Guwahati

in

partial fulfillment of the requirement for the award of the degree of
Doctor of Philosophy in Physics

Department of Physics
Indian Institute of Technology Guwahati
Guwahati – 781039, Assam, India
December 2009

## Statement

The work contained in the thesis entitled "Magnetic properties of Co and Mn substituted Fe-Zr-B alloys prepared by melt spinning and mechanical alloying processes" has been carried out by me under the supervision of Dr. A. Perumal and Prof. A. Srinivasan, at Department of Physics, Indian Institute of Technology Guwahati, Guwahati, India. This work has not been submitted elsewhere for the award of any degree.

29th December 2009

Debabrata Mishra

(Debabrata Mishra)

Roll No: 05612107,

Department of Physics,

Indian Institute of Technology Guwahati,

Guwahati – 781039,

India.

# Certificate

It is certified that the work contained in the thesis entitled "Magnetic properties of Co and Mn substituted Fe-Zr-B alloys prepared by melt spinning and mechanical alloying processes" submitted by Debabrata Mishra, a Ph. D. student of the Department of Physics, Indian Institute of Technology Guwahati, Guwahati, India for the award of degree of Doctor of Philosophy has been carried out under the supervision of myself and Prof. A. Srinivasan. This work has not been submitted elsewhere for the award of any degree.

29th December 2009

(Dr. A. Perumal)
Associate Professor,
Department of Physics,
Indian Institute of Technology Guwahati,
Guwahati – 781039,
India.

*Dedicated to my*

*beloved parents*

## Acknowledgements

It is my privilege to express deep sense of gratitude to my thesis supervisors Dr. A. Perumal and Prof. A. Srinivasan for their resourceful guidance, constructive criticisms and meticulous supervision in guiding me throughout my research work. I am grateful to Dr. A. Perumal for extending his support all through these periods inspiring me for doing a quality research work. His continuous encouragement and intellectual discussions has been a driving force for me to excel in my work. I am very much thankful to Prof A. Srinivasan for his guidance and consistent support during my research period which has enabled me to reach this stage. His comments and great insight in to my work has helped me immensely in improving my thesis. I am grateful to my doctoral committee members, Dr. S. Ravi, Dr. Dilip Pal and Dr. Manabendra Ray for reviewing my research work regularly and giving valuable suggestions for the improvement of my research work. I am thankful to Dr. S. Ravi, HOD, Department of Physics, for his support.

I am very much thankful to Prof. Kazuhiro Hono, NIMS, Japan for allowing us to use melt spinner for making ribbons for my research work. I am also thankful to Dr. P. Saravanan for coercivity measurements.

I express my sincere thanks to the lab personnel, Department of physics, Mr. Atul Deka, Mr. Bimal K. Sarma and Mr. Pankaj Goswami for their support and cooperation during the course of my Ph.D. work.

Mr. Chandan Borgohain and Mr. Kula Senapati, Scientific Officers of CIF, and all the members of mechanical workshop have patiently and enthusiastically extended their expertise in various instruments that I have used for my research work and in fabrication of essential components required for my research work.

I am fortunate to have Dr. Sidananda Sarma, Dr. M.P.C. Kalita, Rajendra and Rahul as my fellow researchers in the same group. Anto, Gourav, Sunish, Veena, Meera, Poulumi, Bishwanath, Biswanath Samantray, Suneeta, Sangeetha, Vindhya and all the research scholars of Physics Department will always be remembered for the wonderful time we shared together. Discussions and fun with Manos, Gouri Shankar and their company has added value during the stay in IITG. I thank Jugal, Subash, Nihar, Naresh and all my friends for the memorable life in IITG campus.

I am deeply indebted to my beloved parents, brother and sisters for their moral support and constant encouragements for my progress. Finally, my sincere thanks are

due to all those who have helped me in whatever manner during my Ph.D. work, some of whom I may have inadvertently forgotten to mention in this acknowledgement.

Debabarta Mishra

## PREFACE

Fe-Zr-B based amorphous and nanocrystalline alloys are well known soft magnetic materials which are characterized by high saturation magnetization ($M_S$) and low coercivity ($H_C$). These soft magnetic alloys find wide applications in high-performance magnetic parts such as in electronic devices, common mode choke-coils, power electronics, bead cores, electrical noise absorbers, magnetic switch cores, transformers, current sensors and electromagnetic shielding, magnetic refrigerants, magnetoimpedance devices etc. These materials are prepared through melt spinning and mechanical alloying (MA) routes by controlled crystallization of amorphous precursors and structural reduction of crystallites by the introduction of defects and dislocations, respectively. Conventional methods of improving the intrinsic and extrinsic soft magnetic properties focus on tailoring composition, control of microstructure with heat treatment under different environments, reduction of $H_C$, increase of $M_S$ and control of intergranular exchange coupling in the amorphous and nanocrystalline materials. Hence, preparing Fe-Zr-B based amorphous and nanocrystalline alloys through different synthesis routes and understanding the correlation between the structural and magnetic properties of these materials over a wide composition range are very much important from basic physics as well as application view point.

This thesis work aims to (i) understand the effect of substituting elements (B, Co, and Mn) on the stability of amorphous phase and temperature dependent magnetic properties of amorphous (a-)Fe-Zr based alloys prepared by melt spinning and MA routes, (ii) study the magnetocaloric effect (MCE) in amorphous ribbons, and (iii) investigate the effect of magnetic field annealing on the improvement of soft magnetic properties of the melt-spun ribbons in correlation with microstructure and magnetic domain structure.

The thesis is presented in eight chapters. The first chapter serves as a general introduction to the materials of interest to this work, motivation behind the work with historical perspective from the literature and the objectives of the thesis work.

A brief description of fundamental aspects of magnetism and the theoretical formalisms relevant to the contents of the thesis can be found in Chapter 2.

In Chapter 3, the experimental techniques used for materials processing and characterization of the materials are outlined.

In Chapter 4, the results and discussion on the physical properties of a-Fe-(Co,Mn)-Zr-B alloy ribbons have been presented. Structural property study showed the formation of single phase Fe rich amorphous structure in all the ribbon samples. The thermal stability of the amorphous phase was improved with the addition of B in a-Fe-Zr alloys and further enhanced with Mn addition in a-Fe-Zr-B alloy ribbons. Room temperature $M_S$, Curie temperature ($T_C$) of the Fe-Zr-B alloys improved with B addition, while $H_C$ decreased largely to 0.015 Oe for 5 at.% B addition and increased slightly with the further increase in B content. Lorentz microscopy studies revealed large-sized domains with relatively smooth and straight domain walls in a-Fe-Zr-B alloys, but the average size decreased when B content was increased above 5 at.%. $T_C$ and $M_S$ decreased (increased) with the addition of Mn (Co) in a-Fe(Co,Mn)-Zr-B alloys. A maximum $M_S$ value of about 130 emu/g and $H_C$ of 0.4 Oe were obtained for a-$Fe_{69}Co_{10}Zr_{11}B_{10}$ alloy ribbon. Moderate values of magnetic entropy ($\Delta S_M$) were obtained for a-Fe-(Co,Mn)-Zr-B alloys. Addition of Co (Mn) in a-Fe-(Co,Mn)-Zr-B alloys increased (decreased) the $\Delta S_M$ value and a maximum $\Delta S_M$ value of 1.93 J/Kg/K at 18 kOe could be achieved for a-$Fe_{74}Co_{10}Zr_{11}B_5$ alloy.

Chapter 5 is devoted to the understanding of the evolution of microstructure and soft magnetic properties in correlation with the magnetic domain structure of nanocrystalline Fe-(Co,Mn)-Zr-B alloy ribbons subjected to longitudinal magnetic field annealing. Annealing at 823 K showed a weak tendency for the formation of $\alpha$-Fe nanocrystals which is associated with other Fe-Zr compounds such as $Fe_3Zr$ at elevated temperatures. The rate of increase of $H_C$ decreased in Fe-Co-Zr-B alloys with the substitution of higher amount of B. Magnetic domain structure analysis revealed the presence of large-sized domains with smooth and straight domain walls in Fe-Co-Zr-B alloys annealed up to 823 K. A maximum $M_S$ value of 175 emu/g and $H_C$ of 0.35 Oe were obtained for the $Fe_{69}Co_{10}Zr_{11}B_{10}$ alloy annealed at 823 K exhibiting excellent soft magnetic properties. A good correlation between nanocrystalline microstructure, magnetic domain structure and resulting magnetic properties in Fe-Co-Zr-B alloy ribbons was obtained.

In Chapter 6, a detailed study of structural, thermal and magnetic properties of a-Fe-(Co,Mn)-Zr-B alloy powders prepared by MA technique is presented. The

milling conditions required for the formation of amorphous phase highly depends on the composition of the alloy systems. The formation of binary a-Fe-Zr alloy powders could be achieved over a wide range of Zr content (25 – 35 at.%). $H_C$ is relatively large both in the nanocrystalline state and amorphous phase due to the induced stress during MA. Low temperature magnetic properties of a-Fe-Zr powders showed strong bifurcation between ZFC and FC curves. The bifurcation was observed even at 10 kOe applied field. $T_C$ in ball milled powders was observed to be high (compared to melt-spun ribbons) due to the enhanced magnetoelastic coupling. Stability of the amorphous phase was enhanced with the addition of B and Mn in Fe-Mn-Zr-B alloy. Also, B and Mn additions were found to decrease the effective anisotropy of the system and make the system more homogeneous. On the other hand, Co substitution in a-Fe-Co-Zr-B alloy reduced the stability of the amorphous phase. $M_S$ and $H_C$ values increased due to the increase in exchange interactions and local anisotropy, respectively.

A comparative study of various properties of Fe(Co,Mn)-Zr-B alloys prepared by melt spinning and mechanical alloying techniques is outlined in Chapter 7.

Chapter 8 serves as a concluding chapter where in the scope for future work in this area is also pointed out in brief.

References and list of publications which have originated out of this thesis work are listed at the end of the thesis.

## CONTENTS


# *Chapter 1*

# *Prologue*

## 1.1. Introduction

Amorphous solids consist of a random aggregate of atoms whose atomic positions are strongly correlated in the nearest neighbor shell but uncorrelated beyond a few atomic spacing. In other words, these materials possess short-range atomic order and the structure of these solids resembles that of liquids from which they have been obtained. Molten metal and metallic alloys invariably crystallize in their equilibrium crystalline structures when cooled below their freezing points. Duwez [DUWE1967] and his co-workers were the first to synthesize amorphous metallic alloys by a rapid solidification technique. This pioneering work initiated a spurt of research activity on synthesizing and exploring the exciting new phenomena exhibited by various amorphous metallic alloys [REVIEW01]. Amorphous alloys can be obtained through two diverse routes, viz., rapid solidification (e.g. melt spinning) and mechanical alloying. Rapid solidification is a non-equilibrium process and is based on the principle of cooling the molten alloy 'fast enough and far enough'. In this process, the molten alloy is not permitted to crystallize and made to solidify into a metastable state. Most of these metastable or super cooled liquids exhibit a 'glass transition' and hence are also referred to as metallic glasses. In the melt spinning technique, the molten alloy is ejected through the orifice at the bottom of the tube by pressurized Argon gas on to a water-cooled copper wheel rotating at a high speed under Ar gas atmosphere [ANAN1984]. This process provides a fast cooling or quenching rate for the molten alloy of the order of $10^5$ K/s [ELLI1986]. On the other hand, mechanical alloying (MA) technique is a complex process involving deformation, fragmentation, cold welding and micro-diffusion of elements in the solid state in a highly energetic grinding media [KOCH1997, SURY2000]. One of the main advantages of studies on amorphous alloys is that one can vary the composition continuously to prepare homogeneous alloys, which can be studied without complicating interference from the structural phase transitions. A special class of amorphous metallic alloys popularly known as bulk metallic glasses (BMG) can be synthesized from the melt with very low cooling rates [SCHN2001]. BMG are not discussed further since this thesis is focused on soft magnetic materials which can be obtained only by rapid solidification or MA techniques.

There are four technologically important classes of magnetic amorphous alloys: (i) Transition Metal (TM) – Metalloid (M), (ii) Early Transition Metal (ETM) – Late Transition Metal (LTM), (iii) Rare earth transition metal and (iv) Alloys with group IIA elements. Magnetism in LTM – ETM amorphous alloys has been extensively investigated from both

fundamental and technological points of view [CHEI1995, KANE1992, LUBO1983]. Also, considerable efforts have been devoted to the understanding of systems with frustration arising either from competing exchange interactions or from random magnetic anisotropy [BAKO1995, HERN1987]. Many alloy systems with competing exchange interactions show novel phenomena such as double magnetic phase transition behavior, invar effect, resistivity anomalies and magnetocaloric behavior in the amorphous phase [FANG2009, KAUL1992, PERU2002, SHEN1991]. Furthermore, these alloys in nanocrystalline state exhibit outstanding soft magnetic properties, such as ultra low coercivity ($H_C$), high saturation magnetization ($M_S$), and high permeability [HONO2002, MCHE1999, LIUY2006, SUZU1990]. Hence, these alloys have been a fertile ground for the exploration of novel magnetism. It is well known that the general composition of such alloys is LTM – ETM – M, where LTM is generally body centered cubic (bcc) Fe in the range 50 – 93 at.%, ETM typically consists of Zr, Nb, Hf, etc. The nanocrystalline materials can be obtained through (i) controlled crystallization of amorphous precursors [MCHE1999] and (ii) MA technique. The obtained nanostructured powders from MA consist of particles composed of nanometer sized crystalline grains linked one to another through grain boundaries, but highly refined and strained [KOCH1997, SURY2000]. These nanocrystalline materials find wide applications primarily for high-performance magnetic parts, such as in electronic devices, common mode choke-coils, power electronics, bead cores, noise absorbers, magnetic switch cores, transformers, current sensors and electromagnetic shielding. Apart from the soft magnetic applications, these materials are used as magnetic refrigerants based on the principle of magnetocaloric effect and are also used in magnetic impedance purposes.

### 1.2. Motivation behind the work with historical perspective from the literature

Amorphous (a-) Fe-Zr binary alloy with high Zr content is chosen as the parent system in the present investigation. The choice is dictated by the fact that this alloy system exhibits complex magnetic properties in the amorphous state due to the existence of noncollinear spin structure [COEY1987, KANE1992, KAUL1985, LUBO1983, SATI1986]. Addition of B in a-Fe-Zr alloys enhances the glass forming range and stability of the amorphous phase. Importantly, the combination of Zr and B has been effective both in expanding the glass formation range and increasing the stability of the amorphous phase against crystallization [MAKI1994, XION2003]. On the other hand, Fe-Zr-B based nanocrystalline alloys are characterized by high $M_S$ and low $H_C$,

which can meet with the requirements of high performance and miniaturization for magnetic devices [HONO2002, LIUY2006, MAKI1994, MCHE1999]. Fe-Zr-B based nanocrystalline alloy was originally developed by Suzuki et al [SUZU1990]. The nanocrystalline microstructure in Fe-Zr-B based alloys consists of $\alpha$-Fe nanoparticles embedded in a residual amorphous phase. Such a microstructure gives rise to outstanding soft magnetic properties as shown in Fig.1.01 [SELL2006], which are generally attributed to the very low magnetostriction and dramatically reduced effective anisotropy [HERN1995]. The soft magnetic properties arise from the strong intergranular magnetic coupling between adjacent nanocrystals through the residual amorphous

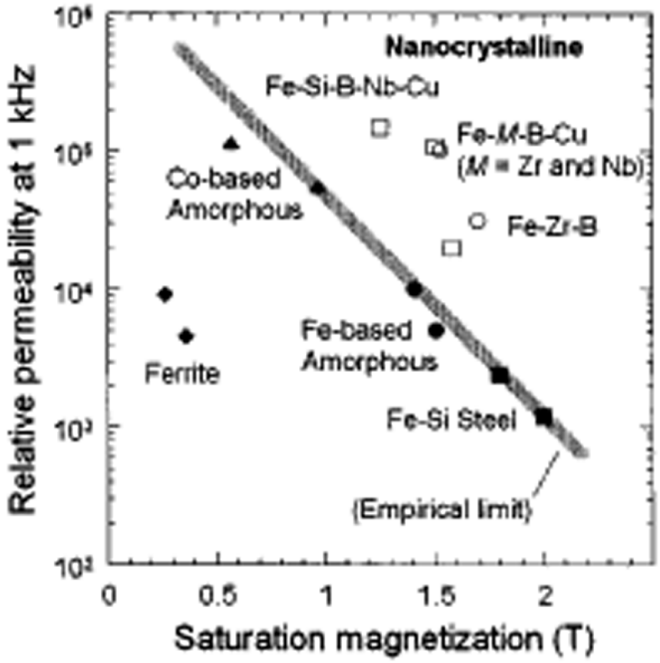


*FIG. 1.01: Saturation magnetization and initial permeability of various soft magnetic materials.*

phase, which enables the suppression of effective anisotropy [SUZU1996, SUZU1999]. Hence, random anisotropy in Fe based nanocrystalline alloys plays an important role on the resulting properties [HERZ1990]. Subsequently, a series of Fe – TM – B (TM = Zr, Hf, Nb) based nanocrystalline soft magnetic alloys was developed under the generic name NANOPERM [MAKI1995]. Also, systematic investigations on the room temperature and temperature dependent magnetic properties of amorphous Fe-Zr-B alloys with different B and Zr concentrations were reported [BARA1996, BARQ2003, KEME2000, OHNU1981, YAOB2003]. Magnetostriction in a-Fe-Zr-B alloys reduced largely with the addition of B [SLAW1996] up to 5 at.% and increases slightly for further increase in B content. Early stage of crystallization in Fe-

Zr-B alloys resulted in magnetic hardening due to the lower volume fraction of nanocrystallites with insufficient exchange coupling between them [GOME1996]. However, the soft magnetic properties of the Fe-Zr-B alloys improved drastically when the crystalline volume fraction increased above 40 % [MALK1997]. Recently, Modak et al obtained excellent soft magnetic properties, i.e., $H_C$ = 6 A/m and $M_S$ = 1.4 Tesla in gradually devitrified Fe-Zr-B alloys [MODA2008]. Also, Fe-Zr-B alloy powders prepared by other techniques such as gas atomization [OGUC1994] and MA [STIL1996, PERE2007] provided an idea about the effect of synthesis routes on material processing. However, it is to be noted that most of the Fe-Zr-B alloys investigated earlier contain lower Zr (≤ 7 at.%) content and no detailed reports are available on the temperature dependent magnetic properties of Fe-Zr based alloy powders.

Thermal properties of the NANOPERM alloys ($Fe_{93-x}Zr_7B_x$ and $Fe_{93-x-y}Zr_7B_xCu_y$) were investigated by using a Differential Scanning Calorimeter (DSC) [KOPC1996, KOPC1997, MCHE2003, SUZU1994, WANR1999, XION2001]. These studies showed that $\alpha$-Fe nanocrystals, and $Fe_xZr$ ($Fe_3Zr$ and $Fe_2Zr$) crystalline phases were the primary and secondary crystallization products. Crystallization temperature ($T_{crys}$) of a-Fe-Zr-B alloy depends on the B content and $T_{crys}$ value increases with the addition of B [KOPC1995]. Also, substitution of other nucleating elements such as Ag, Au, Pt, Sb, Cu and Ga in Fe-Zr-B-M alloys lowers the primary $T_{crys}$ due to the lower binding energy with Zr and B, which results in early stage crystallization in Fe-Zr-B-M alloys [KOPC1995, VARG1994]. However, the soft magnetic properties of the Fe-Zr-B-M alloys improved in this process due to the refinement of nanostructure. It has been observed that the substitution of higher B content in $Fe_{93-x}Zr_7B_x$ alloys (~12 at.%) resulted in the formation of more than one crystallization product [XION2003]. Nevertheless, with increasing B content up to 30 at.% in a-$Fe_{91-x}Zr_5B_xNb_4$ alloys, the glass forming ability, thermal stability and soft magnetic properties were improved [YAOB2004]. The crystallization behavior of the NANOPERM alloys was also analyzed through transport properties [PEKA1996] and the role of various elements has been discussed. Recently, Huang et al [HUAN2008] reported that the crystallization stages of the amorphous $Fe_{80}Zr_{12}B_8$ alloy under controlled heating were observed to be different from those observed in Fe-Zr-B alloys with low Zr content [WANR1999]. This suggests that the crystallization kinetics and magnetic properties of Fe-Zr-B alloys are dependent on the relative amounts of both Zr and B in the alloy. However, no systematic work has been reported so far on the development of soft magnetic properties vis-a-vis its microstructure and

magnetic domain structure. Moreover, a detailed knowledge of the devitrification process of Fe-Zr-B based alloys would be invaluable in any attempt to tune the microstructure for optimized properties.

Nanocrystalline microstructure and magnetic domain structure of the alloys play an important role in shaping out the resulting magnetic properties of the materials. There are many reports available on the microstructural investigations of Fe-Zr-B alloy using advanced techniques such as Transmission Electron Microscopy, Atom-Probe Field Ion Microscopy, Extended X-ray Absorption Fine Structure, Scanning Tunneling Microscopy techniques [MATS2001, NOGU1995, OHOD2009, ZHAN1996]. Zhang et al reported the coexistence of bcc Fe and residual amorphous phase in NANOPERM alloy [ZHAN1996]. The residual amorphous phase is enriched with Zr and B. Moreover, the convenient arrangement of Zr atoms around the moving interface of Fe crystallites helps in the control of the grain growth. Magnetic domain structure of the NANOPERM alloys was investigated using optical Kerr microscope by Schafer et al [SCHA1996], magnetic force microscopy (MFM) by Suzuki et al [SUZU1997], and Lorentz microscopy by Gao et al [GAOY2003]. The magnetic domain structure of the optimum soft magnetic nanocrystalline $Fe_{91}Zr_7B_2$ alloy was observed to be curved domains separated by $180^o$ walls and the domain wall width estimated from the MFM image is in good agreement with the exchange correlation length determined from the magnetic measurements [SUZU1997]. These studies revealed that the excellent soft magnetic properties in Fe-Zr-B based alloys are due to the averaging of the magnetocrystalline anisotropy over the order of $10^4$ grains. Ohkhubo et al investigated the structural changes in the primary crystallization process of a-$Fe_{90}Zr_7B_3$ alloy using modern electron microscope techniques [OHKU2001]. From the electron diffraction pair distribution function analysis of the amorphous matrix and the reverse-Monte-Carlo simulation, medium range order was found to develop in the amorphous phase in as-quenched state. However, recent investigations on Fe-Zr-B alloys using Mossbauer technique did not support the possibility of the formation of $\alpha$-Fe nanoclusters in the as-made a-$Fe_{90}B_3Zr_7$ sample [STAN2005].

Conventional methods of improving the intrinsic and extrinsic soft magnetic properties have been focused on tailoring composition, control of microstructure with heat treatment under different environments, reduction of $H_C$, increase of $M_S$, and control of intergranular exchange coupling in the amorphous and nanocrystalline materials. Co substituted Fe-Co-Zr-B alloy generally falls under the generic name HITPERM [BEDN2006, BEDN2007, GRAB2007,

MAJU2007, SKOR2006, WILL1998, WILL1999]. Addition of Co in Fe-Co-Zr-B alloys increases $H_C$, $M_S$ and Curie temperature ($T_C$), but lowers the $T_{crys}$ [BLAZ2002, BLAZ2005, MAOX2005, SUZU2002]. In addition, the small amount of Co addition helps to optimize the magnetostriction properties as shown in Fig.1.02 [SELL2006]. Lorentz microscopy coupled with focused ion beam was used by Saito et al to investigate the effect of high Co addition in the magnetic domain structure of Fe-Co-Nb-Si-B-Cu alloys and to obtain the relation between the induced magnetic anisotropy and magnetic domain structure [SAIT2006]. However, high Co addition in Fe based alloys restricts the crystallization process due to exhaustion of Fe in the

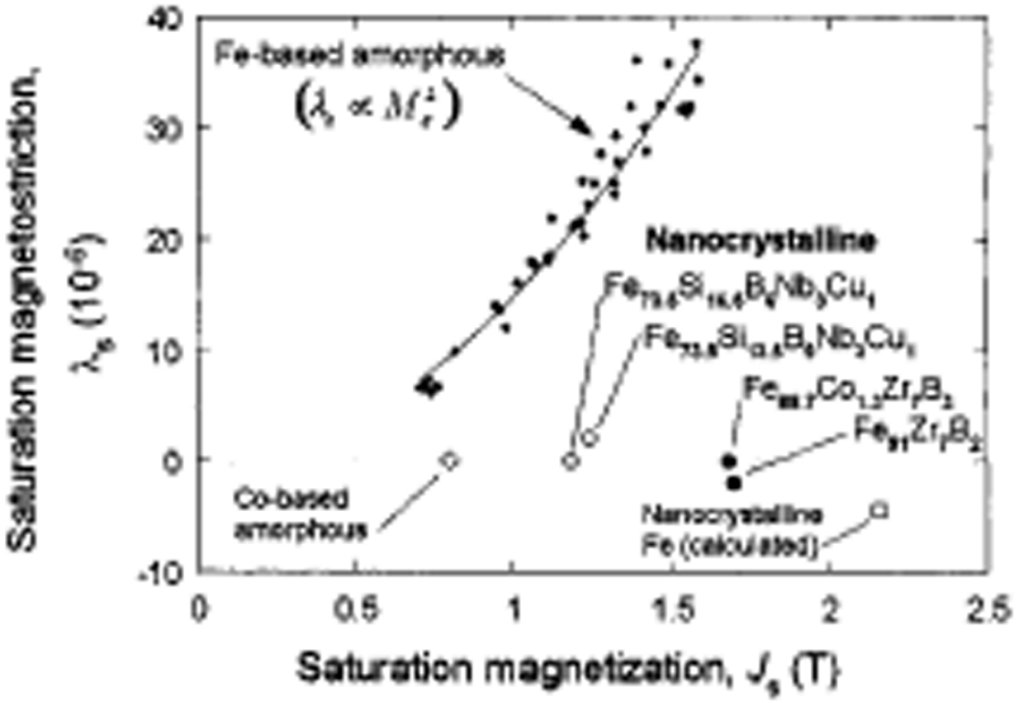


*FIG. 1.02: Relation between saturation magnetostriction and saturation magnetization for amorphous and nanocrystalline soft magnetic materials.*

amorphous matrix [BLAZ2003]. Recently, it has been shown that the structure of Co-rich nanograins can be tuned by means of static magnetic field annealing [MARI2009]. Similarly, rotating-magnetic field annealing helped to reduce coherence uniaxial anisotropy and the reduction in $H_C$ values was observed for NANOPERM alloys due to the decrease of fluctuating amplitude of the effective anisotropy [SUZU2008]. On the other hand, the addition of Mn in Fe(Co) based alloys not only shifts the $T_{crys}$ to higher temperature [BAYR2009], but also helps to

enrich the nanocrystals with Fe and Co [MILL2009]. Also, the partial substitution of Mn in Fe based alloys such as FINEMET [MONE2009], NANOPERM [BITO1999, HASI2003] and HITPERM [BENA2008] alloys has been a subject of great interest. Interestingly, the substitution of Mn in Fe-Al alloy powders prepared by MA process reduces $H_C$ considerably [REST2001, RICO2008] in contrast to the behavior observed in melt-spun ribbon alloys [KIMK2007]. However, no systematic studies have been reported on the temperature dependent magnetic properties in these alloys.

Magnetic field annealing helps to induce uniaxial anisotropy in Fe based nanocrystalline soft magnetic alloys. Thus, the microstructure, magnetic domain structure and resulting magnetic properties can be tailored for suitable applications [CHIK1986, OHAN1999]. However, the questions related to the influence of nanocrystalline microstructrue on magnetic domain structure and magnetic properties of Fe-(Co,Mn)-Zr-B alloys with high Zr (>7 at.%) content prepared by different synthesis routes are still open because of the complexity of the problem. Also, understanding how magnetic properties are optimized in conjunction with the microstructures and domain structures would be useful for designing high-performance nanocrystalline materials. Detailed investigations of microstructure, temperature and field dependent magnetic properties and the evolution of room temperature magnetic properties of Co and Mn substituted a-Fe-Zr-B alloys having higher Zr content have not been reported. Hence, investigating the influences of additive elements such as B, Co, and Mn in Fe-Zr alloy powders and ribbons prepared by MA and melt spinning techniques is important.

### 1.3. Objectives of the thesis work

A). To prepare (i) amorphous $Fe_{89-x-y}(Co,Mn)_yZr_{11}B_x$ alloy ribbons ($x$ = 0 – 10 and $y$ = 0 – 10) by melt-spinning technique, (ii) $Fe_{100-x-y-z}(Co,Mn)_zB_yZr_x$ alloy powders ($x$ = 20 – 35, $y$ = 0 – 10, $z$ = 0 – 20) by mechanical alloying technique, and (iii) nanocrystalline alloys by devitrifying the amorphous precursors.

B). To carry out a systematic study of the prepared alloys with the intention to (i) investigate the effect of substituting elements on the structural properties, stability of the amorphous phase, room temperature ferromagnetic properties, and magnetic softness of the amorphous ribbons and powders, (ii) study the enhancement of magnetocaloric effect with the addition of Co and Mn in amorphous Fe-Zr-B ribbons, (iii) investigate the nature of

the magnetic state of amorphous Fe-(Co,Mn)-Zr-B alloy ribbons and powders over a wide range of temperatures, (iv) understand the effect of longitudinal magnetic field annealing on the evolution of nanocrystalline microstructure, magnetic domain structure and resulting magnetic properties of two-phase structured Fe-(Co,Mn)-Zr-B alloy ribbons, and (v) make a comparative study of structural, thermal, and magnetic properties of amorphous Fe-(Co,Mn)-Zr-B alloys prepared through two different synthesis routes.

# Chapter 2

## Fundamental Aspects and Theoretical Modeling

## 2.1. Ordered and Disordered alloys

Physical properties of alloys are greatly influenced by the arrangement of atoms at the atomic scale or the nature of short-range order. In crystalline materials, long-range ordering in the position of atoms and orientation of atomic rows exists. There is a definite probability of an atom in its lattice position, and the translational periodicity is a consequence of the Bloch's theorem [DRES2008]. Though positional order for the atomic sites in alloys is present, the occupation of different sites by different species of atoms is random. Thus, the Bragg's diffraction in a crystalline material results in well-defined peaks having Gaussian or Lorentzian shape [WARR1990], as shown in Fig.2.01. On the other hand, in amorphous solids, the atomic positions are strongly correlated in the nearest neighbor shell, but are uncorrelated beyond a few atomic spacing. Therefore, the amorphous or glassy alloys possess short-range atomic order and

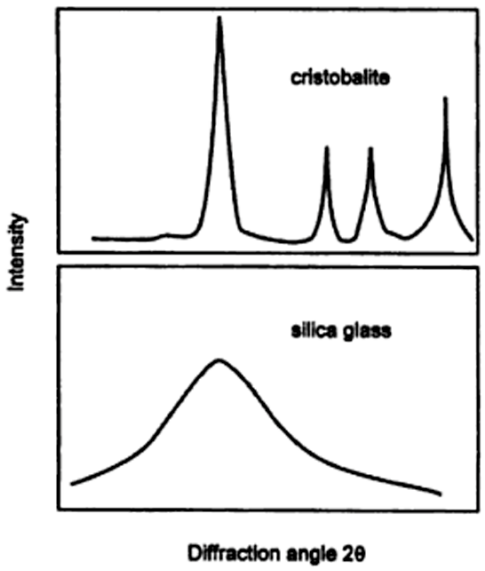


*FIG. 2.01: XRD patterns from crystalline cristobalite and silica glass.*

exhibit broad peaks (or humps) in the Bragg's diffraction pattern (Fig.2.01). The structure of glassy solids resembles that of liquids from which they have been obtained. Amorphous metallic alloys are fascinating from both theoretical and experimental points of view. For the experimentalists, they provide an opportunity to study systematically the electronic structure of a disordered alloy series in a *'single phase'* over the whole concentration range without having to be unduly concerned about stoichiometry and other metallurgical problems associated with crystallinity. The presence of disorder can affect the electronic properties of materials due to the presence of defect states.

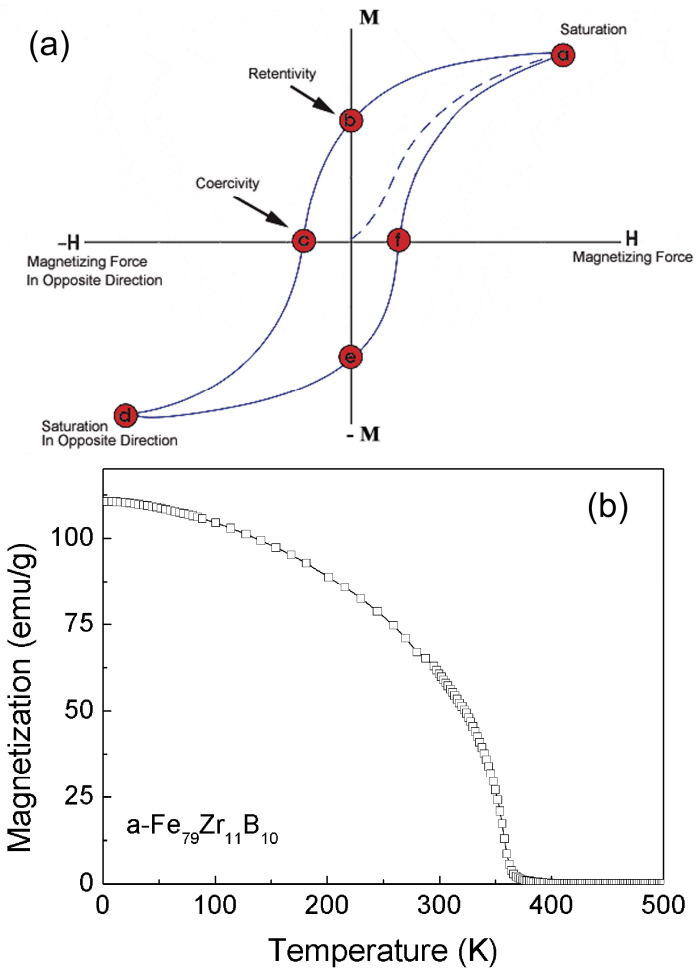


*FIG. 2.02:(a) Response of a FM material to applied magnetic field at a particular temperature, and (b) Response of a FM material to temperature at constant applied magnetic field.*

## 2.2. Ferromagnetic materials

Ferromagnetic (FM) materials are spontaneously magnetized materials that exhibit a large increase in magnetization when placed in a small magnetic field. The response of a FM material to an applied magnetic field ($H$) at a constant temperature is non-linear and is characterized by a magnetic hysteresis phenomenon as shown in Fig.2.02a. The dotted curve from origin to the point '*a*' represents the initial magnetization curve of a demagnetized material. Magnetization increases with increasing applied magnetic field and saturates at higher magnetic fields. The maximum (saturated) magnetization achievable is known as saturation magnetization ($M_S$). The typical magnetic hysteresis (**M** – **H**) loop of a FM material is shown by the solid curve '*a-d-a*' in Fig.2.02a. Significant parameters characterizing a magnetic material associated with the

hysteresis loop are retentivity or remanence ($M_R$, value of magnetization when $\boldsymbol{H} = 0$, point *b*) and coercivity ($H_C$, the reverse magnetic field required to reduce the net magnetization to zero, point *c*). Another important parameter is the magnetic induction [$\boldsymbol{B} = \mu_o (\boldsymbol{H} + \boldsymbol{M})$, where $\mu_o$ is the permeability of free space], which is the total flux of magnetic field lines through a unit cross sectional area of the material. From the initial magnetization curve, the initial magnetic permeability $\mu_I$ (= $\boldsymbol{B/H}$, for very small applied magnetic field) and maximum permeability $\mu_{max}$ [=$(\boldsymbol{B/H})_{max}$] can be obtained. These parameters indicate the amount of induction generated by the material in a given magnetic field, and are useful in characterizing magnetic materials. $\mu_I$ and $H_C$ have a reciprocal relationship. So, materials exhibiting low $H_C$ necessarily have a high $\mu_I$.

When we heat these FM materials, they become paramagnetic (PM) above a particular temperature as shown in Fig.2.02b. The temperature at which the magnetic phase transition from FM to PM phase occurs is known as Curie temperature ($T_C$), which is also an important parameter characterizing a FM material. FM materials exist in two forms, e.g. crystalline and amorphous state. With the addition of suitable glass forming elements, amorphous phase can be achieved quite easily. These materials can be engineered for specific applications with suitable selection of elements and composition.

## 2.3. Intrinsic and extrinsic properties of magnetic materials

Intrinsic properties such as spontaneous magnetization, $T_C$, and magnetocrystalline anisotropy (MCA) of a FM material describe the equilibrium properties of the material on the atomic scale. By contrast, extrinsic magnetic properties such as $H_C$ and $M_R$ reflect the magnet's real-structure (morphology and microstructure) [BLOC1932, LAND1935, KERS1943, SKOM1999]. A brief discussion on intrinsic and extrinsic properties of magnetic materials is presented below.

### 2.3.1. Magnetic moment

Magnetic moment in an atom arises due to the motion and interaction between the electrons. Orbital magnetic moment and spin magnetic moment are the mainly contributions to the total magnetic moment of the atom. The contribution from nuclear magnetic moment is quite negligible by comparison. The maximum magnetic moment ($\boldsymbol{\mu}$) of a single atom in a particular direction is given by [BLUN2001]

$$\boldsymbol{\mu} = g\boldsymbol{J}\mu_B \qquad (2.1)$$

where, $g$ is the Lande factor (ratio of the magnetic moment to the angular momentum), $\mu_B$ is the Bohr magnetron ($1\mu_B = 9.274\times10^{-24}$ $JT^{-1}$) and $\boldsymbol{J}$ is the total angular momentum of the atom. $\boldsymbol{J}$ is defined as $\boldsymbol{J} = \boldsymbol{L} \pm \boldsymbol{S}$, where $\boldsymbol{L}$ is orbital angular momentum and $\boldsymbol{S}$ is the spin angular momentum. The sign ± is determined by the Hund's rule.

Table 2.1: Number of valence electrons ($n$) and atomic magnetic moment ($\boldsymbol{\mu}$) for the FM 3$d$ transition metals [JOHN1996].

| **Element** | $\boldsymbol{n}$ | $\boldsymbol{\mu}$ ($\mu_B$) |
|---|---|---|
| Fe | 8 | 2.23 |
| Co | 9 | 1.73 |
| Ni | 10 | 0.62 |

The magnetic moment of the transition metal elements Fe, Co and Ni originates due to the 3$d$ band electrons. To explain the measured magnetic moments (given in Table 2.1) in a simple way, the concept of strong and weak ferromagnetism has been introduced. Co and Ni are the strong FMs, where the spin up band is completely filled with 5 electrons. On the other hand, Fe is an example of weak FM in which the spin up band is partially filled. Since a strong FM has the spin up band completely filled, its magnetic moment can be estimated from the number of valence electrons in the atom [JILE1991]. When the spin up band is completely filled and contains 5 electrons, and the atom has $n$ valence in total (the number of 3$d$ and 4$s$ electrons), the atomic magnetic moment can be calculated as

$$\boldsymbol{\mu} = [5 - (n - x - 5)]\mu_B = (10 - n + x)\mu_B \qquad (2.2)$$

where, $x$ is the number of 4$s$ electrons per atom. In isolated atoms of Fe, Co and Ni, the number of 4$s$ electrons is 2 but in a metallic crystal, the 4$s$ electrons will spill into 3$d$ band. In order to reproduce the measured magnetic moments, the 4$s$ band must contain only about 0.65 electrons [SKOM1999]. This will lead to the relation

$$\boldsymbol{\mu} = (10.65 - n)\mu_B \qquad (2.3)$$

which yields $n$ = 8 for Fe, $n$ = 9 for Co, and $n$ = 10 for Ni results in magnetic moments of 2.65 $\mu_B$, 1.65 $\mu_B$ and 0.65 $\mu_B$, respectively. These estimated values agree well with the measured values given in Table 2.1.

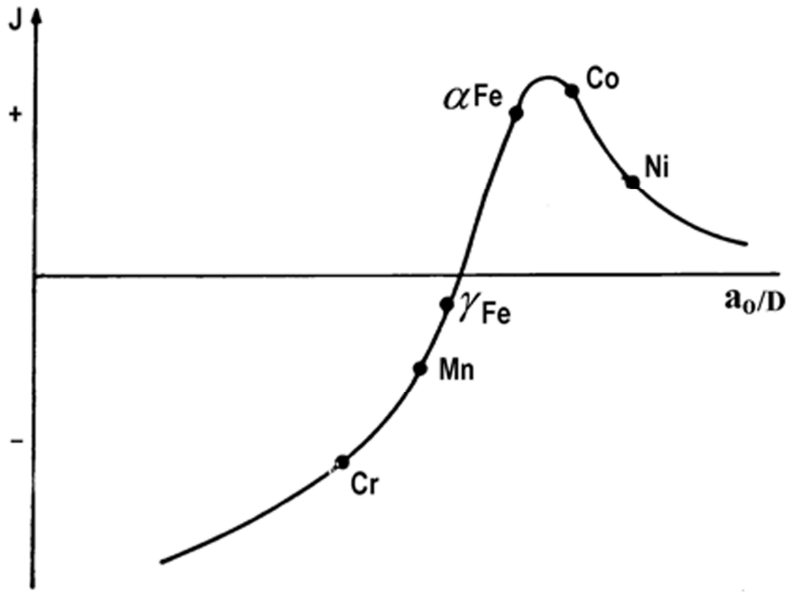


*FIG. 2.03: Variation of exchange coupling with the distance between spins of 3d transition metals.*

### 2.3.2. Exchange interaction

The orientation of adjacent local magnetic moments is determined by the exchange interaction between them. The exchange interaction between the neighboring atoms can be expressed in terms of a Heisenberg's Hamiltonian [BLUN2001]

$$\hat{\mathcal{H}} = -2\sum_{i>j} J_{ij}\boldsymbol{S_i}.\boldsymbol{S_j} \qquad (2.4)$$

Where, $J_{ij}$ is the exchange constant between the $i^{th}$ and $j^{th}$ spins, $J_{ij}$ is positive for a FM interaction (spins coupled parallel) and negative for antiferromagnetic (AFM) interaction (spins coupled anti-parallel), $i > j$ avoids the 'double counting' and hence the factor of two returns. In metals like Fe, Co and Ni, the exchange interaction between the atoms can be mediated by the conduction electrons. A localized magnetic moment spin polarizes the conduction electrons and this polarization in turn couples to a neighboring localized magnetic moment at a distance *r* away. It is known as RKKY (named after the initials of surnames of the discoverers Ruderman, Kittel, Kasuya and Yoshida) interaction or also as itinerant exchange [BLUN2001]. The oscillations of *J* occur from the interference of the scattered outgoing spherical waves with the incident Bloch waves. Structural disorder in the materials has important effects on the exchange integral. Thus, a distribution in magnitude and sign of *J* is expected in amorphous alloys. *A*

*distribution in magnitude of J* comes from interatomic distance dependence of the *J* (Fig.2.03), which fluctuates in amorphous materials. Also, a *distribution in sign of* ***J*** is encountered because *J* oscillates, i.e., change in sign of *J* as a function of interatomic distance. Depending on the width of the distribution of *J*, the exchange forces ranging from positive to negative values are simultaneously present in amorphous solids (Fig.2.03), leading to the so-called *frustration* effects [TOUL1977]. These result in complex magnetic structures, which are rarely found in crystalline solids. Also, the value of *J* is equal to zero for a number of atoms suggesting that the exchange paths are broken [DEGE1976].

In the case of localized electrons with small variations of the spin orientation between neighboring atoms and only nearest-neighbor interactions ($J_0$), the exchange energy density may be written as [KRON2003]

$$\phi'_{ex}(r_i) = -\frac{1}{\Omega} 2S^2 J_0 . z_0 + \frac{J_0 S^2}{3\Omega} \sum_{j \neq i}^{nn} \sum_{n=1}^{3} r_{ij}^2 . \left(\nabla \gamma_{n,i}\right)^2 + \cdots \quad (2.5)$$

Where, $r_{ij}$ denoted the nearest-neighbor distances. Here the first term corresponds to the exchange energy of a homogeneously magnetized material and the second term represents the magnetic inhomogeneities. For cubic lattices with edge length *a* of the cube, the second term in eqn.(2.5) can be written as

$$\phi'_{ex}(r) = A \sum_{n=1}^{3} (\nabla \gamma_n(r))^2 \quad (2.6)$$

with the exchange stiffness constant (*A*),

$$A = \frac{2J_0 S^2}{a} . c \quad (2.7)$$

where $c = 1$ for the simple cubic (sc) (primitive) lattice, $c = 2$ for the body centered cubic (bcc) lattice and $c = 4$ for the face centered cubic (fcc) lattice. By replacing the spin quantum number with $M_S$ value, the eqn.(2.7) can be written as

$$A = \frac{2J_0 M_S^2 c}{N^2 g^2 \mu_B^2 a} \quad (2.8)$$

Since the exchange integral is related to the $T_C$, within the framework of molecular field theory [MORR1965], eqn.(2.8) may be written as

$$A = \frac{3k_B T_c S.\, c'}{2a(S+1)} \tag{2.9}$$

with $c'$ = 1/6, 1/4, and 1/3 for sc, bcc and fcc lattices, respectively. Table 2.2 presents intrinsic magnetic material parameters [$\boldsymbol{B_S}$, $A$ and $T_C$] of transition metals.

Table 2.2: Intrinsic magnetic material parameters such as saturation magnetic induction ($B_S$), exchange stiffness constant ($A$), and Curie temperature ($T_C$) of transition metals.

| **Magnet** | $\boldsymbol{B_S}$ **(Tesla)** | $\boldsymbol{T_C}$ **(K)** | $\boldsymbol{A}$ **(pJ/m)** |
|---|---|---|---|
| $\alpha$ – Fe | 2.185 | 1043 | 20.7 |
| Co | 1.79 | 1403 | 30.2 |
| Ni | 0.62 | 627 | 7.2 |

### 2.3.3. Magnetocrystalline anisotropy

In FM materials, there exist certain preferred crystallographic directions (easy axes) of magnetization along which less field is needed to magnetize the material than along other axes (so called hard axes). The origin of this feature is attributed to the spin-orbit coupling which can be simply visualized as the interactions between crystal lattice, orbit, and spin of the electron. The orbits are strongly coupled to the lattice and even large fields cannot change them. The microscopic explanation is that neighboring atoms in a crystal will exert an electric field, known as the crystal field, on the orbiting electrons. This will force the orbits to align themselves with the crystal fields. Further, there is also a coupling between the spin and the orbital motion of each electron called spin-orbit coupling. If an external magnetic field is applied, it tries to reorient the spin of the electron. The orbit of that electron also tends to get reoriented. As the orbit is strongly coupled to the lattice, it tries to resist the attempt to rotate the spin axis. The energy required to spin away from the easy axis is the just the energy required to overcome the spin-orbit coupling, which is also known as MCA energy.

The angular dependence of MCA relates to the symmetry of the crystal itself. Thus, MCA can be expanded as a power series of direction cosines which satisfies the crystal symmetry. For a cubic crystal, the lowest order direction cosine is the fourth order and the anisotropy energy in spherical polar coordinate can expressed as [BERT1998]

$$E_a = K_1\left(\frac{1}{4}\sin^2\theta\sin^2 2\phi + \cos^2\theta\right)\sin^2\theta + \frac{K_2}{16}\sin^2 2\phi\sin^2 2\theta\sin^2\theta \quad (2.10)$$

In the case of cubic anisotropy, a one-constant anisotropy equation can be used as a first approximation [JILE1991], leading to the relation

$$E_a = K_1(\cos^2\theta_1\cos^2\theta_2 + \cos^2\theta_2\cos^2\theta_3 + \cos^2\theta_3\cos^2\theta_1) \quad (2.11)$$

where $\theta_1$, $\theta_2$, and $\theta_3$ are the angles the magnetization makes relative to the three crystal axes.

In the case of hexagonal crystals, the anisotropy constant can be expressed by the one-constant approximation as [JILE1991]

$$E_a = K_{u_1}\sin^2\phi \quad (2.12)$$

where, $\phi$ is the angle of magnetization with respect to the unique axis, which for $K > 0$ is the easy axis, whereas, for $K < 0$ it is the hard axis. The anisotropy constants of Fe, Co and Ni are presented in Table 2.3.

Table 2.3: MCA constants of Fe, Co and Ni [JILE1991]

| Material | $K_1$ ($10^5$ Jm$^{-3}$) | $K_{u1}$ ($10^5$ Jm$^{-3}$) | $K_2$ ($10^5$ Jm$^{-3}$) | $K_{u2}$ ($10^5$ Jm$^{-3}$) |
|---|---|---|---|---|
| Fe (cubic) | 0.480 | - | 0.050 | - |
| Ni (cubic) | -0.045 | - | 0.023 | - |
| Co (hexagonal) | - | 4.1 | - | 1.0 |

### 2.3.4. Magnetoelastic anisotropy

When a FM material is exposed to a magnetic field, its dimensions changes and thereby it experiences a strain. This effect is known as magnetostriction. The inverse effect *i.e.* the change of magnetization with stress also occurs and produces a unique easy axis of magnetization giving rise to magnetoelastic anisotropy (MEA). The anisotropy energy associated with the magnetoelastic effect can be expressed as [JOHN1996]

$$E_{mea} = -K_{mea}\cos^2\phi \quad (2.13)$$

where $\phi$ is the angle between the magnetization and the plane of isotropic anisotropy and

$$K_{mea} = -\frac{3}{2}\lambda\sigma = -\frac{3}{2}\lambda E\varepsilon \quad (2.14)$$

where, $\lambda$ is the magnetostriction coefficient and $\sigma$ is the stress which relates to the strain ($\varepsilon$) through the elastic modulus $E$. The experimental values of $\lambda_S$ for Fe, Ni and $Fe_3O_4$ are $-7\times10^{-6}$, $-33\times10^{-6}$ and $-40\times10^{-6}$, respectively.

### 2.3.5. Magnetic domains and domain walls

A FM material consists of magnetic domains in which the magnetic moments are aligned parallel within the volumes containing large number of atoms. In the demagnetized state, domains are randomly oriented but get aligned when a small magnetic field is applied to the material [KITT1949, KITT1956, DILL1963]. In a FM material, the number and size of domains are determined by the balance between magnetostatic versus domain wall energies. The change of the spontaneous magnetization from a domain to its neighbor occurs at the domain wall. The width of the boundary between magnetic domains (the domain wall) is determined by the balance between the exchange energy and the manetocrystalline energy. The spins near to the wall point to the non-easy directions. Therefore, the anisotropy energy is higher within the wall than in its adjacent domains. The exchange energy tries to make the wall as wide as possible. In order to make the angle between the adjacent spins as small as possible, the anisotropy energy tries to make the wall thin i.e. reducing the number of spins pointing in non-easy directions. This competition leads to certain finite domain wall width by minimization of the total energy. The domain wall width $\delta$ is related to the exchange length [BROW1970] by the relation

$$L_{ex} = \sqrt{\frac{A}{K_U}} \tag{2.15}$$

(where $A$ is the exchange stiffness constant and $K_U$ is the MCA constant of the material) by the relation [BLUN2001]

$$\delta = \pi L_{ex} \tag{2.16}$$

The typical domain wall widths are about 5 and 1000 nm for hard and soft magnetic materials, respectively.

### 2.3.6. Magnetic hysteresis

Magnetic properties derived from the magnetic hysteresis loop are extrinsic properties, because they describe the real structure of the magnet. The response of a FM material to an applied

magnetic field at a constant temperature is characterized by a magnetic hysteresis phenomenon as discussed in section 2.2. Fig.2.04 shows typical $M - H$ loops of different types of FM materials. Two very important extrinsic properties derived from $M - H$ loops are $H_C$ and $M_R$. $B - H$ loops are used to determine the energy product $(BH)_{max}$, which is the manifestation of the maximum magnetostatic energy per magnet volume stored outside the magnet. Magnetic hysteresis is a complex nonlinear, non-equilibrium and nonlocal phenomenon, as shown in inset of Fig.2.04, reflecting the existence of metastable energy minima. A change in the applied magnetic field destroys local minima, and the magnetization is forced to jump into another minimum. The nonlocal character of extrinsic properties originates due to the magnetostatic dipole interactions [SKOM1999].

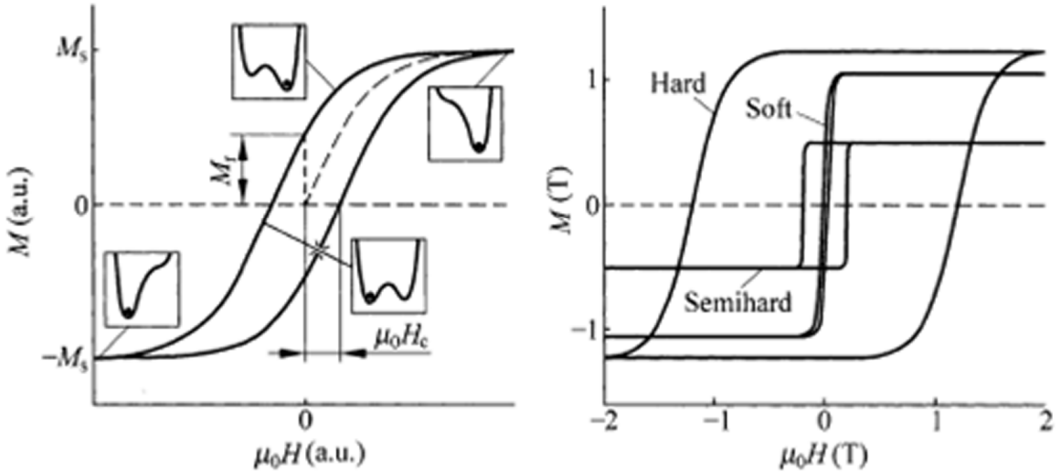


*FIG. 2.04: Typical M – H loops of different types of FM materials.*

### 2.3.7. Coercivity

$H_C$ the most intriguing aspect of the hysteresis describes the stability of the remanent state and gives rise to the classification of magnets into (i) soft magnetic materials having low $H_C$ (<10 Oe), (ii) semihard materials having moderate $H_C$ values (2000 Oe $\leq H_C \leq$ 10000 Oe, storage media) and (iii) hard magnetic materials having large $H_C$ (>10000 Oe, permanent magnets). A phenomenological expression for $H_C$ is

$$H_C = p\frac{2K_1}{\mu_0 M_S} - D_{eff}M_S - \Delta H(T,\eta) \qquad (2.17)$$

where $p$ is a Kronmuller parameter [KRON1987, KRON1988], $D_{eff}$ is a magnetostatic interaction parameter and $\Delta H$ is fluctuation-field contribution caused by thermal activation [NEEL1951, COEY1996, SKOM1999]. $H_C$ also depends on the sweep rate $\eta$ (= $dH/dt$). $H_C$ is mainly governed by two mechanisms such as nucleation and pinning. Nucleation-controlled magnets are almost defect-free, and the $H_C$ is essentially given by the nucleation field. There are several types of nucleation process such as coherent rotation in very small particles, curling in large perfect ellipsoids of revolution, and localized nucleation in imperfect structures [SKOM1998]. In contrast to nucleation type magnets, pinning-type magnets contain many defects, which ensure large $H_C$ by impeding the motion of the domain walls.

## 2.4. Effect of different anisotropies on magnetic softness

Good soft magnetic properties are obtained when both the domain wall motion and domain rotation occur with a small change in the energy of the system. Magnetic anisotropy strongly affects the energy of the system. Different magnetic anisotropies in practical magnetic materials include (1) MCA, (2) induced anisotropies (stress or annealing) and (3) shape anisotropy. Of these, the MCA reflects the symmetry of the crystal structure. Stress induced anisotropy [magnetoelastic anisotropy (MEA)] originates from the magnetostriction, which itself is one of the intrinsic magnetic characteristics of materials.

$H_C$ of an assembly of non-interacting single domain particles is given by the relation

$$H_c = P_C \frac{K_U}{M_S} \tag{2.18}$$

where the pre-factor $P_C$ depends on the anisotropy symmetry of $K_U$ and has the value of 0.96 and 0.64 for uniaxial and cubic crystals, respectively [HERZ1989]. $H_C$ due to blocking of wall motion can be related to the spatial fluctuation of anisotropy energy $<K>$ and the wavelength of the anisotropy fluctuation ($<\lambda_a>$) by the relation

$$H_c \approx \frac{<K>}{M_S} \frac{\delta}{\lambda_a} \tag{2.19}$$

where $\delta$ is domain wall width. In general, both MCA and MEA have considerable effect on $<K>$. For isotropic magnetostriction ($\lambda_S$) and residual stress (uniaxial), MEA energy can be written as

$$E_{el} = K_{ind} \sin^2 \alpha = \frac{2}{3} \lambda_S \sigma \sin^2 \alpha \tag{2.20}$$

where $\alpha$ is the angle between $M_S$ and $\sigma$. On the other hand, the MCA energy can be written as,

$$E_K = K_U \sin^2 \theta \tag{2.21}$$

where $\theta$ is the angle between $M_S$ and easy axis. Hence, the total anisotropy energy of a material can be written as,

$$< K > = \sqrt{K_U^2 + \left(\frac{2}{3}\lambda_s \sigma\right)^2} \tag{2.22}$$

The eqn.(2.22) suggests that both the MCA and MEA energies have to be reduced for achieving excellent soft magnetic properties.

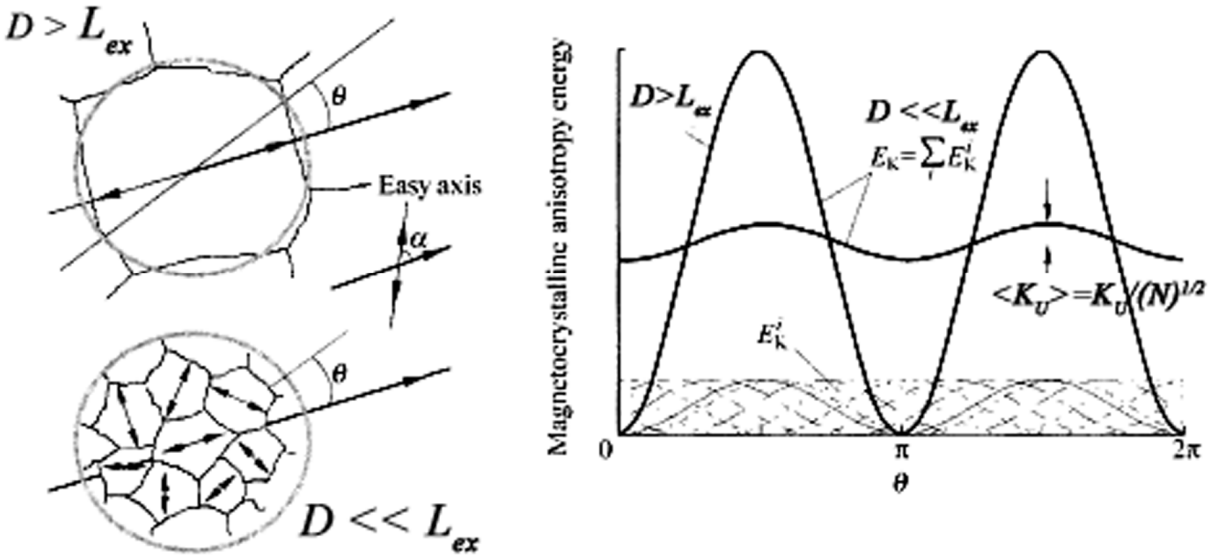


*FIG. 2.05: Change in the MCA energy ($E_K$) for conventional ($D > L_{ex}$) and nanocrystalline ($D << L_{ex}$) materials (for uniaxial anisotropy symmetry).*

## 2.5. Random Anisotropy Model (RAM)

### 2.5.1. RAM in single phase system

The key to understanding the reduction of the amplitude of $E_K$ in nanocrystalline materials is to realize the correlation between the magnetic and structural correlation lengths. The competition between exchange energy and anisotropy energy is determined by exchange correlation length, as defined in eqn.(2.15) [BOZO1951, HERZ1989, HERZ1990, HERZ1995]. This natural exchange correlation length corresponds to the critical grain size below which the amplitude of $E_K$ starts to decrease with grain refinement. Fig.2.05 describes the reduction process of $E_K$ in

nanocrystalline materials. On the other hand, $E_K$ for larger grains ($D << L_{ex}$) is given by the sum of the contributions from a number of grains,

$$E_K = \sum_{i=1}^{N} E_K^i \tag{2.23}$$

where $N$ is the number of the magnetically correlated grains. An important physical assumption in the above equation is that anisotropy energy inside each correlation length is mutually transmitted to each other via exchange interaction. The $E_{MCA}$ of each grain can be described by taking into account the angle between its easy axis and the reference axis at $\theta = \gamma_i$. So the above equation becomes

$$E_K^i = \frac{K_U}{N} \sin^2(\theta - \gamma_i) \tag{2.24}$$

Provided that the grains are oriented at random, the mean square amplitude of the anisotropy energy is composed of the quadratic contributions of the random local anisotropies from different grains. Hence, the amplitude of the $E_K$ is obtained by the random walk consideration:

$$< K_U > = \sqrt{N\,(\tilde{E}_K^i)^2} = \frac{K_U}{\sqrt{N}} \tag{2.25}$$

where $\tilde{E}_K^i$ is the amplitude of the local anisotropy energy. Since this random MCA corresponds to the spatial fluctuation of anisotropy energy in the sample, which dominates the domain wall motion, a small $H_C$ is obtained even for materials with large intrinsic $K_U$. It is worth mentioning that the intrinsic $K_U$ in each grain remains the bulk value and only the amplitude of the $E_K$ is reduced. This can be understood from the fact (Fig.2.05) that the integrated area of the $E_K \sim \theta$ curve is independent of the grain size. In addition, the anisotropy symmetry is preserved in the fluctuating part of the $E_K \sim \theta$ curve for $D << L_{ex}$. The number of grains in a magnetically coupled volume is

$$N = \left(\frac{L_{ex}}{D}\right)^3 \tag{2.26}$$

Provided that the random MCA is the dominant anisotropy in the system and effective anisotropy is approximated by $<K> \approx <K_U>$. Hence

$$< K > = < K_U > = \frac{K_U^4 D^6}{A^3} \tag{2.27}$$

### 2.5.2. RAM in two-phase systems

Most of the nanocrystalline soft magnetic materials prepared by primary crystallization of amorphous precursor contain two-phase microstructure, i.e., a nanocrystalline precipitate co-exists in a residual amorphous phase in the intergranular region. The extension of RAM model to two-phase system was carried out with two distinct exchange stiffness constants corresponding to amorphous and nanocrystalline phase. It is to be noted that the volume fractions of both of these phases affect the effective anisotropy [HERZ1995, HERN1995, HERN1998, LOFF1999]. A modified RAM for two-phase structure can be expressed by,

$$< K > = p\,(1 - V_{am})^4 K_1^4 D^6 \left[\frac{1}{\sqrt{A_{cr}}} + \frac{(1 - V_{am})^{-0.33} - 1}{\sqrt{A_{am}}}\right]^6 \tag{2.28}$$

where $A_{cr}$ and $A_{am}$ are the exchange stiffness constants for crystalline and amorphous phase, respectively, having the volume fraction of the amorphous phase as $V_{am}$.

### 2.5.3. RAM under the influence of induced anisotropy

The total anisotropy in the nanocrystalline materials may have contributions from induced anisotropy and MCA. Hence, the effective anisotropy constant is given as,

$$< K > = \sqrt{K_U^2 + \sum_i K_{ind,i}^2} \tag{2.29}$$

If $K_{ind,i}^2$ is more dominant than $K_U$, then one may no longer see the effect of grain refinement on the $H_C$ variation. Also, the critical condition $< K > = < K_U >$ obviously does not hold and the contribution of $K_{ind}$ to <$K$> alters the re-normalization process of exchange correlation length.

## 2.6. Law of approach to saturation

The theoretical model based on micromagnetism of FM materials was developed by Brown to describe the law of approach to saturation magnetization [BROW1940, BROW1941]. A generalized equation derived for the high-field magnetization [KRON1959] is

$$M(H) = M_S\left(1 - \frac{a_1}{\sqrt{H}} + \frac{a_2}{H} + \frac{a_3}{H^{3/2}} + \frac{a_4}{H^2} + \frac{a_5}{H^3}\right) + \alpha T\sqrt{H} + \chi_p H \tag{2.30}$$

where the terms $a_n$ result from intrinsic properties such as MCA, spin-waves, and the Pauli PM susceptibility, as well as from extrinsic properties such as point defects, dislocations, grain boundaries, and non-magnetic precipitations.

Intrinsic contributions: (1) MCA gives rise to a $1/H^2$ dependence. Local fluctuations of the MCA as in the amorphous alloys result in a $1/H^{1/2}$ term at low fields and a $1/H^2$ term at large fields. (2) The energy gap in the spin-wave spectrum due to the Zeeman energy gives rise the $\sqrt{H}$ term. (3) The linear term $\chi_p.H$ is due to the enhanced Pauli PM of the band structure.

Extrinsic contributions: Inhomogeneous spin states were produced by the stress sources due to the magnetoelastic interactions. Hence, the corresponding deviations of magnetization from the saturation values [$\Delta M = M_S - M(H)$] depend on the geometry of the defects, spatial variation of the stresses and the correlation between the defects. The change in the values of $\Delta M$ due to the defects is as follows: (a) point defects of radius $r$ result $\Delta M = a_4/H^2$, when $r_o > L_{ex}$ (b) straight dislocation dipoles of width $D$ contribute as $\Delta M = a_2/H$, when $D < L_{ex}$ and $\Delta M = a_4/H^2$, when $D > L_{ex}$, and (c) nonmagnetic spherical precipitations of radius $r_0$ contribute as $\Delta M = a_{1/2}/H^{1/2}$, when $r_o < L_{ex}$ and $\Delta M = a_{3/2}/H^{3/2}$, when $r_o > L_{ex}$,

Similarly, the effect of intrinsic fluctuations of the materials parameters such as local spin density, local magnetic anisotropy energy, and local magnetic stray fields resulting from the local fluctuations of the spin density also affect $M_S$. Magnetoelastic coupling due to the stress induced sources has also effect on $M_S$ of the materials.

### 2.7. Magnetic viscosity

The extrinsic time dependence of the magnetization is known as magnetic viscosity, magnetic aftereffect or ageing. The magnetic viscosity determines, for example, the stability of the information stored in magnetic recording media [UJFA1996] and the time-dependent decay of the remanent magnetization of permanent magnets. Experiments reveal that the time dependence of the magnetization is well approximated by the logarithmic magnetic-viscosity law

$$M(H,t) = M(H,t_0) \pm S \ln\left(\frac{t}{t_0}\right) \tag{2.31}$$

where $S$ is the magnetic-viscosity constant [BECK1939, GIVO1996]. It is "+" for an increment in field, while it takes a "–" sign for a decrement of the applied field, and $t$ is the elapsed time since changing the field at time $t_0$. The logarithmic change of the magnetization with time is

predicted if there is a distribution of energy barriers or time-dependent activation energies present in the materials. The barriers associated with the relaxation process are of two types. The intrinsic barriers arising, for example, from the magnetic anisotropy contribute to the reversal of magnetization, whereas the barriers due to the pinning of domain walls are generally attributed to the defects in the materials. Both types of barriers are responsible for the pronounced metastability (hysteresis phenomena) of magnetic systems. The magnetic viscosity constant has been assumed [FOLD1991, GIVO1996, SKOM2008] to be proportional to

$$S = \frac{k_B T}{M_S V^*} \tag{2.32}$$

where, $k_B$ is Boltzmann constant, $T$ is temperature and $V^*$ is the activation volume. The value of $V^*$ depends not only on the physical switching volume but also on temperature.

## 2.8. Magnetocaloric effect

The temperature change of a magnetic material, associated with an external magnetic field change in an adiabatic process is defined as magnetocaloric effect (MCE) [TISH2003]. The magnetic phase transition from FM to PM state in magnetic materials results in a change in the magnetic entropy value associated with magnetization and demagnetization of the material. This change is used in the MCE. The refrigeration action by these materials is more advantageous than the conventional gas-compression process since environment issues such as ozone-depletion can be avoided. According to the thermodynamic theory, the magnetic entropy change caused by the variation of the external magnetic field from 0 to $H_{max}$ is given by [PECH1997]

$$\Delta S_M = \int_0^{H_{max}} \left(\frac{\partial M}{\partial T}\right)_H dH \tag{2.33}$$

The current prototype magnetic refrigeration is based on rare-earth based materials [PHAN2007, ZIMM1998]. For high temperature magnetic refrigeration, materials other than these rare-earth materials are under intensive research. Particularly, soft magnetic amorphous alloys have received a lot of attention as refrigerant materials due to their low cost, low energy loss, higher electrical resistivity and tunable $T_C$ [FRAN1996, JOHN2006, MINS2005].

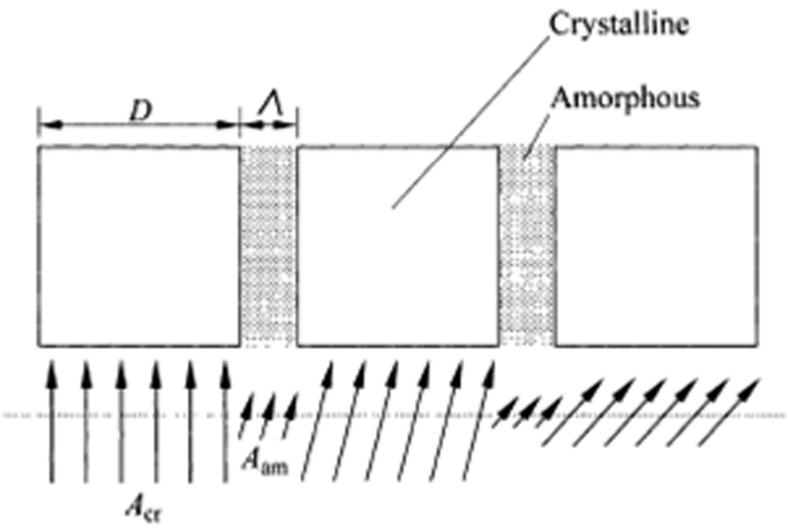


*FIG. 2.06: Schematic diagram of exchange coupling in two-phase microstructure.*

### 2.9. Two-phase microstructure and intergranular exchange coupling

Most of the soft magnetic nanocrystalline materials consist of two-phase microstructure having fine crystals of average sized between 5 and 20 nm embedded in a FM amorphous matrix (Fig.2.06). The nanocrystallites are magnetically coupled to each other via exchange coupling through amorphous matrix below the $T_C$ of the residual intergranular amorphous phase. However, this coupling chain is diminished in the temperature range above $T_C$ of the amorphous phase ($T_{C,A}$) and the nanocrystalline alloys behave as an assembly of isolated magnetic particles losing magnetic softness. Consequently, we observe a significant increase in $H_C$ in the temperature range above $T_{C,A}$ [HERZ1989]. This effect is a possible disadvantage of the nanocrystalline soft magnetic alloy from the application view point. On the other hand, the intergranular residual amorphous phase plays important roles. The presence of the residual amorphous phase is essential to maintain the metastable thermodynamical equilibrium of the nanostructure. In addition, the random magnetocrystalline anisotropy is diluted by the volume of the residual amorphous phase. Hence, the presence of the residual amorphous phase may be favorable to magnetic softness while the magnetic decoupling in the intergranular region is unfavorable to it. Therefore, the volume fraction and the exchange stiffness of the residual amorphous phase are particularly important with regard to the magnetic softness in two-phase nanocrystalline systems. Exchange stiffness constant of a material depends on the square of the

spontaneous magnetization. The spontaneous magnetization of the amorphous phase near $T_C$ varies as [HERZ1989, SLAW1992]

$$M_S^{am}(T) = M_0^{am}\left(1 - \frac{T}{T_{C,A}}\right)^{\beta} \tag{2.34}$$

where $\beta$ (= 0.36) is the critical exponent. Thus, the effective anisotropy varies as

$$< K(T) > = \left(T_{C,A} - T\right)^{-6\beta} \tag{2.35}$$

Since $H_C$ varies with anisotropy, the plot between $(H_C)^{-1/6\beta}$ and $T$ is a straight line, which deviates sharply at the $T_C$ of the amorphous phase in the alloy.

## 2.10. Soft magnetic materials and their applications

There are various types of soft magnetic materials available for industrial applications. Apart from conventional soft magnetic materials, amorphous and nanocrystalline soft magnetic materials are widely used for applications [MARI2000, LIUY2006, KRON2007]. A brief description on soft magnetic materials for various applications is discussed below.

### 2.10.1. Conventional soft magnetic materials

Fe-Si alloys are used for transformer cores in exclusion of all other soft magnetic alloys and are commonly known as 'electrical steel' or 'silicon steels'. With the introduction of Si into iron a significant increase in resistivity and a large drop in core loss were observed [BARR1900]. This is very much suitable for soft magnetic applications. However addition of more than 3% of Si makes the alloy brittle, which is a drawback for specific applications [BOZO1953]. Addition of Al in Fe-Si improves the ductility of the alloy, as in commercially available alloy "Sendust". With high Si and Al content, saturation induction decreases to 1.2 T and hence is not used in power transformer applications. Due to the high mechanical hardness and magnetic softness, it is used in some magnetic recording heads [BOZO1993]. Among other conventional soft magnetic alloys, Fe-Ni based alloys under the generic name "Permalloy" have been commercially used. Permalloy has high initial permeability and low magnetostriction as well as magnetocrystalline anisotropy. There are special grades of Ni-Fe alloys that have zero magnetostriction and anisotropy [JILE1991]. On the other hand, Fe-Co based alloys (Permendur) are used as soft magnetic materials due to their high saturation induction ($B_S$ = 24 kG) and relatively low

magnetic anisotropy [LIUY2006]. These alloys are basically used in transformers and generators on aircraft power system and magnetic shield applications.

### 2.10.2. Amorphous and nanocrystalline soft magnetic materials

Amorphous and nanocrystalline materials are mainly used for soft magnetic applications. Amorphous metallic alloys are basically formed by rapidly quenching molten alloys. Due to the lack of long range order, amorphous alloys have no MCA and hence magnetic softness prevails. Mostly transition metal based alloys such as Fe-(B, P, Si), Fe-(Zr, Nb, Hf) are used as soft magnetic materials. Due to the high electrical resistivity of these materials, they are used for high frequency applications. Apart from Fe based amorphous alloys, Fe-Co-B based alloys are used for soft magnetic purposes due to the zero magnetostriction. By changing the Fe/Co ratio, magnetostriction of the material can be tuned and accordingly soft magnetic properties can be improved. Soft ferrites such as manganese-zinc ferrite and nickel-zinc ferrite are used as soft magnetic materials. The major advantages of these ferrites are high electrical resistivity and low cost. However, these alloys have low magnetizations [MOOR1984, OHAN1987].

Nanocrystalline materials are developed by controlled annealing of amorphous precursors. There are mainly three types of nanocrystalline alloys: FINEMET, NANOPERM and HITPERM. Fe-Si-B-Nb-Cu based alloys belong to the FINEMET family. In this case, $\alpha$-Fe(Si) nanocrystals with a $DO_3$ structure gives rise to the soft magnetic properties [YOSH1988]. NANOPERM (the original composition was Fe-Zr-B) was developed in Prof. Masumoto's laboratory at IMR Tohoku University in 1989. Upon crystallizing the amorphous precursor of NANOPERM alloys, $\alpha$-Fe nanocrystals developed inside amorphous matrix. The presence of two-phase microstructure is responsible for the magnetic softness in these alloys [SUZU1991, MAKI1994]. The strong intergranular exchange coupling between the nanocrystals through the FM amorphous matrix results very low MCA, which is averaged out and improves the soft magnetic properties. The presence of only $\alpha$-Fe enhances the saturation induction. However, the formation of $Fe_3Zr$ compounds inside the matrix as the secondary crystallization product was observed when the annealing temperature is increased. This deteriorates the soft magnetic behavior. Hence, optimization of annealing condition is very much essential to obtain excellent soft magnetic properties. HITPERM alloy mainly consists of Fe-Co-Zr-B. The primary crystallization product of HITPERM alloy is $\alpha$-Fe(Co) upon annealing. Due to the presence of Fe(Co) phase, saturation

induction is quite high. Also, $T_C$ is higher than that of NANOPERM type alloys. So, these alloys are used for high temperature applications.

### 2.10.3. Applications of soft magnetic materials

Amorphous and nanocrystalline soft magnetic alloys are used in various applications. Among these, a few prominent ones are summarized below:

(i) Amorphous alloys are basically used in power transformer, inductive mode choke coil, magnetic shields, magneto-elastic transducers, and magnetic heads for data storage applications. These materials should have higher permittivity, large magnetic induction and high resistance for the above applications [VELI1970, MARI2000, KRON2007].

(ii) FINEMET type alloys are used for the attenuation of pulse voltages in choke coils. These choke coils can be used over a wide frequency range as well as for protection from high voltage noise caused by lightning. These alloys are superior to Fe based alloys for this type of applications [ZHAN1996, MCHE1999].

(iii) NANOPERM type alloys are used for applications as transformer core materials, including high frequency transformers due to the higher thermal stability and higher induction [MAKI1995]. Nanocrystalline alloy films have been proposed as core materials for thin-film magnetic heads as well as high frequency transformers and inductors. Apart from that these materials are used as power transformers, common-mode choke coils, pulse transformers and flux gate magnetometers [MAKI1994]. A choke coil is an active filter used to prevent signal distortion in the reactor elements of phase modifying equipment. They provide line current corrections in all current signals. The core material of a choke coil needs large saturation induction, $B_S$ and low core losses as well as small magnetostrictive coefficients. Since NANOPERM alloys have higher $B_S$ values comparable to amorphous Fe-Si based alloys and lower core losses, these materials are suitable for above mentioned applications.

(iv) Fe-Co based HITPERM alloys are used in high temperature applications. These materials are used in space power systems. Other applications include core materials and winding wires for audio and radio frequency transformers. Due to the higher $T_C$ of these materials they are used in aero-space applications [PARK1997, YOSH1998].

(v) Co rich alloys in particular (Fe-Co)-Si-B exhibit vanishing magnetostriction in the as-made state, but exhibits outstanding properties related to a high initial susceptibility despite the low $M_S$ [GOME1993]. A large field induces variations in the impedance of soft magnetic amorphous wires and ribbons, an effect known as the magnetoimpedance effect [BEAC1994, PANI1994]. The effect as a magnetic field sensor can be adapted to monitor the passage of moving pieces or vehicles in many industrial processes. This would act as a position sensor based on magnetoimpedance effect. Also, this type of alloy can be used in antitheft system based on FM resonance.

# *Chapter 3*

## *Experimental procedures*

In the course of the present investigations, several experimental techniques were used for the preparation and characterization of the samples. This chapter gives a brief description of these experimental techniques.

### 3.1. Techniques used for materials processing

Material processing has been carried out by two different preparation routes viz. melt spinning technique and mechanical alloying process. So, the final products were in the form of ribbons (with 2 – 3 mm width and 20 – 30 μm thickness) or powders (with average size below 40 nm). Subsequently, the ribbons were annealed at different temperatures in vacuum under constant magnetic field applied along the length of the ribbons. A brief discussion on both the preparation techniques and the corresponding equipment is given below.

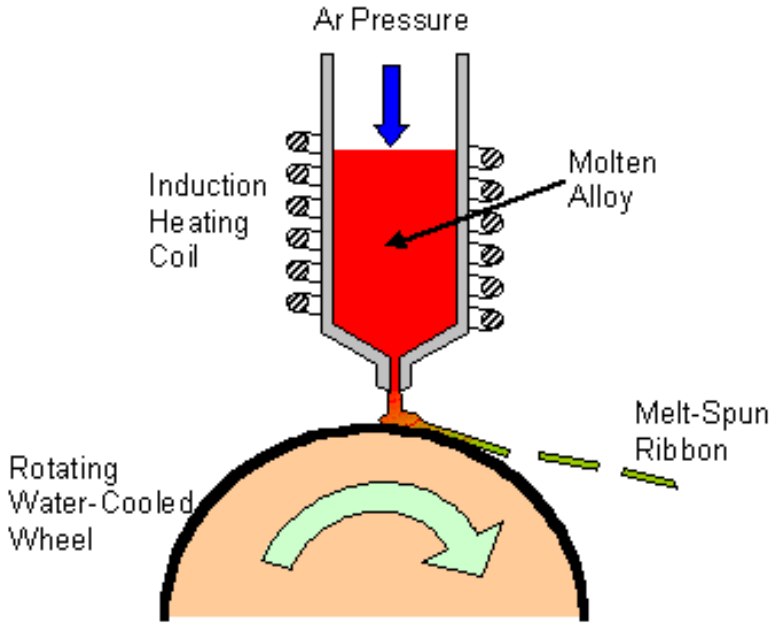


*FIG. 3.01: Schematic diagram of melt-spinning technique.*

#### 3.1.1. Melt spinning technique

Fig.3.01 shows the schematic diagram of a melt spinning apparatus. The alloy ingot is placed in a fused silica tube, which is situated inside a water-cooled RF-coil of an induction heater. When the induction coil is energized, the ingot kept inside the tube is melted. The molten alloy is ejected through the orifice at the bottom of the tube by pressurized Argon gas on to a water-cooled copper wheel rotating at a high speed. The molten jet strikes the surface of the wheel and

immediately quenched. The quenching rate of the alloy is around $10^5$ to $10^7$ K/sec [ANAN1984, HARG1981, LUBO1983]. This results in the formation of long continuous ribbon samples with 1 – 10 mm width and 10 – 50 μm thickness. The instrument is suitable for making amorphous transition metal – transition metal based alloys, transition metal – metalloid based alloys and some types of polygrained quasicrystals.

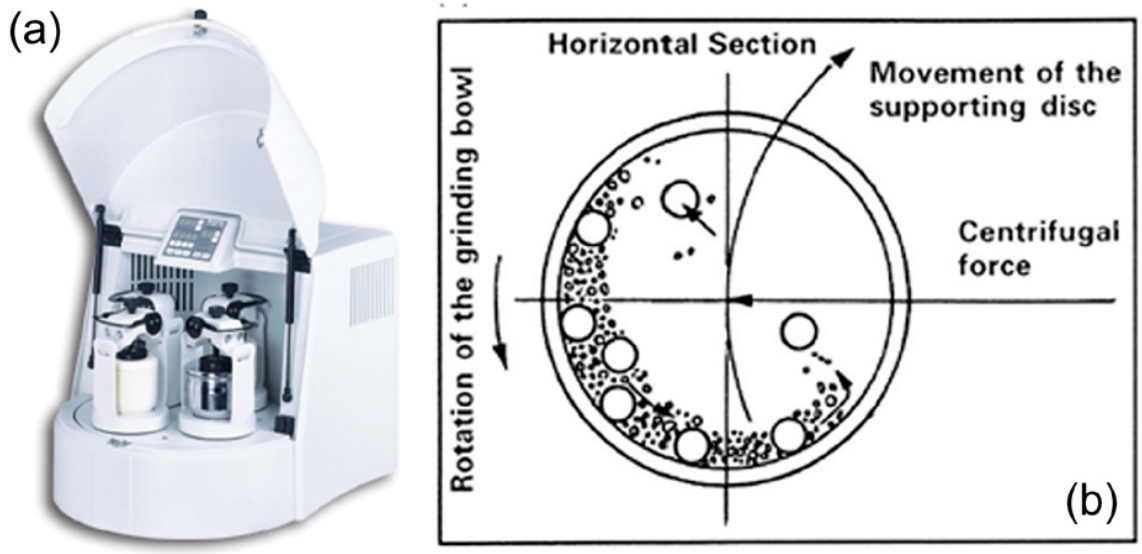


*FIG. 3.02: (a) Photographic view of planetary ball mill and (b) schematic view of mechanical milling process.*

### 3.1.2. Mechanical alloying technique

Mechanical alloying (MA) of elemental powders was carried out by high-energy ball milling in a planetary ball mill (Insmart, India). The photographic view of the planetary ball mill, comprising of a horizontal support disc on which vials are mounted, and the schematic view of mechanical milling process are shown in Fig.3.02. The vial rotates in a direction opposite to that of the disc, thereby simulating a planetary motion. This planetary motion results in large centrifugal force acting on the balls kept inside the vial. This causes the balls to collide with themselves and to the wall of the vial with high impact. When a mixture of elemental powders corresponding to a particular composition is placed in the vial along with the balls, the powders are subjected to repeated cold welding and fracture at the surfaces of the balls and the vial. This process leads to disintegration of the powders, resulting first in refinement of crystallite size and ultimately in atomic level mixing of the elements and in alloy formation [SONI2001, KOCH2002, SURY2004]. Hence, size refinement is a natural consequence of a MA process. As the milling

time progresses the alloy becomes amorphous. The refinement and alloying processes are determined by the milling parameters such as powder to ball weight ratio, ball size, rotation speed, milling time, *etc*. Nature of the milling vial and balls also plays an important role in the process along with the milling media.

In the present work, dry milling of high purity elemental powders has been carried out under argon gas atmosphere. Hardened steel vial and hardened steel balls were used for milling all the powder compositions. The ball to powder ratio of 20:1 and the rotating speed of 500 rpm were maintained during milling process. In order to avoid excessive heating, mill was stopped for 10 minutes after every 15 minutes of continuous milling. In addition, Ar gas was periodically filled inside the vial to maintain an inert atmosphere.

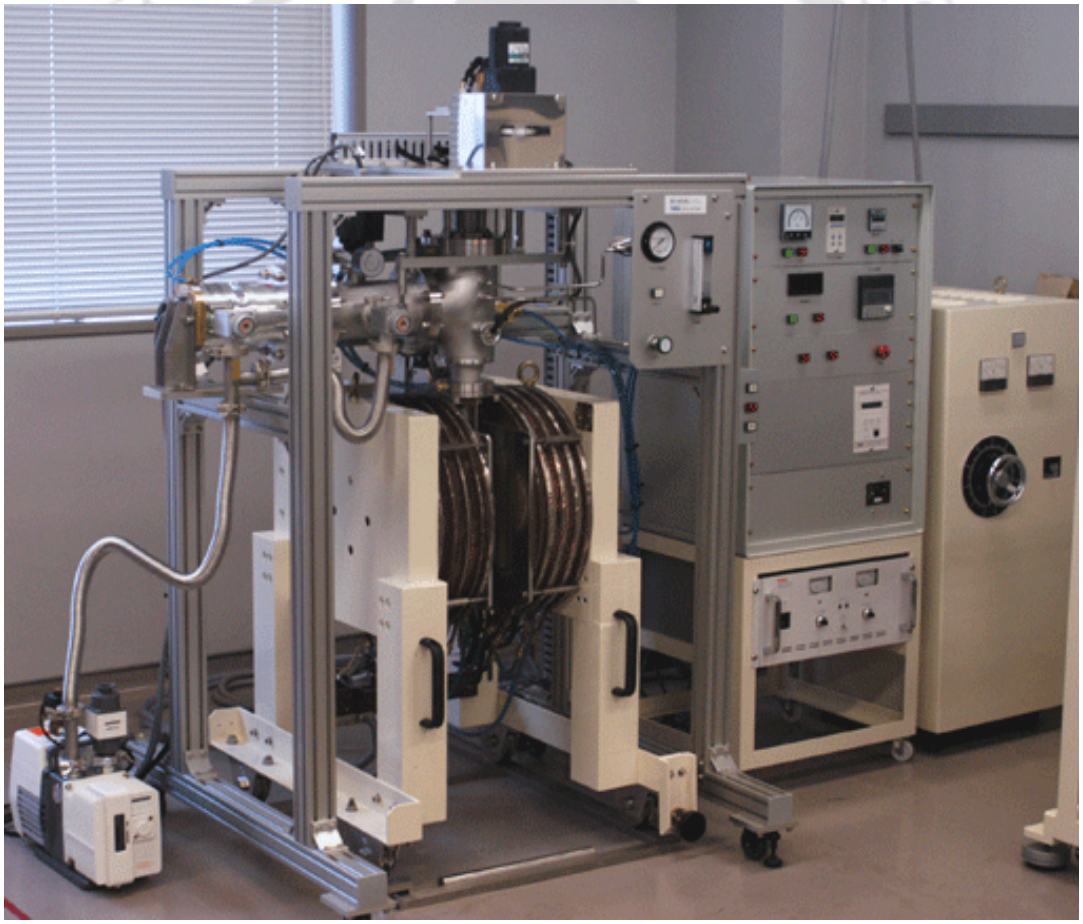

*FIG. 3.03: Photographic view of typical magnetic field annealing set up used for the heat treatment of the amorphous ribbons.*

### 3.1.3. Magnetic field annealing at elevated temperatures

In order to understand the evolution of nanocrystalline microstructure in the amorphous alloys and to avoid oxidation, heat treatment of the amorphous ribbons were carried out in vacuum. Fig.3.03 shows the photographic view of typical set up used for magnetic field annealing. The amorphous ribbons were cut into many pieces of equal length and wrapped in an aluminum foil. The foil was kept inside the sample chamber such that the length of the ribbons was parallel to the applied magnetic field direction. The sample chamber was then evacuated to $10^{-5}$ Pa with a turbomolecular pump backed by a rotary pump. The magnetic field of 6 kOe was applied after evacuating the chamber. Subsequently, the furnace temperature was raised to the desired annealing temperature under a heating rate of about 10 K/min. The annealing temperature was controlled to ± 2 K with a temperature controller. Samples were annealed at different elevated temperatures between 473 K and 923 K for one hour duration. After the completion of heat treatment at a particular temperature, the heater was switched off and the sample was allowed to cool down naturally to the room temperature.

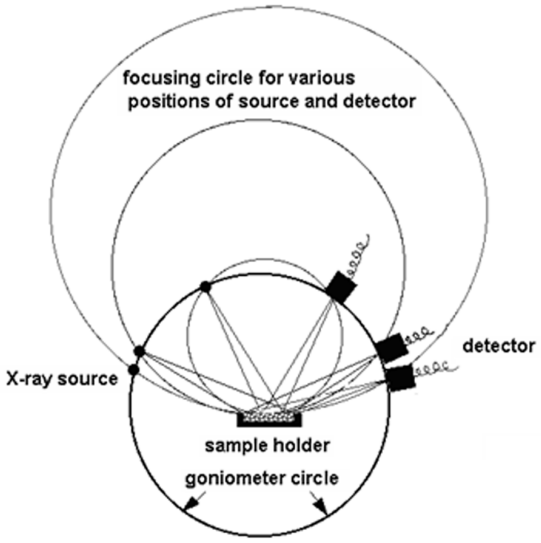


*FIG. 3.04: Schematic view of Bragg-Brentano diffraction geometry.*

## 3.2. Structural property characterization

### 3.2.1. X-ray diffractometer (XRD)

Three different powder X-ray diffractometers *viz*. Rigaku RINT 2500, Bruker D8, and Seifert 3003 T/T were used in the thesis work, depending upon their availability. Cu-$K_\alpha$ X-ray radiation

with wavelength 1.5406 Å was used in all the cases. The theta-theta ($\theta - \theta$) goniometer was used in the reflection (Bragg-Brentano) geometry (*cf.* Fig.3.04) [CULL2001]. X-ray diffraction (XRD) technique allows identification of various crystalline phases present in the material and provides other structural information such as the average size of the crystallites, strains present inside the crystallites, *etc*. An ideal crystal has a periodic arrangement of atoms. Diffraction of X-rays occurs through constructive interference of X-rays scattered from atoms of a set of parallel planes in crystal lattice at particular angular positions of the incident wave known as Bragg angles. This condition for obtaining constructive interference is known as Bragg's law and given by the relation

$$2d_{hkl} \sin\theta_o = n\lambda \qquad (3.1)$$

where $d_{hkl}$ is the inter-planer spacing, $\theta_o$ is the glancing angle, $\lambda$ is the wavelength of the X-ray and $n$ is the order of diffraction. A sequence of these angles can be used to determine the Miller indices ($hkl$) values and the crystal structure can be identified from the systematic behavior of these indices. Fig.3.05 shows the diffraction of X-rays from crystal lattice planes illustrating Bragg's law. Structural parameters such as average crystallite size, presence of various

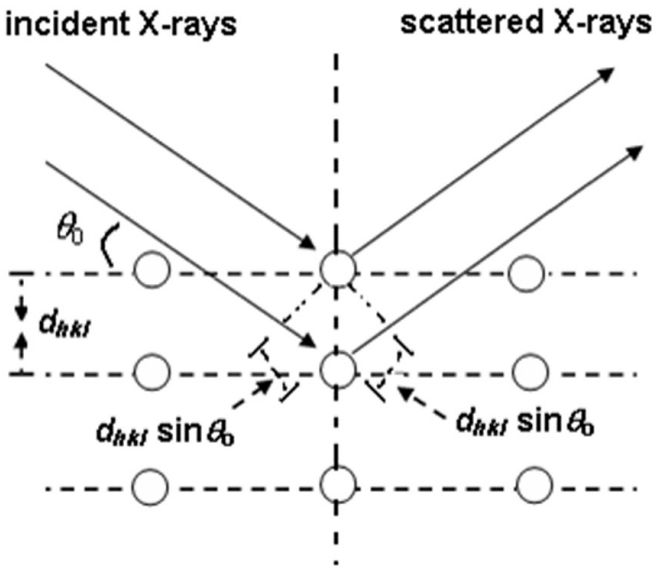


*FIG. 3.05: Schematic ray diagram of diffraction of X-rays by a crystal.*

crystalline phases in the matrix, strain induced inside the materials, degree of crystalline order, etc can be quantitatively determined from the analysis of XRD patterns [CULL2001].

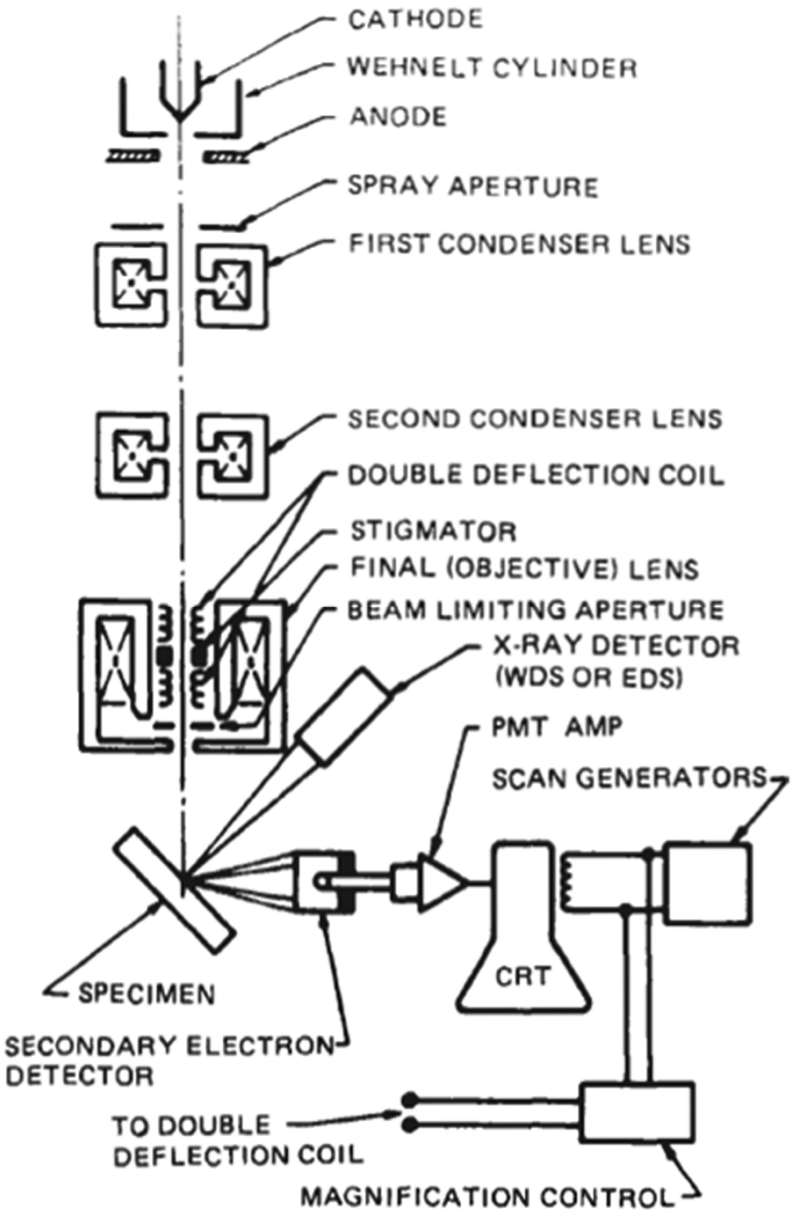


*FIG. 3.06: Schematic view of scanning electron microscope [OHRI1992].*

### 3.2.2. Scanning electron microscopy

Scanning electron microscope (SEM, Leo 1430VP) with energy dispersive spectroscopy (EDS) attachment (Oxford) has been used to study the surface morphology of the powders and elemental compositions of the alloys. SEM is a microscopic technique that uses electrons to form an image of objects and to study surface morphology, fractured components, foreign particles and residues, polymers, electronic components, biological samples and countless others. The schematic view of SEM is shown in Fig.3.06. The thermionically emitted electrons from a tungsten filament are drawn to an anode, focused by two successive condenser lenses into a beam with a narrow fine spot size (~ 50 Å). The shorter wavelength of electrons permits image

magnifications of up to 100,000 times in SEM. Pair of scanning coils located at the objective lens deflect the beam either linearly or in raster fashion over a rectangular area of specimen surface. These primary bombarding electrons on the surface of the specimen dislodge electrons from the specimen. Fig.3.07 shows the interaction of electrons with surface of the sample. Upon electron impingement on the surface, the interaction volume assumes a tear shape. These dislodged electrons are known as secondary electrons, which are attracted and collected by a positively biased grid or detector, and then translated into a signal. These signals are then amplified, analyzed, and translated into images of the topography being inspected. Finally, the image is shown on a cathode ray tube (CRT). The most common imaging mode relies on the detection of the very lowest portion of the emitted energy distribution. Their very lower energy means they are originated from a subsurface depth of no longer than several angstroms.

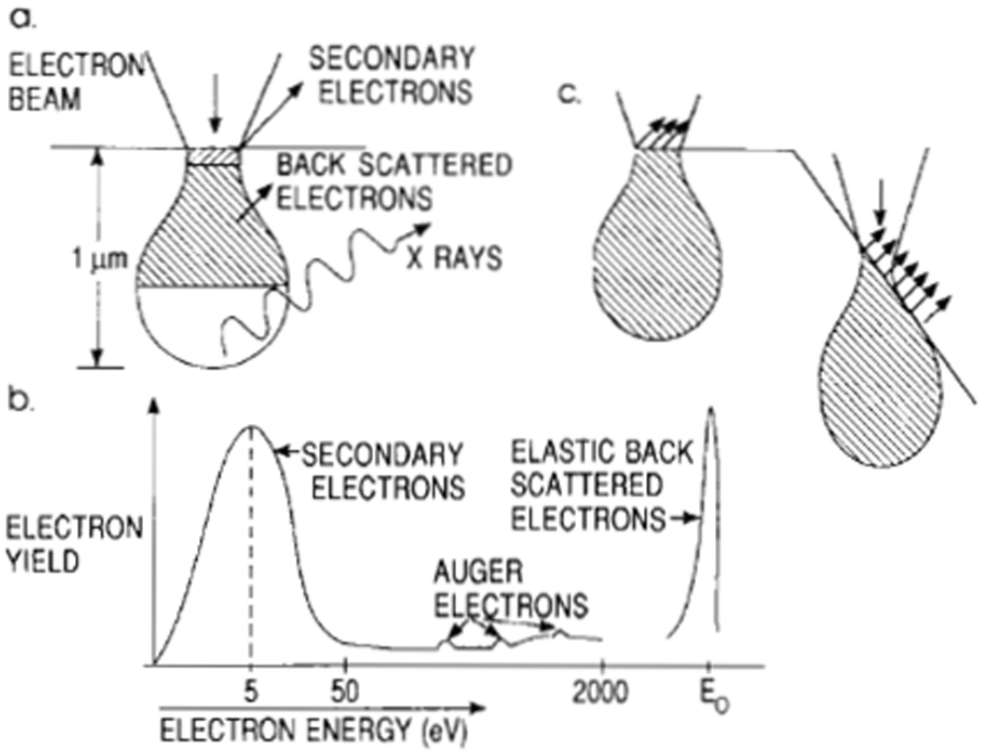


*FIG. 3.07: (a) Electron and photons signals emanating from tear-shaped interaction volume during electron beam impingement on specimen surface, (b) Energy spectrum of electrons emitted from the specimen surface, and (c) Effect of surface topography on electron emission.*

Apart from secondary electrons, the primary electron beam results in the emission of backscattered (or reflected) electrons from the specimen. Backscattered electrons possess more

energy than secondary electrons and have a definite direction. As such, they can not be collected by a secondary electron detector, unless the detector is directly in their path of travel. All emissions above 50 eV are considered to be backscattered electrons.

Backscattered electron imaging is useful in distinguishing one material from another, since the yield of the collected backscattered electrons increases monotonically with the specimen's atomic number $Z$ (~$0.05Z^{1/2}$). Backscatter imaging can distinguish elements with atomic number differences of at least 3, *i.e*. elements with atomic number differences of at least 3 would appear with good contrast on the image.

EDS analysis is useful in identifying materials and contaminants, as well as estimating their relative concentrations on the surface of the specimen. During EDS analysis, the specimen is bombarded with an electron beam inside the SEM. The bombarding electrons collide with the specimen atoms own electrons, knocking some of them off in the process. A position vacated by an ejected inner shell electron is eventually occupied by a higher-energy electron from an outer shell. To be able to do so, however, the transferring outer electron must give up some of its energy by emitting X-rays. The amount of energy released by the transferring electron depends on which shell it is transferring from, as well as which shell it is transferring to. Furthermore, the atom of every element releases X-rays with unique amounts of energy during the transferring process. Thus, by measuring the amounts of energy present in the X-rays being released by a specimen during electron beam bombardment, the identity of the atom from which the X-ray was emitted can be established. The output of an EDS analysis is an EDS spectrum, which is just a plot of how frequently an X-ray is received for each energy level. An EDS spectrum normally displays peaks corresponding to the energy levels for which the most X-rays had been received. Each of these peaks is unique to an atom, and therefore corresponds to a single element. The higher a peak in a spectrum, the more concentrated the element is in the specimen.

In the present work, a thin layer of powder was spread on carbon coated tape. Gold coating was then applied over it to yield an electrically conducting surface for SEM observation.

### 3.2.3. Transmission electron microscopy

Transmission electron microscopes (TEM, JEOL 2100; TECNAI $G^2$ F30) were used to study the nanocrystalline microstructure of the samples. Fig.3.08 shows the cut view of TEM and schematic ray diagrams for imaging and diffraction modes. Electrons thermionically emitted

from the gun are accelerated to 100 keV or higher and first projected onto the specimen by means of the condenser lens system. The scattering processes experienced by electrons during their passage through the specimen determine the kind of information obtained. Elastic scattering, involving no energy loss when electrons interact with the potential field of the ion cores, gives rise to diffraction patterns. Inelastic interactions between beam and matrix electrons at heterogeneities such as grain boundaries, dislocations, second-phase particles, defects, density variations, etc., cause complex absorption and scattering effects, leading to a spatial variation in the intensity of the transmitted beam.

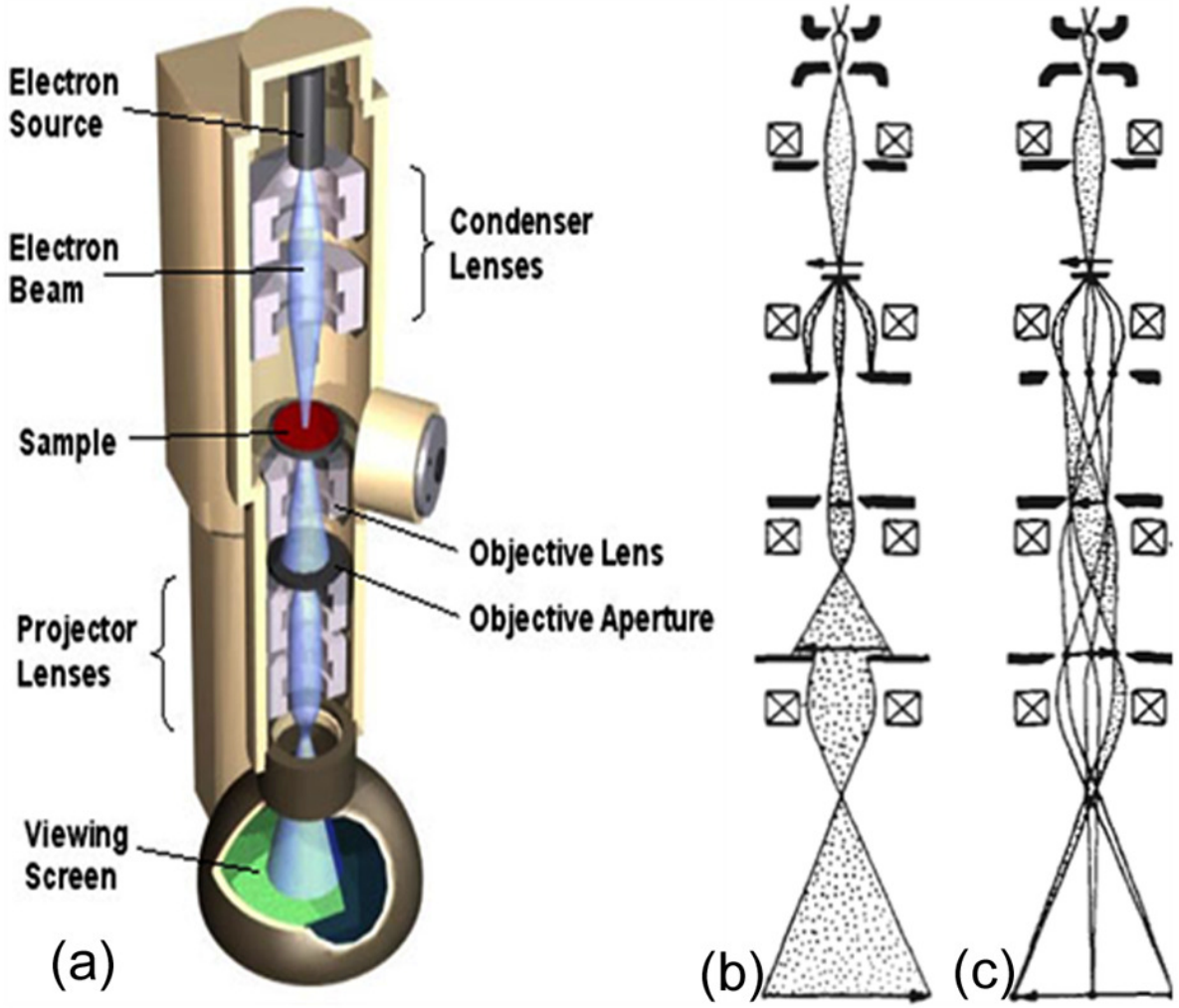


*FIG. 3.08: (a) Cut view of transmission electron microscope (b) Schematic ray diagrams of image mode and (c) diffraction mode.*

Images can be formed in a number of ways. The bright-field image is obtained by intentionally excluding all diffracted beams and only allowing the central beam through the

specimen. This is done by placing suitably sized apertures in the back focal plane of the objective lens. Intermediate and projection lenses then magnify this central beam. Dark-field images are also formed by magnifying a single beam; here one of the diffracted beams is chosen by means of an aperture that blocks the central beam and the other diffracted beams. By selected area diffraction pattern, ring like structure is imaged, which corresponds to the particular plane of that element or compound. If only diffused rings appear then the system must have single amorphous phase. From the high-resolution TEM (HR-TEM) image, average grain size, and dislocations can be evaluated.

In the present study, the melt-spun ribbons were initially polished mechanically to reduce the thickness down to 10 μm and subsequently thinned down using precision ion polishing system (PIPS) to suitable thickness for the TEM observation. In the case of powdered samples, it was first finely dispersed in dimethyl fomamide solution and then a drop of the liquid was placed on a carbon coated grid for the TEM observation [REIM1993, BRAN2008].

### 3.3. Thermal property characterization

Thermal property characterizations involving the measurement of endothermic and exothermic reactions, their enthalpies and specific heats can be performed using an adiabatic calorimeter or a differential scanning calorimeter. The latter technique is quite fast, requires only small amounts of samples and easy to perform with commercially available equipment.

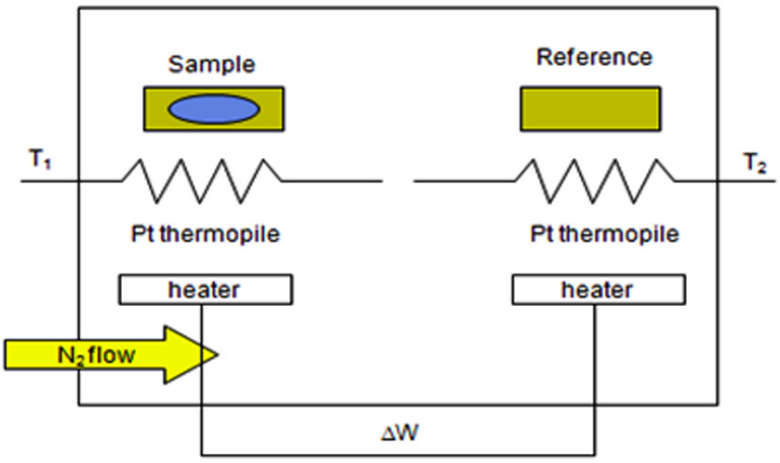


*FIG. 3.09: Schematic diagram of differential scanning calorimeter.*

### 3.3.1. Differential Scanning Calorimeter

A Differential Scanning Calorimeter (DSC, Perkin Elmer DSC 7) was used in the present work to study the thermal properties of amorphous ribbons and powders. Fig.3.09 shows the schematic diagram of a DSC. DSC is a thermo-analytic technique in which the difference in the amount of heat required to increase the temperature of a sample and a reference material is measured as a function of temperature [HOHN2003]. The DSC curves are recorded either under a constant heating (or cooling) rate or under isothermal conditions (time scan at a constant temperature). A typical DSC consists of two isolated sealed pans, one containing the sample and the other a reference material (generally, $Al_2O_3$ or just the empty Al pan). The pans are covered with Al covers, which act as a radiation shield. The two pans are heated or cooled uniformly while the heat flow difference between the two is monitored. The basic principle underlying this technique is that, when the sample undergoes a physical transformation such as phase transition, more or

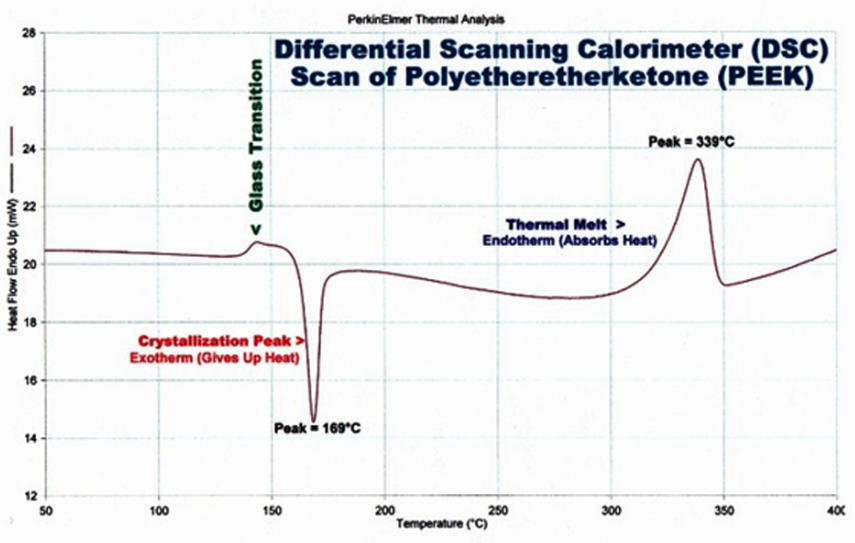


*FIG. 3.10: Thermal evolution of polyetheretherketne sample observed using differential scanning calorimeter.*

less heat will need to flow to it than the reference in order to maintain both at the same temperature [HOHN2003]. More or less heat flowing would depend on the process being exothermic or endothermic. In the power compensation type DSC, heat is supplied to either of the pans so that both are maintained at the same temperature. The heat flow (*dH/dt*) is then estimated from this data. Fig.3.10 shows thermal evolution of polyetheretherketne sample observed using DSC. As the temperature increases the sample under goes glass-transition

followed by crystallization which is an exothermic process. As the temperature increases, another peak corresponding to the melting of the sample is traced which is an endothermic process. Different heating rates such as 10, 15, 20, and 30 K/min have been used to calculate the activation energy of the samples.

A commercial DSC (PerkinElmer, DSC 7) based on the power compensation technique was used in the current investigations. About 10 mg of powder and/or ribbons was taken in an alumina pan and the thermal transformations occurring during heating cycle under a constant heating rate was studied. The runs were programmed and the DSC curves (*dH/dt* versus *T* data) were recorded and analyzed using the Pyris™ software. Temperature and enthalpy calibrations were performed using standard samples (In and Zn). High purity nitrogen gas was purged continuously throughout the runs.

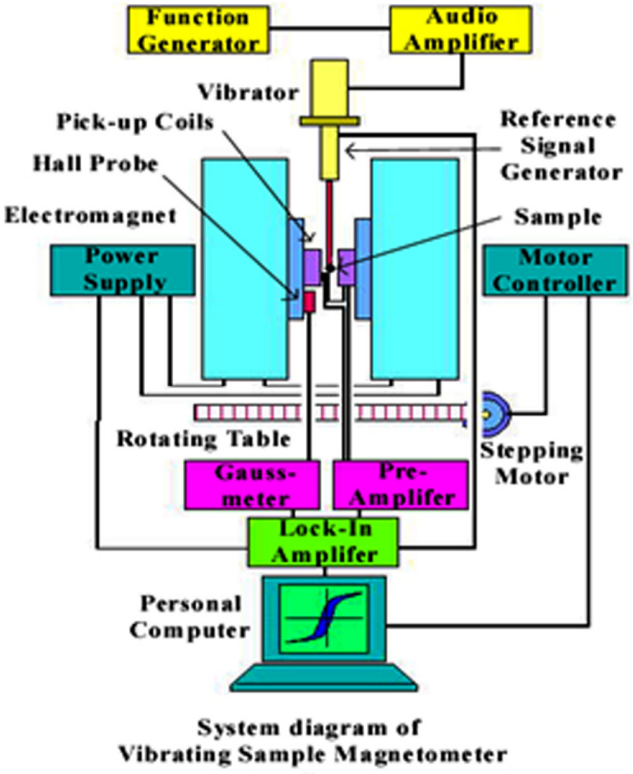


*FIG. 3.11: Schematic diagram of a vibrating sample magnetometer.*

### 3.4. Magnetic property characterization

Magnetic properties of a material can be characterized with various experimental techniques such as vibrating sample magnetometer, superconducting quantum interference device, and

coercimeter, while the magnetic domain structure of the samples was observed using Lorentz microscope mode in a TEM. In this section, a brief outline of the principle involved in various magnetic measurement techniques employed in the present work is given.

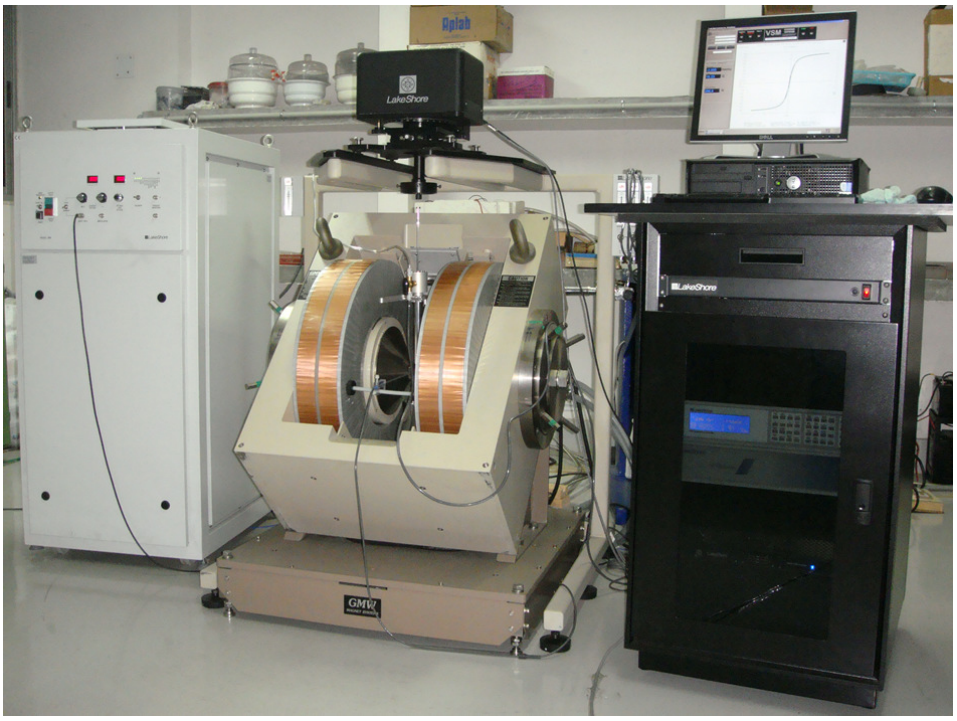


*FIG. 3.12: Photographic view of a vibrating sample magnetometer (Lakeshore Model 7410).*

### 3.4.1. Vibrating sample magnetometer

Vibrating sample magnetometer (VSM, Lakeshore model 7410) was used to investigate the magnetic properties. VSM [JANS2004, HORS2006] measures the net dipole moment when the material is exposed to magnetic field. The magnetic moment of the sample can be obtained either as a function of field (magnetic hystersis loop) or as a function of temperature to investigate the evolution of magnetic properties with temperature and understand the magnetic phase transition of the samples. Figs.3.11 and 3.12 depict a schematic diagram and a photographic view of VSM, respectively.

When a sample is placed in a uniform magnetic field, a dipole moment proportional to the product of the sample susceptibility and the applied field is induced in the sample. If the sample is made to undergo sinusoidal motion, an electrical signal can be induced in suitably located stationary pickup coils (Fig.3.11). This signal has amplitude proportional to the magnetic moment of the sample, the vibrating amplitude and the vibration frequency. Through the use of

lock-in-amplifier and feedback techniques, only that portion of the signal arising from the magnetic moment is picked up and is converted into direct read-out in the unit of magnetization (e.g. *emu*) on a digital panel meter. The VSM consists of the following major parts: 1. Water cooled electromagnet and power supply, 2. Vibration exciter and sample holder (with angular position indicator), 3. Sensing coils, 4. Hall probe, 5. Amplifier, 6. Control chassis, 7. Lock-in amplifier and 8. Computer interface.

The sample was fixed to the lower end of the sample holder after the calibration procedure using standard Ni sample. Subsequently, the measurement sequence is programmed using the software (IDEASVSM) provided with the instrument. The vibration exciter is started and the signal received from the probe and the pick-up coils is converted into the magnetic moment value of the sample. Magnetic field up to 20,000 Oe was applied to the sample. Normally, magnetic field is automatically increased in steps at a constant temperature (magnetization, $M$, *versus* magnetic field, $H$, measurements] by setting the program. For high temperature measurements (magnetization, $M$, *versus* temperature, $T$, measurements), a high temperature attachment (Lakeshore) capable of providing a controlled heating/cooling of the sample from room temperature to 1223 K was used. For $M - T$ measurements a constant (slow) heating rate was maintained using the software supplied with the instrument.

### 3.4.2. Superconducting quantum interference device

Superconducting quantum interference device (SQUID, MPMS XL 7) was used to characterize low temperature magnetic properties with greater accuracy. Fig.3.13 shows a photographic view of the MPMS system. SQUID mainly consists of two Josephson junctions, i.e., two superconducting metals separated by a thin insulating layer, which is typically a metal oxide [ANTO1992]. The tunneling super current across the junction has a phase difference dependent on the magnetic field applied perpendicularly to this. Furthermore, each junction has a maximum value of the current that can flow without voltage drop across and above which normal electrons need to flow and a finite voltage drop appears. This finite voltage drop causes the supercurrent to cease. In particular, in a superconducting ring interrupted by two Josephson junctions, the application of a magnetic field normal to the ring causes an induced supercurrent to screen the magnetic field. When induced supercurrent exceeds the critical value, it allows the magnetic flux to enter the hollow portion of the ring, in multiples of one quantum unit. The process repeats for

an increasing magnetic applied external field and the flux increases each time by one quantum unit. Located coaxially to the ring, a pick-up coil enables measurement of the magnetic field (for a ring of known geometry) by counting the pulses of e.m.f. induced each time the magnetic flux changes.

The sample was fixed in the suitable sample holder and the magnetic field up to 70 kOe was applied to the sample. The magnetic field was increased automatically in steps at a constant temperature (magnetization, *M*, *versus* magnetic field, *H*, measurements] by setting the program. For low temperature *M* – *T* measurements under a constant magnetic field, the temperature was controlled using suitable temperature controllers (Quantum Design) from 5 K to room temperature.

*FIG. 3.13: Photographic view of a Magnetic Property Measurement System (MPMS XL 7, Quantum Design).*

### 3.4.3. Coercimeter

The magnetic characterization of soft ferromagnetic materials having irregular shape is measured by coercimeter [HORS2006]. This instrument measures the coercivity of soft magnetic materials.

Fig.3.14 displays the photographic view of the coercimeter used for measuring ultra-low coercivity of soft ferromagnetic materials. The measurement is automatically executed and driven by the software. The measuring principle is very simple and can be described as follows:

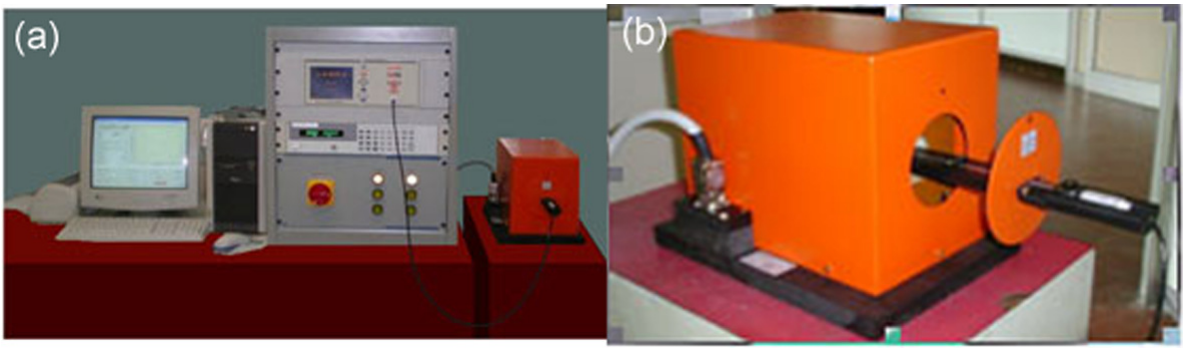


*FIG. 3.14: (a) Photographic view of a Coercimeter set up. (b) Mu-metal shield that permits to prevent disturbance from external magnetic fields.*

The sample, magnetized by the magnetic field produced by the solenoid, produces a field, whose transversal component is detected by a Hall probe. When the field of the solenoid is equal and opposite to the coercivity of the sample, the material becomes completely 'transparent' to the magnetic field, and the transversal component becomes zero. In this condition, i.e. when the Hall probe reading is zero, the solenoid field equates the coercivity of the material. When the coercivity of the sample is lower than 40 A/m (1 Oe = 79.6 A/m), it is necessary to shield the sample, to avoid influences from external magnetic fields (even the Earth magnetic field can affect the result). For this reason, a mu-metal shield is provided, guaranteeing a reduction of external influences to negligible values, and permitting to measure the coercivity lower than few A/m. The software provided with the instrument handles the data acquisition and processing automatically.

### 3.4.4. Lorentz microscopy

Magnetic domain structure can be obtained with the help of Lorentz microscope which is based on the principle of Lorentz force, F [$=-e(v\times B)$] acting on a charged particle in the presence of a magnetic field [WILL1996]. The parameters $v$ and $B$ are the velocity of charged particle and magnetic field on the charged particle. Domain observation can be obtained in two modes *i.e.* Fresnel mode and Foucault mode. For $180^{o}$ domain cases, domains are magnetized in opposite

directions in alternate domains. According to Fleming's left hand rule, the electron beam is deflected in opposite directions in adjacent domains, leading to a deficiency of electrons and an excess of electrons due to overlap in the region below the lower specimen surface. If we observe the specimen on the over-focus condition, the increase and the decrease of the electron intensity are observed at the positions of the domain walls periodically as shown in Fig.3.15(b). On the other hand, if we observe the specimen on the under-focus condition, the reversed image contrast appears as shown in Fig.3.15(c). A typical Lorentz image of nanocrystalline $Fe_{79}Co_{10}Zr_{11}B_{10}$ alloy ribbon observed in Fresnel mode is shown in Fig.3.15(d). Under the just focus condition, there is no definite image contrast, while under the de-focused condition, white or black lines appear at the positions of magnetic domain walls depending on the sign of defocus. The width of the white or black lines directly depends on the focus setting. Taking into account the experimental condition such as focus setting carefully, the wall width can be evaluated quantitatively [HIRS1977, REIM1993].

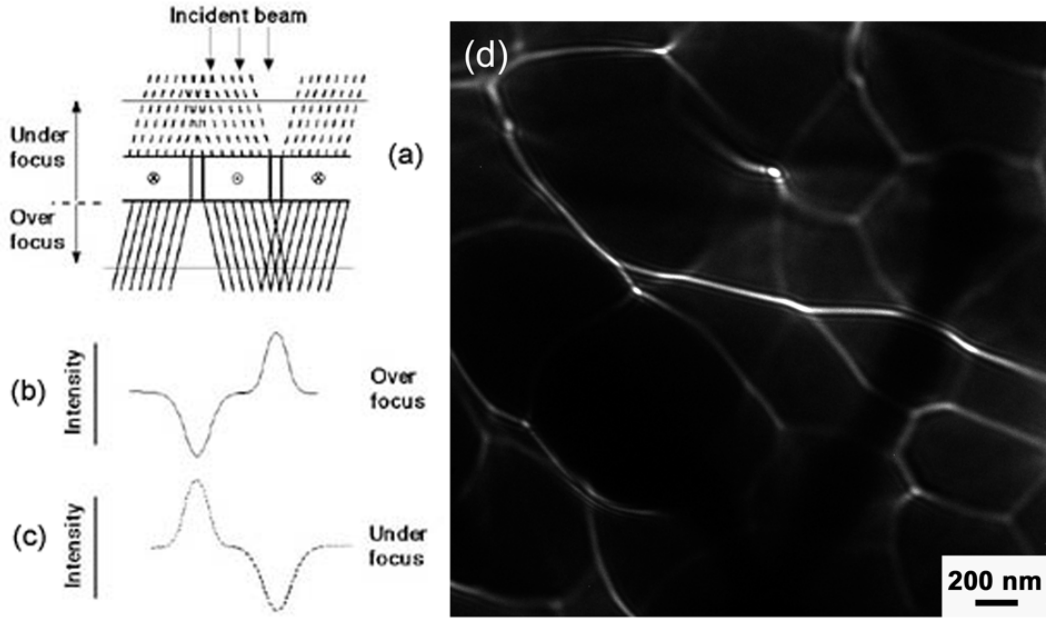


*FIG. 3.15: (a) Schematic illustration of Lorentz microscope in Fresnel mode and the image intensity under (b) over-focus and (c) under-focus conditions. (d) A typical domain image obtained using Lorentz microscope for Fe-Co-Zr-B alloy.*

# Chapter 4

## Properties of amorphous Fe-(Co,Mn)-Zr-B alloy ribbons

Details of preparation of amorphous Fe-(Co,Mn)-Zr-B alloys ribbons and the results of experimental studies carried on these samples are discussed below.

### 4.1. Experimental Details

Alloys with nominal compositions of $Fe_{89-x}Zr_{11}B_x$ ($x$ = 0 – 10) and $Fe_{89-x-y}(Co,Mn)_yZr_{11}B_x$ ($x$, $y$ = 5, 10) were prepared by melting appropriate amounts of high purity Fe, Zr, B, Mn and Co (Strem chemicals) in an arc melting furnace under argon atmosphere. Subsequently, rapidly solidified ribbons of 2 – 3 mm width and 20 – 30 $\mu$m thickness were produced in controlled argon gas atmosphere using a vacuum melt spinner. The linear speed of the copper wheel of the melt spinner was optimized at 35 m/s. Amorphous nature of the as-spun ribbons was confirmed by X-ray diffraction (XRD, Rigaku RINT 2000) technique. The microstructure and domain structure were characterized by transmission electron microscope (TEM, JEOL 2100; TECNAI G2 F30). The magnetic domain structure of the amorphous ribbons was observed using Lorentz microscopy in Fresnel mode, which is an out-of-focus technique meant for identifying domain walls and their features. Thermal stability and crystallization behavior of the as-spun ribbons were determined from 323 K to 923 K using a Differential Scanning Calorimeter (DSC, PerkinElmer DSC7) under a constant heating rate of 20 K/min. Room temperature coercivity ($H_C$) and saturation magnetization ($M_S$) were obtained using coercimeter (Forster Koerzimat, Model 1.095) and vibration sample magnetometer (VSM, Lakeshore model 7410), respectively. Temperature dependent magnetization measurements ($M$ – $T$) were carried out using VSM and superconducting quantum interference device (SQUID, Quantum Design MPMS XL 7) magnetometer. The initial magnetization curves were measured up to 18 kOe applied field at 2 K interval at temperatures near the Curie temperature ($T_C$) of the alloys using the VSM.

### 4.2. Properties of amorphous Fe-Zr-B ribbons

#### 4.2.1. Structural properties

Fig.4.01 shows the XRD patterns of the amorphous (a-) $Fe_{89-x}Zr_{11}B_x$ alloys. All samples exhibit broad humps around $2\theta = 43°$ and 78° indicating that their structure is completely amorphous. In order to investigate the local microstructure of the amorphous alloys, all the samples were investigated by TEM. Fig.4.02 shows high-resolution TEM (HR-TEM) micrographs and selected area electron diffraction (SAED) patterns of a-$Fe_{89-x}Zr_{11}B_x$ ($x$ = 0, 5, 10) alloy ribbons. The

micrographs reveal a characteristic amorphous microstructure without any local lattice fringes, signifying the absence of medium range order in these alloys. Also, the SAED patterns show a halo diffraction ring typical of amorphous structure.

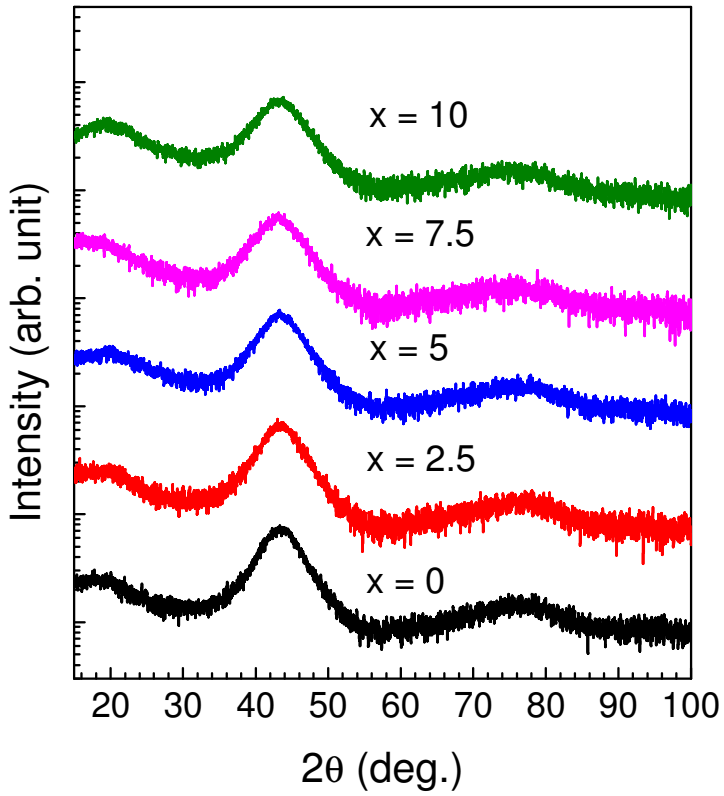


*FIG. 4.01: XRD patterns of amorphous $Fe_{89-x}Zr_{11}B_x$ alloy ribbons.*

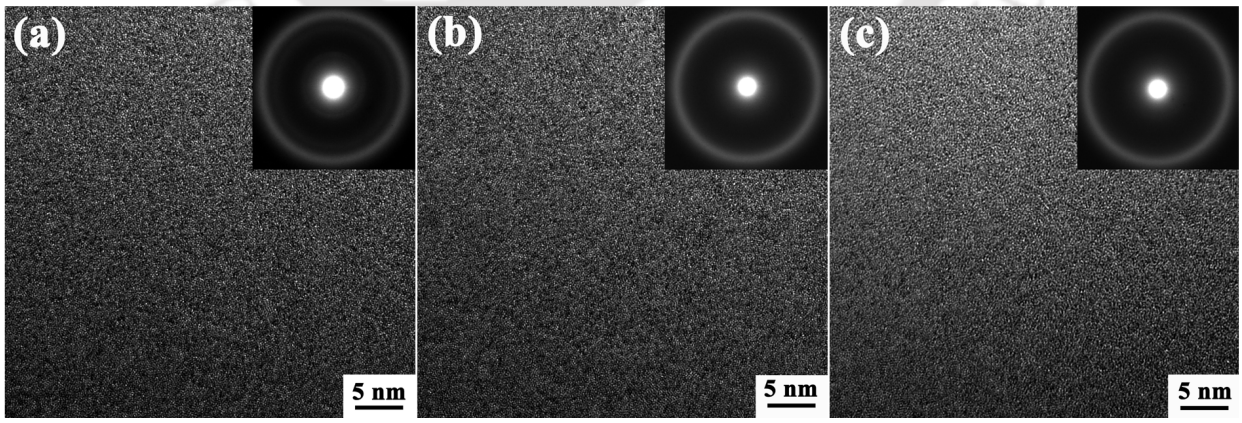


*FIG. 4.02: HR-TEM micrographs and SAED patterns of amorphous $Fe_{89-x}Zr_{11}B_x$ alloy ribbons with (a) x = 0, (b) 5 and (c) 10.*

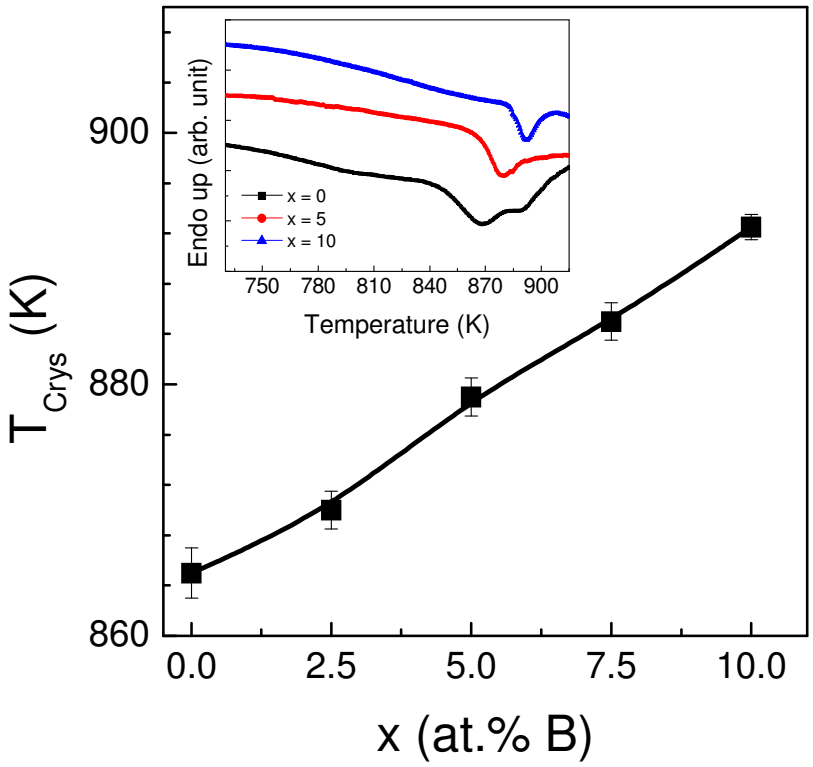


*FIG. 4.03: Variation of crystallization temperature with B substitution in $Fe_{89-x}Zr_{11}B_x$ amorphous alloy ribbons. Inset: DSC curves of amorphous $Fe_{89-x}Zr_{11}B_x$ alloy ribbons.*

### 4.2.2. Thermal properties

The crystallization behavior of a-$Fe_{89-x}Zr_{11}B_x$ ($x$ = 0 – 10) alloys were studied by tracing DSC curves in the temperature range between 323 K and 923 K. With an increase in temperature, crystallization of the amorphous alloys occurred as depicted by exothermic peak(s) in the DSC curve. Fig.4.03 inset shows the DSC curves of the alloys with $x$ = 0, 5 and 10 in the region close to the crystallization temperature(s). Two exothermic peaks corresponding to primary and secondary crystallization processes were observed for the sample with $x$ = 0. The primary crystallization peak temperature ($T_{crys}$) shifts to higher temperatures with the addition of B. The variation of $T_{crys}$ with the addition of B is shown in Fig.4.03. It can be seen that $T_{crys}$ increases almost linearly at a rate of about 2.9 K per at.% B. This indicates that the thermal stability of the amorphous phase against crystallization improves in a-Fe-Zr alloys with the addition of B. The observed results are in good agreement with those reported earlier on similar systems [HUAN2008, MAJU2007]. The reported value $T_{crys}$ of a-$Fe_{90}Zr_7B_3$ sample is around 803 K [XION2003], which is less than the value obtained in the present investigation. Even with 12

at.% B in a-$Fe_{93-x}Zr_7B_x$ alloy, $T_{crys}$ was reported to be only 830 K [XION2003], whereas, the currently studied alloys exhibited $T_{crys}$ > 850 K. Furthermore, other reports in the literature on the crystallization behavior of a-Fe-Zr-B alloys containing low Zr content (Zr =7 at.%) [KIMK1994, KOPC1997, SUZU1998, TATE1998] showed low $T_{crys}$ values (< 800 K). The large difference in the value of $T_{crys}$ is mainly due to the relative content of Zr and B and its influence on the stability of the amorphous phase in a-Fe-Zr-B alloys [HUAN2008].

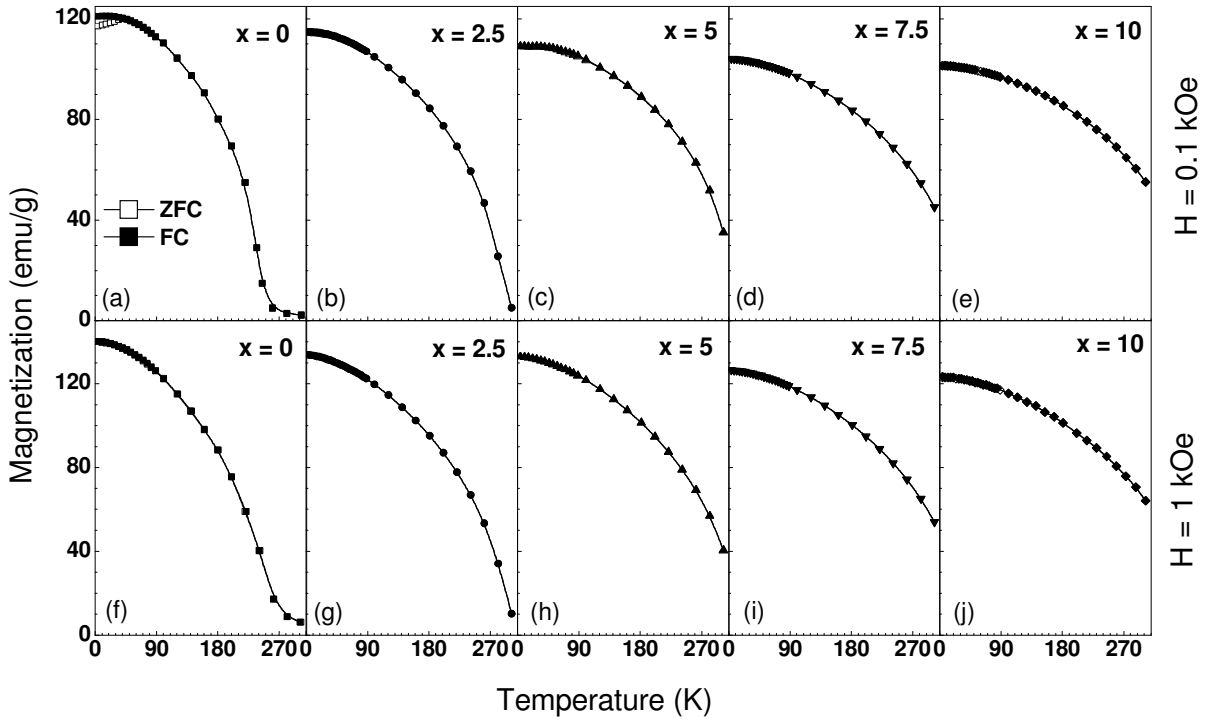


*FIG. 4.04: Temperature dependent ZFC and FC magnetization curves of $Fe_{89-x}Zr_{11}B_x$ amorphous alloy ribbons taken at two different applied magnetic fields between 5 K and 300 K.*

### 4.2.3. Magnetic properties

Temperature dependent magnetic properties of a-$Fe_{89-x}Zr_{11}B_x$ ($x$ = 0 – 10) alloys were measured using SQUID and VSM magnetometers. In the temperature dependent magnetization ($M$ – $T$) measurements, the sample was initially cooled to 4.2 K under zero-field condition. Magnetization was then recorded as the sample was heated to room temperature under a constant applied field [Zero-field cooled (ZFC process)]. Subsequently, the sample was cooled in the same constant applied field to 4.2 K and then the magnetization was recorded as the sample was heated to room temperature [Field-cooled (FC) process]. Fig.4.04 shows the temperature

dependent ZFC and FC magnetization curves obtained at two different applied fields ($H$ = 0.1 kOe and 1 kOe) for a-Fe-Zr-B alloys with different B content. The $M - T$ curves for the sample with $x$ = 0 show a sudden increase in magnetization around 270 K, corresponding to its $T_C$. On cooling the $Fe_{89}Zr_{11}$ sample below 50 K, the observed bifurcation between ZFC and FC curves [Fig.4.04(a)] signals a spin-glass like transition [FISC1991, HEGM1994, HIRO1982,

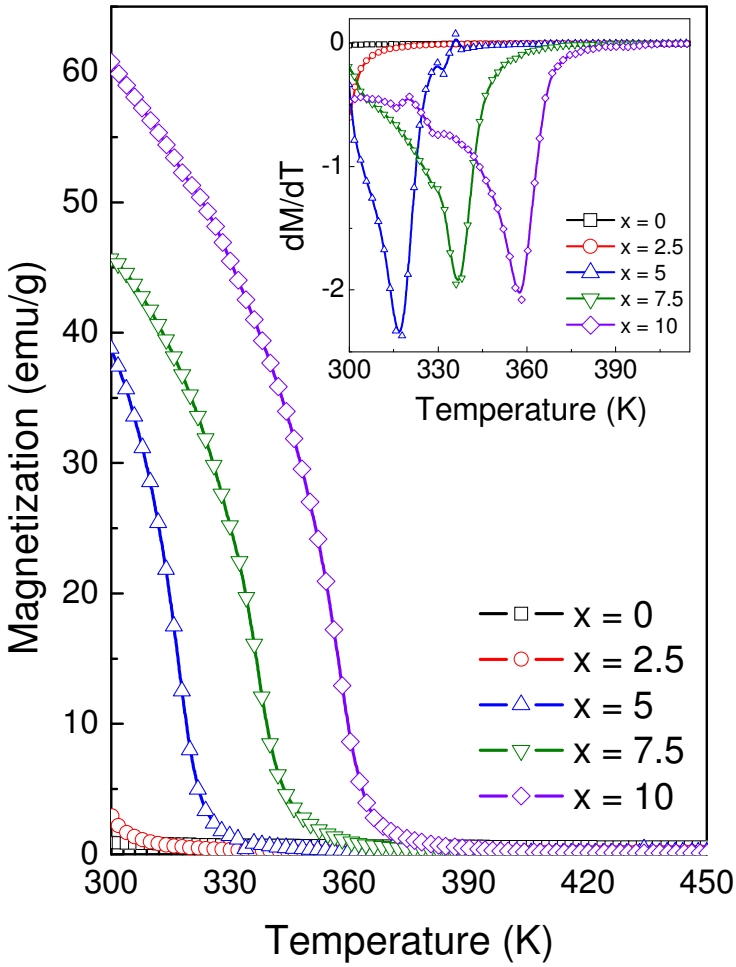


*FIG. 4.05: Temperature dependent magnetization curves and thermal derivative of magnetization curves (Inset) of amorphous $Fe_{89-x}Zr_{11}B_x$ alloy ribbons taken at 100 Oe applied magnetic field between 300 K and 450 K.*

MAHH1991, PAUL1997]. The bifurcation point disappears not only with increasing magnitude of the applied field, but also with increasing B content in this series of a-Fe-Zr alloys. This suggests that with the addition of B, magnetic frustration in the amorphous matrix largely diminishes. Both $T_C$ and room temperature magnetization of these alloys increase with increasing

B content. These results are in good agreement with the previously reported values for a similar alloy system [BARA1997]. It is to be noted that for the samples with $x \geq 2.5$, the no bifurcation between ZFC and FC is observed in the present investigations. However, the existence of bifurcation was observed even for the a-$Fe_{88}Zr_8B_4$ sample [BARA1997] at very low applied field. This could be understood from the fact that the addition of Zr in Fe rich a-Fe-Zr system enhances the ferromagnetic (FM) nature and hence the observed difference may be attributed to the low Zr content in the previously reported alloys. In order to determine the values of $T_C$, $M-T$ curves were obtained between 300 and 450 K for a-$Fe_{89-x}Zr_{11}B_x$ alloys at 100 Oe field using the VSM and the data obtained are depicted in Fig.4.05. The inset of Fig.4.05 displays the thermal derivative of magnetization as a function of temperature. The obtained values of $T_C$ of the amorphous phase for different B substituted alloys are shown in Fig.4.06(a). Also, the variations of $T_C$ of other similar alloys [BARA1994, YAOB2003] are shown for the sake of comparison. The values of $T_C$ in the currently investigated alloys are found to be significantly larger compared to other a-Fe-Zr-B alloys. The rate of increase of $T_C$ with B content can be expressed by a linear expression,

$$T_C(K) = 266.28 + 10.23\, x_B \qquad (4.1)$$

On the other hand, the variation of $T_C$ with B content in a-Fe-Zr-B alloys with lower Zr content [BARA1994] show a rapid increment initially for B content up to 2 at.% and the rate of increment of $T_C$ decreases with further increase in B content [YAOB2003]. Room temperature $M_S$ and $H_C$ of the samples obtained using VSM and coercimeter, respectively, are depicted in Figs.4.06(b) and (c). The values of $M_S$ increase almost linearly at a rate of about 9 emu/g per at.% B and do not show saturation tendency as observed in low Zr content samples [YAOB2003]. Also, it is observed that the rate of increase in $T_C$ increases from 10.2 K per at.% B for the samples with 11 at.% Zr to 18 K per at.% B for the sample with 7 at.% Zr content, while the rate of increase in $M_S$ decreases from 9 emu/g per at.% B for the samples with 11 at.% Zr to 5.5 emu/g per at.% B for the sample with 7 at.% Zr content [SLAW1996]. This suggests that the variations of $T_C$ and $M_S$ in Fe rich a-Fe-Zr-B alloys mainly depend on the relative effects of both the Zr and B contents on the stabilization of the local magnetic structure. On the other hand, $H_C$ decreases abruptly from 13 Oe to 0.015 Oe with the addition of 5 at.% B and increases to 0.063 Oe for the alloy composition with $x$ = 10. This could be ascribed to the variations of magnetostriction [SLAW1996] and local magnetic inhomogeneities (frequently referred as

clusters [KAUL1985, KAUL1992]) of the amorphous alloys [KRON2003] with B addition. Slawska-Waniewska et al [SLAW1996] reported that the magnetostriction of a-Fe-Zr-B alloys decreases largely with the addition of B content up to 5 at.% B and then increases slightly with

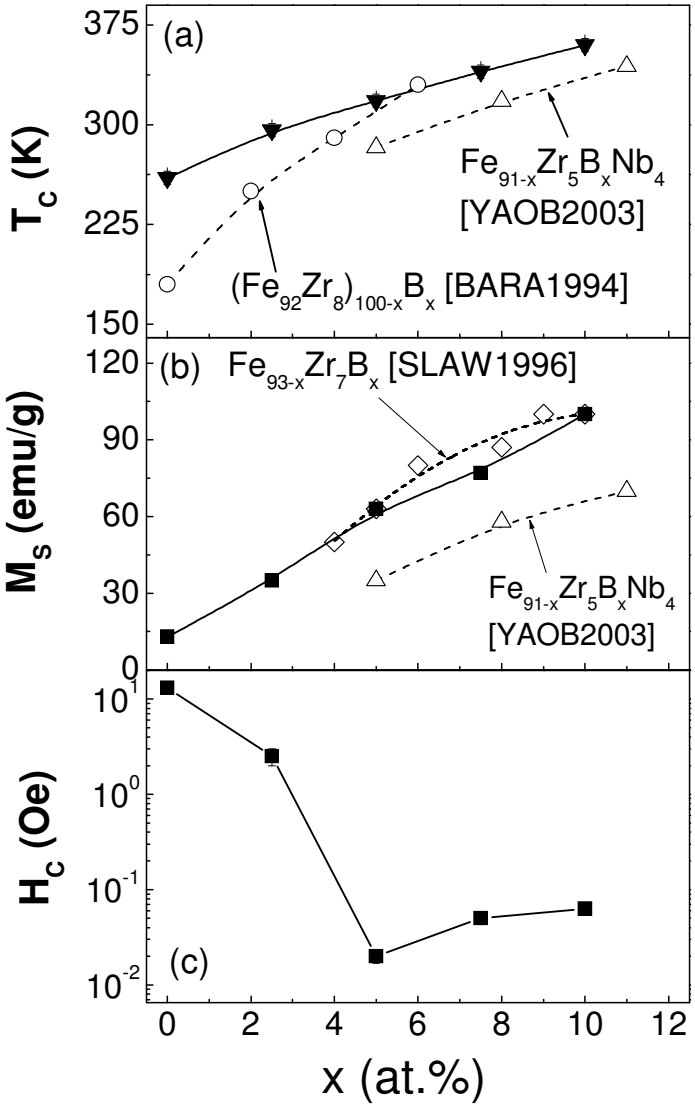


*FIG. 4.06: Variations of Curie temperature, saturation magnetization and coercivity with B substitution in amorphous $Fe_{89-x}Zr_{11}B_x$ alloy ribbons.*

the further increase in B. According to the micromagnetic theory [KRON2003], $H_C$ is directly proportional to the product of the magnetostriction and square root of the domain wall width. In addition, the magnetic inhomogeneities in the amorphous alloys can result in sensible intrinsic pinning of domain walls. Thus, the reductions of magnetostriction and magnetic inhomogenities

with B addition are believed to be responsible for the excellent soft magnetic softness in a-Fe-Zr-B alloys.

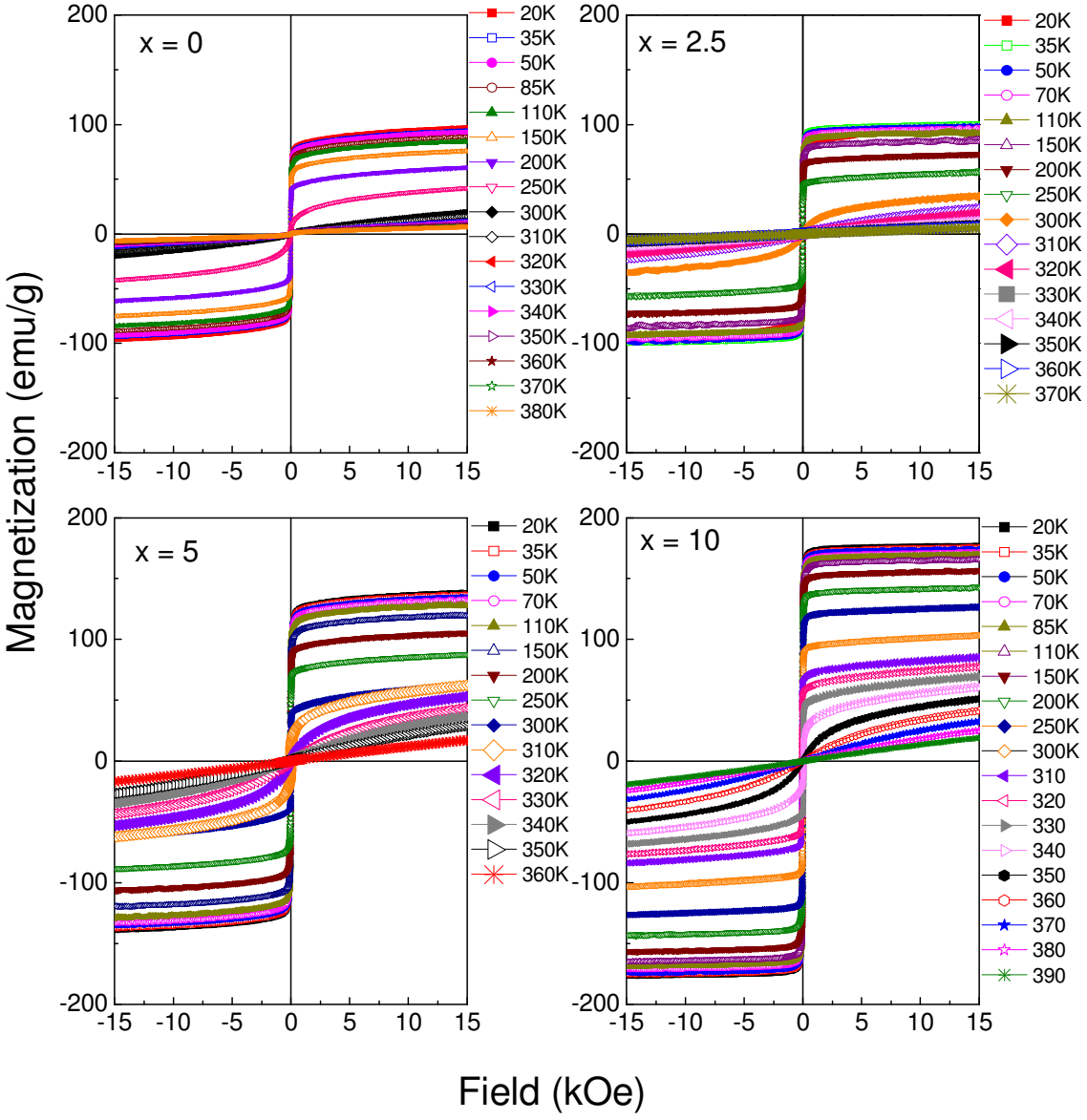


*FIG. 4.07: M – H loops of a-$Fe_{89-x}Zr_{11}B_x$ (x = 0, 2.5, 5, and 10) alloy ribbons recorded at different temperatures.*

It is to be noted that the sample with $x = 0$ shows a $H_C$ value of about 13 Oe at room temperature despite having $T_C$ just below room temperature. To understand this unusual behavior and to study the effect of local magnetic inhomogeneities in a-Fe-Zr-B alloys, temperature dependent $H_C$ and $M_S$ measurements were carried out from 20 K to temperatures above $T_C$. Fig.4.07 shows the $M – H$ loops of a-$Fe_{89-x}Zr_{11}B_x$ ($x$ = 0, 2.5, 5, and 10) alloys recorded at

different temperatures. The $M - H$ curves of a-$Fe_{89}Zr_{11}$ sample obtained above 300 K show an almost linear variation of magnetization with applied field, except close to the origin. The linear behavior supports the predominant paramagnetic state. For temperatures below 300 K, the $M - H$ curves show a non-linear variation of magnetization, which is typical of the FM nature of the samples. On the other hand, the room temperature $M - H$ curves of B substituted a-Fe-Zr-B samples show non-linear variation of magnetization indicating the FM nature of the samples at room temperature. The extracted values of $M_S$ as a function of temperature is shown in Fig.4.08(a). The value of $M_S$ for a-$Fe_{89}Zr_{11}$ sample increases with decreasing temperature and attains saturation below 50 K. On the other hand, the $M_S$ values not only increase with decreasing temperature for a particular sample, but also increase with increasing B content in a-Fe-Zr-B alloys. A maximum $M_S$ value of about 175 emu/g was observed at 20 K for the sample with $x$ = 10. In order to compare the variation of $H_C$ of all the a-Fe-Zr-B samples at different temperatures, the normalized coercivity [$H_C(T)$ / $H_C$(20 K)] as a function of temperature is plotted in Fig.4.08(b). The normalized values of $H_C$ for $Fe_{89}Zr_{11}$ sample decreases initially with increasing temperature up to 200 K as expected for typical FM materials and then shows a rapid increase around 300 K, followed by a large decrease above 320 K. The rapid increase of $H_C$ around $T_C$ of the amorphous phase ($T_{C,A}$) diminishes with increasing B content. For the samples with $x > 2.5$ at.%, $H_C$ just above $T_C$ approaches zero value without any rise around $T_C$. The magnetic hardening close to the $T_{C,A}$ has been observed in a variety of nanocrystalline systems [HERN1994, HERN1998, LIUJ2009, LIUY2006, SUZU1998] with two-phase structure and attributed to the loss of FM exchange coupling between the nanocrystallites through the PM amorphous matrix. However, the structural property results of the presently investigated samples (sec. 4.2.1) using XRD and TEM techniques show amorphous structure without the evidence of any crystallites and/or local lattice fringes. This suggests that the observed magnetic hardening behavior can be attributed to the presence of local magnetic inhomogeneities and/or finite clusters [KAUL1985] in the spin system, which are no longer averaged out. So, the $H_C$ begins to increase (owing to the strong ramification of clusters just above $T_C$) as the temperature is increased above $T_C$. On further increasing the temperature, the magnetic clusters shrink in size and hence a total magnetic disorder in the spin system (PM state) is approached. With increasing B substitution in a-Fe-Zr-B alloys, the local magnetic inhomogeneities decrease and the rise in $H_C$ value around $T_C$ therefore diminishes before approaching zero.

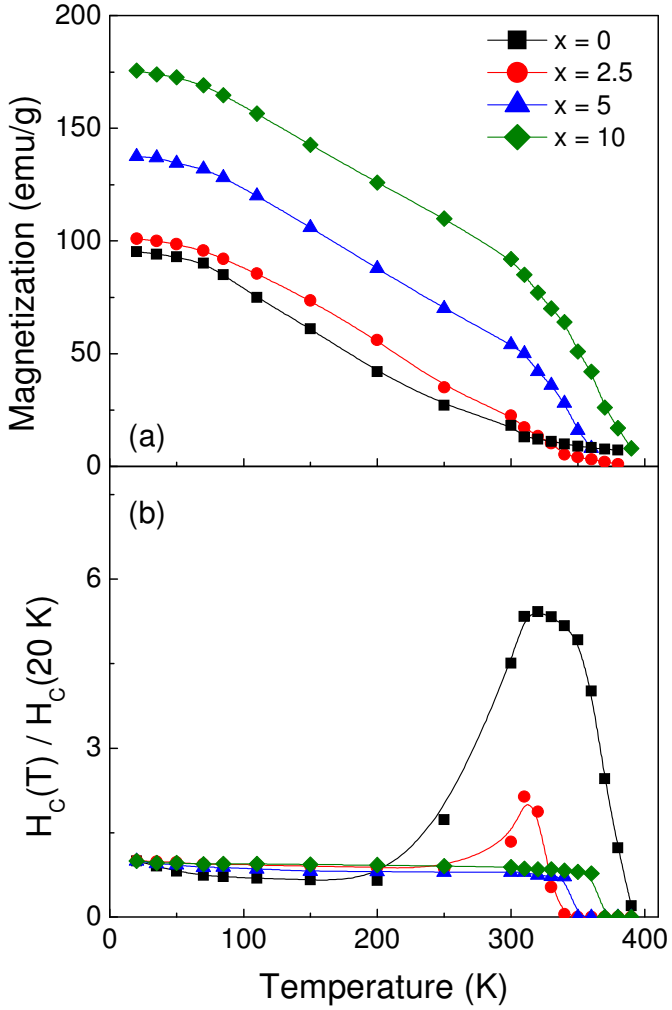


*FIG. 4.08: Variations of saturation magnetization and normalized coercivity with temperature for a-$Fe_{89-x}Zr_{11}B_x$ (x = 0, 2.5, 5, and 10) alloy ribbons.*

The composition dependence of $T_C$ has often been discussed based on the average molecular field model and the following expression has been deduced [OHAN1987],

$$T_C(K) = \frac{[J(r)Z\boldsymbol{S}(\boldsymbol{S}+1)]}{3k_B} \qquad (4.2)$$

where $J(r)$ is the distance dependent inter-atomic exchange integral, $Z$ is the coordination, $\boldsymbol{S}$ is the atomic spin quantum number and $k_B$ is Boltzmann constant. However, this model has mainly focused on materials with either pure FM or pure antiferromagnetic (AFM) state, which is not the case in the presently investigated samples. Amorphous $Fe_{89-x}Zr_{11}B_x$ samples show a linear variation of $T_C$, which is similar to that of a-Fe-Zr based alloys [BARA1994]. The double transition behavior observed in $Fe_{89}Zr_{11}$ has been supported with the concept of noncollinear spin

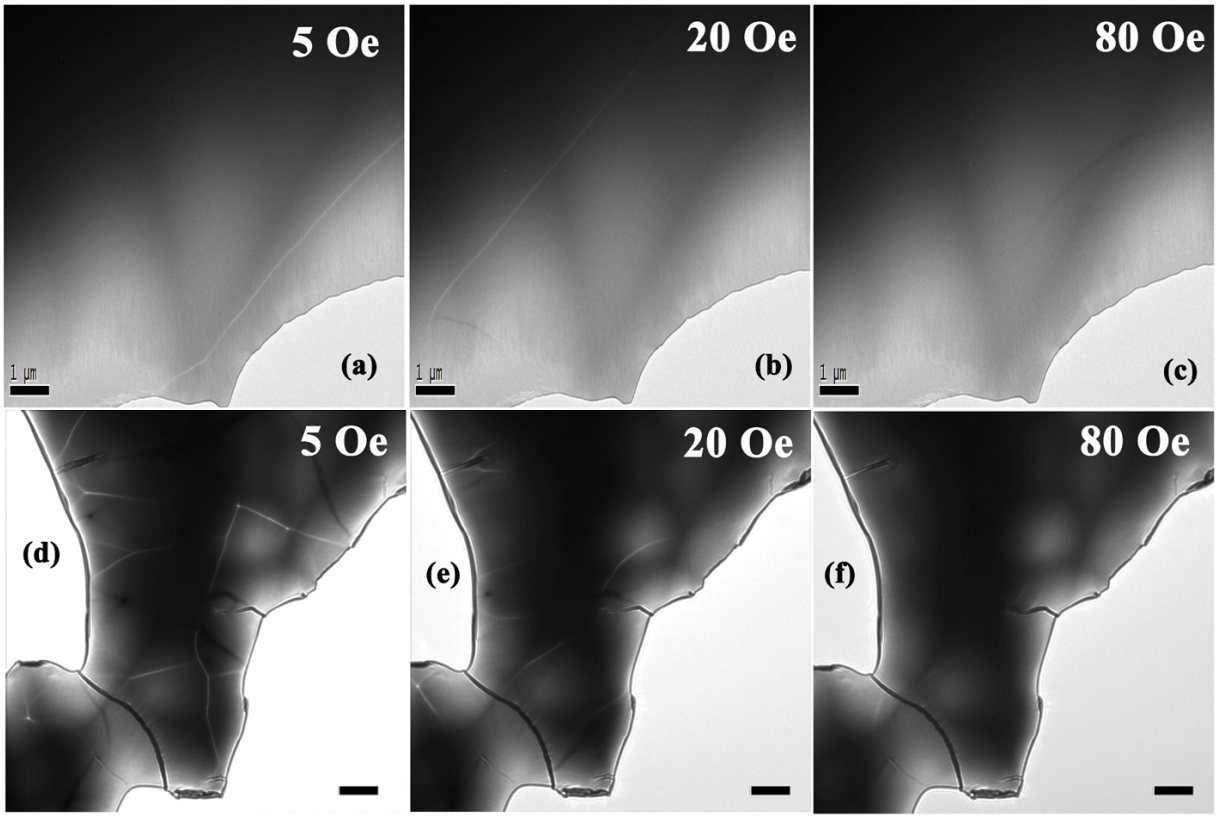


*FIG. 4.09: Magnetic domain structures of amorphous $Fe_{89-x}Zr_{11}B_x$ alloys with x = 5 (a-c) and x = 10 (d-f) observed at different fields. The horizontal bars correspond to a scale of 1 μm.*

structure [KANE1992] resulting from the co-existence of FM and spin-cluster of AFM couplings [HIRO1982, READ1989, RHYN1985, SATI1986]. This is mainly due to the sensitivity of the Fe–Fe exchange interaction to atomic distance, which in turn causes fluctuations in the magnitude and even a change in the sign of the magnetic exchange integral (see sec. 2.3.2) [BARA1996]. According to the model proposed by Ryan et al [RYAN1987, RYAN2003], the compositional dependence of $T_C$ in a-Fe-Zr-B alloys can be attributed to the variation in local spin structure and its correlation length resulting from the concentration effect on the number of AFM couplings existing in the a-Fe-Zr parent alloy. With increasing B content in Fe-Zr-B alloys, the degree of competition between FM and AFM interactions decreases, which destroys the spin-glass like behavior observed at low temperature and stabilizes the FM nature with its spin structure approaching parallel alignments. However, the degree of competition in Fe-Zr-B alloys strongly depends on both Zr and B concentrations.

### 4.2.4. Magnetic domain structure

Since the a-$Fe_{89-x}Zr_{11}B_x$ samples show enhanced FM properties at room temperature with B substitution, it is meaningful to understand their relationship with the magnetic domain structures. Fig.4.09 shows Lorentz microscopy images obtained at different fields for both $x$ = 5 and 10 samples. Large-sized domains with smooth and straight domain walls are observed in samples with both $x$ = 5 and 10. The average domain size in the sample with $x$ = 10 is found to be smaller than that of the sample with $x$ = 5. This suggests that the effective local anisotropy of the samples, resulting from magnetoelastic coupling energy and short-range stresses due to quasidislocation dipoles, and the magnetostriction [SLAW1996] increases slightly for B content above 5 at.% [LIUY2006]. The dynamics of magnetic domain observed with applied field are shown in Fig.4.09. With increasing applied magnetic field, a rapid movement of domain walls [Fig.4.09(a)-(f)] was observed in the case of both $x$ = 5 and 10 samples. This indicates the enhanced FM properties with strong exchange coupling and good magnetic softness in a-Fe-Zr-B alloys.

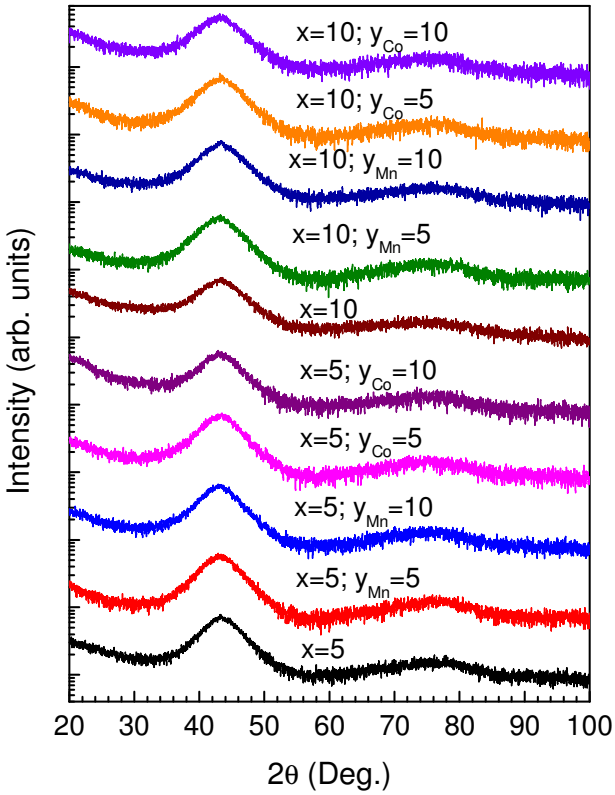


*FIG. 4.10: XRD patterns of amorphous $Fe_{89-x-y}(Co,Mn)_yZr_{11}B_x$ alloy ribbons.*

## 4.3. Properties of amorphous Fe-(Co,Mn)-Zr-B ribbons

### 4.3.1. Structural properties

Fig.4.10 shows the XRD patterns of the as-made $Fe_{89-x-y}(Co,Mn)_yZr_{11}B_x$ ($x$, $y$ = 5, 10) alloy ribbons. All the samples exhibit broad humps near $2\theta$ = 43° and 78° and no sharp diffraction peak corresponding to any crystalline phase is seen. These results indicate that an amorphous single phase is formed in both Mn and Co substituted Fe-Zr-B samples. To investigate the local microstructure of the sample, TEM was used. Figs.4.11(a) and (b) show the bright-field TEM micrographs and SAED patterns for as-made $Fe_{69}Zr_{11}B_{10}Co_{10}$ and $Fe_{69}Zr_{11}B_{10}Mn_{10}$ alloy ribbons, respectively. The micrographs and SAED patterns reveal the characteristic amorphous structure, which is in good agreement with the XRD results.

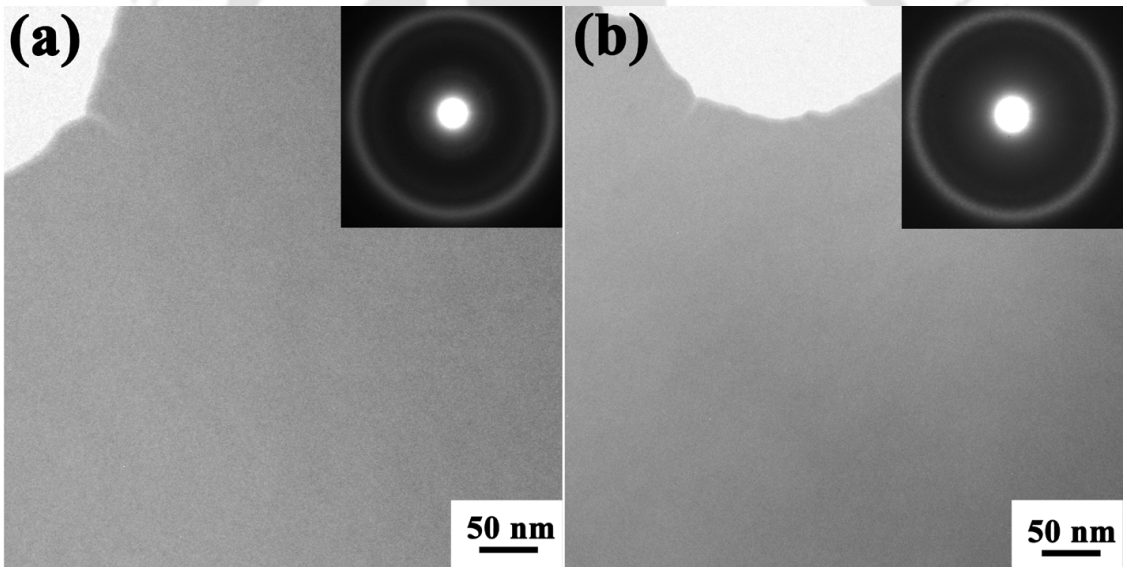


*FIG. 4.11: Bright-field TEM micrographs and SAED patterns of amorphous $Fe_{69}Zr_{11}B_{10}Co_{10}$ and $Fe_{69}Zr_{11}B_{10}Mn_{10}$ alloy ribbons.*

### 4.3.2. Thermal properties

In order to investigate the thermal stability of the Fe-(Co,Mn)-Zr-B alloys with the addition of Co and Mn, DSC curves of all the samples were obtained. All the DSC curves were characterized by an exothermic peak corresponding to the primary crystallization of the amorphous samples. The variations of the peak $T_{crys}$ with Co and Mn addition are shown in Fig.4.12. It can be seen from the figure that with increasing Co content $T_{crys}$ decreases at the rate

of about 1.7 and 1.05 K per at.% Co for the samples with $x$ = 5 and 10, respectively. Mn addition shifts the $T_{crys}$ to higher values at the rate of 1.8 and 1.45 K per at.% Mn. These results confirm that Mn substitution in Fe-Zr-B alloys produces a slowing down of the crystallization kinetics.

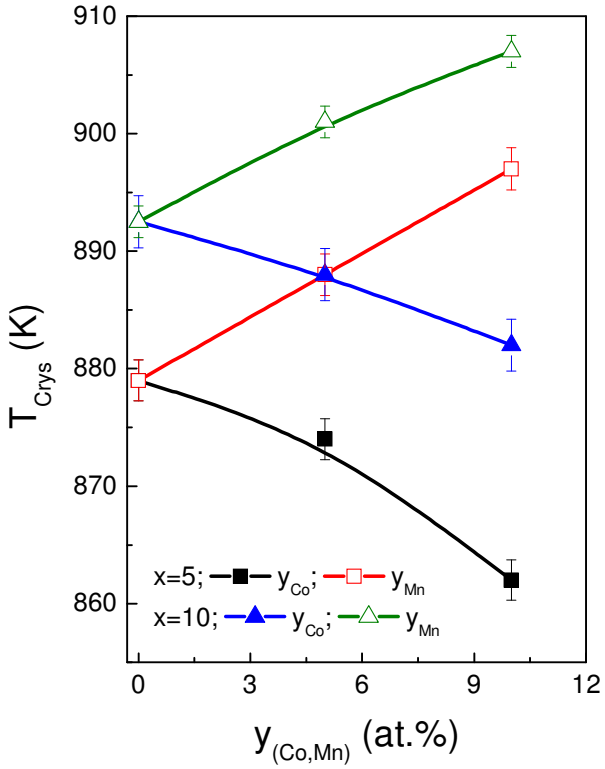


*FIG. 4.12: Variation of peak crystallization temperature with the addition of Co or Mn in amorphous* $Fe_{89-x-y}(Co,Mn)_yZr_{11}B_x$ *alloy ribbons.*

The observed results are in good agreement with the results reported earlier on similar systems [BAYR2009, BENA2008, HESH1999]. Blazquez *et al* [BLAZ2005] reported the $T_{crys}$ value of 773 K for a-$Fe_{78}Co_5Zr_6B_{10}Cu_1$ alloy which is less than the value (874 K) obtained for $Fe_{74}Co_5Zr_{11}B_{10}$ alloy in the present investigations. This suggests that higher amount of Zr (>8 at.%) enhances the stability of the amorphous phase quite considerably. On the other hand, HITPERM alloy ($Fe_{44}Co_{44}Zr_7B_4Cu_1$) having higher Co content showed a low value of $T_{crys}$ (~740 K) suggesting loss of thermal stability with higher Co content [MAJU2007].

### 4.3.3. Magnetic properties

Temperature dependent ZFC and FC magnetization curves were obtained for a-$Fe_{89-x-y}(Co,Mn)_yZr_{11}B_x$ alloys at two different applied fields ($H$ = 0.1 kOe and 1.0 kOe) and the same

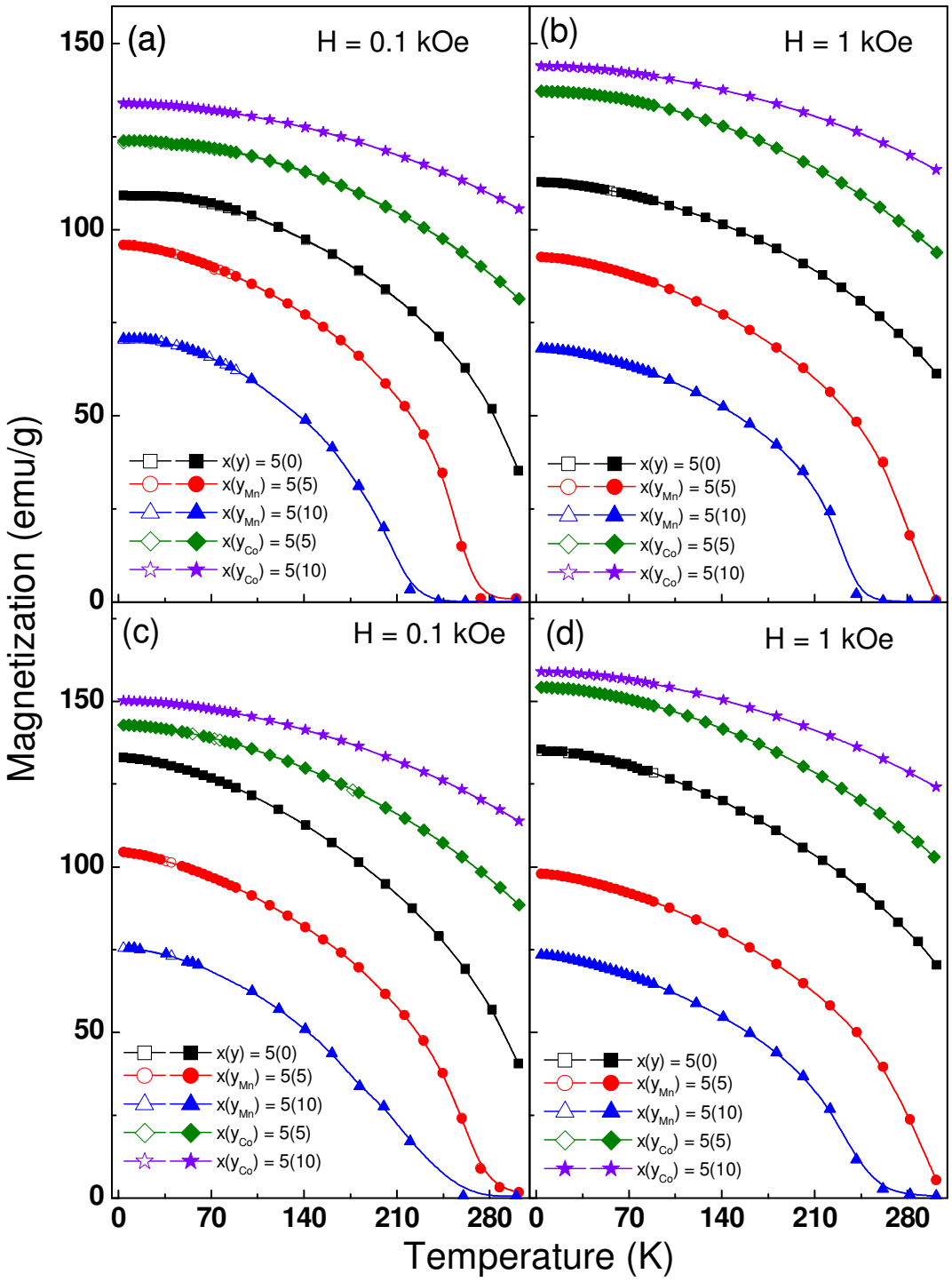


*FIG. 4.13: Temperature dependent ZFC and FC curves obtained at different applied fields for amorphous $Fe_{89-x-y}(Co,Mn)_yZr_{11}B_x$ alloy ribbons.*

are depicted in Fig.4.13. The *M* – *T* curves show the following features: (i) Upon cooling the a-$Fe_{89-x-y}Zr_{11}B_xMn_y$ samples from room temperature, a sudden increase in magnetization

corresponding to a transition from PM to FM phase was observed at $T_C$, (ii) $T_C$ determined from the thermal derivative of the magnetization curves shifts to lower temperatures with increasing Mn concentration, (iii) on cooling the samples further, both ZFC and FC curves show a gradual increase and tend to saturate below 20 K, (iv) bifurcation between the ZFC and FC curves was not observed down to 5 K, (v) when the magnitude of the applied field is increased, the sharpness of the transition around $T_C$ gets broadened, (vi) a-$Fe_{89-x}Zr_{11}B_x$ and a-$Fe_{89-x-y}Zr_{11}B_xCo_y$ samples show continuous increase in magnetization under both ZFC and FC conditions with decreasing temperature, and (vii) increase of B and Co contents in a-$Fe_{89-x-y}Zr_{11}B_xCo_y$ shifts the $T_C$ to temperatures above the ambient as well as increases the room temperature magnetization.

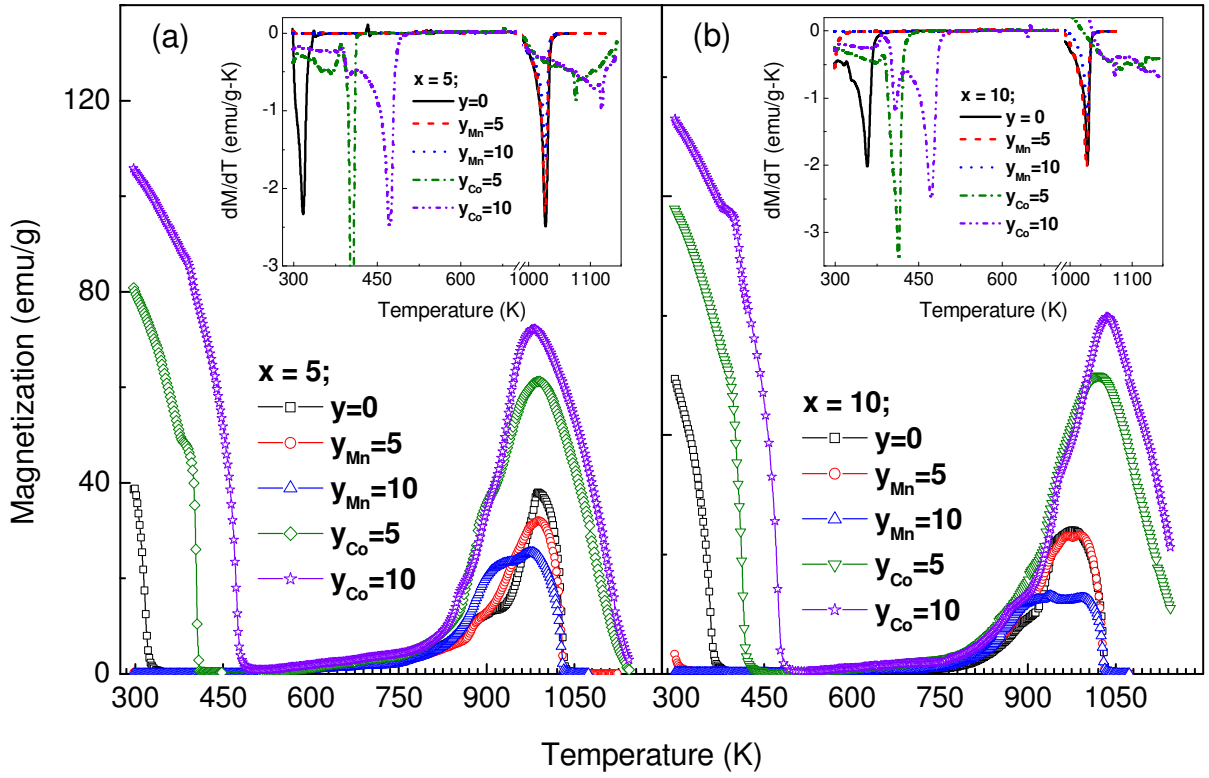


*FIG. 4.14: Temperature dependent magnetization curves obtained at 100 Oe applied field for amorphous $Fe_{89-x-y}(Co,Mn)_yZr_{11}B_x$ alloy ribbons. Inset shows the thermal derivative of magnetization as a function of temperature.*

In order to accurately determine the $T_C$ of a-$Fe_{89-x-y}Zr_{11}B_xCo_y$ samples with B and Co contents and to understand the magnetic properties of a-$Fe_{89-x-y}Zr_{11}B_x(Co,Mn)_y$ at high temperature, $M - T$ measurements were performed at an applied field of 100 Oe between 300 K and 1200 K. Fig.4.14 shows the high temperature $M - T$ curves obtained for a-$Fe_{89-x-}$

$_yZr_{11}B_x(Co,Mn)_y$ alloys. The inset of Fig.4.14 displays the thermal derivative of the magnetization data as a function of temperature. All the a-$Fe_{89-x-y}Zr_{11}B_xMn_y$ samples show nearly zero magnetization close to room temperature due to the paramagnetic nature of the sample. With increasing temperature, a flat region with almost zero magnetization is observed up to 650 K followed by a linear increase in magnetization up to 800 K. The marked increase in magnetization at about 850 K corresponds to the onset of amorphous-to-crystalline transition with the precipitation of $\alpha$-Fe phase. On heating the sample beyond 970 K, the magnetization decreases to zero at about 1030 K. This drop in magnetization is associated with the $T_C$ of $\alpha$-Fe. On the other hand, B and Co additions shift the $T_C$ of the amorphous phase to higher temperatures. $T_C$ of the a-$Fe_{89-x}Zr_{11}B_x$ alloys increases from 314 K to 356 K when B is increased from 5 to 10 at.%, while Co addition in a-$Fe_{89-x-y}Zr_{11}B_xCo_y$ alloys increases the $T_C$ from 314 K (356 K) to 473 K (476 K) in $x$ = 5 (10) samples. This indicates that these two additive elements are effective in enhancing the exchange stiffness of the a-$Fe_{89-x-y}Zr_{11}B_xCo_y$ alloys. With increasing temperature, the magnetization curve follows a similar trend as described earlier for the Mn case. However, the observed marked increase in magnetization around 850 K shifts to higher temperatures in the samples with Co [Fig. 4.14(b)]. This suggests that the precipitation phase in the amorphous-to-crystalline transition is not $\alpha$-Fe, but $\alpha$-FeCo. Accordingly, the $T_C$ of the $\alpha$-FeCo phase increases from 1026 K to 1140 K with increasing Co content.

To understand the development of room temperature magnetic properties and to analyze the variations of $M_S$ and $H_C$ with the substituting elements, the $M$ – $H$ loops were measured at room temperature and shown in Fig.4.15 for a-$Fe_{89-x-y}(Co,Mn)_yZr_{11}B_x$ alloys. The observed $M$ – $H$ loops are typical of soft magnetic material. With increasing Mn content in a-$Fe_{84-y}Zr_{11}B_5Mn_y$, the value of $M_S$ measured at 20 kOe decreases quickly and $M$ – $H$ loops follow almost a linear variation with the applied field, which suggests that the sample is in a paramagnetic state. On the other hand, the addition of Co in a-$Fe_{89-x-y}Zr_{11}B_xCo_y$ results in a large increase in $M_S$, which attains a maximum value of about 130 emu/g for the sample with $y$ = 10 [Fig.4.16(a)]. $H_C$ of the samples was measured using a coercimeter, as described in experimental section and depicted in Fig.4.16(b) for a-$Fe_{84-y}Zr_{11}B_5Co_y$ alloy. $H_C$ increases at a rate of 0.0284 Oe per at.% Co in $Fe_{84-y}Zr_{11}B_5Co_y$ alloys, while the rate decreases abruptly to 0.0035 Oe per at.% Co in $Fe_{79-y}Zr_{11}B_{10}Co_y$ alloys. The increase in the values of $H_C$ with Co addition in a-$Fe_{84-y}Zr_{11}B_5Co_y$ is most likely due to the induced anisotropy effect [SUNY2009]. This is the first time experimental

results where such ultra-low $H_C$ values are reported in a-$Fe_{89-x-y}Zr_{11}B_xCo_y$ ribbons in as-made condition without any post-preparation heat-treatment [HUAN2008, MAJU2007]. The reported value of $H_C$ of a-$Fe_{44}Co_{44}Zr_7B_5$ based alloys with high Co content [Fe:Co = 1:1] is around 0.9 Oe

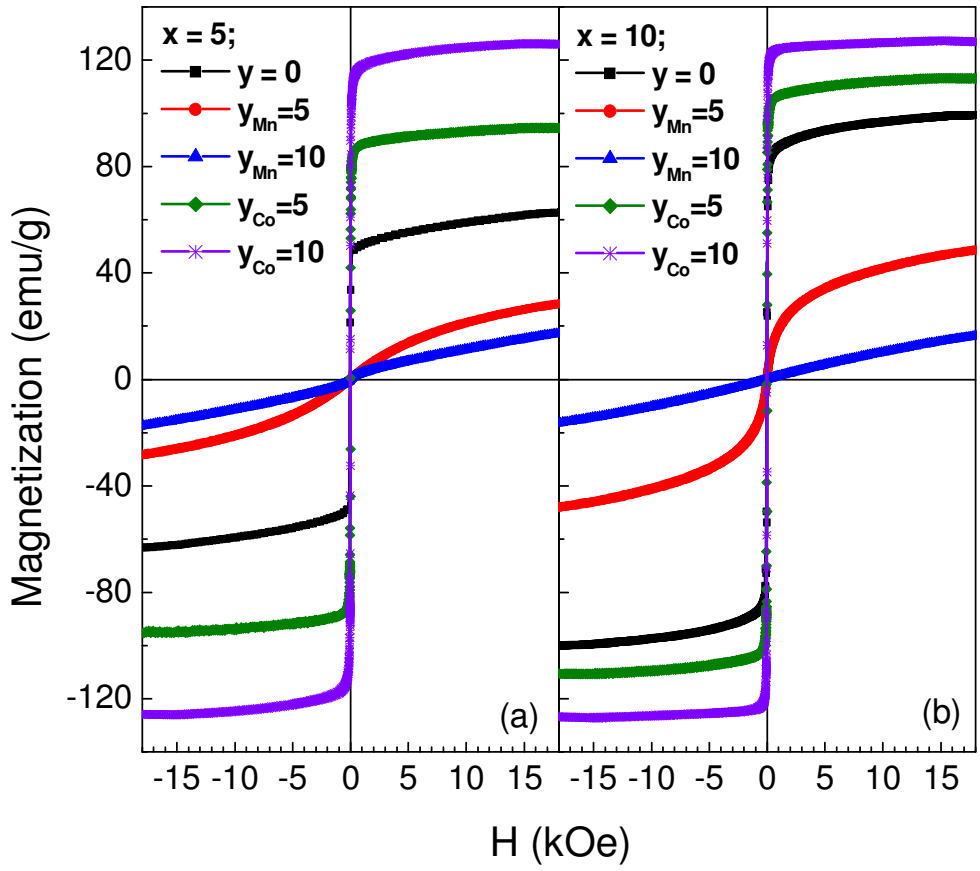


*FIG. 4.15: Room temperature M – H loops for amorphous $Fe_{89-x-y}(Co,Mn)_yZr_{11}B_x$ alloy ribbons.*

[YAOS2009], which is higher than the values of 0.13 (0.3) Oe observed for the presently investigated a-$Fe_{84-x}Zr_{11}B_5Co_x$ samples with $x$ = 5 (10). This suggests that the addition of a small amount of Co helps in retaining the ultra-soft magnetic properties with enhanced values of $M_S$. On the other hand, the room temperature $M_S$ [Fig.4.16(a)] and $T_C$ [Fig.4.16(c)] increase (decrease) almost linearly with Co (Mn) addition. In Fig.4.16, the variations of $H_C$, $M_S$, and $T_C$ as a function of Co or Mn content are illustrated. The variations of $T_C$ with the addition of Co or Mn can be expressed by the following linear functions:

$$\left.\begin{aligned} T_C(K) &= 317.67 - 11.84\, y_{Mn} \\ T_C(K) &= 320.17 + 15.91\, y_{Co} \end{aligned}\right\} \; for\; x_B = 5\; at.\% \qquad (4.3)$$

$$\left.\begin{aligned} T_C(K) &= 353.15 - 13.35\, Y_{Mn} \\ T_C(K) &= 354.66 + 12.02\ Y_{Co} \end{aligned}\right\} \ for\ x_B = 10\ at.\% \qquad (4.4)$$

The composition dependence of $T_C$ and magnetic properties can be explained using the model proposed by Ryan et al [RYAN1987, RYAN2003]. In this model, the concentration dependence of $T_C$ and magnetic properties of a-Fe-Zr based alloys are attributed to the variations in spin structure and the spin-correlation length. When Co is added to the parent a-Fe-Zr-B, the $T_C$ and

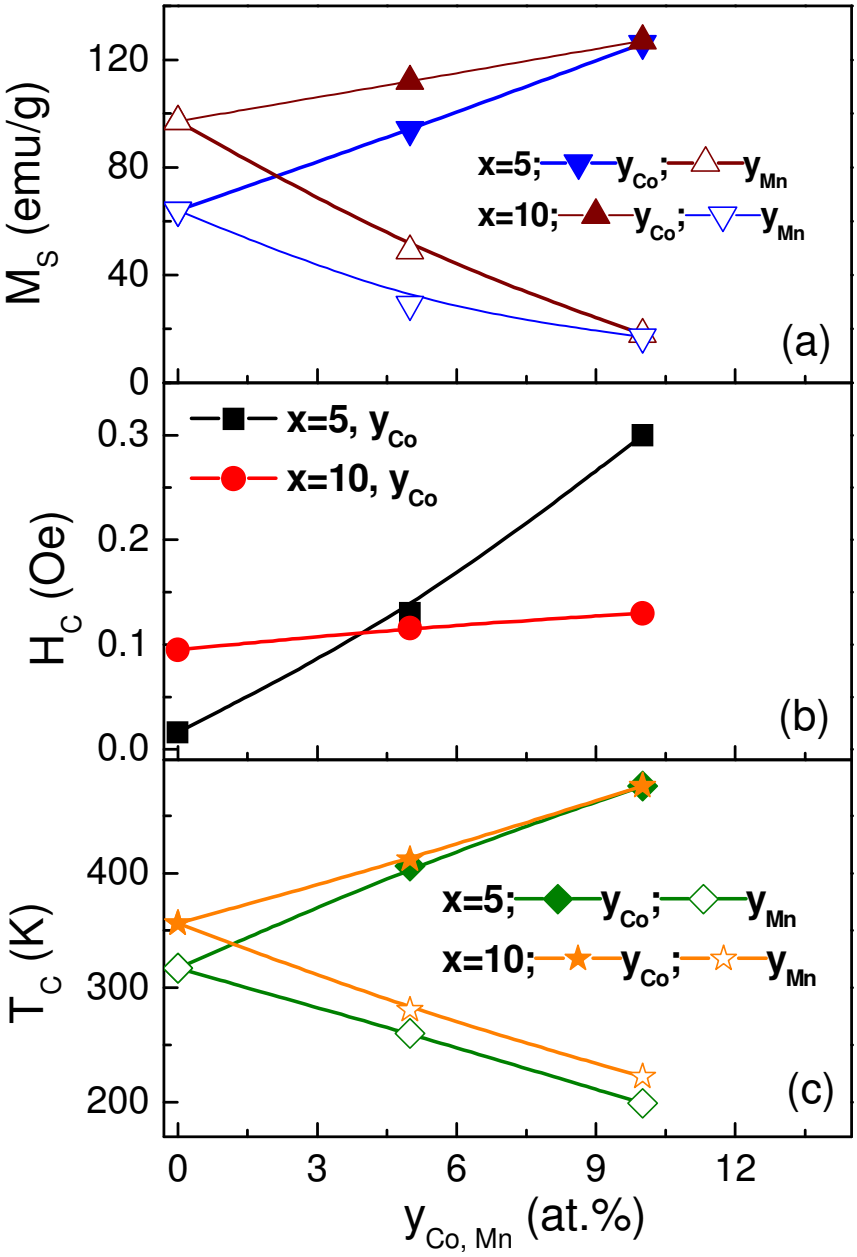


*FIG. 4.16: Variations of (a) coercivity, (b) saturation magnetization, and (c) Curie temperature with Co or Mn addition for amorphous $Fe_{89-x-y}(Co,Mn)_yZr_{11}B_x$ alloy ribbons.*

magnetization increase linearly within the whole concentration range measured. On the other hand, $T_C$ decreases monotonically with increasing Mn content. This behavior might be arising from the decrease (increase) in the degree of competition between FM and AFM interactions with increasing Co (Mn) content. The addition of Co stabilizes the FM nature of a-Fe-Zr-B samples with its spin structure approaching parallel alignments [BABU1997, SHEN1991], while the Mn atoms have less effect on the stabilization of the spin structure in the parent Fe-Zr-B alloy. Hence, the variation of $T_C$ is related to the spin-correlation length. Therefore, by assuming Fe-Mn interaction in a-Fe-Zr-B-Mn alloys [KIMK2007, MINS2005, ULYA2005] and Fe-Co exchange interaction in a-Fe-Zr-B-Co alloys [BLAZ2005, HESH1999, HASI2001], the monotonic variations of $T_C$ can be understood.

The soft magnetic properties are obtained when both the domain wall motion and domain rotation occur with a small change in the energy of the system. One factor that strongly affects the energy of the system is local magnetic anisotropy. Since the currently investigated samples show enhanced soft magnetic properties at room temperature, it is important to understand the variations of the average local magnetic anisotropy and high-field susceptibility components as a function of Mn or Co content. The high-field region of the $M - H$ curves in Fig.4.15 can be best described by an analytical expression [HERZ1980],

$$M(H) = M_0\left(1 - \varepsilon H^{-\phi}\right) + \chi_{HF} H \qquad (4.5)$$

where $M_0$, $\varepsilon$ (the local magnetic anisotropy), and $\phi$ (=0.5) are constants and $\chi_{HF}$ is the high-field susceptibility. In order to determine these constants with better accuracy, a nonlinear fitting procedure was carried out as follows: Initially, the first term in the eqn.(4.5) was set equal to zero and a detailed range-of-fit analysis was carried out on the magnetization data. $\chi_{HF}$ was treated as a free fitting parameter and its value was determined from the analysis. Using the coefficient of the second term as input, the range-of-fit analysis was then performed with both terms included. The values of both $\chi_{HF}$ and $\varepsilon$ constants calculated by the above procedure are depicted in Fig.4.17. It could be clearly seen that Co addition in a-Fe-Zr-B alloys results in a large decrease in both $\chi_{HF}$ and $\varepsilon$, while Mn addition drastically enhances both the $\chi_{HF}$ and $\varepsilon$ values. Large values of high-field susceptibility and local magnetic anisotropy are characteristic features of the Invar effect [HIRO1971], which is mainly caused by the flipping of weakly coupled AFM spins under high magnetic field. The large values of $\chi_{HF}$ for the a-Fe-Zr-B-Mn samples suggest an enhancement of noncollinear spin structure. This is diminished by Co and B additions in Fe-Zr-

B-Co samples resulting in lower $\chi_{HF}$ and $\varepsilon$ values and very good soft magnetic properties at room temperature in the as-made amorphous samples.

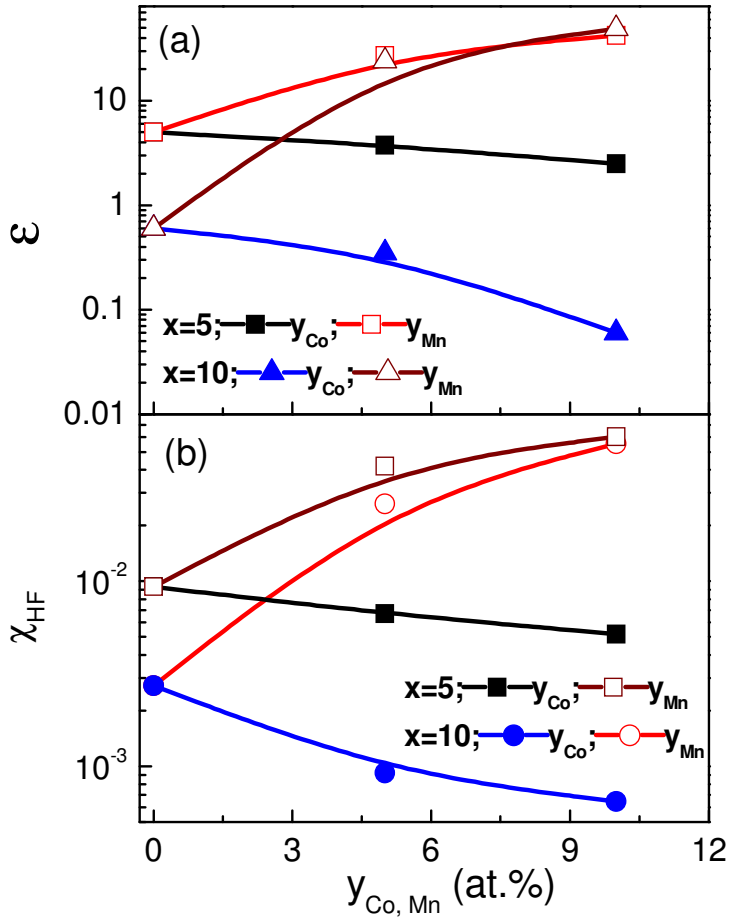


*FIG. 4.17: Variations of high-field susceptibility and local magnetic anisotropy constant with Co or Mn addition for amorphous $Fe_{89-x-y}(Co,Mn)_yZr_{11}B_x$ alloy ribbons.*

### 4.3.4. Magnetic domain structure

To understand the effect of Co substitution on the magnetic domain structure of the a-$Fe_{89-x-y}Co_yZr_{11}B_x$ samples, Lorentz microscopy images were obtained in Fresnel mode and the same are depicted in Fig.4.18. All the samples show large-size domains with smooth and straight domain walls. The large-sized domains indicate strong exchange coupling and good magnetic softness in the Co substituted a-Fe-Co-Zr-B alloys. The average domainsize decreases with increasing Co content. This is in good agreement with the magnetic property results shown in Fig.4.16.

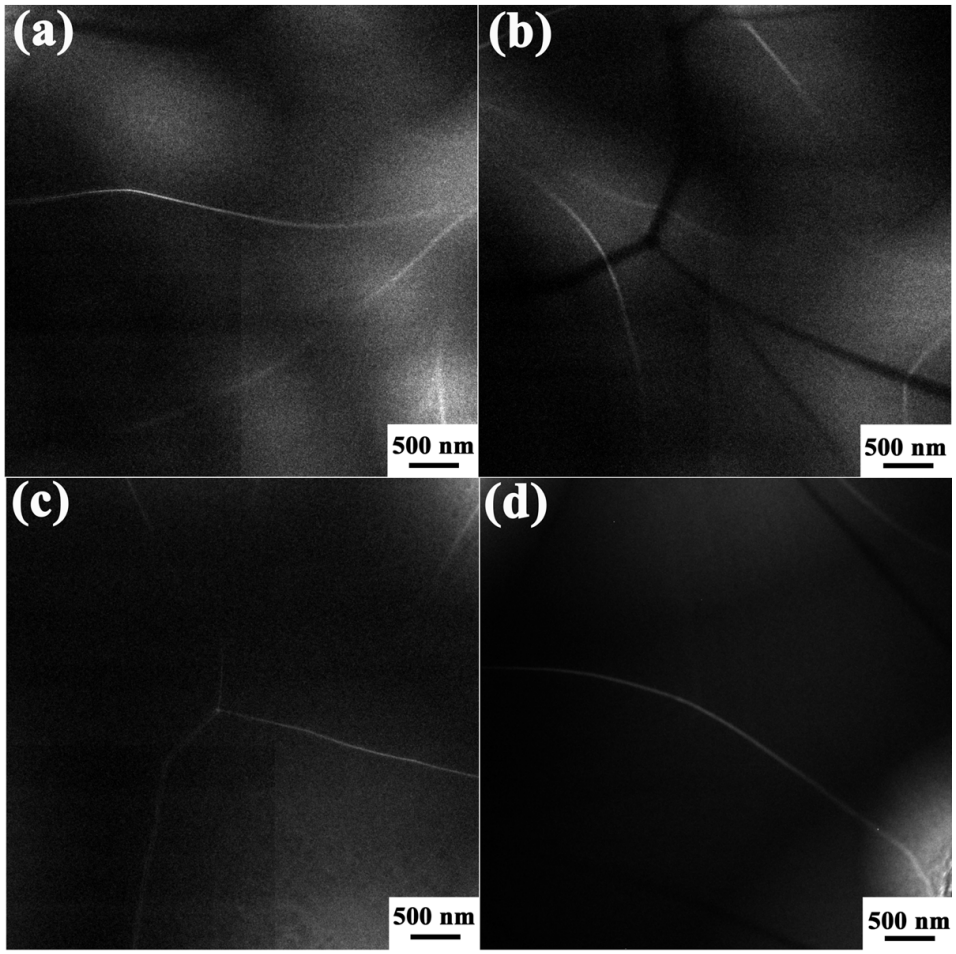


*FIG. 4.18: Magnetic domain structures of amorphous $Fe_{89-x-y}Co_yZr_{11}B_x$ alloy ribbons (a) x = 5, y = 5; (b) x = 5, y = 10, (c) x = 10, y = 5, and (d) x = 10, y = 10.*

### 4.4. Magnetocaloric effect of amorphous Fe-(Co,Mn)-Zr-B ribbons

The temperature change of a magnetic material, associated with an external magnetic field change in an adiabatic process is defined as magnetocaloric effect (MCE). The magnetic phase transition from FM to PM state in magnetic materials results in a change in the magnetic entropy value associated with magnetization and demagnetization of the material. This change is used in the MCE. The current prototype for magnetic refrigeration is based on rare-earth based materials [PHAN2007, PROV2004, ZIMM1998]. For high temperature magnetic refrigeration, materials other than these rare-earth materials are under intensive research. Particularly, soft magnetic amorphous alloys have received a lot of attention as refrigerant materials due to their low cost, low energy loss, higher electrical resistivity and tunable $T_C$ [FRAN1996, FRAN2006, JOHN2006, MINS2005]. Since B and Co additions in a-Fe-Zr alloys yielded enhanced soft

magnetic properties, the effect of substituting elements on the MCE in a-$Fe_{89-x-y}(Co,Mn)_yZr_{11}B_x$ ($x$ = 0, 5, 10; $y$ = 5, 10) alloys has been investigated.

Results discussed in the previous sections suggest that the $T_C$ of a-Fe-(Co,Mn)-Zr-B alloys can

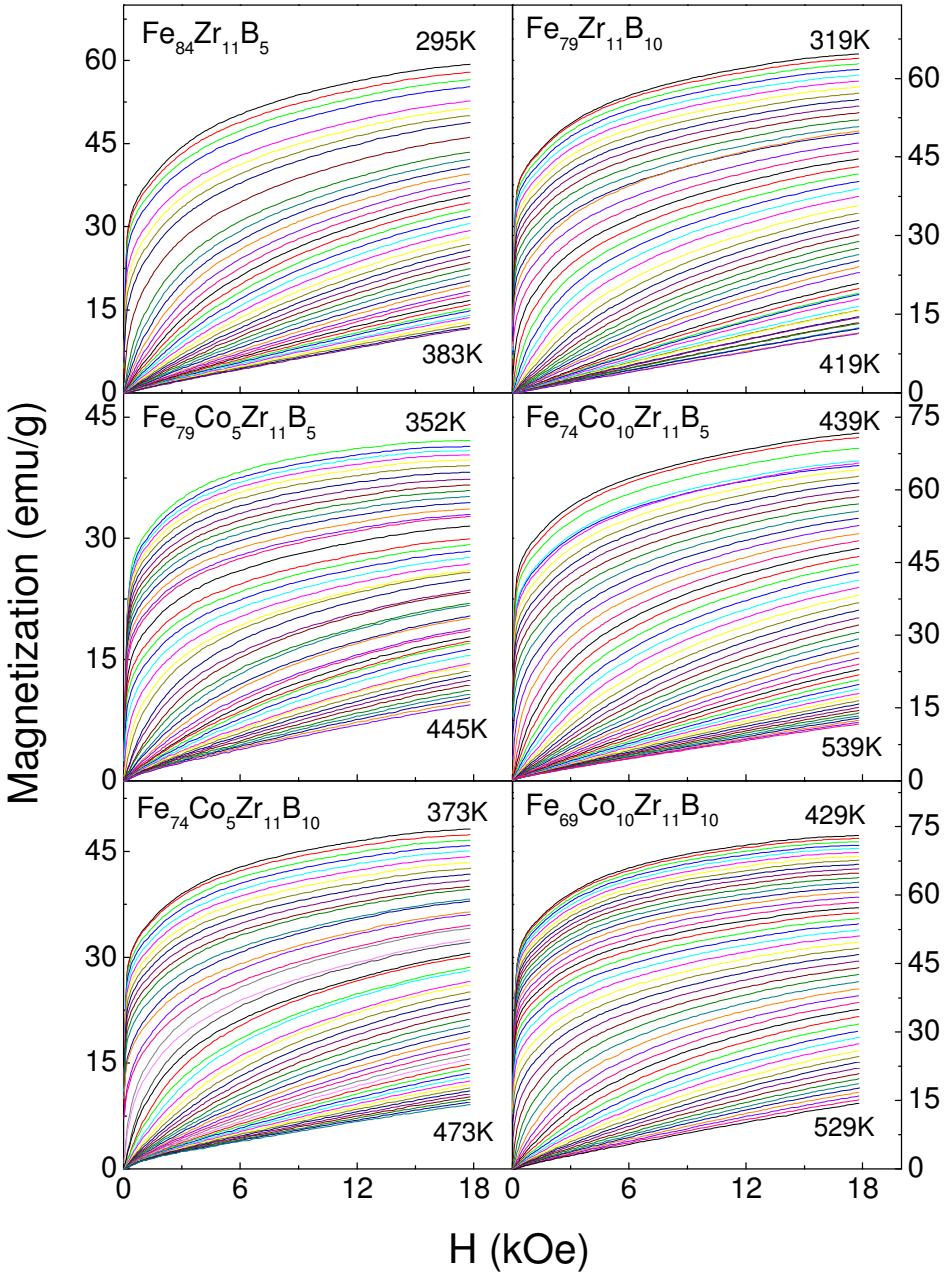


*FIG. 4.19: Isothermal magnetization curves of B and Co substituted $Fe_{89-x-y}Co_yZr_{11}B_x$ amorphous alloy ribbons around $T_C$.*

be well-controlled with the addition of B, Co and Mn. In addition, these samples exhibit very low $H_C$ in the range of 0.015 Oe to 0.063 Oe, indicating good soft magnetic properties in the

amorphous ribbons. The good soft magnetic properties in these samples would prove to be advantageous in magnetic refrigeration applications [PROV2004]. Fig.4.19 shows the isothermal magnetization curves of B and Co substituted a-$Fe_{89-x-y}Co_yZr_{11}B_x$ alloys around $T_C$. With increasing temperature, all the samples show a gradual change in magnetization from nonlinear to linear variations with field. MCE of a magnetic material can be evaluated from the field dependent magnetization curves using a numerical approximation to the equation,

$$\Delta S_M = \int_0^H \left(\frac{\partial M}{\partial H}\right)_H dH \qquad (4.6)$$

where the partial derivative is replaced by finite differences and the integration is performed numerically. The change in the entropy was calculated from the area under the $M - H$ curves at different temperatures using eqn.(4.6). Fig.4.20 shows the variations of $\Delta S_M$ with temperature calculated up to 18 kOe field for B, Co and Mn substituted a-Fe-Zr alloys. With increasing B content in Fe-Zr alloys [Fig.4.20(a)], the $\Delta S_M$ value increases from 1.34 J/kg/K for $Fe_{89}Zr_{11}$ sample to 1.73 J/kg/K for $Fe_{79}Zr_{11}B_{10}$ sample. In addition, the width of the $\Delta S_M$ curves decreases

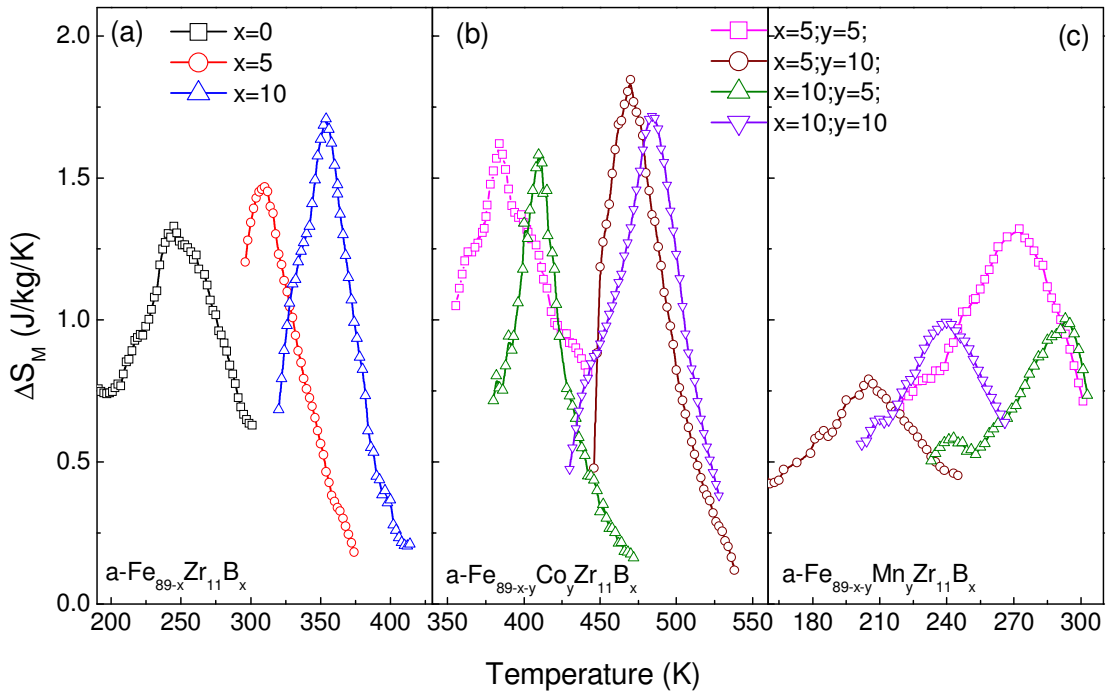


*FIG. 4.20: Variations of $\Delta S_M$ with temperature calculated up to 18 kOe field for B, Co and Mn substituted amorphous $Fe_{89-x-y}(Co,Mn)_yZr_{11}B_x$ alloys.*

with increasing B content. The increase in the $\Delta S_M$ value is mainly due to the enhanced FM properties of a-Fe-Zr-B alloys with B addition [BARA1994]. It is to be noted that the $\Delta S_M$ values obtained in the currently investigated systems are higher compared to those (1.4 J/kg/K) reported for a similar system with low Zr (~6 at.%) content [FRAN2008] and FINEMET (1.1 J/kg/K) alloys [FRAN1996]. Taking note of the enhancement in FM nature of a-Fe-Zr alloy with the addition of Zr [BARA1994], one can attribute this observed increase in $\Delta S_M$ to the relative influences of both Zr and B on the stabilization of local magnetic structure of a-Fe-Zr alloy.

Figs.4.20(b) and 4.20(c) show the variations of $\Delta S_M$ with temperature for Co and Mn substituted a-Fe-Zr-B alloys. With increasing Co content, the $\Delta S_M$ values increase to a maximum of about 1.93 J/kg/K for $Fe_{74}Co_{10}B_5Zr_{11}$ sample. This is due the enhanced magnetic exchange interaction between Fe and Co with the addition of Co [SHEN1991]. On the other hand, the substitution of Mn in $Fe_{84}Zr_{11}B_5$ alloy results in a large decrease in $\Delta S_M$ value down to 0.8 J/kg/K [Fig.4.20(c)] for alloys with 10 at.% Mn. This could be due to the loss of FM properties, resulting from the formation of AFM interactions between Mn-Mn and Fe-Mn. However, the rate of decrease of $\Delta S_M$ in $Fe_{89-x-y}Mn_yZr_{11}B_x$ decreases with increasing B content [Fig.4.20(c)] due to the increase in the relative competition between B and Mn in stabilizing the FM properties of a-Fe-Mn-Zr-B alloys. Min et al [MINS2005] also reported that the $\Delta S_M$ at 50 kOe decreases from 2.78 J/kg/K to 2.33 J/kg/K with increasing Mn content from 8 to 10 at.% in a-$Fe_{90-x}Mn_xZr_{10}$ alloys. A close observation of Fig.4.20(c) suggests that the width of $\Delta S_M$ versus T curve broadens with the addition of Mn and the maximum value of $\Delta S_M$ lies just above $T_C$ of the respective amorphous alloys in contrast to the Co added a-Fe-Zr-B alloys. This broadening can be attributed to the increase in magnetoelastic coupling with Mn substitution [AMRA2004]. The effects of Co and Mn substitutions on the $\Delta S_M$ of a-Fe-Zr-B alloys suggest that the temperature of the peak in the $\Delta S_M$ versus temperature graph can be tuned without changing its magnitude by manipulating the B/Co(Mn) ratio in a-Fe-(Co,Mn)-Zr-B alloys with high B content.

## 4.5. Summary

A systematic study on the temperature and field dependent magnetic properties of a-Fe(Co,Mn)-Zr-B alloys has been carried out. The salient features of a-Fe(Co,Mn)-Zr-B alloys from the current investigations are as follows:

1. Amorphous $Fe_{89-x}Zr_{11}B_x$ ($x$ = 0, 2.5, 5, 7.5, 10) and $Fe_{89-x-y}(Co,Mn)_yZr_{11}B_x$ (x, y = 5, 10) alloy ribbons could be prepared by melt-spinning technique.
2. Amorphous $Fe_{89}Zr_{11}$ alloy showed enhanced crystallization temperature compared to conventional NANOPERM alloys.
3. Addition of B in a-Fe-Zr alloy enhances $T_{crys}$, $T_C$ and room temperature $M_S$ of a-Fe-Zr-B alloys. On the other hand, $H_C$ of a-Fe-Zr-B decreased drastically and a very low value of $H_C$ (0.015 Oe) could be achieved for a-$Fe_{84}Zr_{11}B_5$ alloy.
4. Magnetic domain structure analysis reveals the presence of relatively large-sized domains with smooth and straight domain walls in a-Fe-Zr-B alloys. However, the average size of the domain decreased when B content was increased above 5 at.%.
5. Addition of Mn (Co) in a-Fe-Zr-B alloys shifts the $T_{crys}$ to higher (lower) temperatures.
6. $T_C$ and $M_S$ increase (decrease) with the addition of Co (Mn) in a-Fe(Co,Mn)-Zr-B alloys.
7. A maximum $M_S$ value of about 130 emu/g and $H_C$ of 0.13 Oe were obtained for the sample with 10 at.% Co and the values of $H_C$ lies below 0.4 Oe for a-Fe-Co-Zr-B alloys.
8. Moderate values of $\Delta S_M$ was obtained for a-Fe(Co,Mn)-Zr-B alloys. Addition of Co (Mn) in a-Fe(Co,Mn)-Zr-B alloys enhances (decreases) the $\Delta S_M$ value. A maximum value of $\Delta S_M$ = 1.93 J/Kg/K could be achieved for a-$Fe_{74}Co_{10}Zr_{11}B_5$ alloy.

# Chapter 5

# Effect of magnetic field annealing on the properties of amorphous ribbons

This chapter describes the effect of magnetic field annealing on the properties of amorphous Fe-(Co)-Zr-B alloy ribbons. The structural relaxation process and the formation of nanocrystalline phases by systematic isothermal annealing have been studied. The results of experimental studies carried on these nanocrystalline samples are also discussed below.

## 5.1. Introduction

Two-phase structured Fe-based alloys in which nanosized grains of a soft ferromagnetic (FM) crystalline phase are embedded in a soft FM amorphous matrix have attracted wide attention for their excellent soft magnetic properties and potential application in various magnetic devices [CANT2005, LIUJ2009, MARI2000, MITR2003]. Materials with such a microstructure obtained from gradually devitrified amorphous precursors exhibit excellent magnetic softness, which is generally ascribed to very low magnetostriction and dramatically reduced effective anisotropy due to the strong intergranular magnetic exchange coupling [HERN1995, SUZU1999]. Among the soft magnetic alloys, Fe-M-B (M = Zr, Nb, and Si) based alloys are characterized by high saturation magnetization ($M_S$), which can meet with the requirements of high performance and miniaturization for magnetic devices [CANT2005, MCHE2000, MODA2008, SUZU1990]. Of these, Fe-Zr-B based amorphous and nanocrystalline alloys with different B content have been extensively studied because of their excellent soft magnetic properties in the nanocrystalline state [KEME2000, KIMK1994, MAKI1994, SUZU1991, ZHUD2004]. However, it is to be noted that most of the Fe-Zr-B alloys reported in the literature contain lower Zr ($\leq$ 7 at.%) content. Recently, Huang et al [HUAN2008] reported that the crystallization stages of amorphous (a-) $Fe_{80}Zr_{12}B_8$ alloy under controlled heating were observed to be different from those observed for Fe-Zr-B alloys with low Zr content [CHEN1999, KIMK1994, KOPC1997, SUZU1998, TATE1998, UMAK2000, XION2003]. This suggests that the crystallization kinetics and magnetic properties of a-Fe-Zr-B alloys are quite dependent on the relative amounts of both Zr and B. Moreover, it is well-known that the Fe based amorphous phase exhibits very low Curie temperature ($T_C$), which can be significantly enhanced by substituting additional metalloid and transition metal elements [HASI2008, SUZU2002, YAOB2003].

Conventional attempts of improving the intrinsic and extrinsic soft magnetic properties have been focused on tailoring composition, control of microstructure with heat treatment under different environments such as magnetic field annealing, pressure effect, current through the

sample, reduction of coercivity, increase of magnetic induction, and control of intergranular exchange coupling in the amorphous and nanocrystalline materials. Therefore, a detailed knowledge on the devitrification process of amorphous alloys is invaluable in tuning the microstructures for optimized properties. Recently, it has been shown that the microstructure of Co-rich nanograins can be tuned by means of static magnetic field annealing [MARI2009] and, $M_S$ was found to increase with increasing magnetic field intensity during annealing due to the raise of volume fraction of nanocrystalline phases. On the other hand, the rotating-magnetic field annealing helps to reduce coherence uniaxial anisotropy and the reduction in coercivity values was observed for Nanoperm alloys due to the decrease of fluctuating amplitude of the effective anisotropy [SUZU2008]. The applied magnetic field during the current annealing of a-Co-Fe-Si-B ribbons results in complex domain structure and transverse permeability, but shows enhanced giant magnetoimpedance [HHAN2007].

It is well-known that the evolution of soft magnetic properties is closely related to the microstructural development. Since magnetic domain structure is a direct indication of micromagnetic behavior caused by microstructure such as grain size and grain boundary structure, it is worthwhile to analyze the domain structure to correlating the microstructure with annealing temperature dependent magnetic properties. However, the questions related to the influence of nanocrystalline microstructrue on magnetic domains and magnetic properties are still open because of the complexity of the problem. Also, understanding how magnetic properties are optimized in conjunction with the microstructures and domain structures would be useful for designing high-performance nanocrystalline materials. Therefore, a systematical comparative study between magnetic domain structure, microstructure and resulting magnetic properties is necessary to obtain the information for tailoring their magnetic properties. Since B and Co additions in a-Fe-Zr alloys yielded enhanced soft magnetic properties, the effect of substituting elements on the nanocrystalline $Fe_{89-x-y}(Co,Mn)_yZr_{11}B_x$ ($x$ = 0, 5, 10; $y$ = 5, 10) alloys obtained by isothermal annealing of amorphous precursors at different temperatures ($T_A$) has been investigated.

## 5.2. Experimental Details

To understand the evolution of nanocrystalline microstructure in the a-$Fe_{89-x-y}Co_yZr_{11}B_x$ alloys and to avoid oxidation, heat treatment of the amorphous ribbons was carried out in vacuum.

Amorphous $Fe_{89-x-y}Co_yZr_{11}B_x$ ($x$, $y$ = 5, 10) alloy ribbons were cut into many pieces of equal length and wrapped in an aluminum foil. The foil was kept inside the sample chamber (see Fig.3.3) such that the length of the ribbons was parallel to the applied magnetic field direction. The sample chamber was then evacuated to $10^{-5}$ Pa with a turbomolecular pump backed by a rotary pump. Magnetic field of 6 kOe was applied and the furnace temperature was raised to the desired annealing temperature ($T_A$) under a heating rate of 10 K/min. $T_A$ was controlled to ± 2 K with a temperature controller. Samples were annealed at different $T_A$ between 473 K and 923 K for one hour duration. After the completion of heat treatment at a particular $T_A$, the heater was switched off and the sample was allowed to cool down naturally to room temperature under the magnetic field. The evolution of nanocrystalline microstructure and magnetic domain structure were characterized using transmission electron microscope (TEM, JEOL 2100; TECNAI G2 F30). The magnetic domain structure of the amorphous ribbons was observed using Lorentz microscopy in Fresnel mode. Room temperature coercivity ($H_C$) and $M_S$ were obtained using coercimeter (Forster Koerzimat, Model 1.095) and vibrating sample magnetometer (VSM, Lakeshore model 7410), respectively.

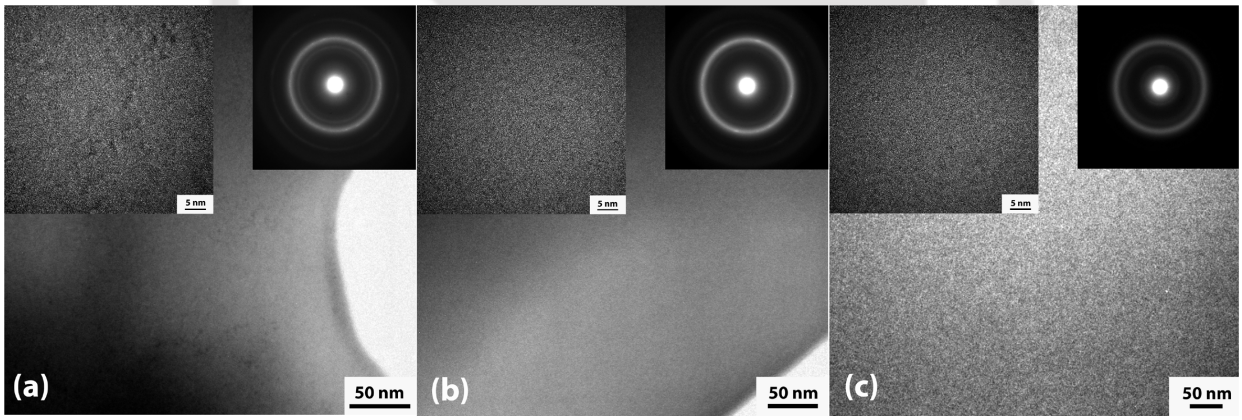


*FIG. 5.01: Bright-field TEM, HR-TEM images and SAED patterns of $Fe_{89-x}Zr_{11}B_x$ (x = 0 (a), 5 (b), 10 (c)) alloy ribbons annealed at $T_A$ = 673 K for 1 hour.*

## 5.3. Effect of field annealing on the properties of Fe-Zr-B ribbons

### 5.3.1. Effect of field annealing on microstructure

Figs.5.01 – 5.03 show bright-field TEM, high-resolution TEM (HR-TEM) micrographs, and selected area electron diffraction (SAED) patterns of $Fe_{89-x}Zr_{11}B_x$ ($x$ = 0, 5, 10) alloys magnetically annealed at $T_A$ = 673 K, 823 K and 923 K, respectively. HR-TEM micrographs and

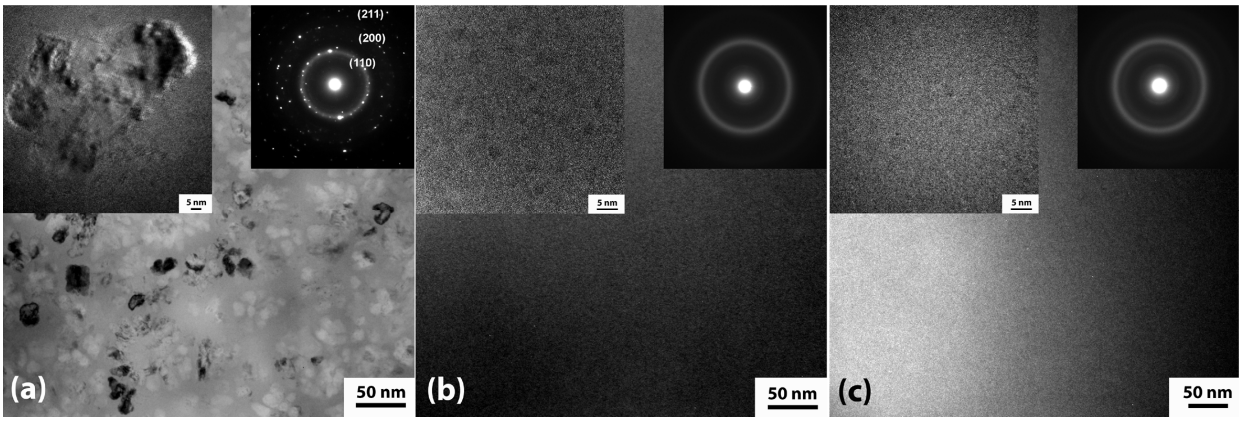


*FIG. 5.02: Bright-field TEM, HR-TEM images and SAED patterns of $Fe_{89-x}Zr_{11}B_x$ (x = 0 (a), 5 (b), 10 (c)) alloy ribbons annealed at $T_A$ = 823 K for 1 hour.*

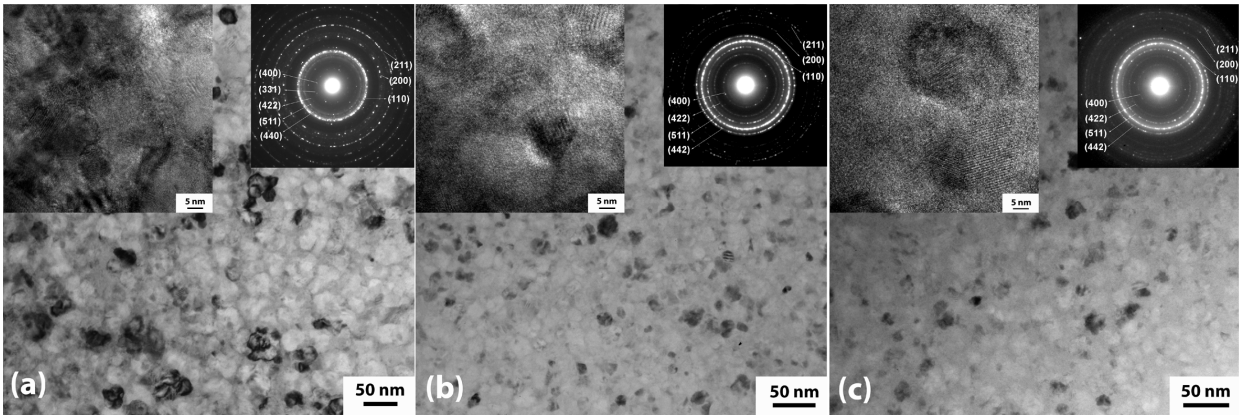


*FIG. 5.03: Bright-field TEM, HR-TEM images and SAED patterns of $Fe_{89-x}Zr_{11}B_x$ (x = 0 (a), 5 (b), 10 (c)) alloy ribbons annealed at $T_A$ = 923 K for 1 hour.*

SAED patterns of all the as-made samples (Fig.4.02 in chapter 4) revealed the characteristic amorphous microstructure and the halo diffraction ring of the amorphous structure, respectively. For the alloy with $x$ = 0 (Fig.5.01a), phase separation and random nucleation of body centered cubic (bcc) Fe crystallites begin at 673 K. At 823 K (Fig.5.02a), a random precipitation of bcc Fe is observed for the alloy with $x$ = 0. In addition, a small volume fraction of additional compounds nucleated randomly can also be observed in the micrographs. To understand the development of additional compounds, SAED patterns were observed from the samples annealed at different temperatures. The SAED patterns for the samples with $x$ = 0 annealed at 823 and 923 K show diffraction patterns typical of polycrystalline materials, with many diffraction rings including the diffraction rings corresponding to the $\alpha$-Fe. These diffraction rings confirm the crystallization of $Fe_3Zr$ crystalline phase with face centered cubic (fcc) crystal structure (Fig.5.03a). When the

temperature was increased above 823 K, a mixed structure of bcc Fe phases and fcc $Fe_3Zr$ compounds was observed. With increasing $T_A$ to 923 K, the average size of the $Fe_3Zr$ compound increased from 13 ± 2 nm to 22 ± 3 nm. On the other hand, for the alloy with $x$ = 5 (Fig.5.01b) annealed at 673 K, no trace of lattice fringes was seen in HR-TEM micrograph, indicating that it is still amorphous. However, formation of fine bcc nanocrystals with average size between 3 and 5 nm was observed for the alloys annealed above 823 K (Fig.5.02b) and the average grain size increased to 13 nm at 923 K. In addition to the homogeneous precipitation of bcc Fe nanocrystals, the SAED pattern reveals the presence of $Fe_3Zr$ crystalline phase. A similar behavior has been observed for the case of $x$ = 10 alloys (Figs.5.01c, 5.02c, 5.03c). Fig.5.04 shows the variations of average particle size ($D$) of the bcc phase with $T_A$ for $Fe_{89-x}Zr_{11}B_x$ alloys. The average size increases from about 5 to 27 nm as $T_A$ is increased from 673 to 923 K. The average size of the crystallites decreases with increasing B content.

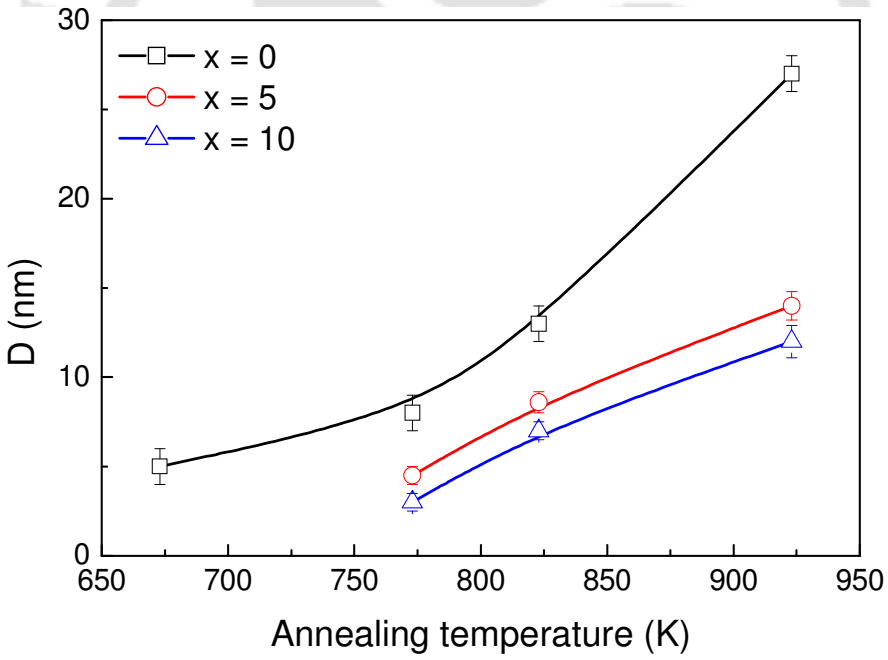


*FIG. 5.04: Variation of average particle size (D) of the bcc α-Fe phase with $T_A$ for $Fe_{89-x}Zr_{11}B_x$ (x = 0, 5, 10) alloy ribbons.*

The grain growth of Fe crystallites takes place in two stages. The first stage is controlled by the diffusion of Zr into the residual amorphous phase [MODA2008, OHOD2009, ZHAN1996]. When Fe crystallites nucleate and grow, both Zr and B have to come out of the growing Fe crystallites. But, B atoms diffuse much faster than Zr into the amorphous phase.

Therefore, there would be a concentration of Zr atoms surrounding the moving interface of Fe crystallites, which would restrict the growth of the Fe crystallites. On the other hand, the second stage of the grain growth is strongly depends upon the transformation of the residual amorphous phase into an appropriate crystalline phase. Such a transformation is quite fast when no long range diffusion is involved and hence consumes Zr to form the Fe-Zr compounds and un-pin the Fe interface, which is now free to grow. From the above results, it can be concluded that the crystallization of amorphous Fe-Zr-B alloys occurred through two transformation stages, viz., amorphous → $\alpha$-Fe (weak) + amorphous residue → $\alpha$-Fe + $Fe_3Zr$. The structural evolution with increasing $T_A$ for the as-made alloys is in good agreement with those reported in the literature [HUAN2008].

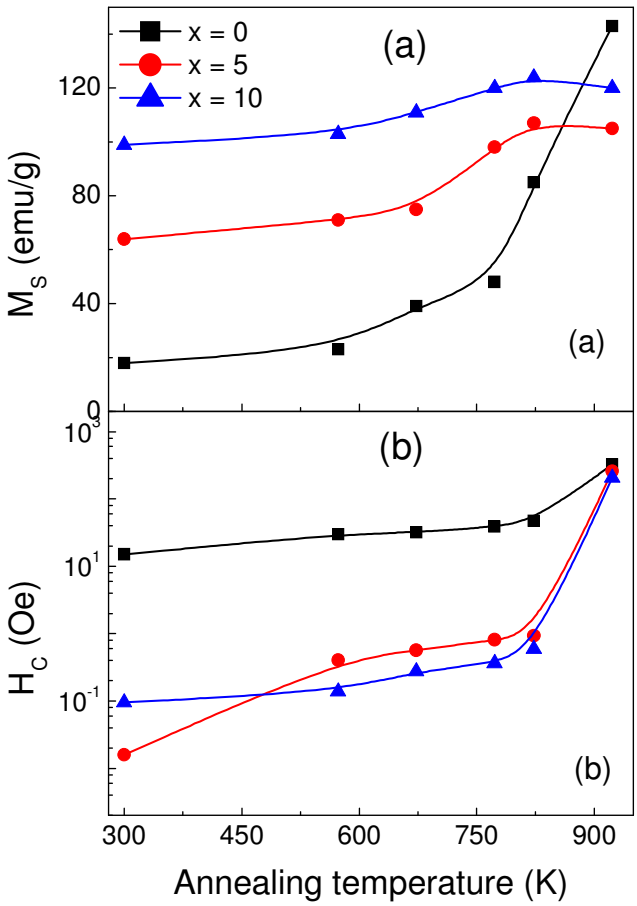


*FIG. 5.05: Variations of (a) $M_S$ and (b) $H_C$ with $T_A$ for the $Fe_{89-x}Zr_{11}B_x$ (x = 0, 5, 10) alloy ribbons.*

### 5.3.2. Effect of field annealing on magnetic properties

To understand the effect of nanocrystalline microstructure on the resulting magnetic properties, the variations of $M_S$ and $H_C$ with $T_A$ were measured for the $Fe_{89-x}Zr_{11}B_x$ alloys using VSM and coercimeter, respectively, and the same are depicted in Fig.5.05. The $M_S$ value is very low in the case of as-made $Fe_{89}Zr_{11}$ and increases almost linearly up to 773 K, followed by a rapid increase up to 923 K. On the other hand, the $M_S$ values of the as-made Fe-Zr-B alloys increase from 18 emu/g to 100 emu/g as B is increased from 0 to 10 at.%. This can be explained using non-collinear spin structure model [BARA1994, BARA1996, SHEN1991, XIAO2005] as discussed in chapter 4. $M_S$ values of Fe-Zr-B alloys increase initially up to 773 K and attain saturation before it decreases slightly at higher temperature. $M_S$ values of $Fe_{89-x}Zr_{11}B_x$ alloys annealed at 823 K are about 108 emu/g and 125 emu/g for $x$ = 5 and 10, respectively. These values are close to those of annealed FeCo based ribbons [MARI2009]. The variation of $M_S$ values is mainly due to the presence of the precipitated nanocrystals in the amorphous matrix and is thus dependent on $T_A$ [CELE2008]. $H_C$ value of the $Fe_{89}Zr_{11}$ alloy is observed to be large and in the range of $10^1$ - $10^2$ Oe for all the annealed alloys. $H_C$ increases almost linearly at about 0.06 Oe per K with increasing $T_A$ up to 823 K. This is mainly due to the weak intergranular exchange coupling (IEC) between nanocrystals through the paramagnetic (PM) amorphous phase. On the other hand, annealed $Fe_{89-x}Zr_{11}B_x$ alloys show very low value of $H_C$, typically, two to three orders lower in the as-made and annealed conditions up to 823 K. With increasing $T_A$, $H_C$ increases at about 0.0017 Oe per K and 0.0016 Oe per K for $x$ = 5 and 10, respectively. This can be attributed to the strong IEC between nanocrystals through the FM amorphous phase [HERN1995]. The average size of the nanocrystal increase slowly up to 823 K, but the rate of increase of $D$ decreases with increasing B content. Although $D$ values of Fe-Zr-B alloys annealed at 923 K is in the range 10–15 nm, $H_C$ values are observed to be high (>100 Oe).

### 5.3.3. Effect of field annealing on domain structure

To improve our understanding on the evolution of soft magnetic properties with $T_A$ and to investigate the correlation between the microstructure, magnetic domain structure, and resulting magnetic properties, the magnetic domain structure was observed at room temperature in the Fresnel mode using Lorentz microscope. Figs.5.06 – 5.08 depict the corresponding micrographs for the $x$ = 0, 5, and 10 samples annealed at different $T_A$. For the as-spun $Fe_{89}Zr_{11}$ alloy, no

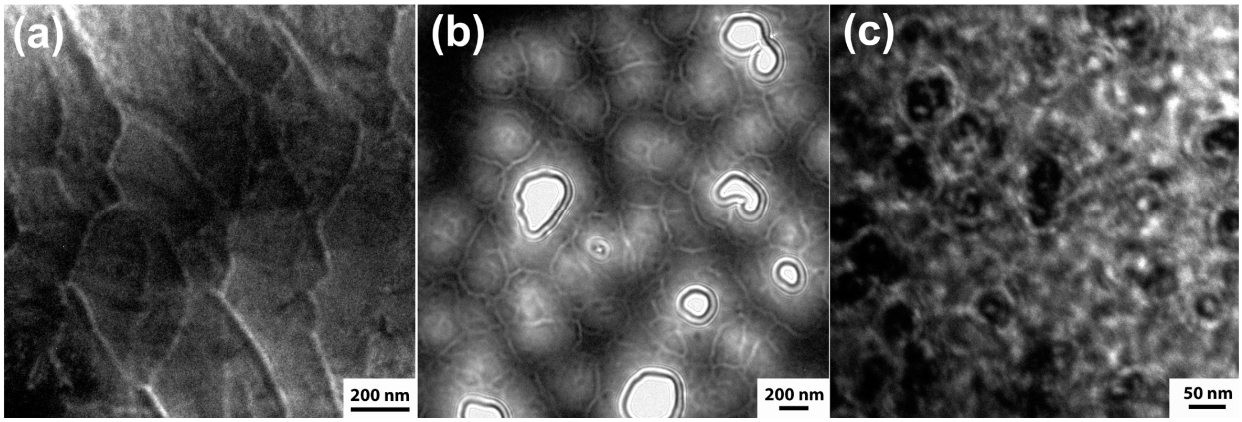


*FIG. 5.06: Magnetic domain images of $Fe_{89}Zr_{11}$ alloy ribbons annealed at (a) $T_A$ = 673 K, (b) $T_A$ = 823 K and (c) $T_A$ = 923 K for 1 hour.*

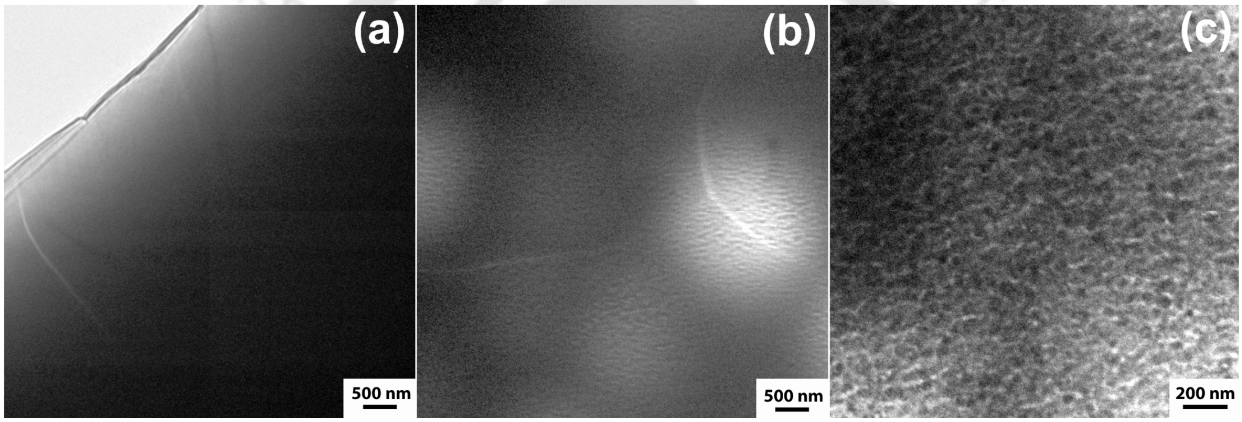


*FIG. 5.07: Magnetic domain images of $Fe_{84}Zr_{11}B_5$ alloy ribbons annealed at (a) $T_A$ = 673 K, (b) $T_A$ = 823 K and (c) $T_A$ = 923 K for 1 hour.*

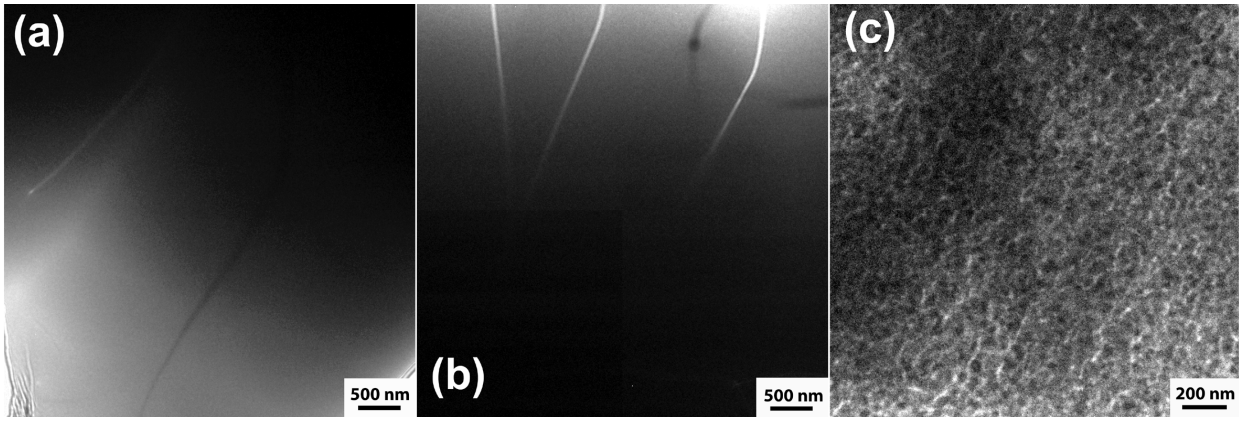


*FIG. 5.08: Magnetic domain images of $Fe_{79}Zr_{11}B_{10}$ alloy ribbons annealed at (a) $T_A$ = 673 K, (b) $T_A$ = 823 K and (c) $T_A$ = 923 K for 1 hour.*

domains were observed due to the PM nature of the sample in the demagnetized state. On the

other hand, the sample annealed at 673 K showed domains with smooth domain walls. The average size of the domains varied between 200 and 400 nm. Increasing $T_A$ to 823 K resulted in smaller domains with the average size between 90 – 150 nm and irregular domain walls. On further increasing $T_A$ to 923 K, the irregular domain walls are believed to be pinned by $Fe_3Zr$ compounds. The smaller domains in the $Fe_{89}Zr_{11}$ samples indicate a weak IEC. On the other hand, Fe-Zr-B samples annealed up to 823 K show very large-sized (2 and 5 μm) domains with smooth and relatively straight domain walls, indicating a strong IEC. These observations can be interpreted in the framework of the Random Anisotropy Model (RAM) [ALBE1978, HERZ1989, HERZ1990] that has been developed to account for the behavior of the $H_C$ with the grain size in nanocrystalline materials. According to this model, the average effective anisotropy resulting from strong (weak) IEC is (not) averaged out. Hence, domain wall pinning is expected by the fluctuation of anisotropy in weakly coupled system. These results are consistent with $T_A$ dependent magnetic parameters depicted in Fig.5.05. For the alloys annealed at 923 K, the average domain size is very much smaller and pinned by the $Fe_3Zr$ compound. This suggests that the deterioration of soft magnetic property is caused by the structural inhomogenities, where the effective anisotropy is not averaged out and can no longer be neglected.

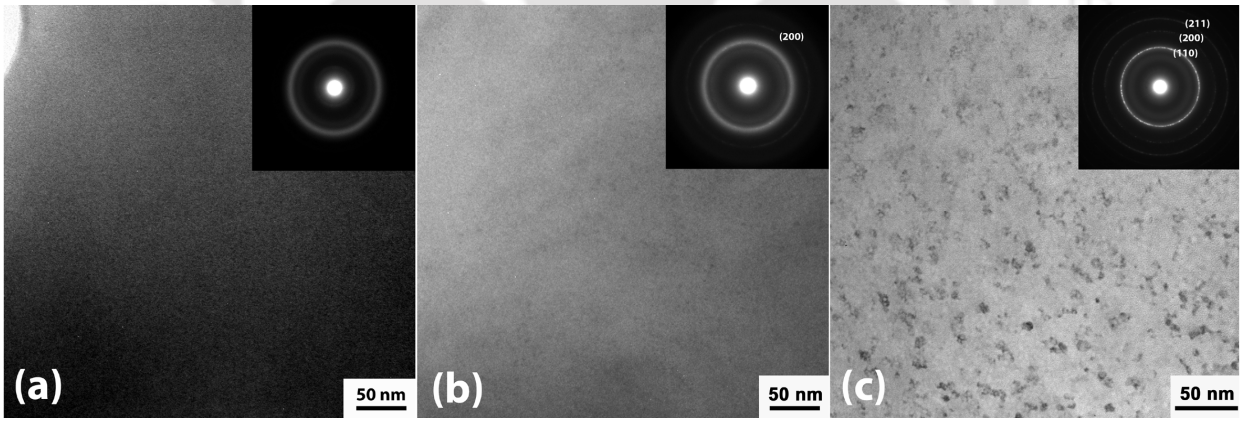


*FIG. 5.09: Bright-field TEM images and SAED patterns of $Fe_{84-y}Zr_{11}B_5Co_y$ (y = 0 (a), 5 (b), 10 (c)) alloys annealed at $T_A$ = 823 K for 1 hour.*

## 5.4. Effect of field annealing on the properties of Fe-Co-Zr-B ribbons

### 5.4.1. Effect of field annealing on microstructure

To understand the effect of Co substitution on the control of microstructure and soft magnetic properties, we have investigated the microstructure, magnetic domain structure and magnetic

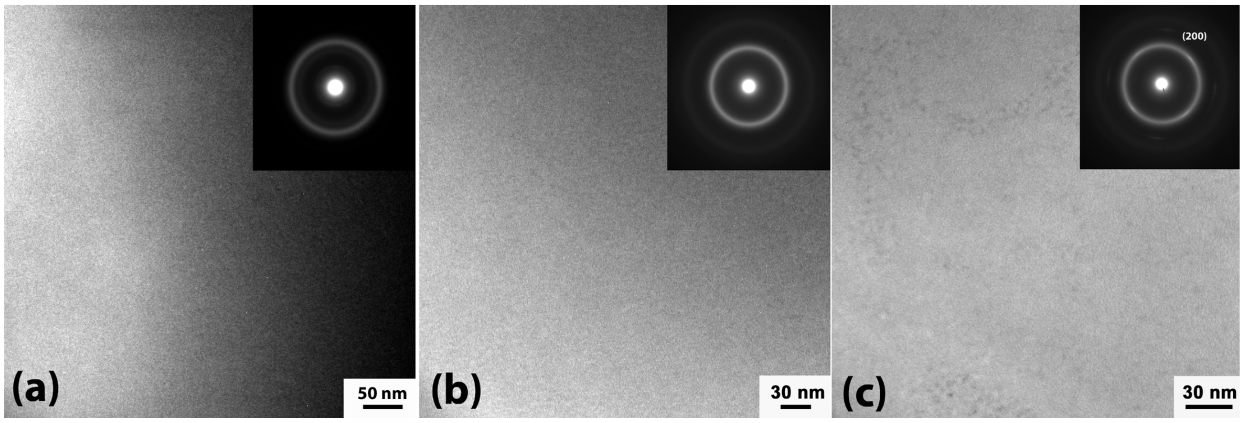


*FIG. 5.10: Bright-field TEM images and SAED patterns of $Fe_{79-y}Zr_{11}B_{10}Co_y$ (y = 0 (a), 5 (b), 10 (c)) alloy ribbons annealed at $T_A$ = 823 K for 1 hour.*

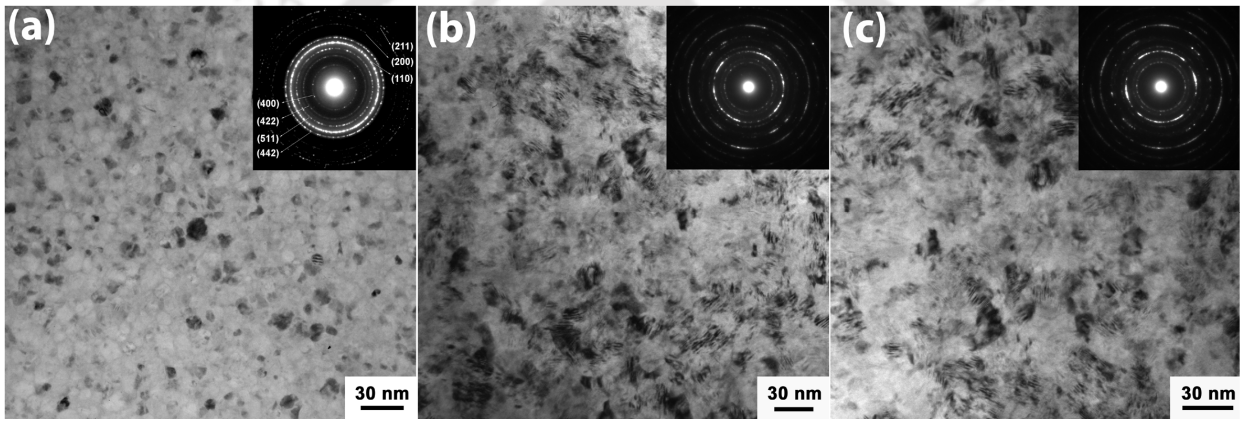


*FIG. 5.11: Bright-field TEM images and SAED patterns of $Fe_{79-y}Zr_{11}B_{10}Co_y$ (y = 0 (a), 5 (b), 10 (c)) alloy ribbons annealed at $T_A$ = 823 K for 1 hour.*

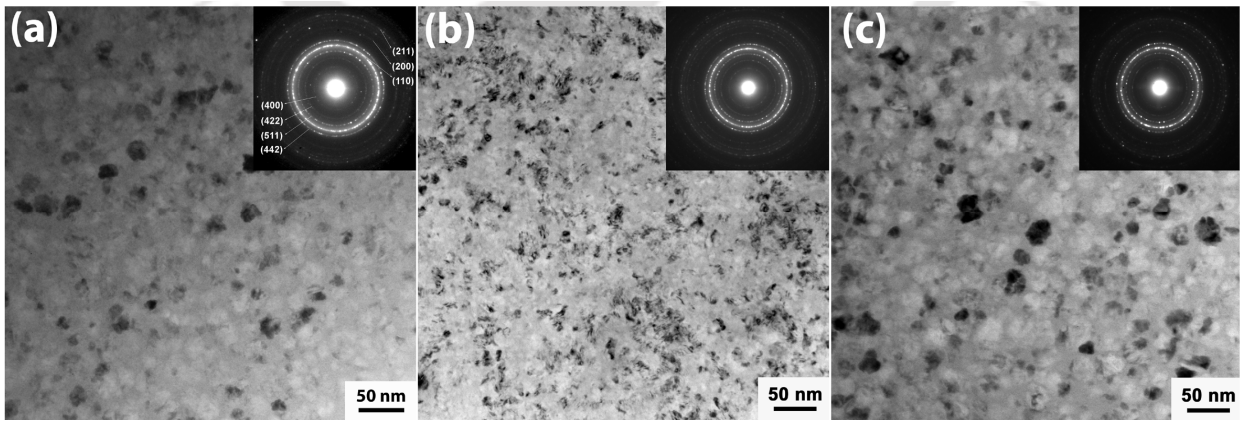


*FIG. 5.12: Bright-field TEM images and SAED patterns of $Fe_{79-y}Zr_{11}B_{10}Co_y$ (y = 0 (a), 5 (b), 10 (c)) alloy ribbons annealed at $T_A$ = 923 K for 1 hour.*

properties of $Fe_{89-x-y}Co_yZr_{11}B_x$ ($x$, $y$ = 5, 10) alloys annealed at different $T_A$. Figs.5.09 – 5.10

show the bright-field TEM micrographs and SAED patterns of the alloys with $x = 5$ ($y = 0, 5, 10$) and $x = 10$ ($y = 0, 5, 10$) annealed at 823 K. It is to be noted that the alloys annealed below 773 K show only amorphous phase. For the $Fe_{84}Zr_{11}B_5$ alloys annealed at 823 K, the formation of fine bcc nanocrystals with average size between 3 and 5 nm was observed. With the increase in Co content to 10 at.% in $Fe_{84-y}Co_yZr_{11}B_5$ alloy annealed at 823 K, the volume fraction of the nanocrystals increase (Fig.5.09c). The ring pattern in SAED supports the existence of nanocrystals. By comparing the SAED patterns of the $Fe_{84-y}Co_yZr_{11}B_5$ alloys, the halo effect in the alloy with $y = 10$ (Fig.5.09c) is weaker than that in the alloy with $y = 5$ (Fig.5.09b), suggesting that the volume fraction of amorphous phase has reduced. In addition, there were extra rings next to the first ring, which are indexed to be (200) and (211) reflections of the bcc Fe(Co) phase [SHUL1999]. On the other hand, for the $Fe_{79-y}Co_yZr_{11}B_{10}$ alloys with $y = 0$ and 5 annealed at 823 K, the bright-field TEM images revealed an even contrast and the SAED patterns contained concentric diffusive rings, a typical characteristic of an amorphous structure. However, for the $Fe_{69}Co_{10}Zr_{11}B_{10}$ alloy, there was an extra ring pattern next to the first ring in SAED supports the existence of fine nanocrystals. The increased volume fraction of nanocrystals in the Co substituted $Fe_{84-y}Co_yZr_{11}B_5$ alloys annealed at 823 K is mainly due to the reduction in the crystallization temperature with increasing Co content. In other words, addition of Co seems to destabilize the amorphous phase [SHUL1999]. These results are in good agreement with the DSC results reported in chapter 4 (sec. 4.3.2). Figs.5.11 – 5.12 depict the bright-field TEM micrographs and SAED patterns of the $Fe_{89-x-y}Co_yZr_{11}B_x$ alloys with $x = 5$ ($y = 0, 5, 10$) (Fig.5.11) and $x = 10$ ($y = 0, 5, 10$) (Fig.5.12) annealed at 923 K. It can be seen that the average grain size increased to 20 – 40 nm and the uniform distribution of the crystalline grains gets changed with Co substitution. The SAED patterns show additional diffraction rings that are attributable to phase(s) other than the bcc Fe(Co) phase. It was found that the additional rings could be indexed to $(Fe(Co))_3Zr$ compound.

### 5.4.2. Effect of field annealing on magnetic properties

To understand the effect of Co substitution in $Fe_{89-x-y}Co_yZr_{11}B_x$ alloys and the nanocrystalline microstructure on the resulting magnetic properties, the variations of $M_S$ and $H_C$ with $T_A$ were measured for the $Fe_{89-x-y}Co_yZr_{11}B_x$ alloys using VSM and coercimeter, respectively. The corresponding data are depicted in Fig.5.13. $H_C$ value of the Co substituted amorphous Fe-Co-

Zr-B alloys is quite low (<0.3 Oe) at room temperature. With increasing $T_A$, $H_C$ values increased up to ($T_A$ =) 673 K and significantly decreased with further increase in $T_A$ up to 823 K. On further increasing $T_A$ to 923 K, the $H_C$ value increased rapidly to about $10^2$ Oe. All the Co substituted Fe-Co-Zr-B alloys annealed at different temperatures show similar behavior. On the

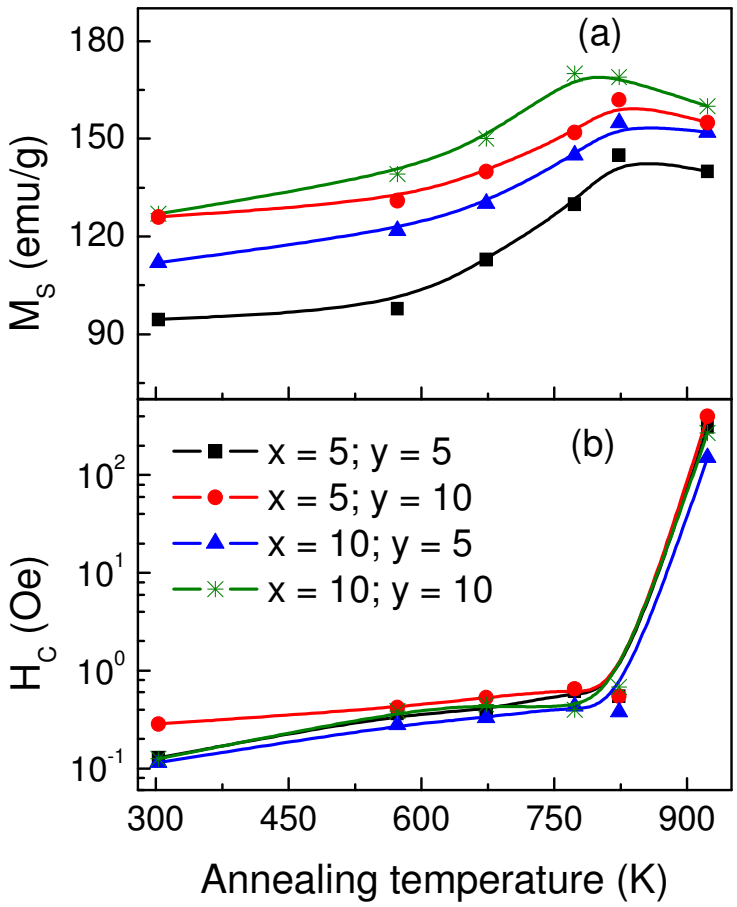


*FIG. 5.13: Variations of (a) $M_S$ and (b) $H_C$ with $T_A$ for the $Fe_{89-x-y}Co_yZr_{11}B_x$ alloy ribbons.*

other hand, $M_S$ values of the annealed Fe-Co-Zr-B alloys increase initially up to 673 K and remains constant before it decrease slightly at higher temperatures. $M_S$ values of Co substituted $Fe_{89-y}Co_yZr_{11}B_x$ alloys annealed at 823 K are found to be above 150 emu/g for $x$ ($y$) = 5 (10) and 10 (10). This is in good agreement with the reported values in the literature on similar alloys [MAJU2007, CELE2008]. The increase in $M_S$ values can be attributed to the precipitation of high-saturation bcc phase (Figs.5.09 – 5.10) which is devoid of B/Zr in the samples annealed at lower temperatures. On increasing the $T_A$ above 823 K, Zr/B concentration in the precipitate phase increases (Figs.5.11 – 5.12), resulting in a decrease of $M_S$. The variations of $H_C$ with $T_A$

can be interpreted well in the frame work of RAM [ALBE1978, HERZ1990]. According to this model, $H_C$ of the amorphous phase is expected to increase at the early stages of the nanocrystallization, when nanocrystals are too sparse for the averaging out of the magnetic anisotropy on multiple nanocrystals to take effect, and acts as pinning centers for the domain walls. When the nanocrystalline phase develops and the exchange length becomes larger than the average distance among the nanocrystals, a progressive reduction of $H_C$ is expected, as observed in the present investigations. The observed results suggest that Co substituted Fe-Co-Zr-B alloys annealed below about 823 K show excellent soft magnetic properties. On the other hand, $H_C$ values of the Fe-Co-Zr-B alloys annealed at 923 K are quite high, as observed in Fe-Zr-B samples.

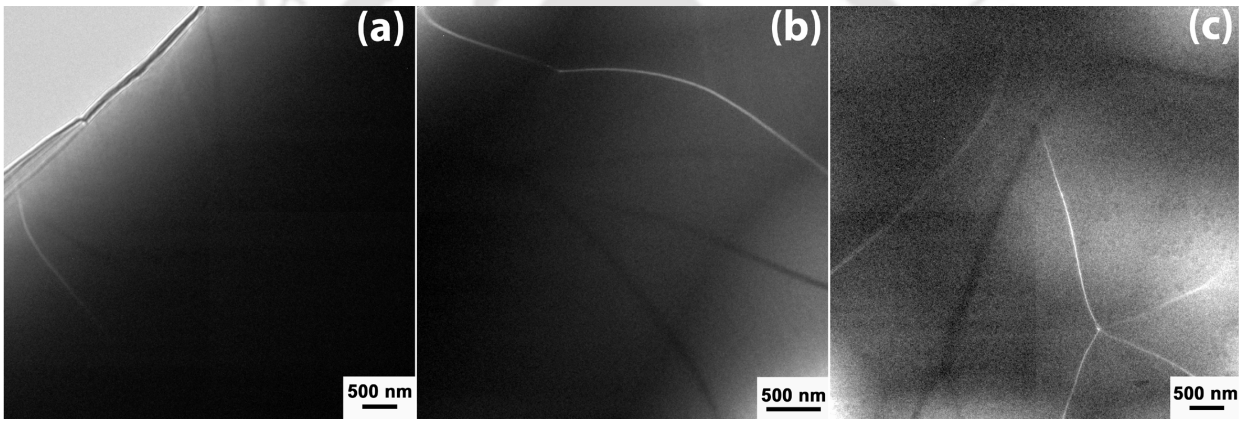


*FIG. 5.14: Magnetic domain images of $Fe_{84-y}Zr_{11}B_5Co_y$ (y = 0 (a), 5 (b), 10 (c)) alloy ribbons annealed at 673 K.*

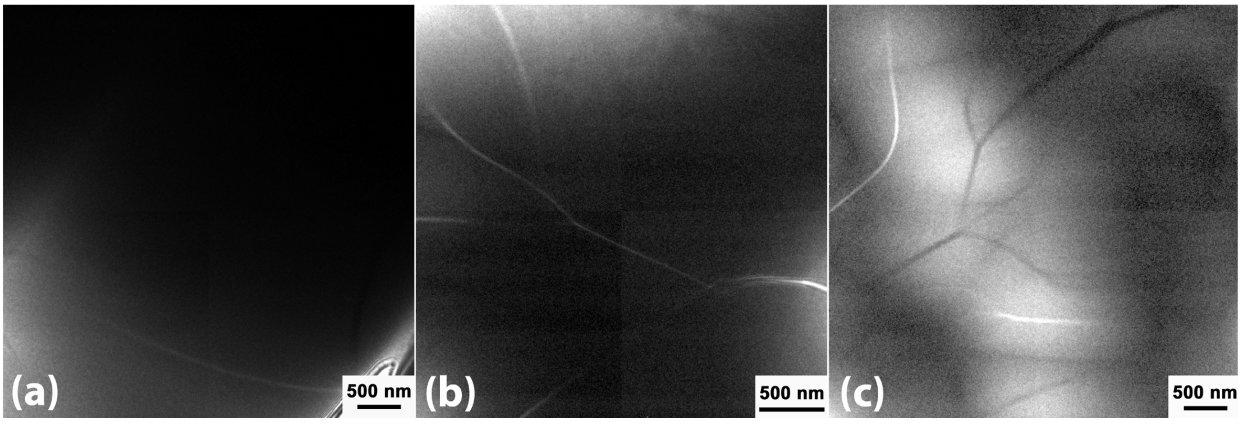


*FIG. 5.15: Magnetic domain images of $Fe_{79-y}Zr_{11}B_{10}Co_y$ (y = 0 (a), 5 (b), 10 (c)) alloy ribbons annealed at 673 K.*

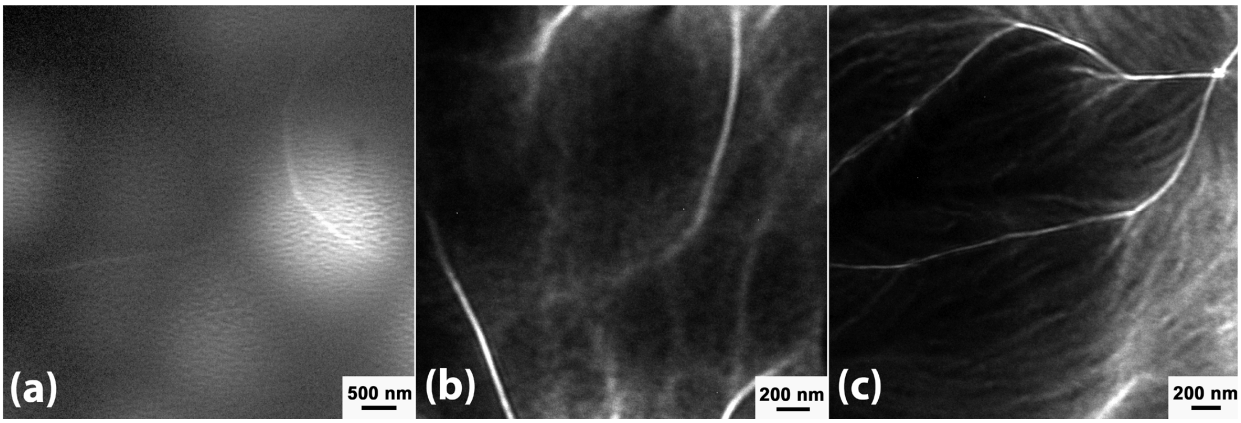


*FIG. 5.16: Magnetic domain images of $Fe_{84-y}Zr_{11}B_5Co_y$ (y = 0 (a), 5 (b), 10 (c)) alloy ribbons annealed at 823 K.*

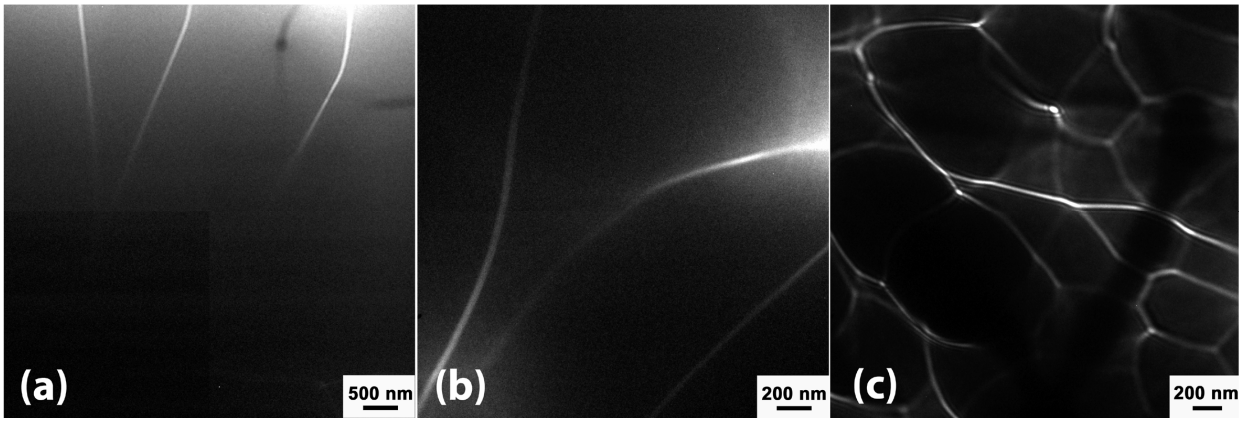


*FIG. 5.17: Magnetic domain images of $Fe_{79-y}Zr_{11}B_{10}Co_y$ (y = 0 (a), 5 (b), 10 (c)) alloy ribbons annealed at 823 K.*

### 5.4.3. Effect of field annealing on the magnetic domain structure

The evolution of microstructure and soft magnetic properties in Co substituted Fe-Co-Zr-B alloys annealed at different $T_A$ show close correlation between them. Apart from helping to optimize the magnetic properties in conjunction with the microstructures, the domain structures would also be useful for establishing high-performance nanocrystalline materials. So, the magnetic domain structure was observed at room temperature in the Fresnel mode and the micrographs depicted in Figs.5.14 – 5.18 correspond to $Fe_{89-x-y}Co_yZr_{11}B_x$ ($x$, $y$ = 5, 10) alloys annealed at different $T_A$. $Fe_{89-x-y}Co_yZr_{11}B_x$ alloys annealed at 673 K (Figs.5.14 and 5.15) show large-sized domains with smooth domain walls. Note that the $Fe_{89-x-y}Co_yZr_{11}B_x$ ($x$, $y$ = 5, 10) alloys annealed at 673 K are still amorphous. The average size of the domains decreases with increasing Co content in $Fe_{89-x-y}Co_yZr_{11}B_x$ alloys. With increase in $T_A$ up to 823 K, the $Fe_{89-x-}$

$_yCo_yZr_{11}B_x$ alloys with $x$ = 5 show low-angle domain walls inside large domains, exhibiting a magnetic ripple structure (Fig.5.16c). With increase in B content up to 10 at.% in $Fe_{89-x-y}Co_yZr_{11}B_x$ alloys, formation of such ripple structure is diminished (Fig.5.17c). However, the average domain size decrease with increasing Co content up to $x$ = 10 in $Fe_{89-x-y}Co_yZr_{11}B_x$ alloys. This could be attributed to an induced anisotropy resulting from either enhanced magnetostriction [SUZU1994] or directional ordering of Fe-Co atomic pairs induced by annealing. On further increasing $T_A$ to 923 K, the $Fe_{69}Co_{10}Zr_{11}B_{10}$ alloy shows only ripple domain structure, in contrast to the pinned domains around the $Fe_3Zr$ compounds as observed in Fe-Zr-B alloys (Figs.5.18a,b) without Co. This suggests that the magnetization ripple in the Co substituted $Fe_{89-x-y}Co_yZr_{11}B_x$ alloys is due to the increase in effective anisotropy caused possibly by the directional ordering and the formation of structural inhomogeneities [or $Fe(Co)_3Zr$ compounds]. Therefore, the soft magnetic properties of the $Fe_{89-x-y}Co_yZr_{11}B_x$ alloys annealed at 923 K deteriorate largely with $H_C$ increasing two orders in magnitude.

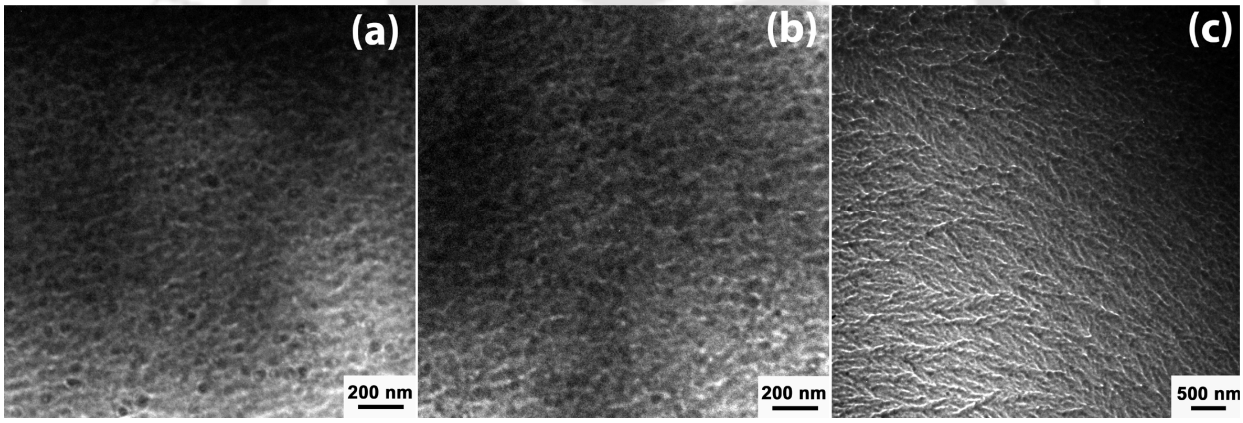


*FIG. 5.18: Magnetic domain images of $Fe_{89x-y}Zr_{11}B_xCo_y$ ((a) x = 5; y = 0; (b) x = 10; y = 0, (c) x = 10; y = 10) alloy ribbons annealed at 923 K.*

## 5.5. Summary

A systematic study on the microstructure, magnetic domain structure and soft magnetic properties of Fe-Co-Zr-B alloys annealed at different temperatures has been carried out. The salient features of the present studies on annealed Fe-Co-Zr-B alloys are as follows:

1. The devitrification process of amorphous Fe(Co)-Zr-B alloys ribbons studied under controlled heating conditions show the crystallization sequence of amorphous → $\alpha$-Fe (weak) + amorphous residue → $\alpha$-Fe + $Fe_3Zr$.

2. The alloys annealed below about 823 K showed weak tendency for the formation of $\alpha$-Fe crystalline phase. Also, the formation of $\alpha$-Fe crystalline phase is associated with other Fe-Zr compounds.
3. Addition of Co in Fe-Co-Zr-B alloys decreases the crystallization temperature, but enhances the Curie temperature and room temperature magnetization of a-Fe-Co-Zr-B alloys.
4. Coercivity of the Fe-Co-Zr-B alloys with and without Co substitution increases slightly with increasing annealing temperature up to 823 K. However, the coercivity of the alloys annealed at 923 K increases by two orders in magnitude due to the increase in effective anisotropy. This increase might have been caused by the formation of structural inhomogeneities or induced by the directional ordering of Fe-Co pairs in Co substituted alloys.
5. Magnetic domain structure analysis reveals the presence of relatively large-sized domains with smooth and straight domain walls in Fe-Co-Zr-B alloys annealed up to 823 K. However, the average size of the domain decreased with increasing Co content. In addition, annealing Fe-Zr-B alloys with Co substitution at 923 K resulted in a change over from pinned domains to magnetic ripple domains.
6. A maximum $M_S$ value of about 175 emu/g and coercivity of 0.35 Oe were obtained for the $Fe_{69}Co_{10}Zr_{11}B_{10}$ alloy annealed at 823 K, which can be claimed to exhibit excellent soft magnetic properties. In addition, the coercivity of $Fe_{89-x-y}Co_yZr_{11}B_x$ alloys annealed up to 823 K lies below 0.7 Oe.

# Chapter 6

# Mechanical alloying of amorphous Fe-(Co,Mn)-Zr-B alloy powders

This chapter describes the structural, thermal and magnetic properties of amorphous (a-) Fe-(Co,Mn)-Zr-B alloys prepared by mechanical alloying (MA) technique. Evolution of structural and magnetic properties with the milling time and the effect of substituting elements (B, Co, and Mn) on the properties of a-Fe-Zr alloys are also discussed below in detail.

### 6.1. Experimental details

In this section, the optimized experimental conditions to prepare a-Fe(Co,Mn)-Zr-B alloys by MA has been discussed. Weighed quantities of elemental Fe, Zr, B, Co, and Mn powders (purity of 99.9 % from Strem Chemicals) corresponding to compositions of $Fe_{100-x-y-z}(Co,Mn)_zZr_xB_y$ (with $x$ = 20 – 35, $y$ = 0 – 10, and $z$ = 0 – 20) were taken in a hardened steel milling vial. 8 mm diameter hardened steel balls corresponding to a ball to powder ratio of 20:1 were added to the vials. The vials were then purged with high purity argon gas and sealed. The ball size and ball to powder ratio were optimized with trial runs on the parent composition prior to the formation of final products. MA of the powder mixture was performed in a planetary ball mill (Insmart, India) under a milling speed of 500 rpm. In order to avoid excessive heating, which may induce the formation of other intermetallic phases during the milling process, the mill was programmed to halt for 10 minutes after every 15 minutes of continuous operation. Powders were taken out at regular time interval during the milling process. The crystal structure of the milled powders was characterized using a powder X-ray diffractometer with Cu-$K_\alpha$ ($\lambda$ = 1.54056 Å) radiation (XRD, Seifert 3003, T/T). The surface morphology and microstructure of the powders were characterized using Scanning Electron Microscope (SEM, Leo 1430 VP) and Transmission Electron Microscope (TEM, JEOL 2100), respectively. The composition of the powders was determined by Energy Dispersive Spectroscopy (EDS) unit attached to the SEM. Thermal analysis of the as-milled powders was carried out using a Differential Scanning Calorimeter (DSC 7, Perkin-Elmer) operated under different constant heating rates of 20, 30 and 40 K/min under dry nitrogen gas atmosphere. Room temperature and temperature dependent magnetic properties of the as-milled powders were obtained using a Vibrating Sample Magnetometer (VSM, Lakeshore Model 7410) in the applied field range of ± 20 kOe and superconducting quantum interference device (SQUID, Quantum design MPMS XL 7) magnetometer in the applied field range of ± 50 kOe. With the optimized conditions, amorphous (a-) $Fe_{100-x}Zr_x$ ($20 \leq$

$x \leq 35$), $Fe_{65-y}Zr_{35}B_y$ ($y = 0 - 10$), and $Fe_{60-z}(Co,Mn)_zZr_{35}B_5$ ($z = 0$ - 20) alloy powders were prepared directly by milling the elemental powders.

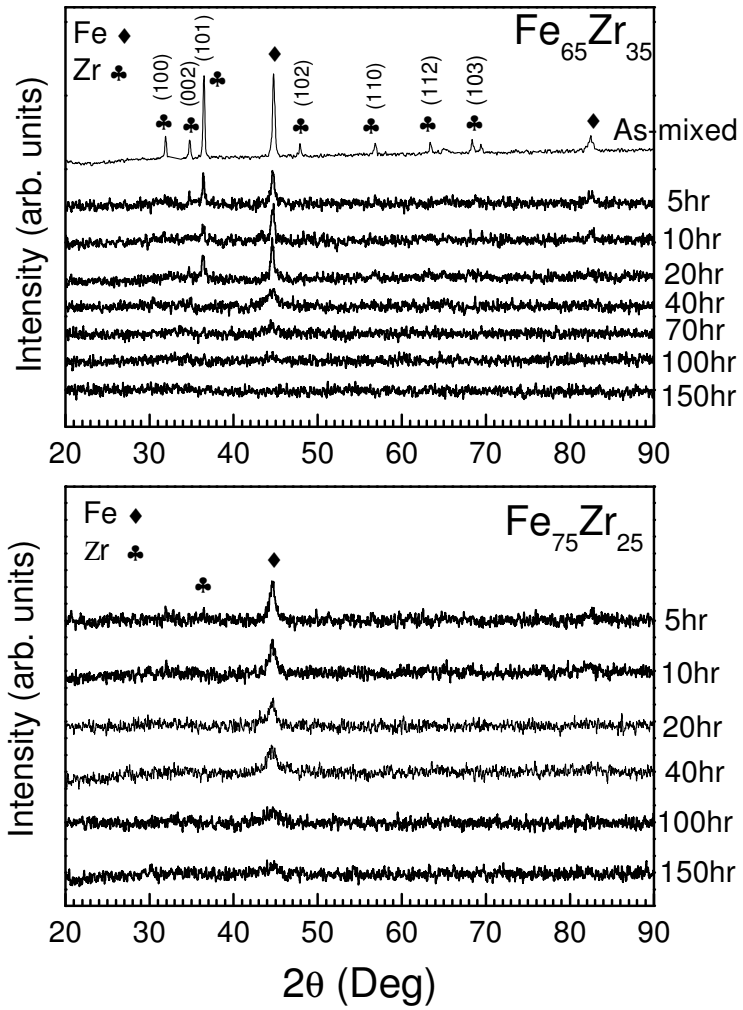


*FIG. 6.01: XRD patterns of $Fe_{65}Zr_{35}$ and $Fe_{75}Zr_{25}$ alloy powders milled up to 150 hours.*

## 6.2. Mechanical alloying of Fe-Zr powders

### 6.2.1. Structural evolution during milling

Fig.6.01 shows the XRD patterns of $Fe_{65}Zr_{35}$ and $Fe_{75}Zr_{25}$ powder alloys milled for different time periods. After 20 (40) hours of milling, only one peak corresponding to the reflection from the (110) plane of Fe remained and all other Bragg peaks corresponding to Zr and Fe disappeared in the case of $Fe_{75}Zr_{25}$ ($Fe_{65}Zr_{35}$) alloy. This suggests that a solid solution of Fe(Zr) was formed after 20 (40) hours of milling $Fe_{75}Zr_{25}$ ($Fe_{65}Zr_{35}$) powder mixture. Different time periods of solid

solution formation for different composition ranges indicate that the solid state reaction depends mainly on the composition. The reactivity in the solid state is due to the repeated fracturing and cold welding of powder particles. As the milling period was increased, the intensity of Fe(110) peak reduced and the width of the peak increased. The average crystallite size of $Fe_{65}Zr_{35}$ ($Fe_{75}Zr_{25}$) alloy calculated from the Scherrer's formula is 25 (13) nm on milling for 10 h, which reduced to 10 (7) nm on milling for 20 h. Optical microscopy studies by Hellstern et al [HELL1988] showed a layered microstructure during the initial stage of milling of this alloy powders due to the cold welding of particles. The broadening of the peak suggests the reduction in average crystallite size and the presence of strain accumulated in the form of defects and dislocations. After 40 h of milling, there is a considerable reduction in the peak intensity indicating further reduction of average crystallite size (6 nm for $Fe_{65}Zr_{35}$ and 5 nm for $Fe_{75}Zr_{25}$). Eventually, the milling results in the formation of the amorphous phase after 70 h of milling. In order to monitor the homogenization and possible recrystallization, the milling was continued up to 150 h. However, no significant formation of other compounds (Fig.6.01) was observed in contrast to the results reported by Ennas et al [ENNA1989]. In their investigation, the amorphous phase was achieved in 17 h of milling, unlike the present case. This is mainly due to the different milling conditions adopted in the two investigations.

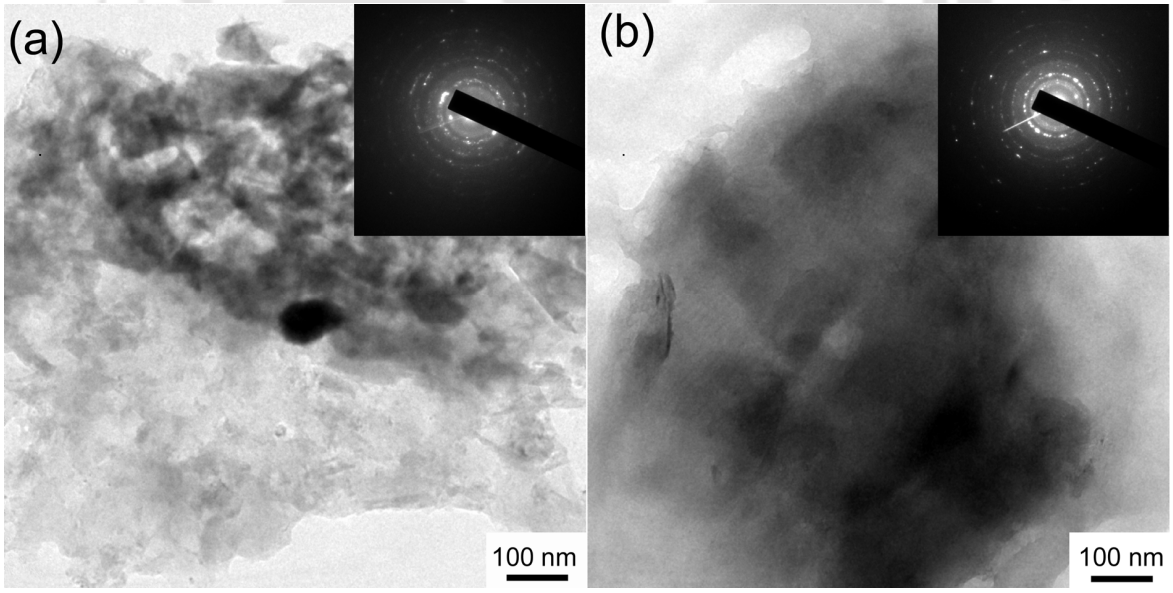


*FIG. 6.02: Bright field TEM images and SAED patterns of (a) $Fe_{65}Zr_{35}$ and (b) $Fe_{75}Zr_{25}$ alloy powders milled for 5 hours.*

To understand the possible deformation behavior and the amorphization process, high-resolution transmission electron micrographs (HR-TEM) were taken for the samples milled for different time periods. Figs.6.02a and b show the bright field TEM images for 5 h milled $Fe_{65}Zr_{35}$ and $Fe_{75}Zr_{25}$ alloy powders, respectively. It could be seen that fracture occurs at the

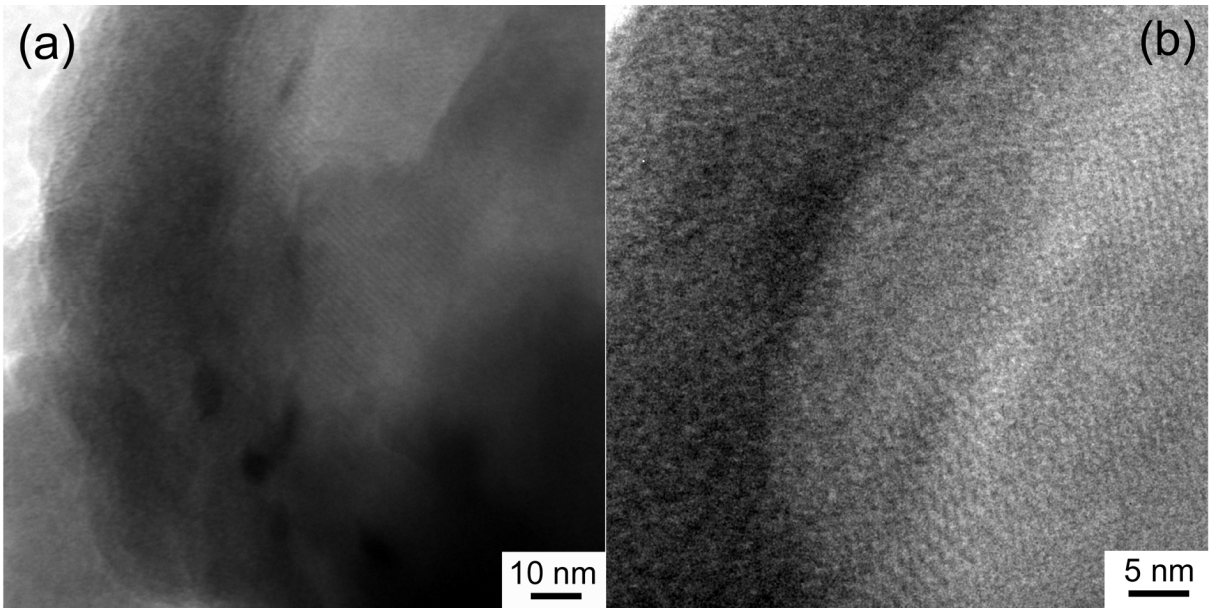


*FIG. 6.03: HR-TEM images of (a) $Fe_{65}Zr_{35}$ and (b) $Fe_{75}Zr_{25}$ alloy powders showing the formation of grain boundary.*

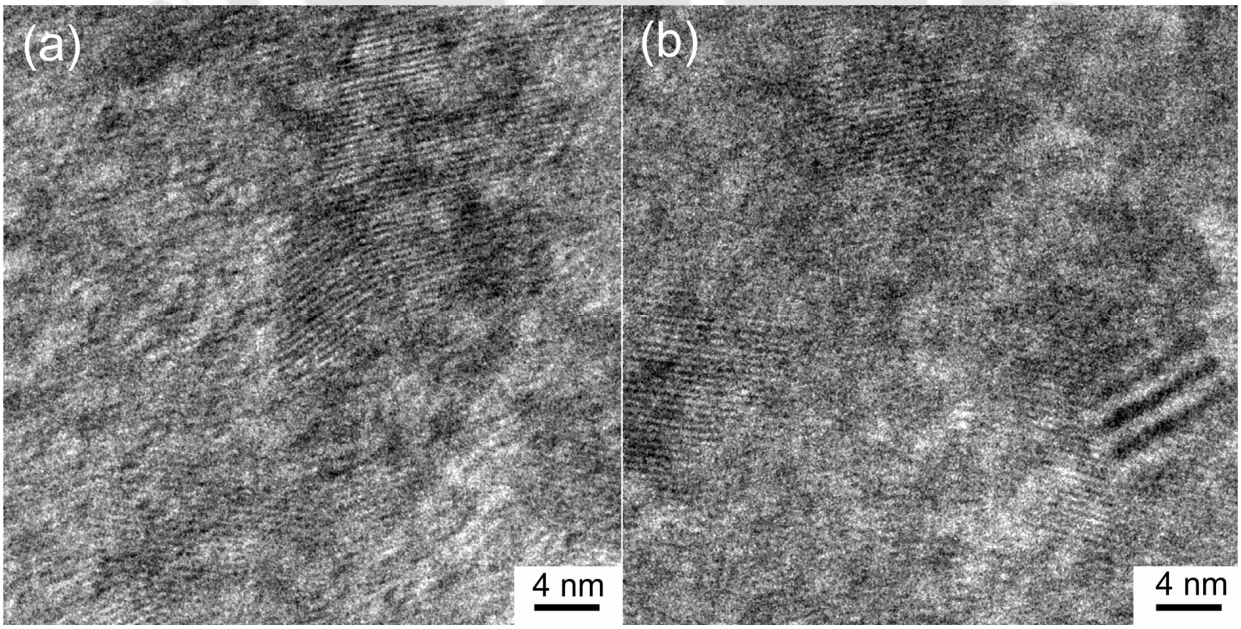


*FIG. 6.04: HR-TEM images of (a) $Fe_{65}Zr_{35}$ and (b) $Fe_{75}Zr_{25}$ alloy powders showing the formation of grain boundary.*

initial stage of the milling due to the repeated grinding of the materials. Selected area electron diffraction (SAED) patterns show highly distorted contrast of the pattern and azimuthal spreading of spots revealing the strain in the powders induced by the heavy grinding of the materials [VALI2000]. This is in good agreement with the earlier reports on Fe-Zr alloy powders [HELL1988]. As the milling time increases, the average size of the crystallites reduces further with the formation of new grain boundary. Accumulation of defects and dislocations cause the fragmentation of crystallites and the size reduction with the formation of additional grain boundaries as shown in Fig.6.03. Fig.6.03a shows the formation of new crystallites from an existing single crystallite with the development of new grain boundary, while Fig.6.03b depicts the grain boundary interface separating crystalline and amorphous phases.

To understand the deformation behavior and formation of grain boundary in detail, HR-TEM images of 40 h milled samples were observed (Fig.6.04). A careful observation of the HR-TEM image shown in Fig.6.04a suggests the formation of twin boundary in $Fe_{65}Zr_{35}$ milled powders. This is in good agreement with reports published on ball milled Co powders [HUAN1996]. Deformation of Fe-Zr alloy occurs via formation of high angle grain boundary.

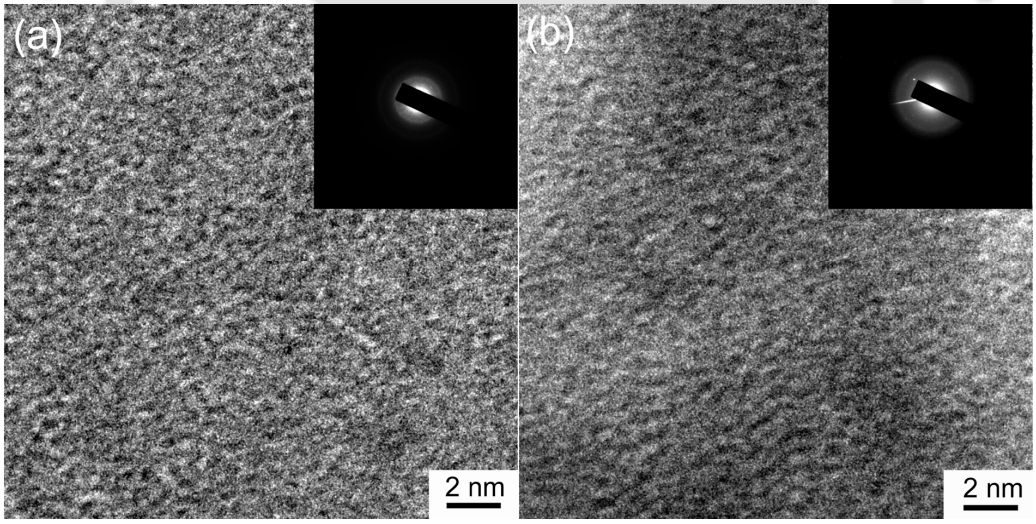


*FIG. 6.05: HR-TEM images and SAED patterns of (a) $Fe_{65}Zr_{35}$ and (b) $Fe_{75}Zr_{25}$ alloys after 70 hours of milling.*

However the grain boundary energies are quite lower than the usual random boundaries. These boundaries only occur at particular misorientations and boundary planes which allow the two adjoining lattices to fit together with little distortion of the inter-atomic bonds. In the presently investigated Fe-Zr alloys, a coherent twin boundary is observed. As the milling time progresses,

the coherent twin boundary becomes incoherent and results in the formation of high-angle grain boundary as shown in Fig.6.04b. In addition, the formation of shear bands inside a crystallite is observed. These shear bands formed due to the piling of dislocations inside the crystal are responsible for the formation of subgrains which facilitates amorphization. It is worth mentioning that shear band formation is one of the typical mechanisms for the grain size reduction during plastic deformation [FECH1990, HANS1982]. Formation of shear bands during ball milling has also been reported earlier on similar systems [HUAN1998]. On further increasing the milling time, the nanocrystals diminish in size and eventually become amorphous after a milling period of 70 h. The formation of amorphous phase is well supported by both XRD patterns and HR-TEM images as shown in Fig.6.05. HR-TEM images with slightly off-focused condition show the absence of any crystallites and the SAED patterns also show only the halo-diffraction rings. From the results, it can be concluded that amorphization occurred when the impurity atom (Zr) penetrates into the Fe system and distorts the lattice locally. When the local distortion reaches some critical value, the long-range order of the lattice gets destroyed (destabilization of the crystalline phase) and the amorphous phase is obtained. The large difference between the atomic sizes of Fe and Zr atoms (ratio between the atomic radii of Fe and Zr is 0.78) [GALE2004] is also an important factor in obtaining the amorphous phase.

### 6.2.2. Evolution of magnetic properties with milling

Since MA involves plastic deformation of the alloy under study, defects, dislocations, internal strain etc. tend to dominate the magnetic properties of the milled alloy powders. To examine the variation of magnetic properties as a function of milling time, magnetic hysteresis ($M - H$) loops were taken for the powders sampled out at regular intervals of time and depicted in Fig.6.06. The extracted values of saturation magnetization ($M_S$) and coercivity ($H_C$) from the $M - H$ loops are shown in Fig.6.07. The variations of $H_C$ with milling time show oscillatory behavior, while $M_S$ which increases initially, shows a large decrease with increasing milling time. The initial decrease in $H_C$ can be attributed to the refinement of grain size. The formation of more grains increases the intergranular exchange coupling. This leads to a decrease in $H_C$ values [HERZ1990]. The increase in $H_C$ after 20 (40) hours of milling can be understood from the induced inhomogeneity in the matrix of the alloys under study (since induced strain, fluctuations in materials parameters etc. tend to deteriorate the magnetic properties). Similar variations of $H_C$

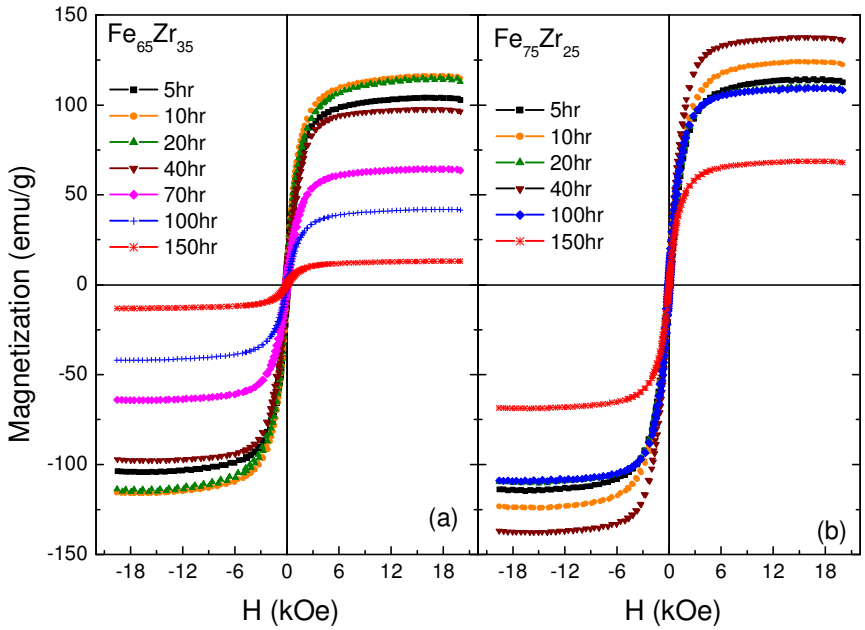


*FIG. 6.06: Room temperature magnetic hysteresis loops of $Fe_{65}Zr_{35}$ and $Fe_{75}Zr_{25}$ alloy powders at different hours of milling.*

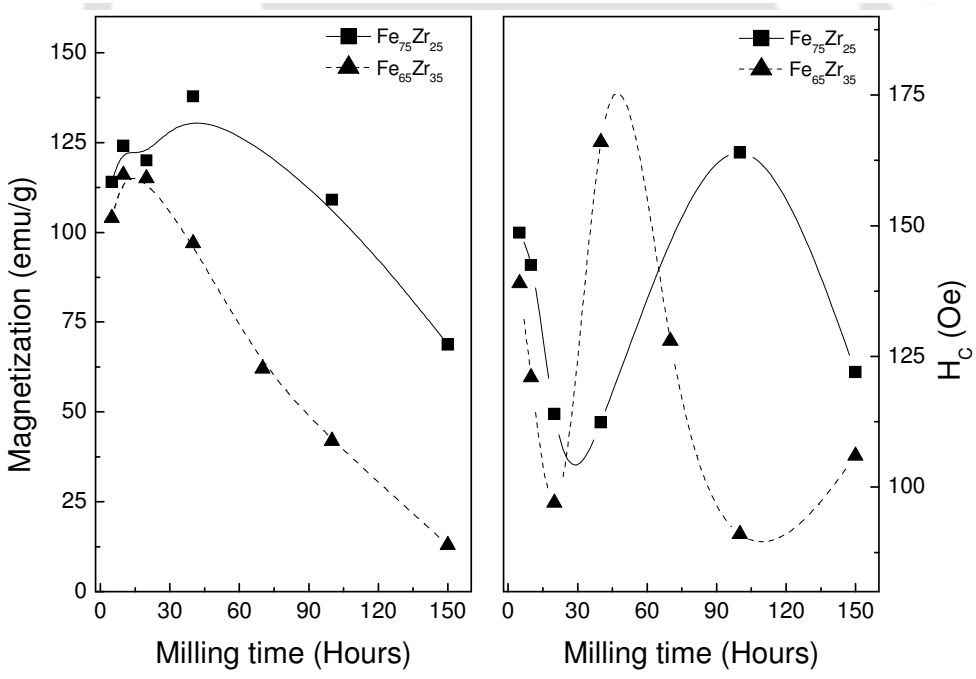


*FIG. 6.07: Variations of coercivity and saturation magnetization for $Fe_{65}Zr_{35}$ and $Fe_{75}Zr_{25}$ alloy powders at different hours of milling.*

with milling time were reported for ball milled Fe-Co powders [ALLE2009]. As the milling time

increases, the average size of the crystallites decreases and the milled powders achieve more homogeneity. Hence the $H_C$ values reduce significantly. On the other hand, $M_S$ value initially increases up to 15 (40) h of milling for $Fe_{65}Zr_{35}$ ($Fe_{75}Zr_{25}$) alloy. This may be due to the enhanced reactivity of the alloys due to the milling [HELL1988, SARA2009]. On further increasing the milling time, the $M_S$ value decreases gradually due to the loss of long range crystallinity when the alloys approach amorphous phase. In addition, the large difference in $M_S$ values between $Fe_{65}Zr_{35}$ and $Fe_{75}Zr_{25}$ alloys after 150 h of milling is mainly due to the increase in Zr content and the reduction in ferromagnetic (FM) component.

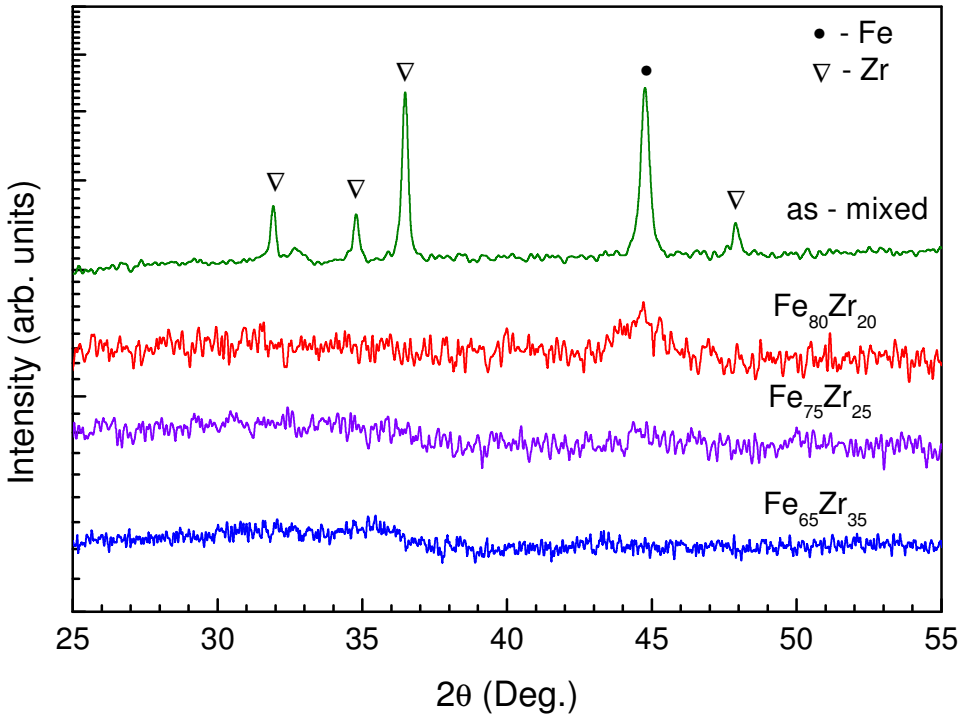


*FIG. 6.08: XRD patterns of as-mixed $Fe_{65}Zr_{35}$ powder and as-milled $Fe_{100-x}Zr_x$ alloy powders.*

### 6.2.3. Structural properties of Fe-Zr powders

With the optimized milling conditions, a series of binary Fe-Zr powders corresponding to the compositions $Fe_{100-x}Zr_x$ ($x$ = 20, 25, 30, 35) was taken and milled for 60 hours to obtain them in amorphous phase. Fig.6.08 shows the XRD patterns of as-mixed $Fe_{65}Zr_{35}$ and as-milled $Fe_{100-x}Zr_x$ alloy powders. The XRD pattern of the as-mixed powder shows individual characteristic peaks of Fe and Zr elements. In the as-milled powders the Zr peaks disappeared completely leaving behind either the body centered cubic (bcc) $\alpha$-Fe reflections centered around $2\theta = 44°$

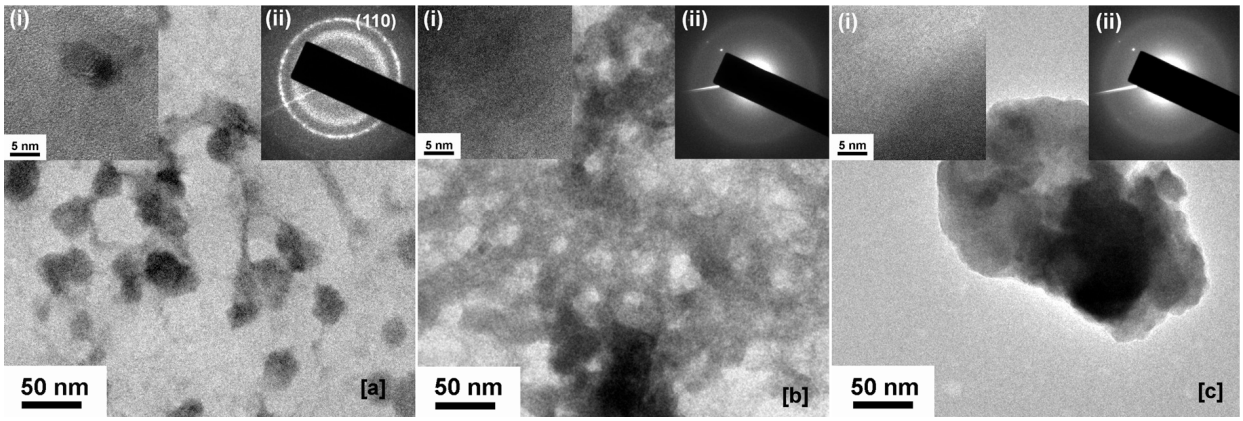


*FIG. 6.09: Bright field TEM images, HR-TEM images, and SAED patterns of as-milled* $Fe_{100-x}Zr_x$ *[x = 20 (a), 25 (b), and 35 (c)] powders.*

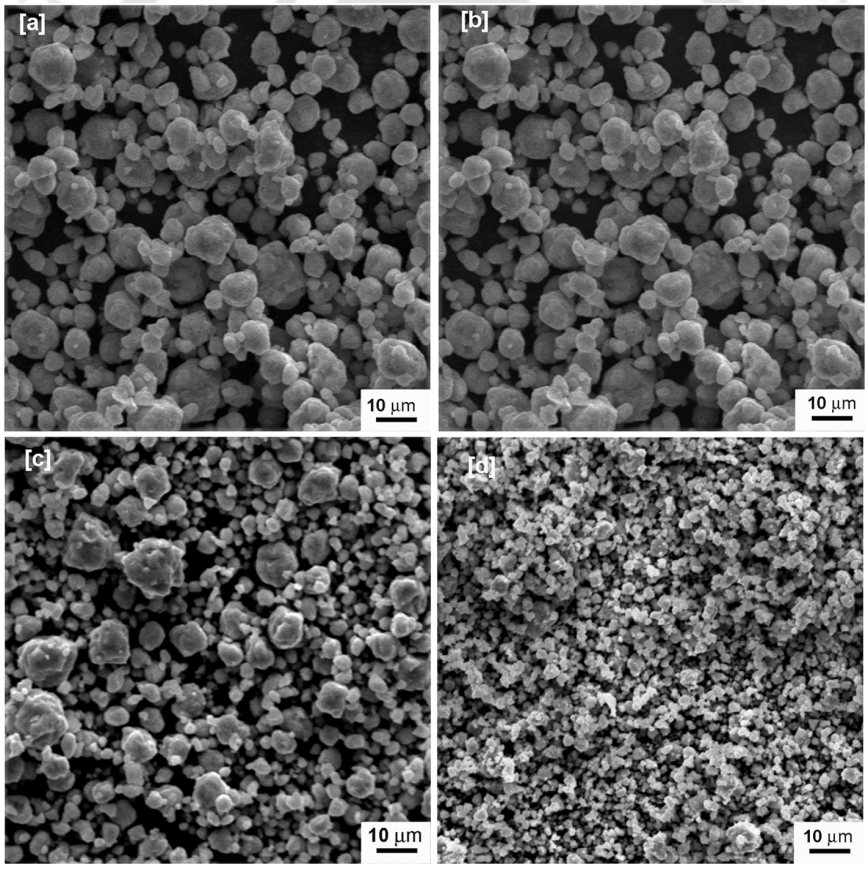


*FIG. 6.10: SEM micrographs of as-milled* $Fe_{100-x}Zr_x$ *(x = 20 [a], 25 [b], 30 [c], and 35 [d]) alloy powders.*

(for $x < 25$ at.%) or a broad low intensity hump centered around $2\theta = 33°$ (for $x = 25$ at.%). The XRD results indicate the formation of either an amorphous structure (for the samples with $x \geq$

25 at.%) or a non-equilibrium solid solution (for the sample with $x$ = 20 at.%) with an average crystallite size of about 8 nm within a residual amorphous phase. To understand the development of nanocrystalline and/or amorphous structure in these powders, we observed TEM micrographs on the as-milled powders. Fig.6.09 shows the bright field TEM images, HR-TEM images and SAED patterns of $Fe_{100-x}Zr_x$ ($x$ = 20, 25, and 35) powders. The SAED pattern of $Fe_{80}Zr_{20}$ powder shows the diffraction rings indicating a reflection from (110) planes of Fe and Zr rich amorphous phase. The HR-TEM image supports the presence of fine nanometer sized crystallites with high degree of strain. The average crystallite size observed from the HR-TEM image is about 9 nm for the as-milled $Fe_{80}Zr_{20}$ powder. These data agree well with those obtained from XRD peak analysis. The increase of Zr composition above 20 at.% in $Fe_{100-x}Zr_x$ results the formation of amorphous structure. The diffused halo ring in the SAED patterns [Fig.6.09b and c] is the typical signature of the amorphous structure present in these powders. Moreover, no nanocrystallites are observed in the HR-TEM images. This suggests that the currently investigated as-milled $Fe_{100-x}Zr_x$ powders with $x$ > 20 at.% exhibit a single-phase amorphous structure. The observed results are different from those reported earlier on the same systems where two different environments of Zr and Fe existed as revealed by Mossbauer spectroscopy [PIZA2000]. This could be attributed to the different experimental conditions such as ball to powder weight ratio, milling speed and milling media, used in the two synthesis route. It is now well-established that the end product of MA is highly dependent on the different parameters involved in the milling process [SURY2000]. Nevertheless, the current investigation demonstrates the optimal milling conditions for the synthesis of single phase amorphous Fe-Zr alloy. The formation of amorphous structure in $Fe_{100-x}Zr_x$ ($20 \leq x \leq 35$) system has been reported earlier focusing mainly on the structural and magnetic homogeneity of the amorphous phase as perceived by low temperature Mossbauer studies [PIZA2000]. The present investigation is the first attempt to study the low temperature magnetic behavior of the amorphous phase in this system. Fig.6.10 shows the SEM micrographs of the as-milled $Fe_{100-x}Zr_x$ ($20 \leq x \leq 35$) powders. It is evident that the surface morphology of the as-milled powders is similar for all the compositions investigated. However, the average agglomerated particle size, resulting from aggregation of crystallites, decreases from 10 μm to sub-micrometer dimensions as the Zr concentration is increased from 20 to 35 at.%, respectively. Aggregation of crystallites is a natural consequence of the MA process in which the elemental powders undergo repeated cold welding and fracture. In order to analyze the

composition of the as-milled Fe-Zr powders and to evaluate possible contamination from the milling media, EDS analysis of the as-milled powders was carried out. The EDS data of the powders averaged over several measurements are listed in Table 6.1. The deviations in the measured concentrations of Fe and Zr are within 3 % of the nominal starting compositions. This confirms the homogeneity of the composition in the as-milled powders.

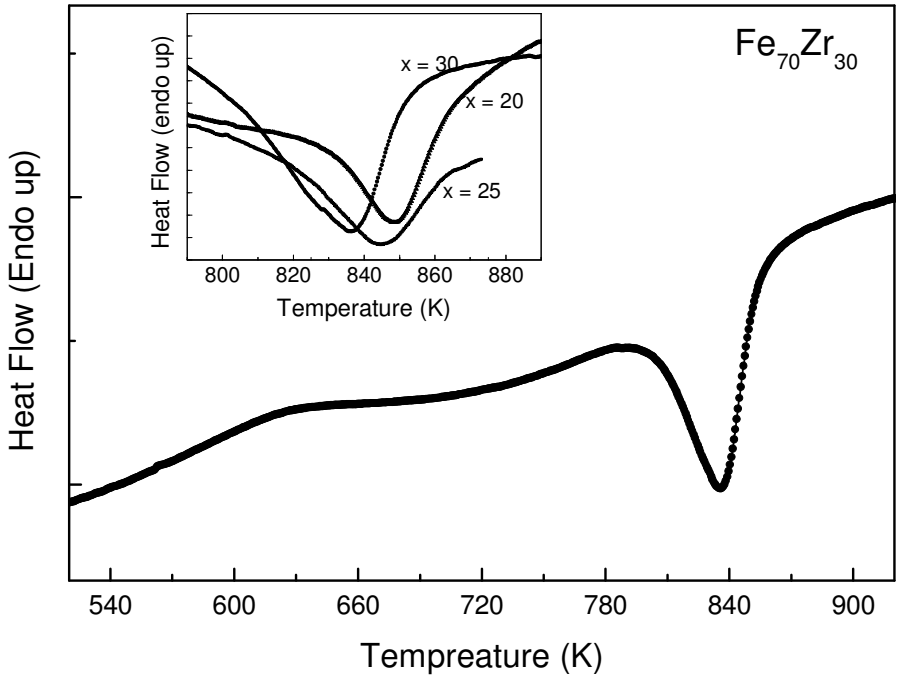


*FIG. 6.11: DSC curve of as-milled $Fe_{70}Zr_{30}$ alloy powder taken at 20 K /min heating rate. Inset: DSC curves of $Fe_{100-x}Zr_x$ powders in the region close to crystallization temperature.*

Table 6.1: Composition from EDS analysis, crystallization temperature, activation energy and enthalpy of as-milled $Fe_{100-x}Zr_x$ ($20 \leq x \leq 35$) alloy powders.

| **Sample** | **EDS Composition** | **Onset $T_{crys}$ (K)** | **Peak $T_{crys}$ (K)** | **Activation energy, $E_A$ (eV/atom)** | **Enthalpy released (J/g)** |
|---|---|---|---|---|---|
| $Fe_{80}Zr_{20}$ | $Fe_{81.97}Zr_{18.03}$ | 837 | 849 | 1.91±0.09 | 6.0 |
| $Fe_{75}Zr_{25}$ | $Fe_{77.14}Zr_{22.86}$ | 835 | 845 | 2.98±0.12 | 7.0 |
| $Fe_{70}Zr_{30}$ | $Fe_{72.54}Zr_{27.45}$ | 827 | 836 | 2.72±0.10 | 8.2 |
| $Fe_{65}Zr_{35}$ | $Fe_{66.79}Zr_{33.21}$ | 875 | 886 | 2.99±0.11 | 9.0 |

### 6.2.4. Thermal properties of Fe-Zr powders

In order to understand the phase transformation induced by heat treatment and to determine crystallization temperature ($T_{crys}$), DSC curves of all the powder samples were recorded at different constant heating rates. Fig.6.11 shows the typical DSC curve for $x$ = 30 at.% sample recorded at a heating rate of 20 K/min. The endothermic baseline shift at 610 K denotes the relaxation of the samples and the exothermic peak near 803 K signifies the on-set of crystallization. The inset in the figure shows the DSC curves in the region close to $T_{crys}$ for all the samples investigated. The crystallization behavior is strongly dependent on the composition of the Fe-Zr amorphous alloys and involves polymorphic transformation to one or more phases. The crystallizing phase might be bcc Fe, $Fe_2Zr$, $Fe_3Zr$, or a combination of these, depending upon the Zr concentration [GORR2002]. The well-defined exothermic peak can be considered to be an evidence of the compositional homogeneity of the milled powders [MEHR1991]. This observation is also supported by the EDS data obtained on these samples. The enthalpy released during the crystallization process shows an increasing trend with Zr concentration. This can be attributed to the enhancement in the reactivity of the samples induced by the applied stress as a function of Zr concentration. DSC curves recorded on the heating cycle revealed that the peak temperature, $T_{crys}$, shifts as a function of heating rate $\alpha$, which indicates a thermally activated process. This behavior was used to calculate the activation energy, $E_A$, of the crystallization using Kissinger's relation [KISS1956],

$$ln\left(\frac{T_{crys}^2}{\alpha}\right) = \frac{E_A}{RT} + C \qquad (6.1)$$

where R is a universal gas constant and C is a constant. The calculated values of $E_A$ (listed in table 6.1) increased from 1.91 *eV/atom* to 2.98 *eV/atom* as the Zr concentration increased from 20 to 25 at.% and then remained constant for higher Zr concentrations. Since the activation energy is a measure of the inhibition to the thermally induced process, higher values of $E_A$ signify that the crystallization is less favored in the samples with higher Zr concentration. In other words, the stability of the amorphous phase increases with higher Zr concentration. Thermal behavior of the mechanically alloyed samples is similar to the case of melt-spun ribbons of Fe rich compositions. However, $T_{crys}$ of the powder samples are slightly higher than those of the ribbon samples [ZARU1992]. This might be due to the higher stability of the amorphous phase and/or large amount of strain present in the as-milled powders. $E_A$ values obtained in this

work may be compared with the value of 2.93 *eV/atom* reported by Um *et al*. [UMCY2005] for $Fe_{91}Zr_7B_2$ ribbons.

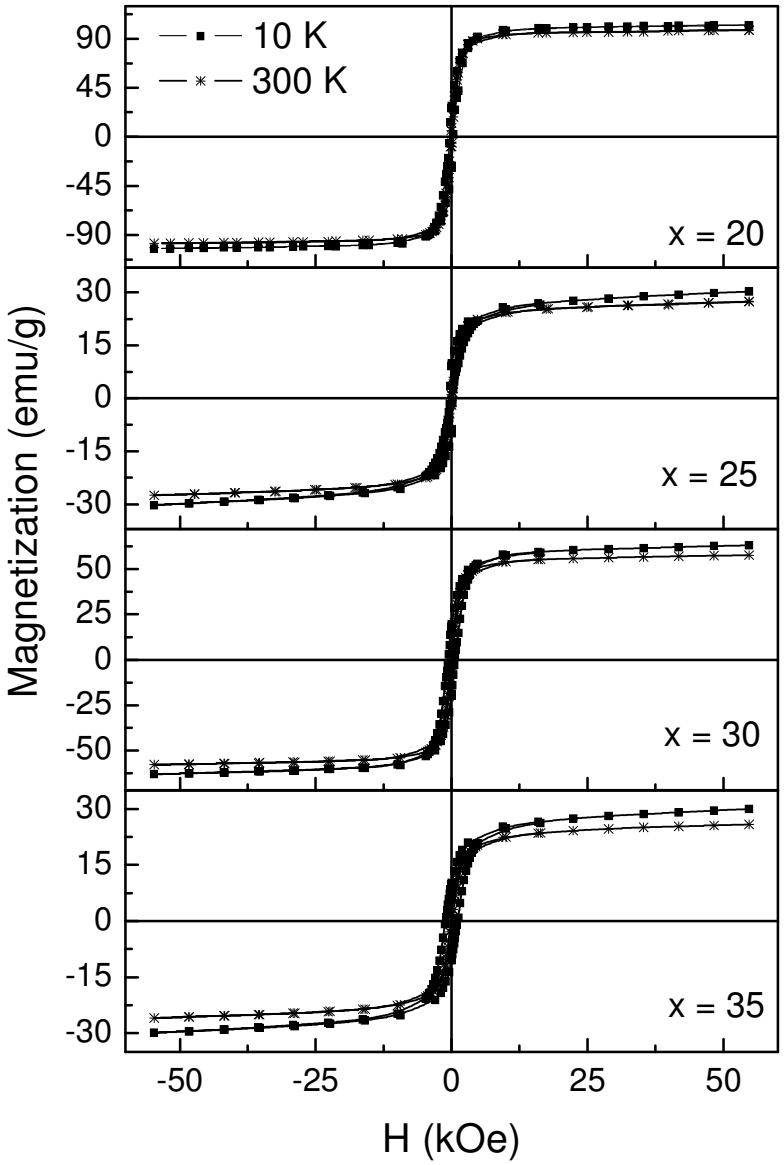


*FIG. 6.12: Magnetic hysteresis loops of as-milled $Fe_{100-x}Zr_x$ ($20 \leq x \leq 35$) alloy powders taken at 10 K and 300 K.*

### 6.2.5. Magnetic properties of Fe-Zr powders

*M – H* loops recorded at 10 K and 300 K for $Fe_{100-x}Zr_x$ ($20 \leq x \leq 35$) samples are shown in Fig. 6.12. The magnetization increases rapidly at lower applied fields followed by a linear increase at high fields. *M – H* loops do not saturate up to an applied field of 55 kOe. The tendency to resist

saturation at 55 kOe increases as the Zr concentration is increased in the samples. $M_S$ values were determined by fitting the experimental high-field magnetization curve to the law of approach to saturation. This procedure also provides information about the effective anisotropy in the system. In general, the magnetization is expressed as a function of applied magnetic field [HERZ1980] using the relation:

$$M = M_S\left(1 - \frac{a}{\sqrt{H}} - \frac{b}{H^2} - ..\right) + \chi_p H \qquad (6.2)$$

where, $H$ is applied field, $\chi_p$ is high-field susceptibility originating from the increase in the number of spins which have the same direction in a domain, and $a$, $b$ are constant coefficients. The coefficient $b$ is related to the effective anisotropy ($K_{\text{eff}}$). The $a/\sqrt{H}$ term arises from point-like defects and intrinsic magnetostatic fluctuations [KRON1979], while the term $b/H^2$ is attributed to magnetoelastic interaction. Stresses accumulated in the powders can cause stress anisotropy *via* magnetoelastic coupling. A least squares fitting procedure was carried out to fit the experimental magnetization data obtained at 300 K and 10 K. $M_S$ values obtained at 300 K and 10 K are plotted as a function of Zr composition in Fig.6.13a. $M_S$ values are less than 110 emu/g for all the samples, which is well below the $M_S$ of pure Fe (= 220 emu/g), and somewhat lower than the value of 120 emu/g reported for mechanically alloyed powders [GRAB2007]. Moreover, the relative increase of magnetization between 10 K and 300 K at 55 kOe is 4 % for $Fe_{80}Zr_{20}$ sample, which increases to 19 % for $Fe_{65}Zr_{35}$ sample. The obtained value of high-field susceptibility is small (Fig.6.13c) and has a magnitude of $10^{-7}$, suggesting that only a small number of spins have the same orientation in a given domain. These observations are consistent with a non-collinear spin arrangement arising due to the co-existence of finite topological disorder (resulting from the MA process) and frustration of magnetic interaction (resulting from the change in the Fe-Fe atomic distance with Zr concentration) [ZHAN2000]. The coefficients of the higher order terms are quite small and contributed only to a slight deviation of the magnetization curves in the measured range of the magnetic field. $K_{\text{eff}}$ was calculated from the constant coefficient $b$ using the following relation [XION2001]:

$$K_{eff} = \sqrt{\frac{105\, b\, \mu_0^2\, M_S^2}{8}} \qquad (6.3)$$

and depicted in Fig.6.13d. With increasing Zr substitution, $K_{eff}$ values show an oscillatory behavior as observed in $M_S$. The oscillatory behavior of $K_{eff}$ is the result of a correlation between

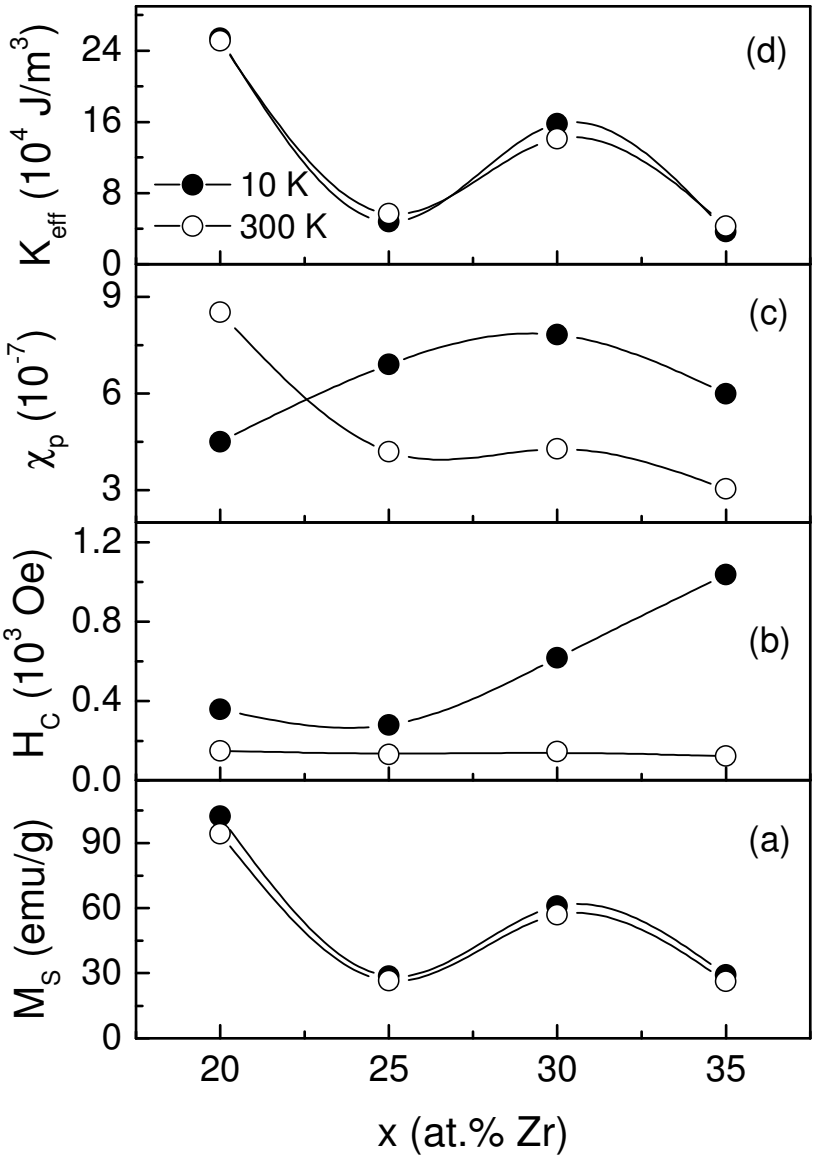


*FIG. 6.13: Variations of saturation magnetization, coercivity, high-field susceptibility, and effective anisotropy with Zr substitution in as-milled $Fe_{100-x}Zr_x$ ($20 \leq x \leq 35$) alloy powders.*

$M_S$ and $K_{eff}$. However, it is important to note that the value of $K_{eff}$ is one order higher than that of bulk Fe ($4.14\times10^4$ J/m$^3$). $H_C$ of the powder obtained at 300 K is almost composition independent, but the $H_C$ at 10 K increases with increased Zr substitution (Fig.6.13b). $H_C$ values are quite large due to the presence of large amount of strain resulting from the plastic deformation induced during the milling process [LIUB2006, ZHOU1999].

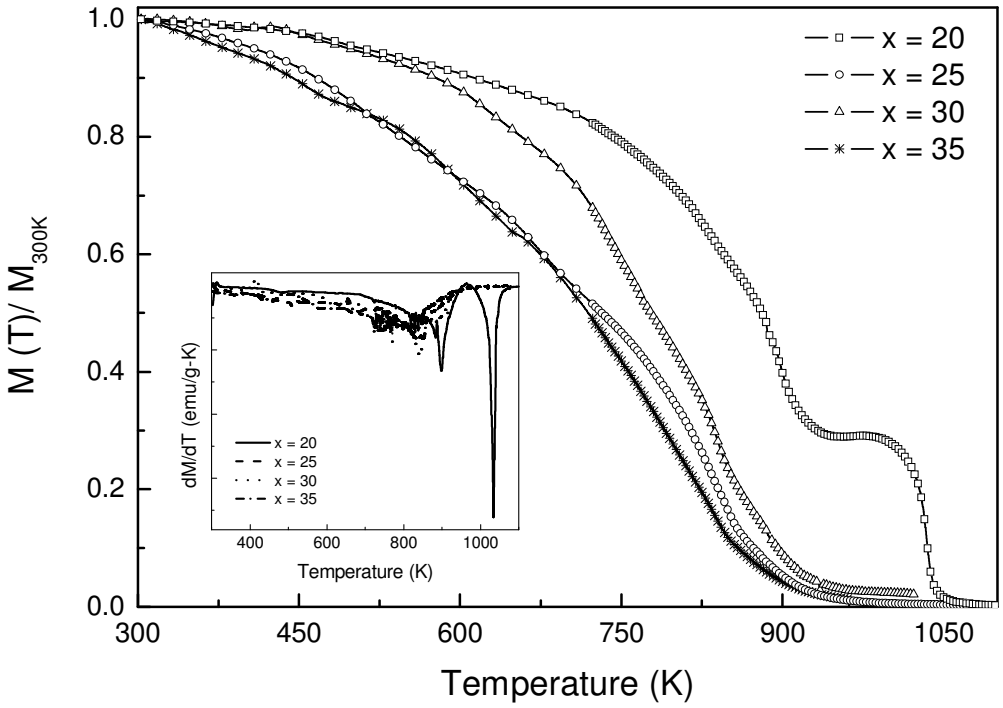


*FIG. 6.14: M – T curves measured at 1 kOe applied field. Inset: Thermal derivative of magnetization as a function of temperature for as-milled $Fe_{100-x}Zr_x$ (x = 20 – 35 at.%) alloy powders.*

Thermomagnetization (*M* – *T*) measurement was carried out up to 1100 K under 1 kOe applied field for as-milled $Fe_{100-x}Zr_x$ powders and the corresponding data are presented in Fig.6.14. In order to accommodate all the *M* – *T* curves and to compare them directly, normalized magnetization with respect to the room temperature magnetization [$M(T)/M_{300K}$] of the corresponding samples is plotted on the *y*-axis. The inset in Fig.6.14 shows the derivative of *M* – *T* for all the samples to identify the magnetic phase transition temperature(s). With increasing temperature, all the samples show a similar variation of magnetization with temperature except for $Fe_{80}Zr_{20}$ sample. The $Fe_{80}Zr_{20}$ sample clearly shows two magnetic phase transitions: one at 898 K and another at 1033 K. These two magnetic phase transitions represent the presence of both amorphous and non-equilibrium solid solution phases in this sample, as described in Fig.6.09. While the first magnetic phase transition at 898 K corresponds to the FM to paramagnetic (PM) phase transition (Curie temperature, $T_C$) in the amorphous phase, the second transition could be attributed to the FM to PM phase transition in Fe rich non-equilibrium

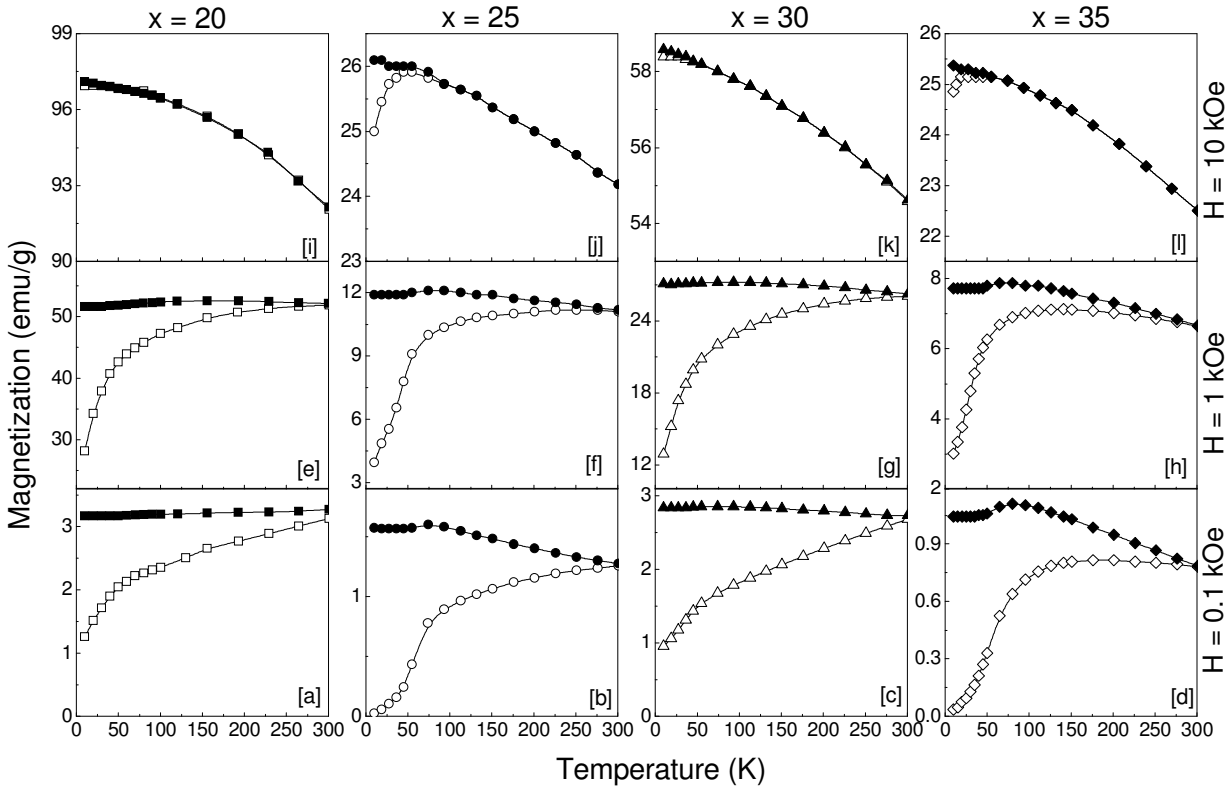


*FIG. 6.15: Temperature dependent ZFC (open symbols) and FC (solid symbols) curves of the as-milled $Fe_{100-x}Zr_x$ ($20 \leq x \leq 35$) alloy powders measured at different applied magnetic fields.*

solid solution. $T_C$ value decreases to about 843 K when Zr is increased from 20 to 25 at.% and then remains almost constant up to 35 at.% Zr. It can also be observed from Fig.6.14 that the manner in which $M - T$ decreases is not smooth. This might be due to the release of the stresses with increasing temperature. It is important to note that these Fe-Zr milled powders exhibit high $T_C$ despite having low average magnetic moment at room temperature. Also, the $T_C$ of these samples is higher than those of amorphous alloys of similar compositions prepared by the melt–spinning technique. Such a difference in $T_C$ could be due to the presence of large internal stresses accumulated during MA process and the existence of finite antiferromagnetic (AFM) sites in FM matrix. As described earlier, the effective anisotropy caused by the induced stresses from the MA process is larger and facilitates improvement of the stability of the local magnetic structure with long range magnetic ordering via magnetoelastic coupling [GAOY2003, MCHE1999]. In addition, the presence of fluctuations of concentration and exchange integral have also considerable effect on the higher $T_C$, as described in an earlier report of micromagnetic theory of

phase transition [GAOY2003]. The increase of $T_C$ on the applied stress has been reported in a similar (FeZrCuB) system [SUNO2007]. Internal stress is a consequence of the milling process, while the existence of finite AFM sites in FM matrix can result from a change in the average Fe atomic distance. Both these factors could have efficiently contributed to the high magnetic stability in these alloy powders and hence the high $T_C$.

To understand the nature of the magnetic behavior as a function of temperature in the as-milled $Fe_{100-x}Zr_x$ ($20 \leq x \leq 35$) powders, low temperature $M - T$ measurement was carried out at different external applied fields ($H$ = 0.1, 1 and 10 kOe) and the data obtained are displayed in Fig.6.15. In the temperature dependent magnetization measurements, the sample was initially cooled to 4.2 K under zero-field condition. Magnetization was then recorded as the sample was heated to room temperature under a constant applied field [Zero-field cooled (ZFC) process]. Subsequently, the sample was cooled in the same constant applied field to 4.2 K and then the magnetization was recorded as the sample was heated to room temperature [Field-cooled (FC) process]. The ZFC and FC data taken at 0.1 kOe are distinctly different up to room temperature for all the compositions. This observation in the as-milled powders is quite different from the behavior reported in ribbon samples of Fe rich Fe-Zr compositions [KAUL1992]. Moreover, with increasing applied field, the bifurcation temperature, which is the temperature at which the ZFC and FC data deviate from each other, decreases for all the samples. For the sample with $x$ = 20 at.%, the bifurcation temperature was not discernible at 10 kOe applied field, while the samples with $x > 20$ at.% show the presence of clear bifurcation temperature even at an applied field of 10 kOe. The decrease of bifurcation temperature with the increase of applied field indicates the existence of considerable amount of interaction between the particles. This conclusion is in agreement with our SEM results (Fig.6.10) which showed that $Fe_{80}Zr_{20}$ sample is in the form of aggregates with a typical dimension of 10 μm. Thus, each aggregate, on an average, consists of approximately $10^9$ interacting nanoparticles. The number of such interacting nanoparticles decreases with increasing Zr concentration as a consequence of the formation of the amorphous phase. Also, the nature of the $M - T$ curves is strongly dependent on the applied magnetic field. This emphasizes the energy differences among distinct equilibrium spin configurations. These results correlate well with the notion of co-existence of strong FM interaction and finite AFM coupling, as evident from the non-saturating $M - H$ loops obtained up to 55 kOe applied field.

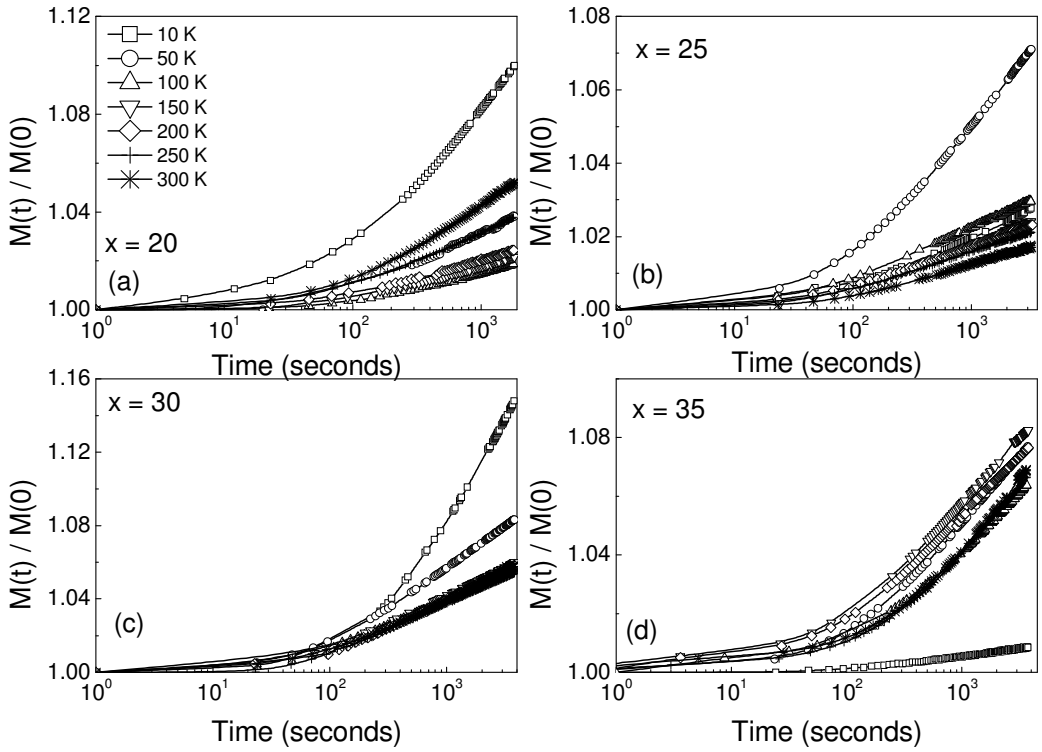


*FIG. 6.16: Magnetic relaxation curves of the as-milled $Fe_{100-x}Zr_x$ ($20 \leq x \leq 35$) alloy powders taken at different temperatures under ZFC condition.*

Magnetic relaxation curves were obtained after cooling the samples to 4.2 K under ZFC condition and then applying a constant field of 0.1 kOe. Fig.6.16 shows the magnetic relaxation curves of all the as-milled $Fe_{100-x}Zr_x$ ($20 \leq x \leq 35$) powders as a function of temperature. In order to facilitate the comparison between magnetic relaxation curves taken at different temperatures, the normalized magnetization, $M(t)/M(0)$, was plotted in semi-logarithmic scale. $M(0)$ is the magnetization value of the first recorded data after time $t$ = 1 s and $M(t)$ is the magnetization value taken as a function of time $t$. The final magnetization data at each temperature was taken after 3600 s. It is interesting to note that all the samples show slow relaxation of magnetization at 300 K. This slow process exhibits an increasing trend with decreasing temperature. The mean slopes at longer time scales of the relaxation curves are positive. For the sample with $x$ = 20 (30) at.%, the mean slope of the curves decreases up to 100 K and then increases (or remains constant) with increasing temperature. This behavior might be due to the increase of temperature dependent magnetization from the non-equilibrium state (*cf.*

ZFC curves in Figs.6.15a and c), since the magnetization in these samples does not reach its

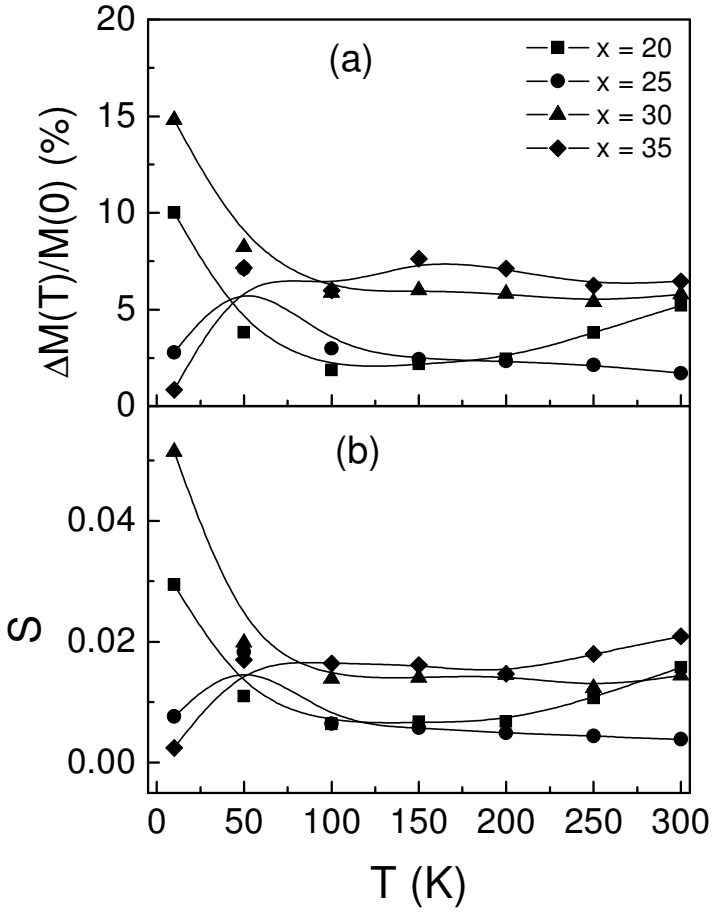


*FIG. 6.17: Variation of fractional change of magnetization and coefficient of magnetic viscosity with temperature for as-milled $Fe_{100-x}Zr_x$ ($20 \leq x \leq 35$) alloy powders.*

equilibrium level at 4.2 K. On the other hand, the sample with $x$ = 25 (35) at.% shows a rapid increase of the mean slope initially up to 50 K and then decreases (or remains constant) with increasing temperature. This is due to the increase of magnetization from nearly equilibrium state at 4.2 K (*cf.* ZFC curves in Figs.6.13b and d). It may be noted that for all the investigated samples, the maximum mean slope was observed in the temperature region in which the ZFC magnetization increases rapidly. The fractional change between the final and first relaxation data, *viz.*, $\Delta M(t)/M(0) = [M(t)-M(0)]/M(0)$, measured at different temperatures for samples with various Zr concentration is shown in Fig.6.17a. The observed variation of fractional change is similar to the mean slope variation in these samples with a maximum of 15 % and 10 % for $x$ = 30 and 20 at.% samples, respectively. The qualitative behavior of magnetic relaxation could be

understood by considering the increase in thermal energy, which stimulates the alignment of spin and consequently increases the magnetization under ZFC condition with increasing temperature.

The magnetic relaxation curves at longer time scale approximately follow the logarithmic law [LIUY2006],

$$\frac{M(t)}{M(t_n)} = 1 + S\, ln\left(\frac{t}{t_n}\right) \tag{6.4}$$

where $S$ is magnetic viscosity, $t_n$ and $M(t_n)$ are the normalization time and the corresponding magnetization at that moment, respectively. The least squares fitting procedure was carried out on all the magnetic relaxation curves using eqn.(6.4) by considering $S$ as the only free variable parameter in the fitting function. Fig.6.17b shows the variation of $S$ with temperature for all the as-milled Fe-Zr powders. This figure displays the main relaxation results of all the samples. The error bars associated with the fitting are smaller than the symbols used in all the cases and the continuous solid lines are merely a guide to the eyes. Note that both the fractional change of magnetization and the magnetic viscosity show similar temperature dependent behavior. The logarithmic magnetic relaxation behavior has been observed in various magnetic materials [CORN2002, MAMI2002] including spin-glass and fine FM particles [LABA1993, PROZ1999] and attributed to (i) the existence of a distribution of energy barriers separating local minima in the free energy, which corresponds to different equilibrium states [MYDO1993], and (ii) the presence of an energy landscape $E$ for the domain walls with a broad distribution of energy barriers around the mean value $\overline{E}$. In the presently investigated samples, the presence of strong FM and finite AFM couplings leads to magnetic frustration. An earlier report [FOLD1991] has claimed that the value of $S$ could be assumed to be proportional to $k_BT/U$, i.e., the magnetic viscosity is expected to have two competing energy factors: (i) the thermal energy, and (ii) an effective pinning energy of the spin system. Thus, the variation of magnetization with time at different temperatures must be due to the thermal activation of domain or domain walls over the free energy barriers, resulting in slow relaxation in the amorphous materials [GARC2005, SCHA1996]. In addition, the magnetic relaxation is affected by the presence of mechanical stress. Stresses invariably present in mechanically alloyed powders induce an effective anisotropy which influences the energy of the domain walls and, hence the intensity of the interaction with the pinning centers. This argument is supported by the observation that the

samples ($x$ = 20 and 30 at.%) with large effective anisotropy show large fractional change in the magnetization and high $S$ as compared to the other samples ($x$ = 25 and 35 at.%).

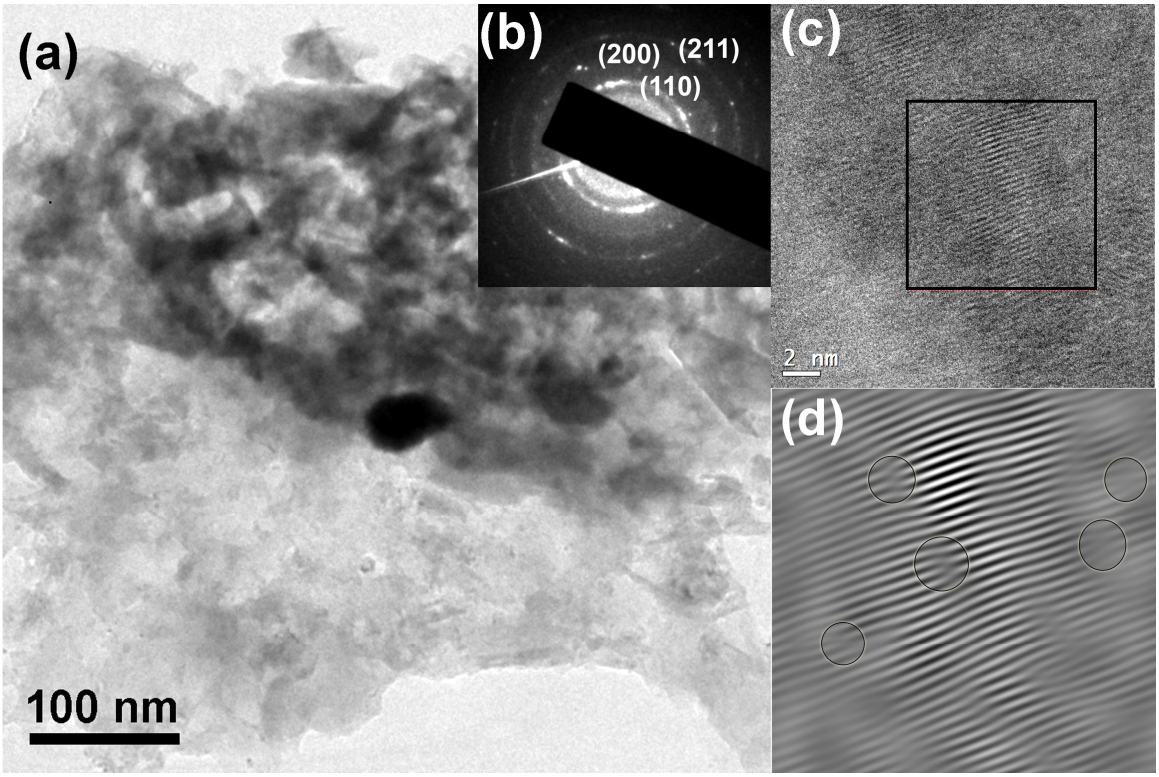


*FIG. 6.18: (a) Bright field TEM image, (b) SAED pattern, (c) HR-TEM image, and (d) iFFT image of the milled $Fe_{80}Zr_{20}$ alloy powder.*

### 6.2.6. Exchange coupling effect in Fe-Zr powders

$Fe_{80}Zr_{20}$ alloy powder milled for 60 hours exhibits two-phase microstructure having 8 – 10 nm sized fine nanocrystals embedded in a FM amorphous matrix. In order to understand the exchange coupling between the nanocrystals through the amorphous phase, temperature dependent magnetic properties were measured and analyzed.

Fig.6.18 shows the bright field TEM image, SAED pattern, HR-TEM image and inverse Fast Fourier Transform (iFFT) image of the HR-TEM image of as-milled $Fe_{80}Zr_{20}$ powder. The bright field image shows the fine-grain structure, which is a typical characteristic of MA powder. SAED pattern shows diffraction rings corresponding to (110), (200) and (211) planes of Fe(Zr) solid solution and a halo ring due to the Zr rich amorphous phase. HR-TEM image supports the presence of nanometer sized (~8 nm) crystallites with a high degree of strain. To analyze the existence of defects and dislocations, HR-TEM image was resolved by iFFT method and

depicted in Fig.6.18d. The presence of dislocations is highlighted by circles. These results confirm the formation of highly strained nanostructures embedded in an amorphous matrix after

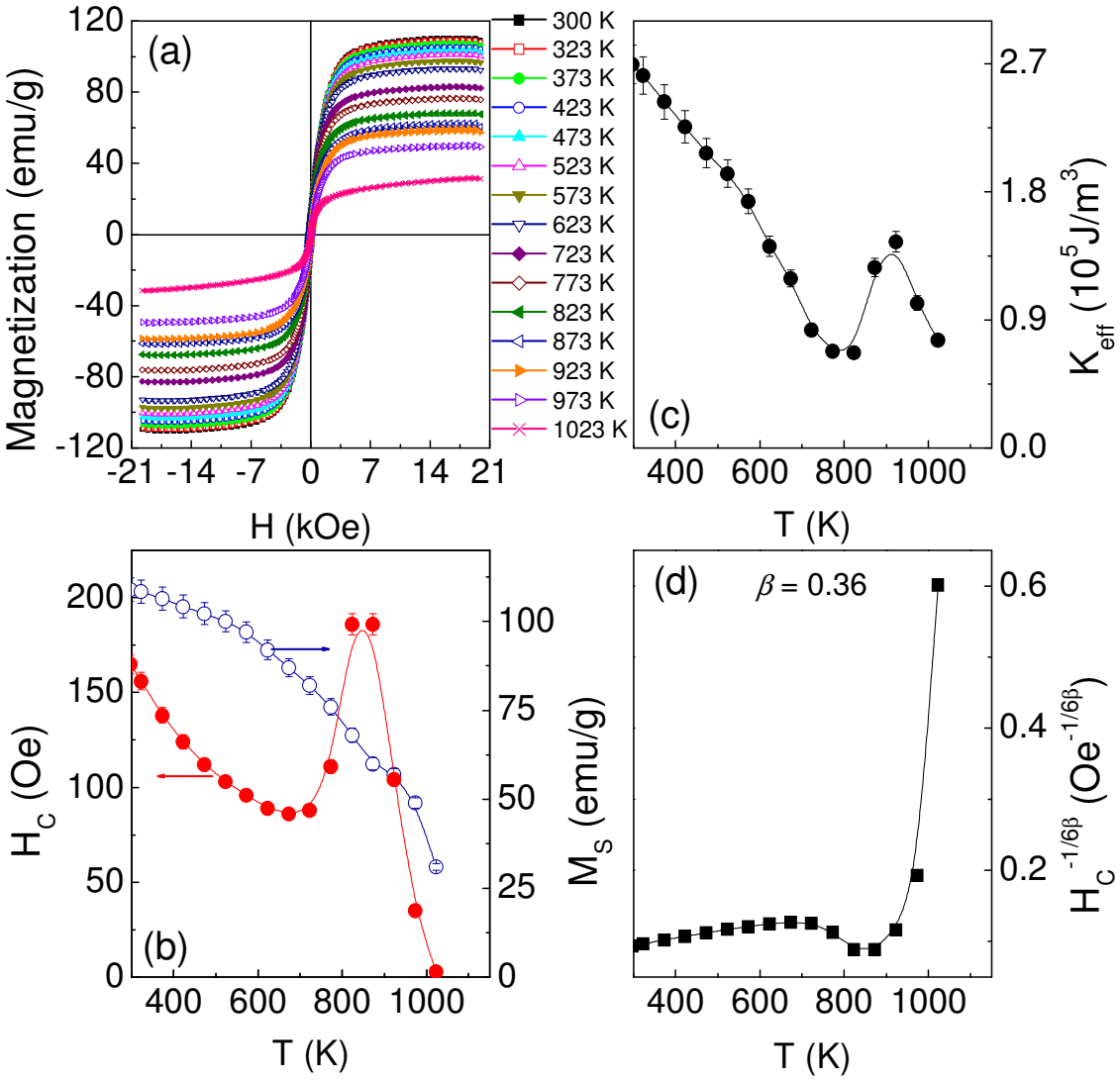


*FIG. 6.19: (a) M – H loops at different temperatures, (b) variation of $H_C(T)$ and $M_S(T)$ with temperature, (c) variation of $K_{eff}$ with temperature, and (d) Plot of the coercivity to the power (-1/6β) (β=0.36) versus temperature for the milled $Fe_{80}Zr_{20}$ alloy powder.*

60 h of milling. To understand the nature of the high temperature magnetic behavior of $Fe_{80}Zr_{20}$ powder, *M – H* loops were obtained at different temperatures between 300 and 1100 K, which are depicted in Fig.6.19a. The extracted values of $H_C$ and $M_S$ at different temperatures are shown in Fig.6.19b. $H_C$ decreases initially from 160 to 80 Oe and shows a rapid increase to 200 Oe around 823 K, followed by a large decrease at higher temperatures. A large value of $H_C$ at 300 K

might result from the accumulation of stress centers in the powder in the form of defects and dislocations in the nanocrystals [LIUB2006, MIST2000], while the magnetic hardening close to the $T_C$ of the amorphous phase ($T_{C,A}$) is mainly due to the loss of FM coupling between the nanocrystallites through the amorphous matrix. Such behavior has been observed in a variety of nanocrystalline systems [HERN1994, HERN1998, SUZU1998]. However, all the earlier reports were solely on melt spun ribbon samples, in which the stresses result in an effective anisotropy ($K_{eff}$) of $10^3$ $Jm^{-3}$. In the present samples, the as-milled powder has an high amount of stresses and hence both magnetoelastic and structural anisotropies would contribute to $K_{eff}$ [HERN1995]. It is well-known that $H_C$ ($=\alpha.K_{eff}/M_S$, where $\alpha$ is a constant) of a magnetic material depends on both $M_S$ and $K_{eff}$. $K_{eff}$ was calculated using eqn.(6.3). The values of $M_S$(T) obtained from the fitting procedure (Fig.6.19b) decrease gradually with increasing the temperature, suggesting that $H_C$ should vary linearly with $1/M_S$ over the entire range. This confirms that $M_S$(T) cannot be responsible for a drastic increase in the values of $H_C$ close to $T_{C,A}$. The values of $K_{eff}$(T) calculated from eqn.(6.3) are depicted in Fig.6.19c. Interestingly, the variations of $K_{eff}$(T) show a behavior similar to the one observed in the $H_C$(T) versus $T$ plot, indicating that the $H_C(T)$ is mainly controlled by the variation of the stress-induced $K_{eff}$. In addition, the value of $K_{eff}$ is one order higher than that of bulk Fe ($4.14\times10^4$ $J/m^3$). To analyze the effect of $A_{ex}$ on the $H_C$ behavior, $H_C$(T) has been plotted using the power law model [SUZU1998],

$$H_C(T) \propto \left(T_{C,A} - T\right)^{-6\beta} \qquad (6.5)$$

where, $\beta$ is critical exponent. According to this model, the $K_{eff}$ in the nanocrystalline materials is governed by $A_{ex}^{-3}$ around $T_{C,A}$. The plot in Fig.6.19d shows a linear variation up to $T_{C,A}$, followed by a drastic increase at higher temperatures, suggesting that the magnetic hardening around $T_{C,A}$ is due to the disappearance of the intergranular exchange coupling through the amorphous matrix. Hence, the variation of $H_C(T)$ is mainly due to the variations of $K_{eff}$ and the $A_{ex}$ of the presently studied system.

## 6.3. Mechanical alloying of Fe-Zr-B powders

### 6.3.1. Structural properties of Fe-Zr-B powders

$Fe_{65-y}Zr_{35}B_y$ ($y$ = 0 – 10) alloy powders were milled to get amorphous structure. Fig.6.20 shows HR-TEM images taken at slightly off-focused condition and SAED patterns of a-$Fe_{65-y}Zr_{35}B_y$ alloy powders with $y$ = 5 and 10. SAED pattern has only diffused rings confirming the

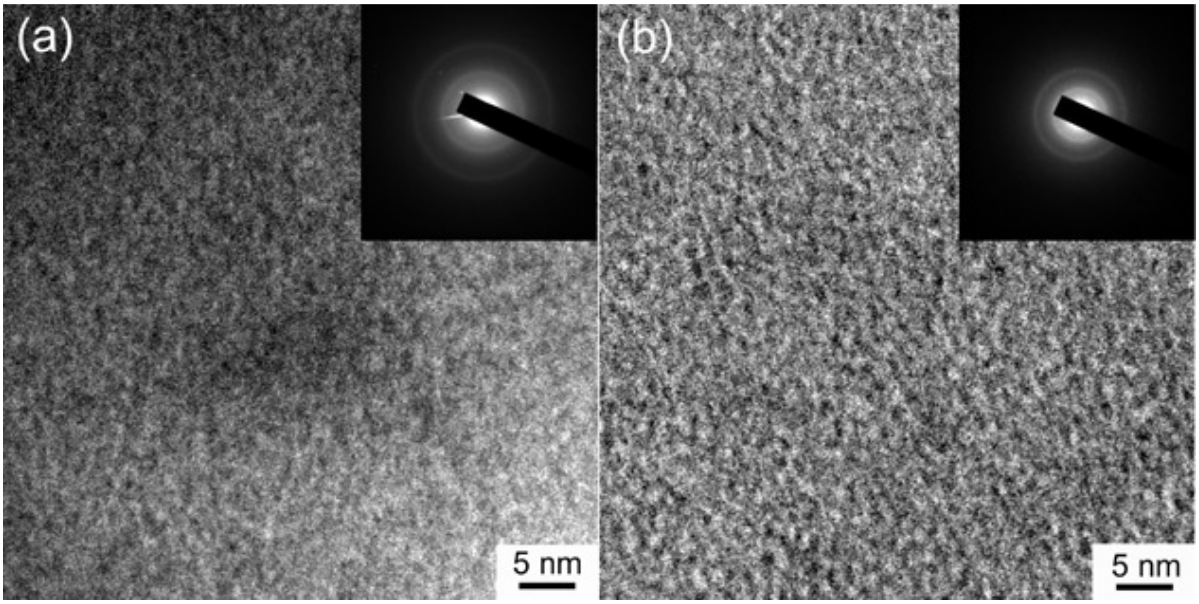


*FIG. 6.20: HR-TEM images and SAED patterns of amorphous $Fe_{65-y}Zr_{35}B_y$ alloy powders with (a) y = 5 and (b) 10.*

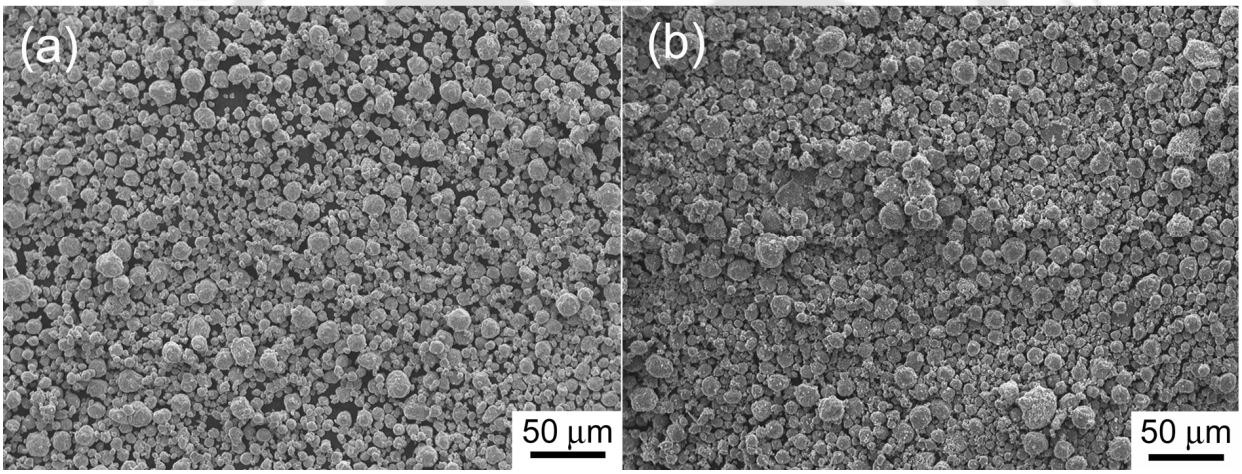


*FIG. 6.21: SEM micrographs of amorphous $Fe_{65-y}Zr_{35}B_y$ alloy powders with (a) y = 5, (b) 10.*

amorphous nature of the milled powder. Also, no crystals were observed in the HR-TEM images. This confirms that the B substituted Fe-Zr-B powders exhibit single-phase amorphous structure. Similar features have been observed in all other compositions studied in the present work. Fig.6.21 displays the surface morphology of the $Fe_{65-y}Zr_{35}B_y$ powders with $y$ = 5 and 10 observed using SEM. The shape of the agglomerated particles are spherical and the average particle size resulting from aggregation increases from about 2 µm to 13 µm with increasing B content up to 10 at.%. Also, the flake shaped agglomerated particles were observed in the case of powders with $y$ = 10.

### 6.3.2. Thermal properties of Fe-Zr-B powders

The stability of the amorphous structure with B addition was investigated using DSC. Fig.6.22 depicts the DSC curves obtained at 20 K/min heating rate for the $Fe_{65-y}Zr_{35}B_y$ powders with $y = 0$

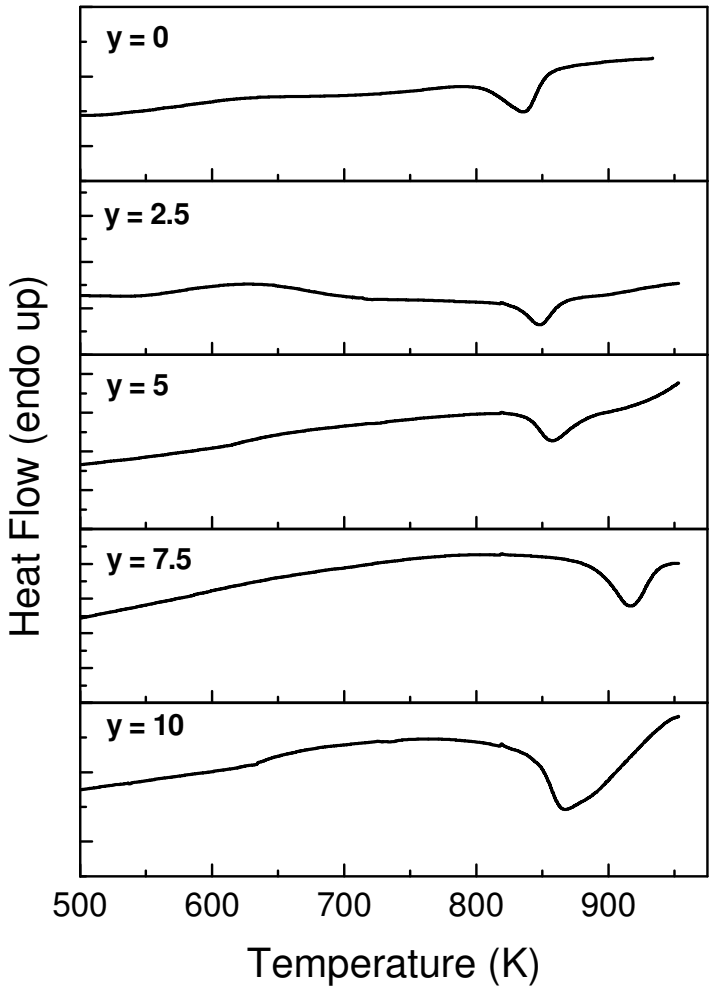


*FIG. 6.22: DSC curves obtained at 20 K/min heating rate for amorphous $Fe_{65-y}Zr_{35}B_y$ alloy powders.*

– 10. The extracted parameters from the DSC curves are listed in Table 2. It could be clearly seen from the table that the peak $T_{crys}$ increases with increasing B addition up to 7.5 at.% and then decreases with the further increase in B (see Fig.6.23d). This suggests that the stability of the amorphous structure increases with addition of B up to a critical concentration of 7.5 at.% B. This is in good agreement with the earlier reports on similar systems [HUAN2008, MAJU2007]. However, with the addition of B, $T_{crys}$ increases much faster in the milled powders compared to

the ribbon samples. $T_{crys}$ of ball milled Fe-Zr-B-Cu alloy is relatively low (750 K) [PERE2007] when compared to that of the currently investigated alloy. This may be due to the difference in the composition of the alloy systems.

Table 6.2: Peak crystallization temperature, activation energy, and enthalpy of a-$Fe_{65-y}Zr_{35}B_y$ ($0 \leq y \leq 10$) alloy powders.

| Sample | Peak $T_{crys}$ (K) | Activation energy, $E_A$ (eV/atom) ± 0.09 | Enthalpy (ΔH) released (J/g) |
|---|---|---|---|
| $Fe_{65}Zr_{35}$ | 836 | 2.99 | 9.0 |
| $Fe_{62.5}Zr_{35}B_{2.5}$ | 848 | 2.71 | 21 |
| $Fe_{60}Zr_{35}B_5$ | 857 | 2.47 | 25 |
| $Fe_{57.5}Zr_{35}B_{7.5}$ | 910 | 2.18 | 46 |
| $Fe_{55}Zr_{35}B_{10}$ | 867 | 2.29 | 120 |

### 6.3.3. Magnetic properties of Fe-Zr-B powders

Fig.6.23a shows the room temperature $M - H$ loops for the a-$Fe_{65-y}Zr_{35}B_y$ ($0 \leq y \leq 10$) alloy powders. The extracted values of $H_C$ and $M_S$ from $M - H$ loops are shown in Figs.6.23b and c, respectively. All the $M - H$ loops shown in Fig.6.23a depict the typical nature of soft magnetic materials. $M_S$ and $H_C$ show a rapid increase in their values for the sample with $y$ = 7.5. These results suggest a close correlation between the stability of the amorphous phase and the room temperature magnetic properties. Similar behavior has also been reported in melt spun ribbons [YAOB2004]. The increase in magnetization with the addition of B is a result of an increase in the local magnetic moment of Fe. $H_C$ value obtained in the present study is higher than that of melt spun amorphous alloy of similar alloy systems [YAOB2004]. This may be due to the different synthesis route adopted for the preparation of materials. Fig.6.24 shows the $M - T$ curves of a-$Fe_{65-y}Zr_{35}B_y$ ($0 \leq y \leq 10$) powders under different applied fields ($H$ = 0.1 kOe, 1.0 kOe, 10 kOe). The nature of the $M - T$ curves depicts a strong dependence on the applied magnetic field and behavior similar to that of the binary Fe-Zr alloys (sec. 6.2.5). With increasing applied field, the bifurcation point between the FC and ZFC curves shifts to lower temperature and disappears at higher applied fields. Furthermore, the addition of B also shifts the bifurcation point to lower temperature. The bifurcation point observed at 35 K for $Fe_{65}Zr_{35}$

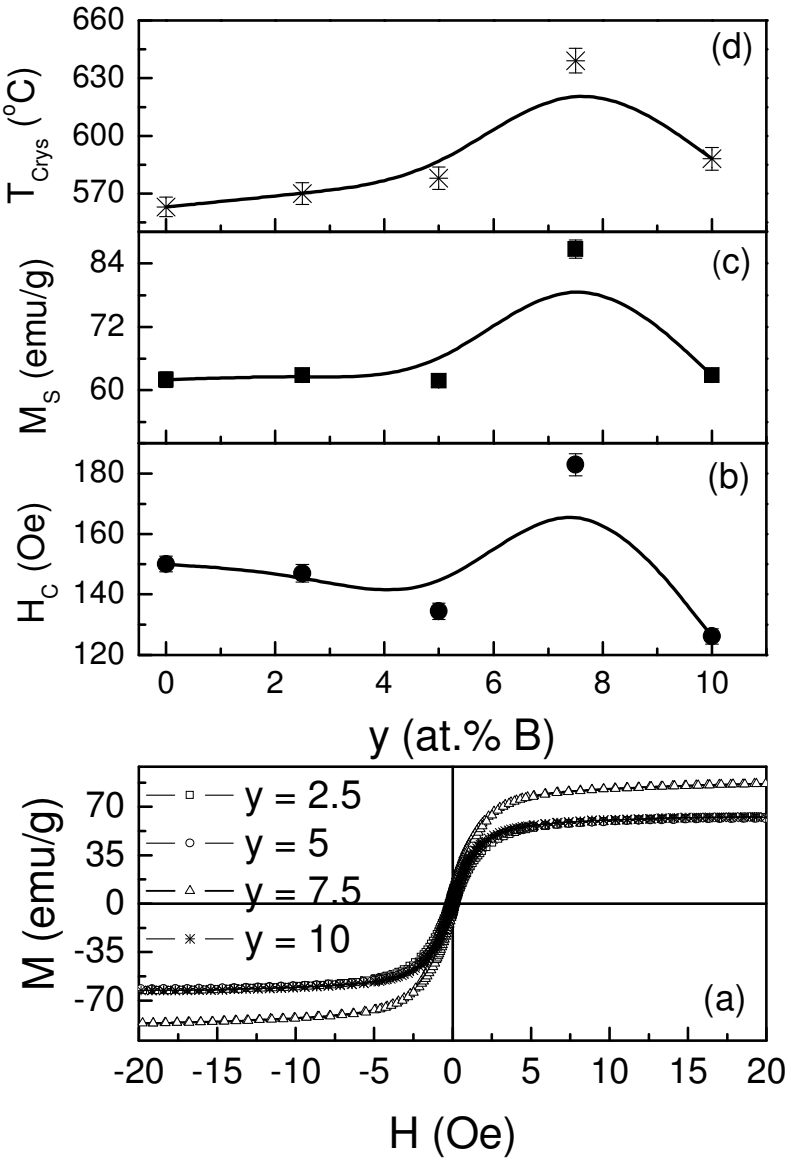


*FIG. 6.23: (a) Room temperature M – H loops and variations of (b) coercivity ($H_C$), (c) saturation magnetization ($M_S$) and (d) crystallization temperature ($T_{crys}$) of $Fe_{65-y}Zr_{35}B_y$ amorphous alloy powders.*

decreases to 20 K for $Fe_{62.5}Zr_{35}B_{2.5}$ and disappears eventually for further increase of B content at 10 kOe applied field. This suggests that the effective anisotropy decreases and FM properties enhances with the addition of B. Fig.6.25 shows the high temperature *M – T* curves a-$Fe_{65-y}Zr_{35}B_y$ ($0 \leq y \leq 10$) powders recorded at 100 Oe applied field. With increasing temperature, all the samples show a similar variation of magnetization with temperature. However, $T_C$ value increases significantly from 790 K to 850 K for the increase of B from 0 to 7.5 at.% in a-$Fe_{65-}$

$_{y}Zr_{35}B_{y}$ alloy powders. This also confirms the enhancement of FM properties with B addition in a-$Fe_{65-y}Zr_{35}B_{y}$ alloy powders.

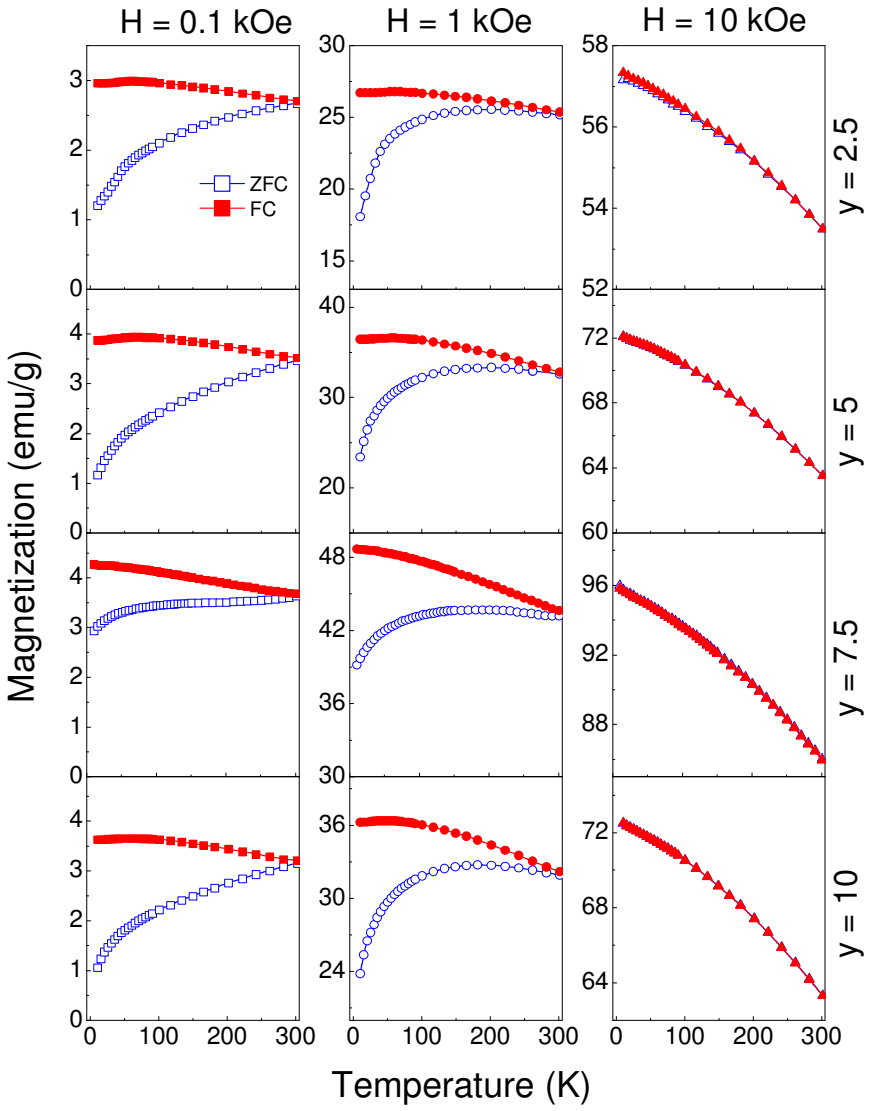


*FIG. 6.24: Temperature dependent ZFC (open symbols) and FC (solid symbols) curves of the amorphous $Fe_{65-y}Zr_{35}B_{y}$ alloy powders measured at different applied magnetic fields.*

## 6.4. Mechanical alloying of Fe-Mn-Zr-B powders

### 6.4.1. Structural properties of Fe-Mn-Zr-B powders

$Fe_{60-z}Mn_{z}Zr_{35}B_{5}$ (z = 0 – 20) alloy powders were milled continuously to get amorphous structure. Fig.6.26 shows the plane-view bright-field TEM images and SAED patterns of $Fe_{60-z}Mn_{z}Zr_{35}B_{5}$ alloy powders. The plane-view micrographs show the fine particle structure with the average

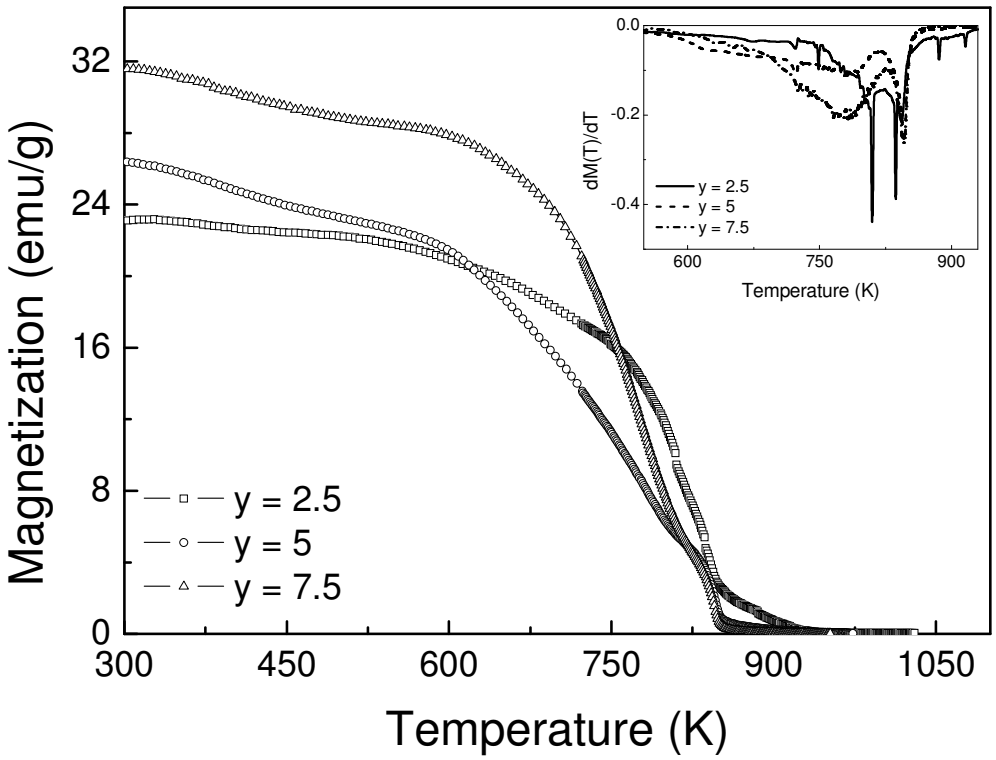


*FIG. 6.25: M – T curves measured at 100 Oe applied field. Inset: Thermal derivative of magnetization as a function of temperature for amorphous $Fe_{65-y}Zr_{35}B_y$ alloy powders.*

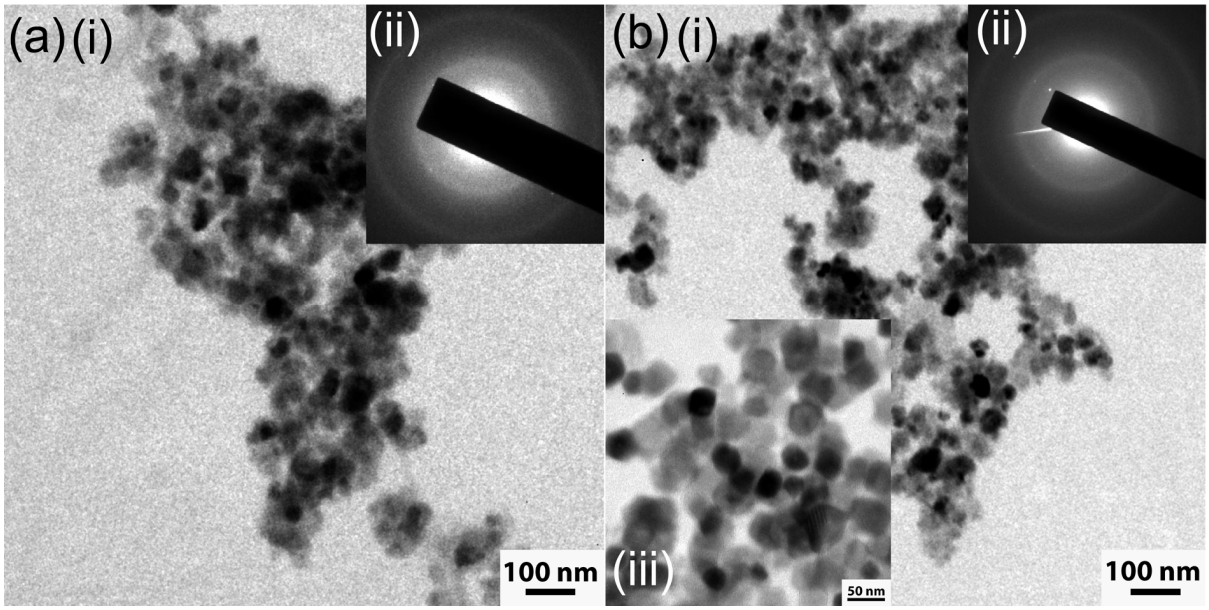


*FIG. 6.26: Bright-field TEM images and SAED patterns of amorphous $Fe_{60-z}Mn_zZr_{35}B_5$ alloy powders with (a) z = 5 and (b) 15.*

particle size of 40 nm for the sample with $z$ = 5, which decreases to 12 nm for the sample with $z$

= 15 and remains almost constant in samples with higher *z*. The SAED patterns depicted in inset of Fig.6.26 show diffused halo rings, confirming the amorphous structure of the powders. The vitrification ability in the $Fe_{60-z}Mn_zZr_{35}B_5$ alloy powders can be understood from many different factors such as large atomic size ratios, attractive bonding nature between the constituent elements and difficulty of redistribution of these elements for crystallization [SURY2000, KOCH1997]. Cheng et al reported that the amorphous Fe-Zr ball milled powders has particle size below 50 nm [CHEN2006]. Earlier report by Hasiak et al using Mossbauer technique suggested that the substitution of 3 at.% Zr by Mn in Fe-Zr-B alloys improves the microstructure of the alloy [HASI2003]. To understand the surface morphology of the a-$Fe_{60-z}Mn_zZr_{35}B_5$ alloy powders with Mn addition, SEM micrographs were obtained and shown in Fig.6.27. All the samples show almost similar surface morphology and the shape of the agglomerated particles is spherical. This is in good agreement with the earlier report on similar systems prepared by MA technique [RICO2008, MEDI2006]. The spherical nature could be attributed to the fact that Mn acts as a partitioning element in the amorphous matrix and controls the atomic reorganization

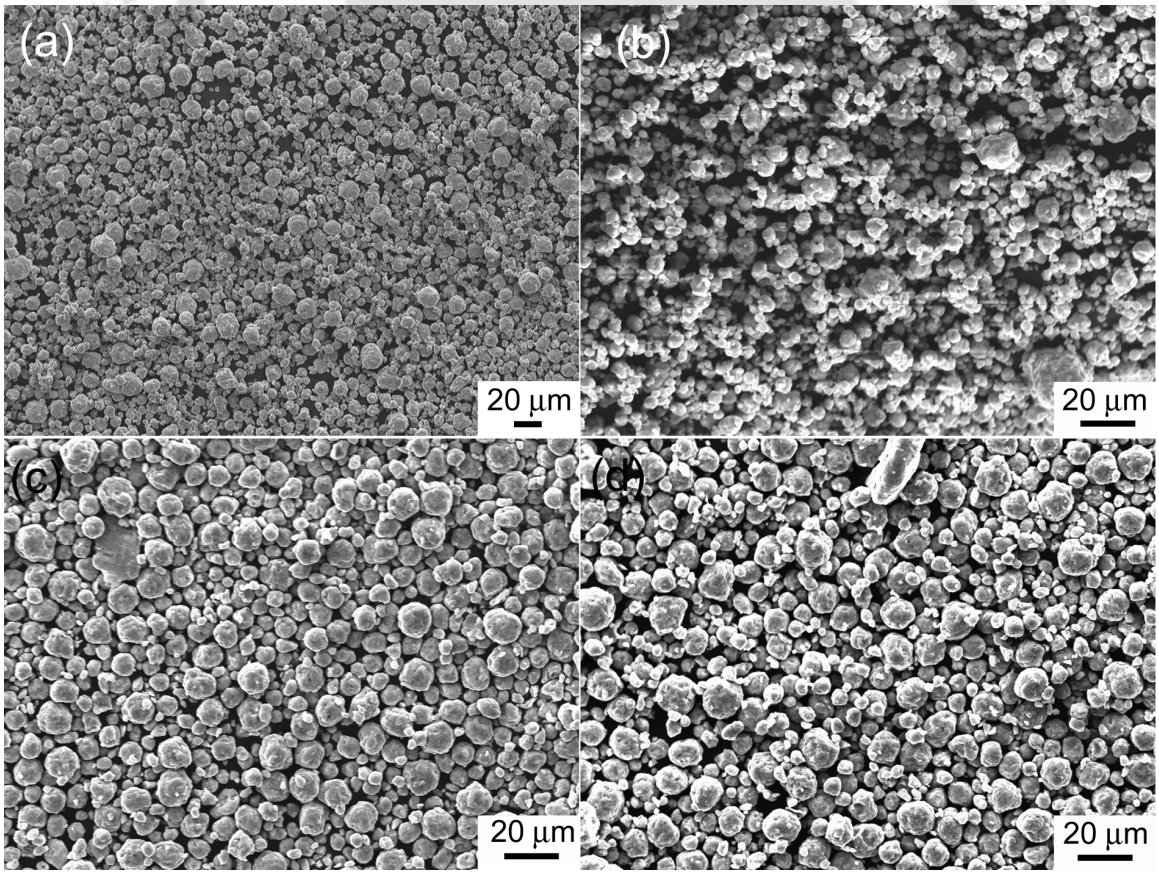


*FIG. 6.27: SEM micrographs of amorphous $Fe_{60-z}Mn_zZr_{35}B_5$ alloy powders with (a) z = 0, (b) 5, (c) 10 and (d) 15.*

[HASI2003, KIMK2007]. The average agglomerated particle size decreases initially to 2 µm for the addition of 5 at.% Mn and then increases to about 10 µm for sample with 10 at.% Mn. With further increase in Mn content to 20 at.%, the agglomerated particle size remains constant. The presence of spherical particles suggests that the stress has become more uniform throughout the matrix.

### 6.4.2. Thermal properties of Fe-Mn-Zr-B powders

Thermal stability of the amorphous phase with Mn addition in a-$Fe_{60-z}Mn_zZr_{35}B_5$ alloy powders was investigated using DSC. DSC curves for the a-$Fe_{60-z}Mn_zZr_{35}B_5$ sample were recorded at a heating rate of 20 K/min and peak $T_{crys}$ was extracted from DSC curves. The values of $T_{crys}$ increase from 857 K to 890 K with the addition of Mn from 0 to 10 at.%. Due to the limitation in the DSC apparatus, $T_{crys}$ values for a-$Fe_{60-z}Mn_zZr_{35}B_5$ alloy powders with $z > 10$ could not be determined. It is however evident that the substitution of Mn in a-$Fe_{60-z}Mn_zZr_{35}B_5$ enhances the thermal stability of the amorphous phase. These results are in good agreement with the reports on similar systems [BAYR2009, BENA2008].

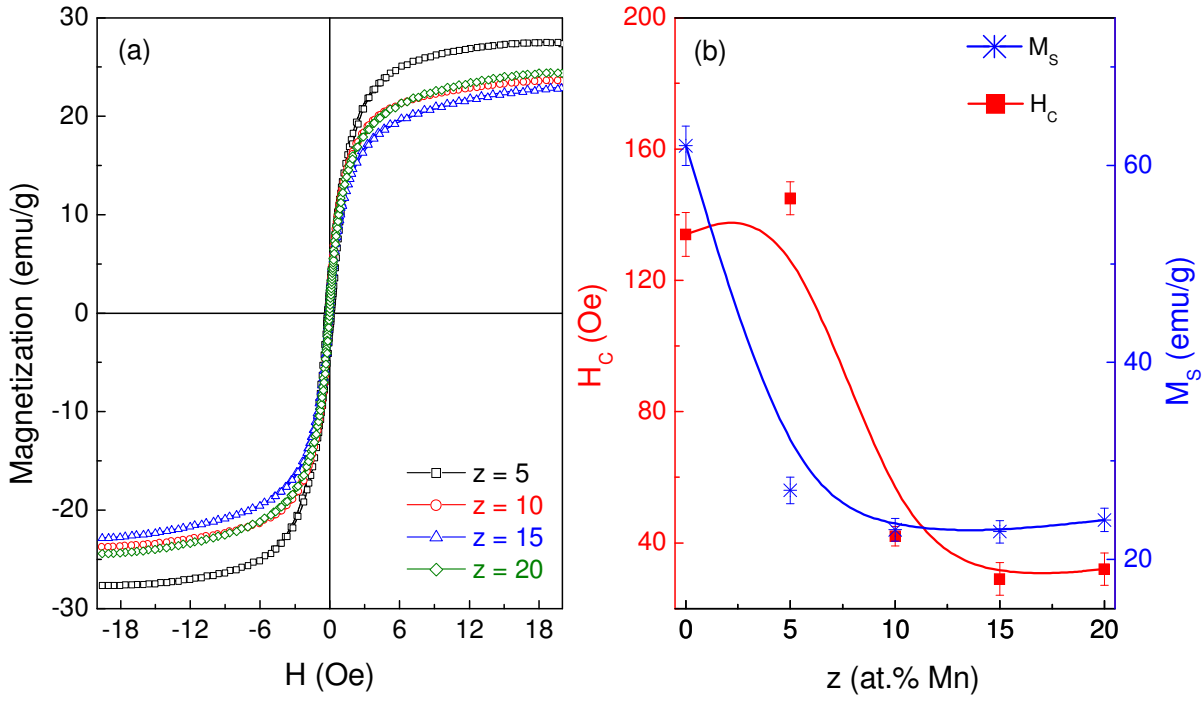


*FIG. 6.28: (a) Room temperature M – H loops and (b) variations of coercivity and saturation magnetization of amorphous $Fe_{60-z}Mn_zZr_{35}B_5$ alloy powders.*

### 6.4.3. Magnetic properties of Fe-Mn-Zr-B powders

Fig.6.28a shows the $M - H$ loops measured at room temperature for a-$Fe_{60-z}Mn_zZr_{35}B_5$ ($5 \leq z \leq 20$) powders with the maximum applied field of ±20 kOe. $M_S$ values measured at 20 kOe and $H_C$ values extracted from the $M - H$ loops are shown in Fig.6.28b as a function of Mn addition. The magnetization curves do not saturate up to 20 kOe and $M_S$ value decreases sharply for low amounts of Mn and remains constant for subsequent Mn addition. This suggests that the addition of Mn results in the formation of various types of exchange interactions such as Fe-Fe FM, and Fe-Mn and Mn-Mn AFM interactions as has been observed in a similar alloy system prepared by ball milling technique [MEDI2006]. The reduction in magnetic moment has also been seen in similar alloy systems with the substitution of Mn [RICO2008]. In the case of melt-spun Fe-Mn-Zr-B ribbons (see chapter 4), the $M_S$ values decrease almost linearly with increasing Mn content.

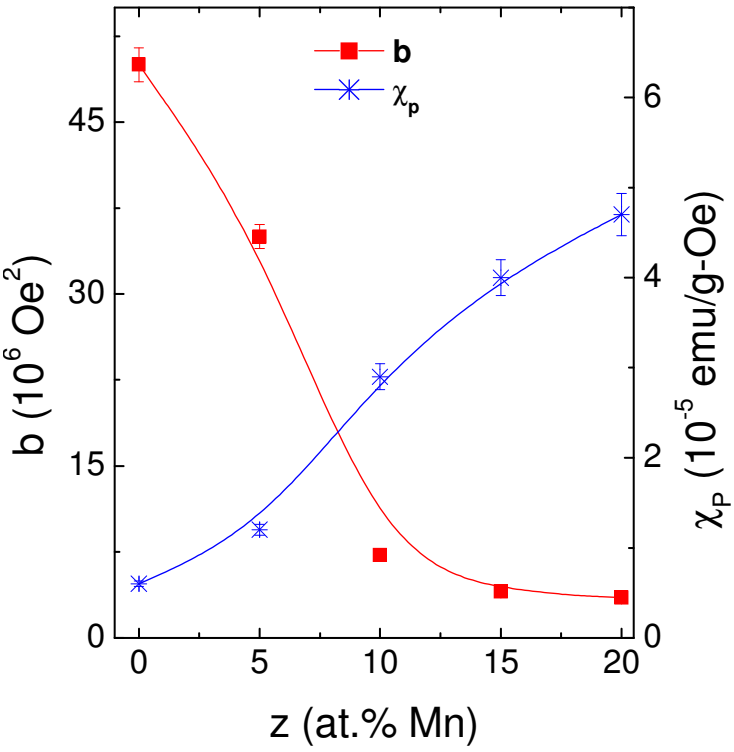


*FIG. 6.29: Variations of constant b and high-field susceptibility with Mn substitution for amorphous $Fe_{60-z}Mn_zZr_{35}B_5$ alloy powders.*

Fig.6.28b also shows that $H_C$ decreases sharply from 145 Oe for $z$ = 5 case to 25 Oe for $z$ = 20 case. Though it is known that $H_C$ values in mechanically alloyed powder decreases with

increasing Mn substitution [RICO2008], a large decrease in $H_C$ with Mn substitution has been observed for the first time in the present work. The decrease in $H_C$ can be attributed to (i) effect of agglomerated powder size and (ii) effect of anisotropy (structural and/or magnetoelastic). Recent reports on Fe based alloy powders [TORR2009, HERN2004] prepared by ball milling technique have suggested that $H_C$ reduces considerably with larger particle size. In mechanically alloyed powders, the fluctuations of local spin density and effective anisotropy are considerably high when compared to melt-spun ribbons. Therefore, it is expected that these parameters greatly affect the magnetic free energy of the system so as to considerably modify the approach to saturation. In order to determine the effective local anisotropy, the magnetization curves were fitted using eqn.(6.2). Stresses accumulated in the as-milled powders can cause stress-induced anisotropy *via* magnetoelastic coupling. An earlier study on amorphous Fe-B-Si and Fe-P-C powders shows a linear variation of $H_C$ with stress [SATO1990]. A least squares fitting procedure was carried out to fit the experimental magnetization data obtained at 300 K. Fig.6.29 shows the variations of constant $b$ and $\chi_p$ with Mn substitution. It can be observed that the value of $b$ decreases faster up to $z$ = 10 and then varies slowly with further increase in Mn. On the other hand, the values of $\chi_p$ are initially in the range of $10^{-5}$, gradually increase with increasing Mn substitution. In amorphous alloys, the nonsaturation magnetization behavior may results from the following contributions [KRON2003]:

$$\Delta M = M_S - M(H) = \Delta M_{SW} + \Delta M_{intrin} + \Delta M_{MEC} \qquad (6.6)$$

where, $\Delta M$ is deviation from saturation magnetization, $M(H)$ is the variation of magnetization with the field, $\Delta M_{SW}$ represents the effect of thermally excited spin waves, $\Delta M_{intrin}$ represents the effect of intrinsic materials parameter such as local spin density, local magnetic stray fields resulting from local fluctuations of spin density, $\Delta M_{MEC}$ denotes magnetoelastic coupling energy, resulting from spin inhomogeneities induced by the magnetoelastic coupling energy around the stress sources. In the mechanically alloyed powders, the contributions from stress induced effects are high and hence the contribution from $\Delta M_{MEC}$ is expected to be dominant. The observed results suggest that the magnetic inhomogenities induced by the magnetoelastic coupling energy around the stress sources and short range stresses due to quasi-dislocations dipoles diminish with the addition of Mn. Also, the agglomerated particle size increases with Mn addition. As a result, the effective anisotropy decreases sharply with Mn addition, leading to a decrease in $H_C$ of the powder. The increase of $\chi_p$ is mainly caused by the flipping of weakly coupled AFM spins under

high magnetic field. However it is difficult to estimate exactly the contribution of agglomerated particle size and anisotropy in the present case [HERN2004]. In contrast, Mn substitution in melt-spun ribbons shows a gradual increase in the $H_C$ values with Mn concentration due to the inhomogeneous magnetic mixture of high magnetization clusters through a lower magnetization matrix [KIMK2007]. These results suggest that in addition to the effect of substituting element, the material synthesis route also plays an important role in controlling the development of microstructure and its relation with the magnetic properties.

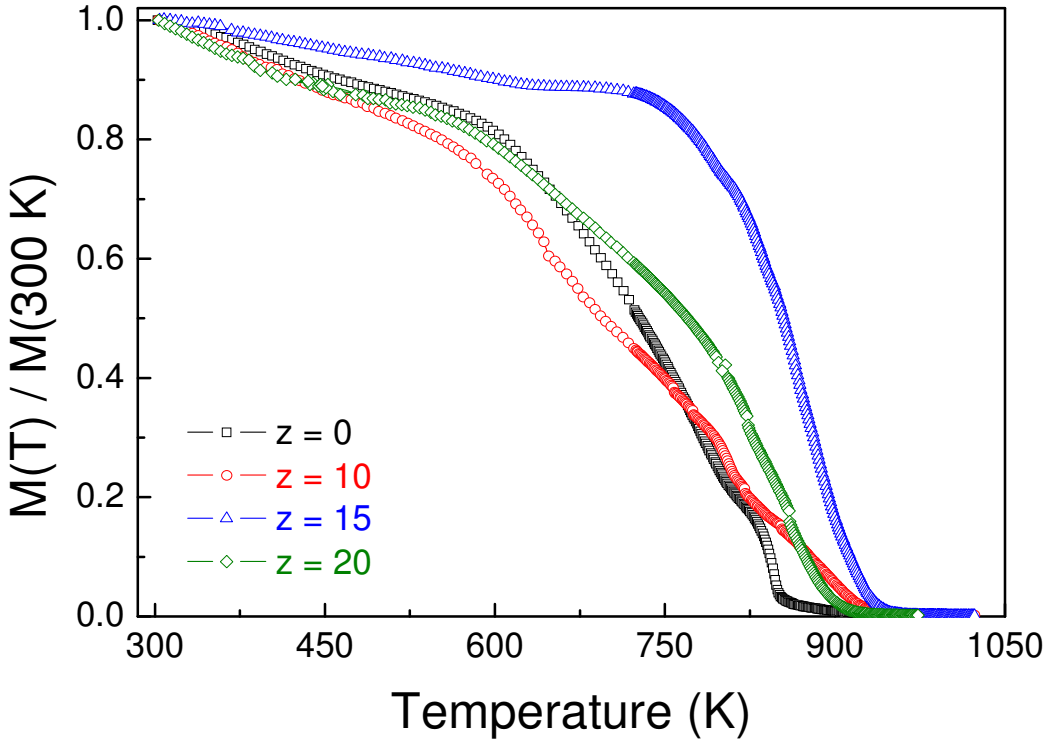


*FIG. 6.30: M – T curves measured at 100 Oe applied field for amorphous $Fe_{60-z}Mn_zZr_{35}B_5$ alloy powders.*

To understand the effect of Mn substitution on the temperature dependent magnetic properties of a-$Fe_{60-x}Mn_xZr_{35}B_5$ powders, $M$ – $T$ measurement was carried out at a constant applied magnetic field of 100 Oe. Fig.6.30 shows the normalized magnetization data as a function of temperature. In order to facilitate comparison between all the curves, the data were normalized with respect to their room temperature magnetization values. For the sample with $z$ = 0, magnetization decreases gradually with increasing temperature and attains zero magnetization value at about 920 K, indicating that the materials magnetically transforms from FM state to PM

state at higher temperatures. $T_C$ value increases from 845 K for the $z = 0$ case to 872 K for the $z = 15$ case, and then decreases to 861 K for the sample with $z = 20$. It is important to note that the as-milled powders exhibit very high $T_C$ [GRAB2007] despite having low magnetic moment at room temperature. Also, the $T_C$ of these samples is much higher than those of amorphous alloys prepared by the melt-spinning technique [KIMK2007]. Such a large difference in $T_C$ could be due to the presence of internal stresses and various types of magnetic interactions. On the other hand, for the sample with $z = 15$, the magnetization curve is nearly flat up to 750 K and then drops to zero value around 950 K, resulting a sharp transition as compared to the other samples.

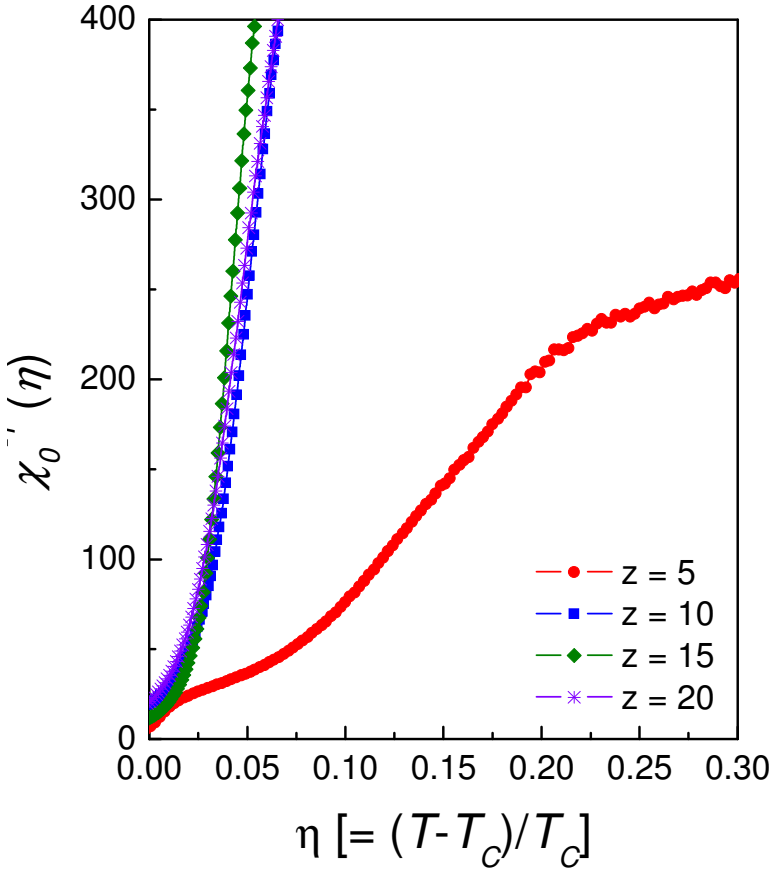


*FIG. 6.31: Plot of $\chi_0^{-1}$ versus reduced temperature, $\eta$ [= $(T - T_C)/T_C$] for amorphous $Fe_{60-z}Mn_zZr_{35}B_5$ alloy powders.*

Also, this sample shows lower coercivity of ~25 Oe at room temperature, indicating that the spatial fluctuations of the exchange coupling due to the magnetic inhomogeneity introduced during the milling process diminishes considerably with the addition of Mn and attains homogeneity both structurally and magnetically at a critical concentration of $z = 15$. This could

be inferred from the fact that Mn addition refines the microstructure and results in spherically shaped interacting nanoparticles. The sharp nature of the magnetic phase transition is a possible manifestation of the homogeneous nature of the alloys. In a homogeneous system, when the temperature approaches $T_C$, the mean size of the spin cluster diverges and then the spins as a whole reacts more cooperatively to give a sharp magnetic phase transition [KRON2003].

In order to confirm the effect of spatial inhomogeneity on the magnetic phase transition of the currently investigated samples, temperature dependent $\chi_0^{-1}$ plots were constructed. Fig.6.31 shows the plot of $\chi_0^{-1}$ versus reduced temperature, $\eta$, [= $(T - T_C)/T_C$] for $Fe_{60-z}Mn_zZr_{35}B_5$ powders with $z$ = 0 – 20. For the case of $z$ = 5, $\chi_0^{-1}$ varies slowly with an upward

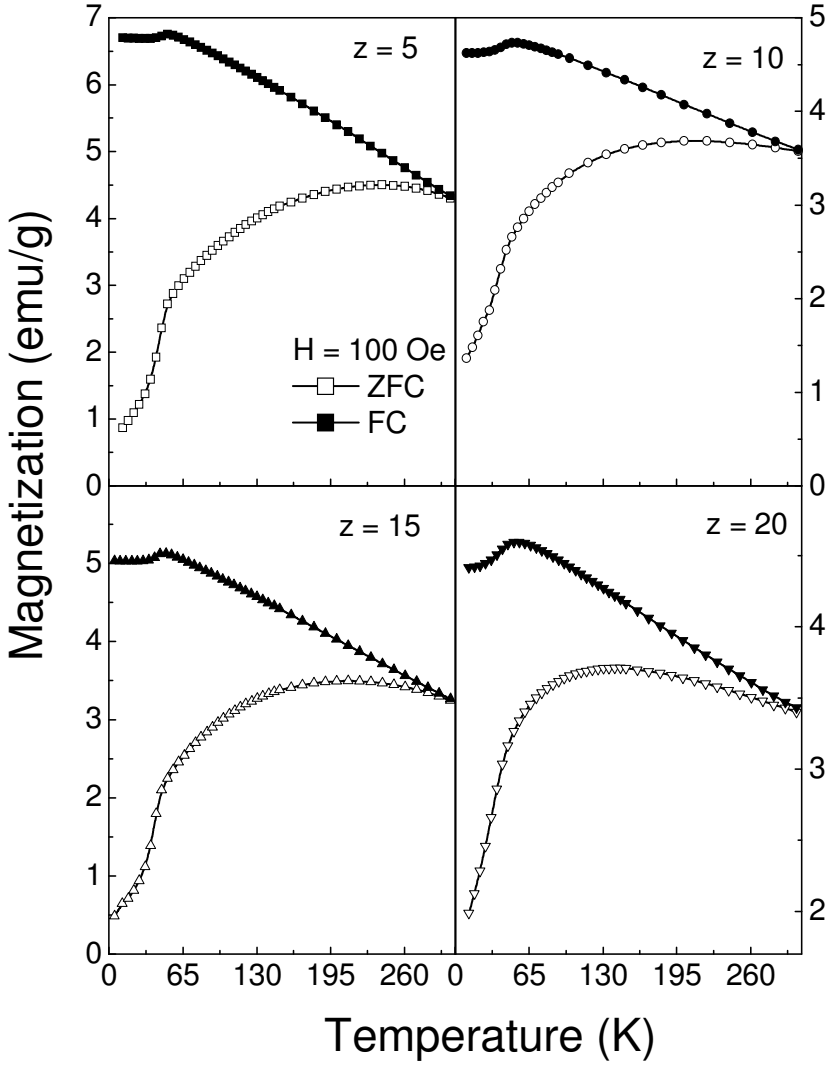


*FIG. 6.32: Temperature dependent ZFC (open symbols) and FC (solid symbols) curves measured at 100 Oe applied magnetic field for amorphous $Fe_{60-z}Mn_zZr_{35}B_5$ alloy powders.*

curve and increases nonlinearly with increasing $\eta$. On the other hand, for the samples with $z$ = 10 – 20, $\chi_0^{-1}$ increases rapidly with $\eta$. According to the correlated molecular field theory, the slow variation of $\chi_0^{-1}$ close to the origin of $\eta$ is due to the (i) nonlinear interactions between the correlated spin fluctuations, and (ii) divergence of spin clusters resulting from spatial fluctuations of the materials parameter with increasing temperature [MASK1976]. However, for the samples with $z$ > 5 at.%, the mean size of the cluster decreases upon increasing temperature and the nonlinear interaction between the correlated spin fluctuations turns out to be small, resulting in a sharp increase in $\chi_0^{-1}$. This suggests that a-$Fe_{60-z}Mn_zZr_{35}B_5$ powders attain homogeneity with increasing Mn concentration. This conclusion is also supported by the rapid reduction in $H_C$ and the $K_{eff}$ constant with increasing Mn content.

Temperature dependent magnetic properties of a-$Fe_{60-z}Mn_zZr_{35}B_5$ powders at low

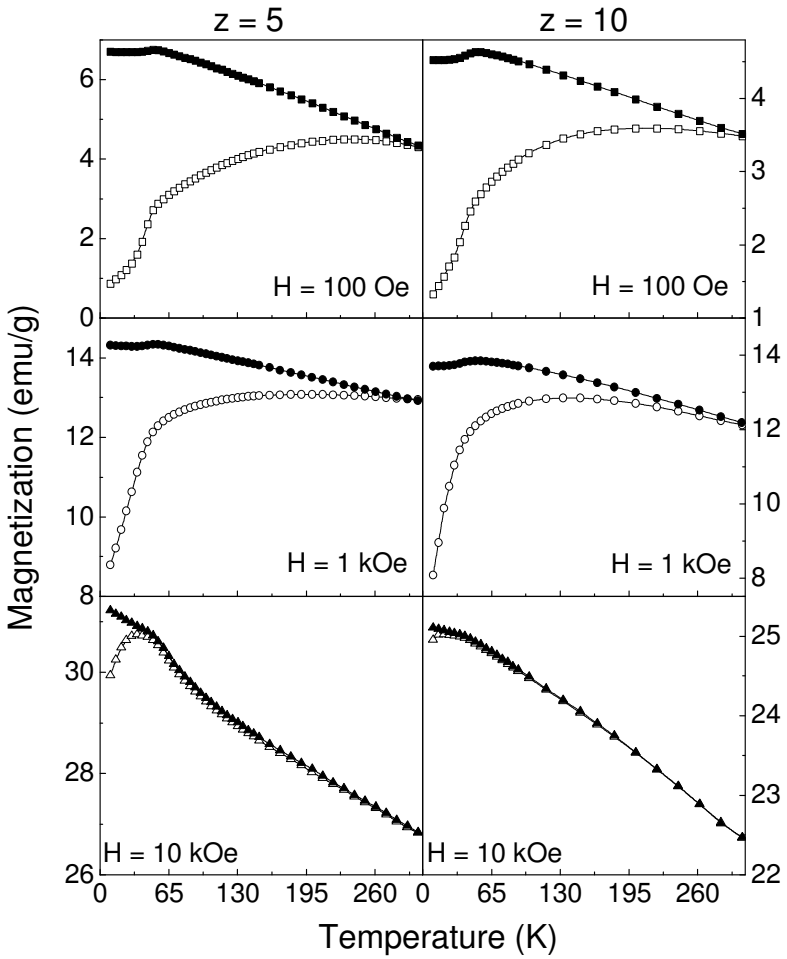


*FIG. 6.33: Temperature dependent ZFC (open symbols) and FC (solid symbols) curves measured at different applied magnetic fields for amorphous $Fe_{60-z}Mn_zZr_{35}B_5$ alloy powders.*

temperature were measured using SQUID magnetometer at different external applied fields ($H$ = 0.1, 1 and 10 kOe). Fig.6.32 shows the $M - T$ curves taken under a constant applied magnetic field of 0.1 kOe. The ZFC and FC curves are quite different up to room temperature for all the compositions. The flattening of FC curve at temperatures below 50 K is an evidence of the presence of strong interactions between the amorphous magnetic nanoparticles [BIAS2002]. Such a behavior has also been observed by Borzi et al in mechanically alloyed powders where interparticle interactions dominate the magnetic behavior [BORZ1999, SLAW2006]. Fig.6.33 shows the $M - T$ curves taken under different applied fields for $z$ = 5 and 10. The bifurcation between the ZFC and FC curves decreases with increasing applied field and does not vanish even up to 10 kOe. Also, with increasing Mn concentration, the bifurcation point shifts to lower temperature and vanishes in samples with high Mn content. This behavior also supports the homogenization of the system with Mn addition.

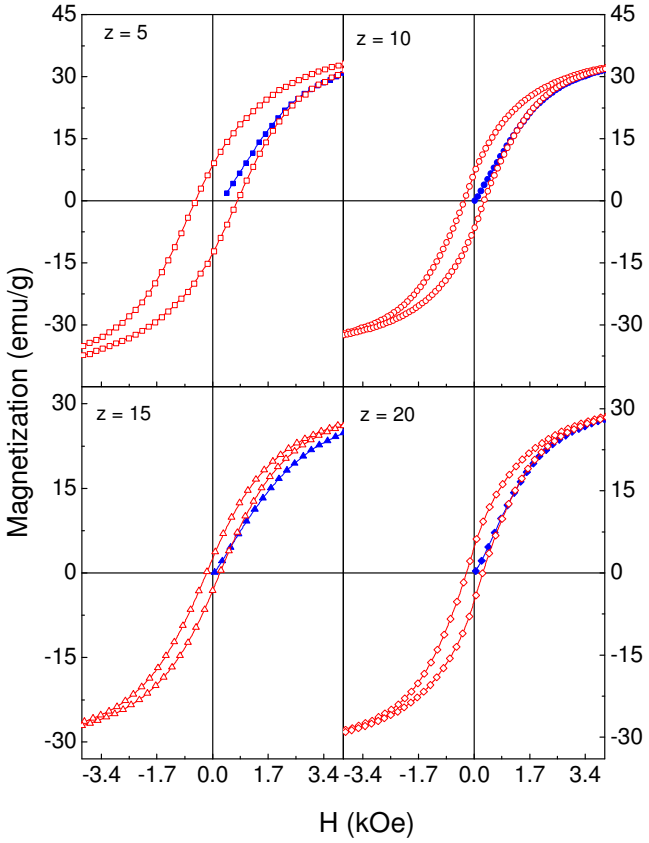


*FIG. 6.34: M – H loops measured at 20 K for amorphous $Fe_{60-z}Mn_zZr_{35}B_5$ alloy powders.*

Fig.6.34 shows the $M - H$ loops of $Fe_{60-z}Mn_zZr_{35}B_5$ powders with $z$ = 0 – 20 taken at 20 K. It is interesting to note that the initial magnetization curves of the $M - H$ loops have different

behaviors for each sample revealing different degree of interparticle interactions in them. With increasing Mn concentration up to $z$ = 10, the virgin (initial) magnetization curves tend to lie below the remagnetized one. It then crosses the remagnetized curves, but lies outside the cycle for a certain field range and finally meets it again at higher fields. With further increasing Mn to 20 at.%, the virgin curve comes back into the regular loop. Such a behavior has been seen in various types of systems such as Ce-Fe-Al [MANE2002], $Fe_2O_3$ [TRON2003], Mn-Si [ROYS2007]. While this behavior in Mn-Si and Ce-Fe-Al-like magnetoresistive materials has been explained on the basis of metamagnetic transition, inter particle interactions are said to play important role in $Fe_2O_3$ and Fe-Ni-B based amorphous nanoparticles. This behavior indicates the enhanced stability of the initial magnetic configuration of the highly interacting particles against the applied magnetic field. This configuration is destroyed by large enough fields and not restored upon demagnetizing. Hence, this should be due to the presence of short-range correlated regions of particle moments forming close magnetic circuits and minimizing the magnetostatic energy [FIOR2002, FIOR2005]. However, the reduction of $H_C$ with increasing Mn substitution suggests that the random pinning of particle moments decreases with Mn content. This brings homogeneity to the amorphous Fe-Mn-Zr-B powders, which results in a sharp magnetic phase transition from FM to PM state as shown earlier. In order to supplement the idea of interparticle interaction through the surface of the nanoparticles, $H_C$ of the sample was measured at different temperatures starting from 20 K to 300 K and is shown in the Fig.6.35.

The nature of the curve is exponential supporting the enhanced surface effect at low temperature. In order to establish this idea a plot between $ln(M.H_C)$ versus $T$ was plotted and is shown in Fig.6.36. According to the domain wall pinning model [BOYX1989], it should be a straight line. However, in the current samples, a good relation between $ln(M.H_C)$ and $T$ exists at two different temperature zones. A linear behavior up to 50 K (70 K) for $z < 10$ ($z \geq 10$) indicates that the $H_C$ variation is dominated by the fluctuations of effective anisotropy due to the wall-pinning mechanism [BOYX1989]. The low temperature sharp increase in $H_C$ can be attributed to a modification of surface properties and interparticle interactions in amorphous nanoparticles, which contribute additional anisotropy to the total effective anisotropy [FIOR2005]. For the alloy with $z$ = 5, the agglomerated particle size is small and hence the surface effect was prominently experienced at lower temperature (50 K) as compared to the samples with higher Mn content (70 K).

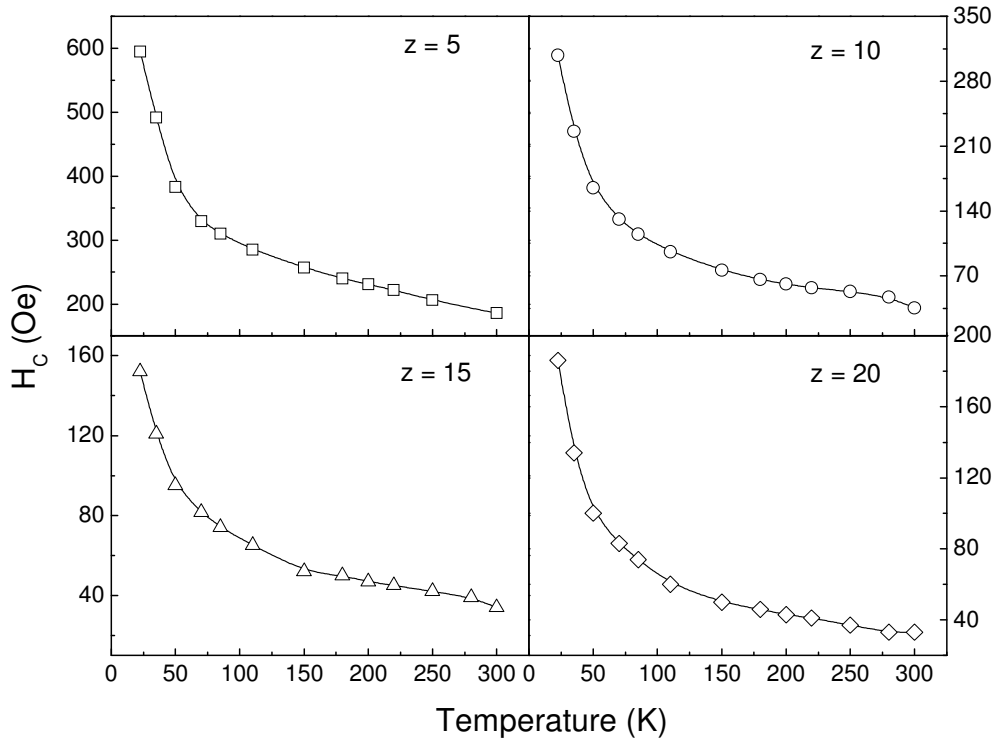


*FIG. 6.35: Coercivity variation with temperature for amorphous $Fe_{60-z}Mn_zZr_{35}B_5$ alloy powders.*

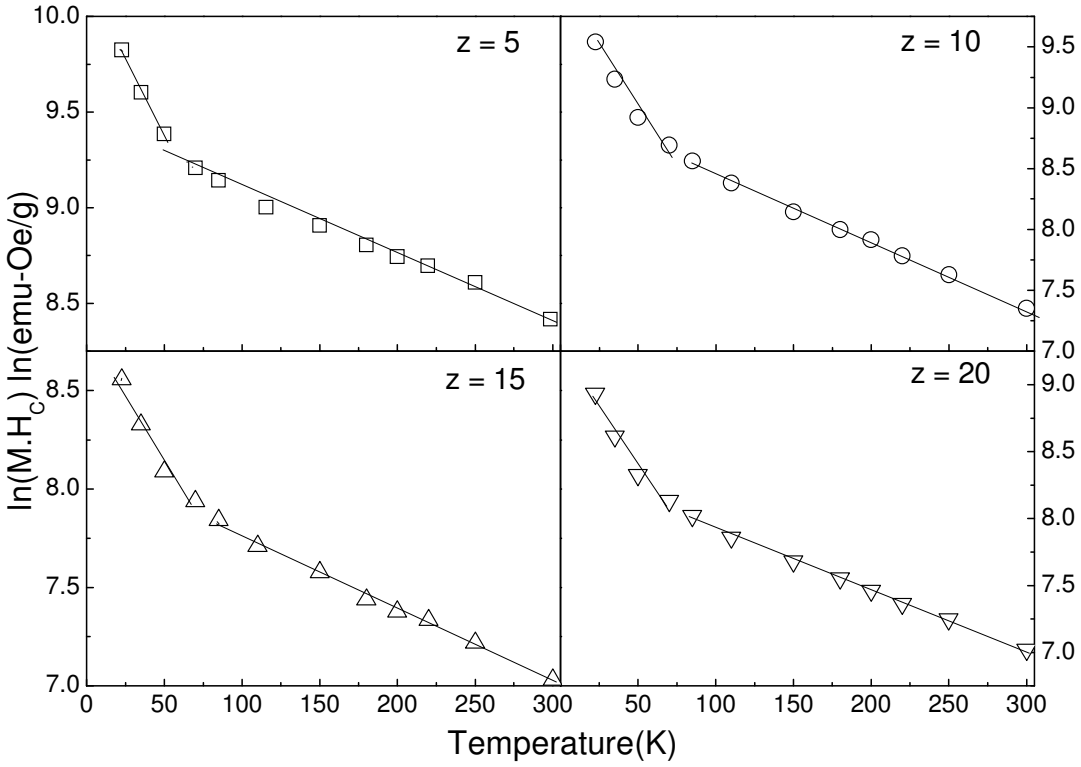


*FIG. 6.36: Plot of ln(M.$H_C$) versus T for amorphous $Fe_{60-z}Mn_zZr_{35}B_5$ alloy powders.*

## 6.5. Mechanical alloying of Fe-Co-Zr-B alloys

### 6.5.1. Structural properties of Fe-Co-Zr-B alloys

$Fe_{60-z}Co_zZr_{35}B_5$ (z = 0 – 20) alloy powders were milled by MA technique. Fig.6.37 shows the HR-TEM images and SAED patterns of $Fe_{60-z}Co_zZr_{35}B_5$ alloy powders. HR-TEM image for the alloy with $z$ = 10 (Fig.6.37a) shows the absence of any crystallites and SAED pattern exhibits

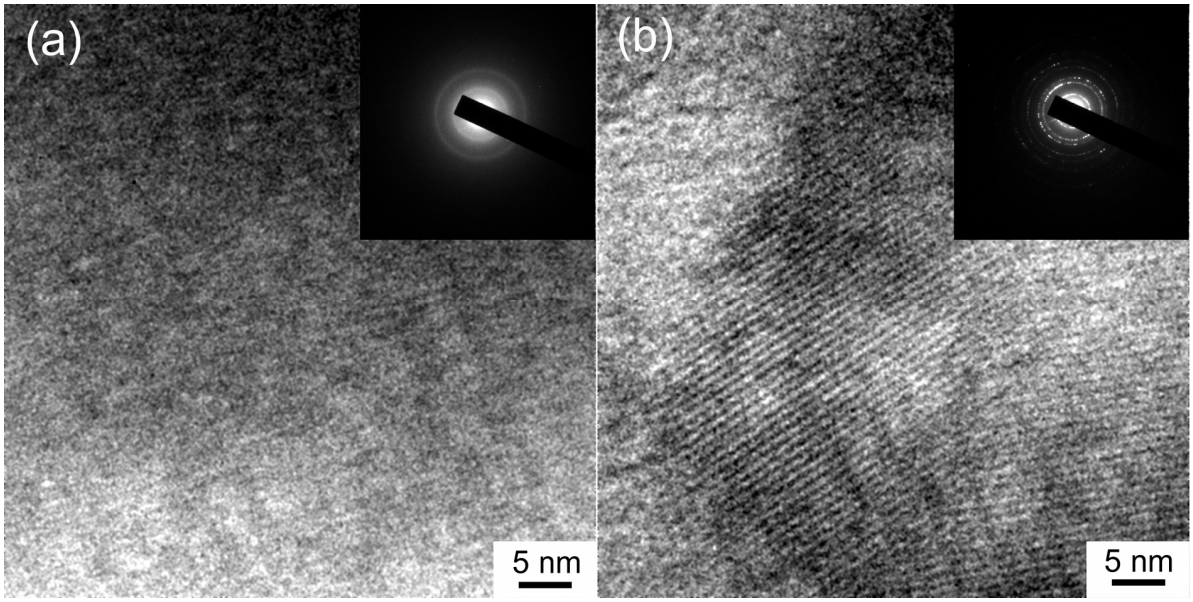


*FIG. 6.37: HR-TEM images and SAED patterns for as-milled $Fe_{60-z}Co_zZr_{35}B_5$ alloy powders with (a) $z$ = 10, (b) 15.*

only diffused halo rings, confirming the amorphous structure of the powders. On the other hand, HR-TEM image and SAED pattern of the alloy with $z$ = 15 shows the presence of crystallites and diffraction rings corresponding to various phase formation, respectively after milling for 150 h. This suggests that the final product of the $Fe_{60-z}Co_zZr_{35}B_5$ alloy powders strongly depend on the composition. To understand the surface morphology of the agglomerated powders with Co addition, the SEM micrographs were observed and shown in Fig.6.38. The morphology of the 5 at.% Co substituted $Fe_{60-z}Co_zZr_{35}B_5$ alloy powders remains same as the Co free powders. With the addition of more than 10 at.% Co, the morphology of the powder becomes highly non-uniform. In addition, flake-like particles and large-sized agglomerated particles with the average size of more than 50 μm were also observed. These results confirm that the single phase amorphous structure in $Fe_{60-z}Co_zZr_{35}B_5$ alloy powders could be obtained for $z \leq 10$.

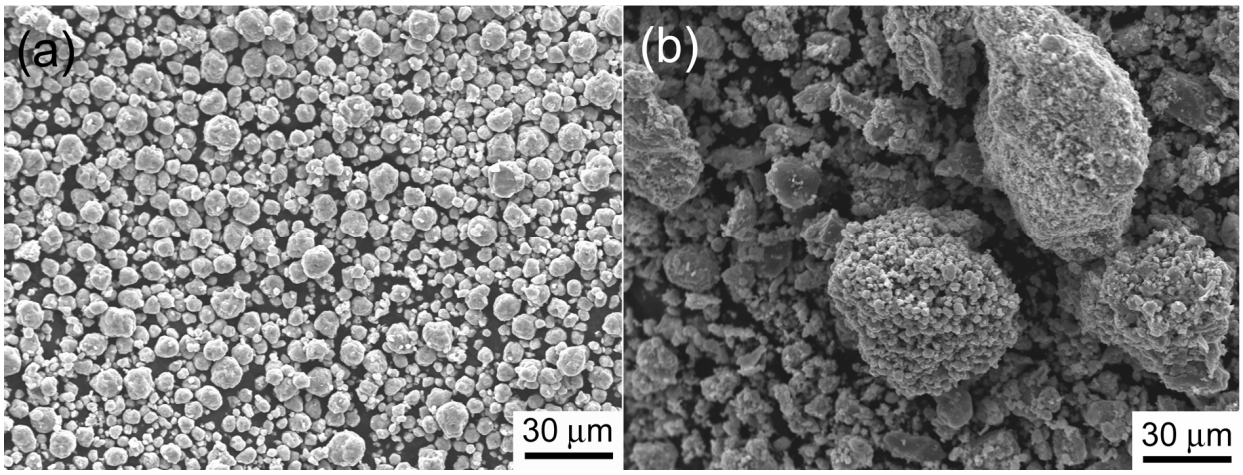


*FIG. 6.38: SEM micrographs of as-milled $Fe_{60-z}Co_zZr_{35}B_5$ alloy powders with (a) z = 5, (b) 10.*

### 6.5.2. Thermal properties of Fe-Co-Zr-B alloys

The stability of the amorphous phase with the Co addition was investigated using DSC. The peak $T_{crys}$ values extracted from DSC curves decrease from 857 K to 840 K for the increase of Co from 0 to 10 at.%. The decrease in $T_{crys}$ is in good agreement with the reports on similar alloy systems [BLAZ2005, MAJU2007, MAOX2005, SHUL1999].

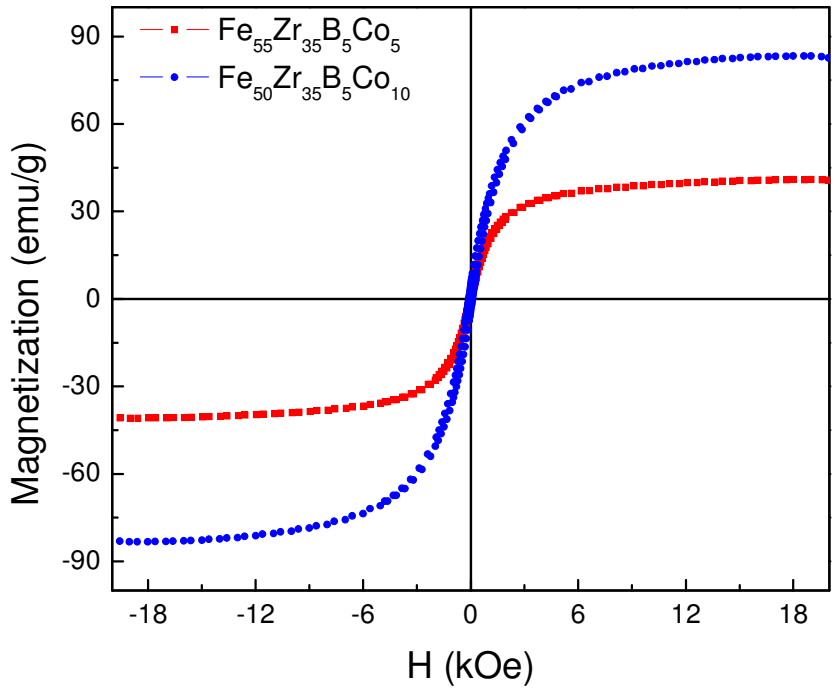


*FIG. 6.39: Room temperature M – H loops for as-milled $Fe_{60-z}Co_zZr_{35}B_5$ alloy powders with z = 5 and 10.*

### 6.5.3. Magnetic properties of Fe-Co-Zr-B alloys.

Room temperature $M - H$ loops of the a-$Fe_{60-z}Co_zZr_{35}B_5$ ($z \leq 10$) alloy powders were measured and the same are depicted in Fig.6.39. $M_S$ value increases from 41 emu/g to 83 emu/g with the substitution of Co up to 10 at.% in a-$Fe_{60-z}Co_zZr_{35}B_5$ alloy powders. This is due to the increase in FM exchange interaction with Co substitution. MA of Fe-Co nanocrystalline powders showed a high value of $M_S$ (greater than 200 emu/g) [ZELE2007]. This large difference is mainly due to the difference in the structural properties. On the other hand, $H_C$ increases from 55 Oe to 99 Oe with the substitution of Co up to 10 at.%. This can be attributed to (i) increase in magnetic anisotropy with Co substitution, (ii) change in the surface morphology, which may act as pinning centers for magnetic domains. To calculate $K_{eff}$, we have fitted the experimental $M - H$ data using eqn.6.2. The determined values of $b$ increases from $1.5\times10^5$ to $8\times10^5$ with the addition of

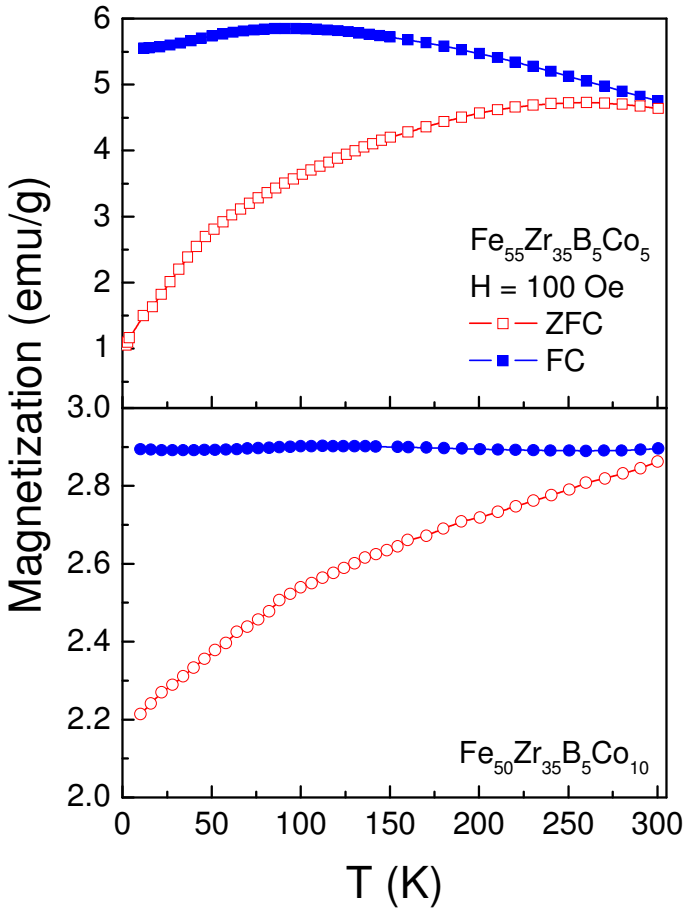


*FIG. 6.40: Temperature dependent ZFC (open symbol) and FC (solid symbol) curves taken at 100 Oe applied magnetic field for amorphous $Fe_{60-z}Co_zZr_{35}B_5$ alloy powders with z = 5 and 10.*

Co from 5 to 10 at.%. This indicates that there is a considerable enhancement of anisotropy with the addition of Co. To understand the temperature dependent behavior with the Co addition, low temperature $M - T$ curves were measured under ZFC and FC conditions with the applied field of 100 Oe. Fig.6.40 shows the $M - T$ curves for a-$Fe_{60-z}Co_zZr_{35}B_5$ alloy powders with $z = 5$ and 10. Both the samples show similar variation of magnetization with the temperature, i.e., exhibiting the bifurcation between ZFCand FC curves up to room temperatures. A similar behavior has been observed in all the milled powders. Fig.6.41 shows the high temperature $M - T$ curves taken under 100 Oe applied magnetic field. $T_C$ of the Co substituted a-$Fe_{60-z}Co_zZr_{35}B_5$ ($z \leq 10$) alloys shifts to higher temperature due to the enhancement of the magnetic moment with the addition of Co.

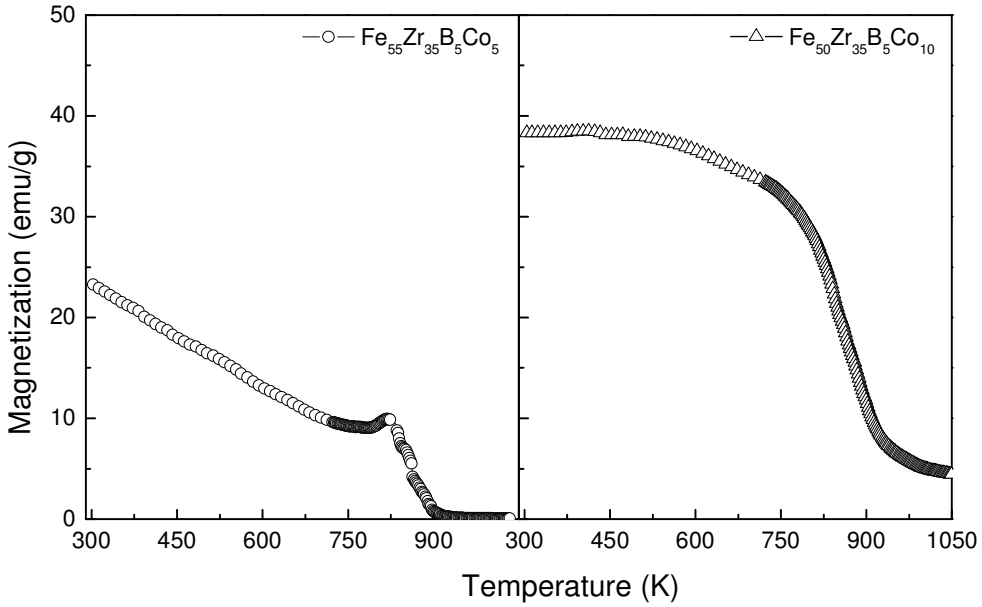


*FIG. 6.41: M – T curves measured at 100 Oe applied magnetic field for $Fe_{60-z}Co_zZr_{35}B_5$ amorphous alloy powders with z = 5 and 10.*

## 6.6. Summary

A systematic study on the preparation and magnetic characterization of mechanically alloyed $Fe_{100-x-y-z}(Co,Mn)_zZr_yB_x$ ($x = 20 – 35$, $y = 0 – 10$, $z = 0 – 10$) alloys powders has been carried out. The salient features of the present studies on a-Fe-(Co,Mn)-Zr-B alloys are as follows:

1. Amorphous Fe-(Co,Mn)-Zr-B alloys powders could be prepared by MA technique over a wide range of compositions. The milling time for the formation of amorphous structure depends on the alloy constitution.
2. Fe-Zr binary amorphous phase could be achieved in a wide range of Zr (25 – 25 at.%) content. Crystallization temperature decreases initially with the Zr substitution up to 30 at.% and then increases.
3. Structural evolution during the milling suggests the formation of twin boundary as a result of mechanical deformation.
4. Coercivity is relatively high in the nanocrystalline state due to the strain present in the materials. The coercivity increases considerably when the intergranular amorphous phase become paramagnetic.
5. Low temperature magnetic properties show strong bifurcation between ZFC and FC curves and the bifurcation exists even up to 10 kOe applied field. In addition, a slow logarithmic relaxation of magnetization was observed in Fe-Zr binary alloys. $T_C$ in ball milled powders was observed to be high (compared to melt-spun ribbons) due to the enhanced magnetoelastic coupling.
6. Stability of the amorphous phase was enhanced with the addition of B in Fe-Zr-B alloy. Crystallization temperature increases with the addition of B up to 7.5 at.%.
7. Saturation magnetization increases with the addition of B due to the enhanced ferromagnetic interactions. Coercivity, saturation magnetization and crystallization temperatures show anomaly at 7.5 at.% B.
8. Stability of the amorphous phase in Fe-Mn-Zr-B alloy powders was further enhanced with Mn addition. The average agglomerated particle size increased with Mn addition.
9. Coercivity of the Fe-Mn-Zr-B powder decreases largely with the increase in Mn content. Also, a sharp magnetic phase transition was observed for 15 at.% Mn.
10. Amorphous Fe-Co-Zr-B powders could be prepared only for Co up to 10 at.%. With the addition of Co in Fe-Co-Zr-B alloy powders, the stability of the amorphous phase is significantly weakened.
11. Saturation magnetization and coercivity increase with the Co addition due to the increase in exchange interactions and local anisotropy, respectively.

# Chapter 7

# Comparative study between the properties of melt-spun and mechanically alloyed samples

In this chapter, a comparative study of the properties of Fe-(Co,Mn)-Zr-B alloys prepared by melt spinning and mechanical alloying (MA) techniques has been carried out. Though the compositions of the Fe-(Co,Mn)-Zr-B alloys are not same for both processing routes, some basic properties and their dependence on the compositions of amorphous and nanocrystalline Fe-(Co,Mn)-Zr-B alloys are worth pointing out. Some of the salient distinctions between the materials obtained from the two diverse processes are listed below:

### 7.1. Structural properties

a. Formation of amorphous phase by melt spinning technique in $Fe_{100-x}Zr_x$ binary alloys was limited to 20 at.% Zr. However, in the present investigation, the amorphous phase could be formed for a wide concentration range of Zr up to 35 at.% Zr by MA technique. In the case of melt spun ribbons, the amorphous phase formed was a single Fe rich phase in all the compositions investigated. On the other hand, both Fe rich (for $x > 20$) and Zr rich (for $x = 20$) amorphous phases were observed in the mechanically alloyed powders.

b. Formation of amorphous phase in the melt spun Fe-(Co,Mn)-Zr-B alloy ribbons depends on the quenching rate (i.e., Cu wheel speed). However, many different factors such as large atomic size ratios, attractive bonding nature between the constituent elements and difficulty of redistribution of these elements for crystallization, milling speed, milling media, ball to powder weight ratio, and milling time decide the formation of amorphous in the mechanically alloyed powders.

c. Nanocrystalline state in Fe-(Co,Mn)-Zr-B melt spun alloys was achieved by controlled annealing around the crystallization temperature, whereas, nanocrystals were obtained directly in the powders by the structural reduction of crystallites with the introduction of defects and dislocations.

### 7.2. Thermal properties

Thermal stability of the amorphous phase in Fe-(Co,Mn)-Zr-B alloy increased with the addition of B and Mn, but the addition of Co deteriorates the stability in both melt spun ribbons and mechanically alloyed powders. The present results suggest that the thermal stability of the amorphous Fe-(Co,Mn)-Zr-B alloys is not dependent on the synthesis route.

### 7.3. Magnetic properties

a. Room temperature ferromagnetic properties of the Fe-Zr alloys improved with the substitution of B and Co in amorphous Fe-Zr alloy ribbons. Excellent soft magnetic properties were achieved in the case of amorphous ribbons. Ultralow coercivity of 0.015 Oe was obtained for the amorphous $Fe_{84}Zr_{11}B_5$ alloy ribbons. The rate of increase of coercivity with the substituting elements decreases with increasing B and Co concentrations in amorphous Fe-Co-Zr-B alloy ribbons. On the other hand, coercivity lies between 30 and 150 Oe for the mechanically alloyed powders. Such large values are mainly due to the stress induced anisotropy in the milled powders. With the addition of Mn in Fe-Zr-B alloys, coercivity increased significantly in the amorphous ribbons. But a large decrease in coercivity from 145 Oe to 25 Oe was observed in the powders for the first time in this investigation. Substitution of Co in Fe-Zr-B alloys increased the coercivity and the saturation magnetization in both the ribbons and amorphous powders.

b. Curie temperature of the amorphous Fe-Zr alloy ribbons is below the room temperature, which increased with the substitution of B and Co and decreased with the addition of Mn. In contrast, Curie temperature of the mechanically alloyed powder is found to be high and weakly dependent on the substituting elements. The large difference in the Curie temperature values is mainly due to the effective anisotropy caused by the induced stresses from the MA process, which improves the stability of the local magnetic structure with long range magnetic ordering via magnetoelastic coupling.

c. The bifurcation between the zero-field cooled and field-cooled magnetization curves was observed only for the Fe-Zr alloy ribbons. This bifurcation phenomenon disappeared not only with the increase in the magnitude of the applied field, but also with the addition of substituting elements. In the case of mechanically alloyed powders, the bifurcation exists even up to 10 kOe applied field.

d. The magnetic hysteresis loops measured at low temperature in amorphous alloy ribbons show the typical nature of soft magnetic materials. But, the initial magnetization curves of magnetic hysteresis loops of amorphous Fe-Mn-Zr-B alloy powders lies outside the main loop for a certain field range and finally meets it again at higher field. This is due to the presence of short-range correlated regions of particle moments forming close magnetic circuits and minimizing the magnetostatic energy.

e. Intergranular exchange coupling exists in both the nanocrystalline alloy ribbons and powders. However, the effect of exchange coupling between the nanocrystals through the ferromagnetic amorphous matrix results excellent magnetic softness in the ribbons. But in the non-equilibrium solid solution produced by MA technique, the stress induced anisotropy is more dominant and the magnetic softness could not be achieved in amorphous alloy powders.

The above comparison brings out the important features observed in the melt spun and mechanically alloyed samples induced by the respective processes. As seen from the examples cited above, some properties are enhanced while some others get deteriorated by the synthesis route. Thus it is possible to tailor the properties of these alloys to some extend by the proper choice of the processing methodology.

# Chapter 8

## Conclusion and scope for future work

## 8.1. Conclusions

In this thesis work, amorphous (a-) Fe-(Co,Mn)-Zr-B alloys were prepared by melt spinning and mechanical alloying (MA) techniques. Detailed studies of structural, thermal, magnetic properties and magnetic domain structure were carried out on the samples using various experimental techniques. Salient features of the current investigations are summarized below:

Structural investigations of a-Fe-(Co,Mn)-Zr-B alloy ribbons suggest that a single Fe rich amorphous phase could be achieved in all the ribbon samples. The thermal stability of the amorphous phase improved with the addition of B in a-Fe-Zr alloys. Crystallization temperature ($T_{crys}$) increases almost linearly with B addition in a-Fe-Zr-B alloys. Importantly, these results showed higher $T_{crys}$ value when compared to the conventional NANOPERM alloys. Temperature dependent coercivity ($H_C$) measurements revealed that the inhomogeneities present in the binary Fe-Zr alloy ribbons disappeared upon B substitution. Also, the room temperature saturation magnetization ($M_S$), Curie temperature ($T_C$) of the Fe-Zr-B alloys improved with B addition. On the other hand, $H_C$ decreased drastically to 0.015 Oe for B addition of 5 at.% and increased slightly on further increase in B. Magnetic domain structure analyses revealed the presence of large-sized domains with relatively smooth and straight domain walls in amorphous Fe-Zr-B alloys. But the average size of the domains decreased when B content was increased above 5 at.%.

Addition of Mn (Co) in a-Fe-(Co,Mn)-Zr-B alloy ribbons shifts the $T_{crys}$ to higher (lower) temperatures. $T_C$ and room temperature $M_S$ decreased (increased) with Mn (Co) addition in a-Fe(Co,Mn)-Zr-B alloys. A maximum $M_S$ value of about 130 emu/g was obtained for the sample with 10 at.% Co and the values of $H_C$ lies below 0.4 Oe for a-Fe-Co-Zr-B alloys. The rate of increase of $H_C$ in a-Fe-Co-Zr-B alloy ribbons decreases with the increase in B and Co substitutions. Moderate values of magnetic entropy ($\Delta S_M$) was obtained for a-Fe-(Co,Mn)-Zr-B alloys. Addition of Co (Mn) in a-Fe-(Co,Mn)-Zr-B alloys increased (decreased) the $\Delta S_M$ value. A maximum $\Delta S_M$ value of 1.93 J/Kg/K at 18 kOe could be achieved for a-$Fe_{74}Co_{10}Zr_{11}B_5$ alloy. The $\Delta S_M$ value obtained in the presently investigated samples is higher than the conventional NANOPERM alloys.

In order to obtain the nanocrystalline microstructure and to improve the soft magnetic properties, a-Fe-Co-Zr-B alloy ribbons were annealed under magnetic field applied along the length of the ribbons. Also, the close correlation between the microstructure, magnetic domain structure and magnetic properties was investigated. Annealing at 823 K showed a weak tendency for the formation of $\alpha$-Fe nanocrystals with lower volume fraction in Fe-Co-

Zr-B alloy. Also, the formation of $\alpha$-Fe crystalline phase is associated with other Fe-Zr compounds such as $Fe_3Zr$ at elevated temperatures. $H_C$ of Fe-Co-Zr-B nanocrystalline alloys with and without Co substitution increases significantly with increasing annealing temperature up to 823 K. The rate of increase of $H_C$ decreased in Fe-Co-Zr-B alloys with the substitution of higher amount of B. However, $H_C$ of the Fe-Co-Zr-B alloys annealed at 923 K increases by two orders in magnitude due to the increase in effective anisotropy, directional ordering of Fe-Co pairs in Co substituted alloys and structural inhomogeneities. Magnetic domain structure analysis revealed the presence of large-sized domains with smooth and straight domain walls in Fe-Co-Zr-B alloys annealed up to 823 K. However, the average size of the domains decreased with increasing Co content. In addition, annealing Co substituted Fe-Zr-B alloys at 923 K resulted in a changeover from pinned domains to ripple domain structure. A maximum $M_S$ value of 175 emu/g and $H_C$ of 0.35 Oe was obtained for the $Fe_{69}Co_{10}Zr_{11}B_{10}$ alloy annealed at 823 K exhibiting excellent soft magnetic properties. Furthermore, $H_C$ of $Fe_{89-x-y}Co_yZr_{11}B_x$ alloys annealed up to 823 K remained below 0.7 Oe. A good correlation between nanocrystalline microstructure, magnetic domain structure and resulting magnetic properties in Fe-Co-Zr-B alloy ribbons was obtained.

Amorphous Fe-(Co,Mn)-Zr-B alloy powders could be prepared by MA techniques over a wide range of Zr compositions. The milling conditions required for the formation of amorphous phase highly depends on the composition of the alloy systems. The formation of binary amorphous Fe-Zr alloy powders could be achieved over a wide range of Zr content (25 – 35 at.%). Formation of twin boundary during MA as a result of mechanical deformation was observed for the first time in Fe-Zr alloy. $T_{crys}$ decreased initially with the Zr substitution up to 30 at.% and then increased. $H_C$ is relatively large both in the nanocrystalline state and amorphous phase due to the induced stress during MA. Temperature dependent $H_C$ in two-phase structured Fe-Zr alloy increased largely when the intergranular amorphous phase became paramagnetic. Note that the exchange coupling effect in mechanically alloyed Fe-Zr alloy powders was investigated for the first time. The results suggest that stress induced effective anisotropy is dominant and hence lower $H_C$ may not achievable in case of ball milled powders. Low temperature magnetic properties of Fe-Zr amorphous powders showed strong bifurcation between ZFC and FC curves. The bifurcation was observed even at 10 kOe applied field. In addition, a slow logarithmic relaxation of magnetization was observed. $T_C$ in ball milled powders was observed to be high (compared to melt-spun ribbons) due to the enhanced magnetoelastic coupling. Stability of the amorphous phase was enhanced with the

addition of B in Fe-Zr-B alloy. $T_{crys}$ increased with the addition of B up to 7.5 at.%. $H_C$, $M_S$ and $T_{crys}$ values show anomaly at 7.5 at.% B. Stability of the amorphous phase in Fe-Mn-Zr-B alloy powders could be further enhanced with Mn addition. The average agglomerated particle size increased with Mn addition and the particle shape also became spherical. A large decrease in $H_C$ value of a-Fe-Mn-Zr-B alloys powder with Mn addition was observed for the first time. Addition of Mn was found to decrease the effective anisotropy of the system and makes the system more homogeneous. On the other hand, a-Fe-Co-Zr-B alloy powders could be prepared only for Co content up to 10 at.%. With the addition of Co in Fe-Co-Zr-B alloy powders, the stability of the amorphous phase is significantly reduced. $M_S$ and $H_C$ values also showed an increase due to the increase in exchange interactions and local anisotropy, respectively. In the end, a comparative study between the properties of Fe-(Co,Mn)-Zr-B alloy prepared by MA and melt spinning techniques has been done to bring out the salient differences in the materials synthesized using the two diverse routes.

## 8.2. Scope for future work

The current investigations have brought out some new and interesting features of the alloys processed through the two diverse routes. These observations have not only revealed the potential of these materials for applications but have also shown paths for further work in these materials. Some of the possibilities are briefly discussed below to serve as fitting conclusion to this thesis report.

Since amorphous and nanocrystalline Fe-Co-Zr-B alloy ribbons show ultra soft magnetic properties, it would be interesting to perform magnetic impedance measurements to determine the change in the magnetoimpedance with the improved soft magnetic properties. Temperature dependent electrical resistivity and magnetotransport measurements of these alloys would help in understanding the role of substituting elements on the various scattering mechanisms involved and their effective contributions to the total electrical resistivity. As the magnetic properties of the Fe-Co-Zr-B nanocrystalline alloys improved with B and Co substitution, the investigation of magnetocaloric effect in these alloys could be rewarding. Effect of mechanical milling of the amorphous Fe-Co-Zr-B alloy ribbons on the microstructure and magnetic properties would be useful for optimizing the properties for specific applications. The influence of transverse and rotating field annealing on the control of induced anisotropy and resulting magnetic properties could be another topic of interest. Similarly, amorphous Fe-(Co,Mn)-Zr-B alloy powders prepared by mechanical alloying can be compacted in different shapes and sintered systematically for the improvement of soft

magnetic properties in powders. The effect of Mn substitution in a-Fe-Mn-Zr-B alloys can be studied in more detail using Mossbauer spectroscopy. Such studies on the local magnetic structure might help in understanding the enhancement in the soft magnetic properties of these alloys.

**PUBLICATIONS**

**IN JOURNALS:**

1. Effect of Co or Mn addition on the soft magnetic properties of amorphous $Fe_{89-x-y}Zr_{11}B_x(Co,Mn)_y$ (x = 5, 10 and $0 \leq y \leq 10$) alloys, **Debabrata Mishra**, A. Perumal, P. Saravanan and A. Srinivasan, Journal of Magnetism and Magnetic Materials 321 (2009) 4097.

2. High temperature coercive field behavior of Fe-Zr alloy, **Debabrata Mishra**, A. Perumal and A. Srinivasan, Journal of Applied Physics 105 (2009) 07A306.

3. Magnetic properties of mechanically alloyed $Fe_{100-x}Zr_x$ ($20 \leq x \leq 35$) powder, **Debabrata Mishra**, A. Perumal and A. Srinivasan, Journal of Physics D: Applied Physics 41 (2008) 215003.

4. High temperature magnetic properties of mechanically alloyed Fe–Zr powder, **Debabrata Mishra**, A. Perumal and A. Srinivasan, Materials Letters 62 (2008) 2640.

5. Structural, Kinetic And Magnetic Properties Of Mechanically Alloyed Fe-Zr Powders, **Debabrata Mishra**, A. Perumal and A. Srinivasan, AIP Conference Proceedings 1003 (2008) 219.

6. Studies on Ferromagnetic Nanocrystalline Fe-Zr-B alloys, **Debabrata Mishra**, A. Perumal and A. Srinivasan, Proc. DAE-SSP Symp. 51 (2006) 273.

7. Role of microstructure and domain structure on the soft magnetic properties of magnetic field annealed $Fe_{89-x}Zr_{11}B_x$ alloys**, Debabrata Mishra**, A. Perumal and A. Srinivasan, Int. J. Nanoscience (Under review).

8. Magnetic properties of interacting amorphous Fe-Zr-B-Mn magnetic nanoparticles, **Debabrata Mishra**, A. Perumal and A. Srinivasan, J. Alloys Compd. (to be submitted).

9. Magnetic properties and magneto-caloric effect of amorphous Fe-Zr-B alloy ribbon, **Debabrata Mishra**, A. Perumal and A. Srinivasan, Physica B (to be submitted).

10. Evolution of structural and magnetic properties of Fe-Zr binary alloys, **Debabrata Mishra**, A. Perumal and A. Srinivasan, (Manuscript under preparation).

**IN CONFERENCES:**

1. Role of microstructure and domain structure on the soft magnetic properties of magnetic field annealed $Fe_{89-x}Zr_{11}B_x$ alloys, **Debabrata Mishra**, A. Perumal, and A. Srinivasan, International Conference on Advanced Nanomaterials and Nanotechnology – 2009, Indian Institute of Technology Guwahati, Guwahati – 781 029, INDIA.

2. Composition dependent properties of mechanically alloyed amorphous Fe-Zr-B powders, **Debabrata Mishra**, A. Perumal and A. Srinivasan, International conference on mechanical alloying(INCOME-2008), Jamshed pur, India.

3. High temperature coercive field behavior of Fe-Zr alloy, **Debabrata Mishra**, A. Perumal and A. Srinivasan, MMM Conference 2008, Austin, Texas.

4. Structural, Kinetic And Magnetic Properties Of Mechanically Alloyed Fe-Zr Powders, **Debabrata Mishra**, A. Perumal and A. Srinivasan, International conference on magnetic materials, Kolkata (ICMM 2007).

5. Studies on Ferromagnetic Nanocrystalline Fe-Zr-B alloys, **Debabrata Mishra**, A. Perumal and A. Srinivasan, DAE Solid State Symp., 2006, Bhopal, India.

6. Coercivity and magnetic relaxation behaviors of interacting Fe-Mn-Zr-B nanoparticles, **Debabrata Mishra**, A. Perumal and A. Srinivasan, ICONSAT2010 (Accepted).